STUDY OF CO_2 INJECTION AT CITRONELLE OIL FIELD USING LUMPED MASS MODELING AND FIELD DATA VALIDATION

by

Yangguang Liu

A dissertation submitted to the faculty of
The University of North Carolina at Charlotte
in partial fulfillment of the requirements
for the degree of Doctor of Philosophy in
Infrastructure and Environmental Systems

Charlotte

2014

Approved by:

_____
Dr. Shen-En Chen

_____
Dr. Jy S. Wu

_____
Dr. Vincent O. Ogunro

_____
Dr. Andy R. Bobyarchick

_____
Dr. Thomas Nicholas

ABSTRACT

YANGGUANG LIU. Study of CO_2 injection at Citronelle Oil Field using lumped mass modeling and field data validation. (Under the direction of DR. SHEN-EN CHEN)

Carbon sequestration in geological formation is an ongoing effort of the research community to address the issue of curbing excessive anthropogenic CO_2 emissions. This dissertation focuses on the development of a theoretical framework in establishing the criteria for geophysical monitoring using passive seismic method. The theoretical framework is established via modeling geological formation using a multi-degree of freedom model. Three main aspects are introduced in this dissertation: 1) the DoReMi passive sensing technique used to monitor CO_2 injection at Citronelle Oil Field in Alabama; 2) the multi-physical MDOF lumped mass model employed to simulate wave propagation in an oil field in both linear and nonlinear conditions; and 3) comparisons of the shear wave velocity obtained from the experimental data and numerical simulation results.

Field test results show that shear wave velocity of the strata in the reservoir and the stress changes are consistent. Stress change at oil bearing layer and calcite strata in inverse relationship.

The proposed MDOF model accounts for the influence of stiffness of the geomaterial, which include oil-bearing layer and calcite and saline sand stones. The geological formation of Citronelle Oil Field is used in the numerical simulation. A fourth order Runge-Kutta method is employed for the time integration and a Matlab program was developed for this study. The wave response from the MDOF lumped mass model

are changing with the changing properties of CO_2 storage layer and overburden layers (calcite and saline sand layer).

In linear condition, as the stiffness of oil bearing layer changes, spectral amplitude percentage difference (SAPD) value change is frequency dependent and higher frequency experienced larger changes than lower frequency amplitudes. $\Delta V/V$ (velocity changes) derived from the simulation results show that the changes varied with depth are detectable. As the stiffness of calcite and saline layer increases, $\Delta V/V$ has significant changes on the magnitude (as large as 0.35) and similar to the $\Delta V/V$ obtained from experimental results.

In nonlinear condition, as the stiffness of oil bearing layer changes is controlled by positive or absolute displacement, simulation results show some frequency modes are more sensitive than other frequencies. However, nonlinear phenomenon is not fully understood and need further investigation.

Tripartite spectral plots (TSP) show good visual differences for site condition changes in both linear and nonlinear conditions, but are too complicated to interpret.

The study of the research provided a theoretical understanding of the wave phenomena involved in a typical oil field that is undergoing CO_2-EOR process, and the modeling technique can be used to guide the design of geophysical monitoring scheme in the oil field with different geological conditions.

DEDICATION

This dissertation is dedicated to my wife and daughter.

ACKNOWLEDGMENTS

I would like to thank my advisor Dr. Shen-En Chen who has been a wonderful mentor, that not only taught me the inspiration to be a good researcher but also serve as a great role-model as a person. This dissertation would not have been possible without Dr. Chen's encouragement and supports.

I would also like to thank my co-advisor Dr. Jy S. Wu for recruiting me to the INES program, helping me to arrange research schedule and answering many questions in my daily life and studies.

I would to thank my committee members, Dr. Vincent O. Ogunro, Dr. Andy R. Bobyarchick and Dr. Thomas Nicholas for their support and guidance in completing this dissertation.

I would also like to acknowledge financial support of the China Scholarship Council (CSC), the U.S. Department of Energy, the Graduate Assistant Support Plan (GASP) from the University of North Carolina at Charlotte (UNCC).

I would also like to acknowledge the technical supports and advices from Dr. Peter M. Walsh of the University of Alabama at Birmingham.

I would also like to thank six people that have the most influence in my student study and help me get here: Drs. Jianhua Yue, Zhengfu Bian, Shucai Liu, Shouhua Dong, Zhixin Liu and Zhihai Jiang from China University of Mining and Technology (CUMT).

TABLE OF CONTENTS

LIST OF TABLES

LIST OF FIGURES

LIST OF ABBREVIATIONS

BOPD	barrels of oil per day
BSEM	borehole-to-surface electromagnetic
CAES	compressed air energy storage
CCS	carbon capture and storage
COV	coefficient of variation
CO_2	carbon dioxide
DFT	discrete Fourier transform
DoReMi	Derivation of ReMi
DOE	Department of Energy
EOR	enhanced oil recovery
EM	electromagnetic
ESP	electric submersible pump
FEM	finite element method
FFT	fast Fourier transform
GHG	greenhouse gas
MC	multicomponent
MEMS	Micro-Electro-Mechanical Systems
MDOF	multiple degree of freedom
N	Newton
P-wave	longitudinal wave
psig	Pounds per squre inch guage

ReMi	Refraction Microtromer
ROV	remotely operated vehicle
SAPD	spectral amplitude percentage difference
SDOF	single degree of freedom
TSP	Tripartite spectral plot
1-D	one-dimensional
2-D	two-dimensional
3-D	three-dimensional
4-D	time-lapse three-dimensional

CHAPTER 1: INTRODUCTION

1.1. Background

This study originated from the research project: “Carbon-Dioxide-Enhanced Oil Production from the Citronelle Oil Field in the Rodessa Formation, Southern Alabama”, which is funded by the U.S. Department of Energy (US DOE), National Energy Technology Laboratory. The goal of the research project is to demonstrate the feasibility of enhanced oil recovery (EOR) using carbon dioxide (CO_2) at the Citronelle Oil Field in Mobile County, Alabama.

Global CO_2 emission from the consumption of energy, including petroleum, natural gas, coal, electricity and renewables, from 1980 to 2011, is shown in FIGURE 1.1, which indicates CO_2 emission has increased rapidly in recent years. Geological CO_2 sequestration has been recognized by the US DOE and many parts of the world (i.e. Europe, Australia) as the most viable technique for reducing greenhouse gas (GHG) emissions (Bachu 2008; Holloway 2005; Plasynski et al. 2009; Reichle et al. 1999; Webre 2012; White et al. 2003). However, CO_2 capture and storage is an expensive process. To add cost benefit to the process, CO_2 injection has been suggested to enhance oil recovery in depleted oil fields (Blunt et al. 1993; Esposito et al. 2008; Gaspar Ravagnani et al. 2009; Lake 1989). This technique is called CO_2-EOR. There are currently, several well-known commercial CO_2-EOR projects in the U.S. including the Permian Basin of Texas and New Mexico, the Williston Basin of Saskatchewan, and the

Gulf of Mexico Basin of Mississippi (Esposito et al. 2008). A recent EOR practice survey shows that there are about 114 active commercial CO_2-EOR projects in the U.S. and produced total over 280,000 BOPD (barrels of oil per day) by injecting over 2 billion cubic feet of CO_2 (OGJ 2010).

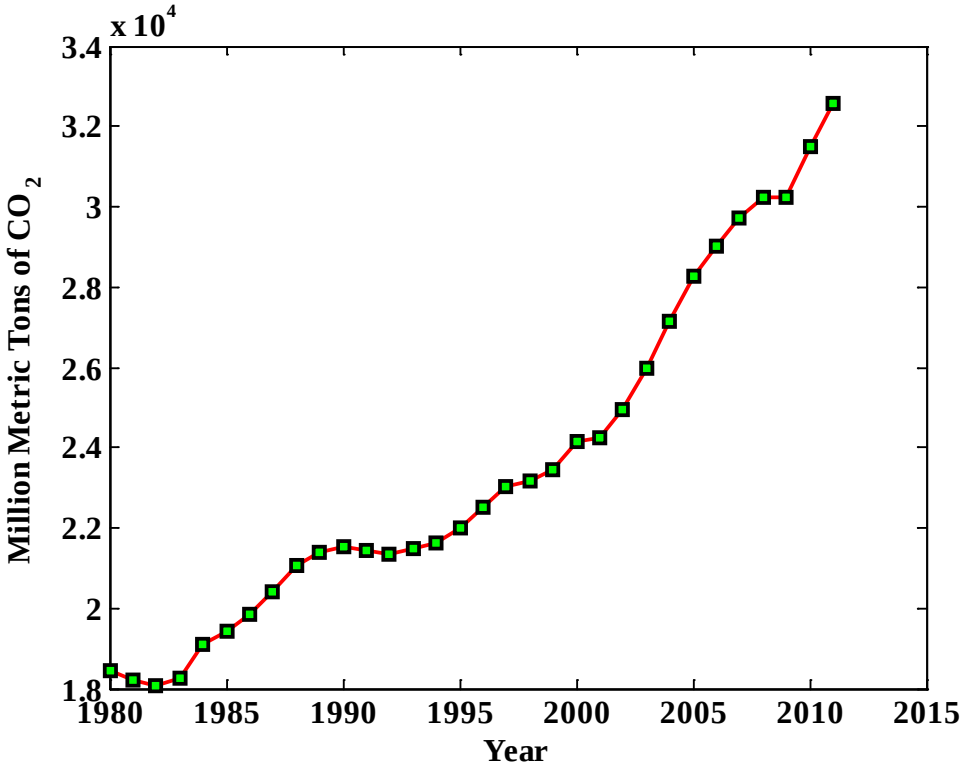

FIGURE 1.1: Total CO_2 emission from the consumption of energy (EIA 2014)

Geophysical testing, using seismic measurements, plays an important role in detecting changes in the presence and migration of CO_2 during and after injection (Chadwick et al. 2009; McKenna et al. 2003; White 2009). The success of geophysical testing in monitoring CO_2 migration in the oil reservoir can prevent possible leakage of CO_2 back into the atmosphere; hence reduce its environmental impacts.

While no CO_2 leakage has been reported at any injection site, it is important to install careful monitoring programs for such practices. Recent studies of remote sensing

data indicated that some of the injection sites may have experienced surface uplift: Using satellite SAR data, Rutqvist et al. (2010), Morris et al. (2011) and Onuma et al. (2011) were able to detect surface uplifts at the InSalah, Algeria injection site. Surface uplifting may have significant geomorphic implications at the injection site and should be carefully monitored. An effective monitoring program is therefore necessary at the injection sites in order to detect changes in geomorphology and the migration of CO_2 within the storage reservoir (Arts et al. 2004; Chadwick et al. 2009; Giese et al. 2009; Hoversten et al. 2002; White 2009).

Most geophysical techniques used to monitor the storage of CO_2, are field applications without strong theoretical validation, because it is very difficult to determine the exact field conditions. Site specific geology, topography and project financing often limit the application of specific techniques to other regions or geologies. Therefore, it is necessary to obtain a theoretical understanding of the wave phenomena involved in the seismic monitoring of a typical oil field that is undergoing CO_2-EOR process.

Passive seismic sensing is proposed because the field of study, the Citronelle, has several wells located on private properties. Therefore, it is prohibitive to perform active seismic investigations near residences. These conditions required us to find an unconventional monitoring method to study the influence of CO_2 injection, sequestration and oil production. Pumps commonly used in petroleum production include downhole power oil pump, electric submersible pump (ESP), etc; and mechanical vibrations will occur when the downhole pumping unit is operating (Kirby et al. 2005). These vibration waves propagate through the subterranean layers can be monitored using passive sensing.

However, there are no detailed studies that show the effects of vibration caused by ESP for a CO_2-EOR field to date.

1.1.1 Problem Statement

The goal of this research is to provide a theoretical understanding of passive wave propagation phenomena involved in a simulated oil field that is undergoing the CO_2-EOR process. The theoretical understanding can help determine the sensitivity requirements of geophysical testing method, which is essential for an effective monitoring scheme using passive seismic sensing. In addition, uncertain strata information in the Citronelle Oil Field to the depth of 5,500 ft (1,676.4 m) needs through-depth (full-field) detection by using a reliable geophysical testing. With reliable geophysical monitoring method, site condition changes related to the CO_2-EOR process may be detected. In this study, the site conditions at the Citronelle Oil Field will be simulated and used for the theoretical wave propagation process modeling.

Previous works on seismic sensing at oil fields have demonstrated the effectiveness in using geophysical testing to detect the change in strata stress due to CO_2 injection (Chen and Liu 2011; Qi 2010), the migration path of gas-oil displacement (Angerer et al. 2002; Chadwick et al. 2009; White 2009) and the temporal transition of oil field conditions (Chadwick et al. 2009). The complex multi-physical problem of mechanical waves propagating through a porous media is originally proposed by Biot (1956a, 1956b). However, the poromechanics principles are extremely difficult to expand to global monitoring techniques. In particular, the interaction of supercritical CO_2 under high pressure with the in situ pore fluid, which is likely a mix of oil, gas and water, and wave propagation, is not yet fully understood. Hence, detailed simulation is very

challenging to perform without exact site parameters, which are typically required of commercial geophysics simulators.

In this study, a simple numerical simulation assuming lumped mass models is proposed. Multiple Degree of Freedom (MDOF) models are widely used in numerical analysis of complex dynamic problems, such as structural seismic responses (Ching and Glaser 2001), and wave propagations (Newmark 1959; Smith and Newmark 1958). The method simplifies the dynamic system into a series of discrete points (lumped masses) that satisfy the requirements of the equations of motion. Here, the suggested MDOF model is used to simulate the wave propagation at the Citronelle Oil Field. With sufficient discretization, it can provide an approximation of the propagating waves that travel through the media where CO_2 injection and oil production occur.

1.1.2 Significance of the Research

This research will gain a theoretical understanding of the basic wave propagation mechanism as a result of CO_2 injection in the oil extraction process. With the injected CO_2 pressure increase, the properties of CO_2 storage layer will change and reflect in the wave responses of the suggested MDOF dynamic model. According to the outcomes of the wave propagation in the oil field, the sensor sensitivity requirements for geophysical testing is then determined. The proposed study can then be developed into a methodology that can be used to guide geophysical detection in the oil field with different geological conditions.

Even though the MDOF dynamic model may be archaic, it provides a simple, first order explanation of the otherwise complex physical phenomenon, which can be simulated with relative ease.

1.2. Scope of Work

The proposed research involves first a statistical analysis of the field data to understand the monitoring outcomes at Citronelle. Second, Matlab program for the MDOF model simulates wave propagation through the Citronelle Oil Field is developed. Several assumptions about the oil field will be made to generate the model parameters including discrete, lumped mass, stiffness and damping terms. As a validation, shear wave profiles derived from numerical simulation will be used to compare to the field results.

The input excitation to the MDOF model is assumed to come from pumping units at the wells, which is assumed to be ESPs (downhole pump). The MDOF model will be used to study the following issues:

(1) Effect of discreteness to wave phenomena using MDOF technique

(2) Effect of stiffness change on the model

(3) Sensor sensitivity

(4) Effect of nonlinearity and linearity

(5) Time scale issues

1.3. Research Objectives and Methodology

The primary objectives of this research are: 1) using lumped mass modeling to investigate, the wave propagation and the sensitivity requirement of geophysical seismic testing during CO_2 injection monitoring; 2) to determine accuracy of the lumped mass model by comparing to the field results; and 3) to investigate approaches (indices) that can reflect on the change of conditions.

Based on the field seismic test results collected at the Citronelle Oil Field and the pressurization history at the site, statistical (covariance) analysis is performed on the field geophysics data. New understanding of the wave responses from field injection is then applied to the numerical modeling technique. The research mainly discusses the geophysical method used to monitoring CO_2 injection, but the methodology developed can also be extended to the inquisition of many other engineering and environmental problems, such as soil and ground water pollution, etc. This is especially relevant in the 21^{st} century where we see more peaceful times and the global population and economic growth are resulting in unprecedented impacts on the environments, particularly, on climatic changes (Pielke et al. 2008; Ranger and Niehörster 2012). A detailed discussion of the applied methodology to other applications is included in the dissertation (Chapter 6).

The research methodology then proceeds to develop an analytical tool to simulate the wave propagation and compare the simulation data with the experimental results. Numerical simulation is performed by using 1-D MDOF lumped mass model. The variable stiffness values of oil bearing layer are used in both linear and nonlinear conditions. In addition, the variable stiffness values of Saline and Calcite layers are also performed by the MDOF model. Finally, the study continues to observe and investigate the simulation results from the MDOF model including the development of new approach for data interpretation.

1.4. Anticipated Outcomes and Contributions

The outcomes of the research include:

(1) A substantially improved understanding of the wave propagation in the reservoir at Citronelle Oil Field, including the effects of phase change in the oil bearing layer.

(2) A recommendation for sensor sensitivity for geophysical testing sensor selection.

(3) An application software for simulation of wave propagation through the oil field with fluid injection project. A Matlab^{TM} simulator, DeepCO_2MDOF, is developed for this study. The structure of the software is shown in FIGURE 1.2.

1.5. Dissertation Structure

This dissertation composed of nine chapters: Chapter 2 is related to limited literature review on numerical simulation and field monitoring of geophysical methods in CO_2-EOR and CO_2 sequestration, general application of geophysical method and the lumped mass modeling methods to engineering and environmental problems; Chapter 3 describes the Citronelle field monitoring works and presents the experimental results of the more than three years of monitoring of CO_2 and water injections; Chapter 4 describes lumped mass modeling, assumptions made and the numerical analysis approach. The parametric study of the MDOF model is also listed in this chapter. Chapter 5 describes the simulation of the MDOF linear model and the corresponding results. Chapter 6 documents the analysis of the simulation results of the MDOF nonlinear model and discussion there upon. Chapter 7 presents detailed comparisons of the different indices. Chapter 8 presents the conclusions of the research. Finally, Chapter 9 describes

recommendations for future studies. The main parts of the dissertation are shown in FIGURE 1.3.

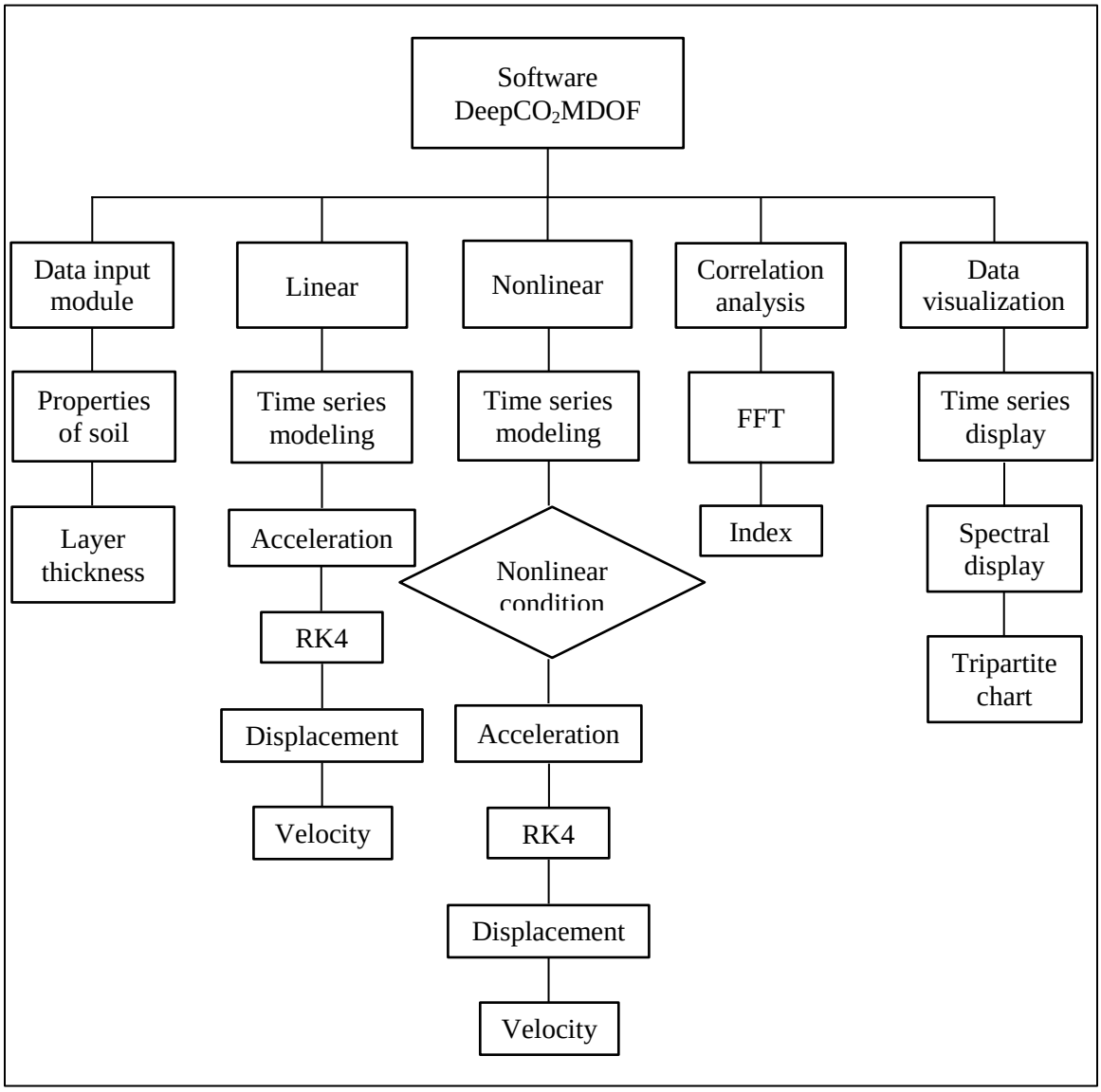

FIGURE 1.2: Software structure

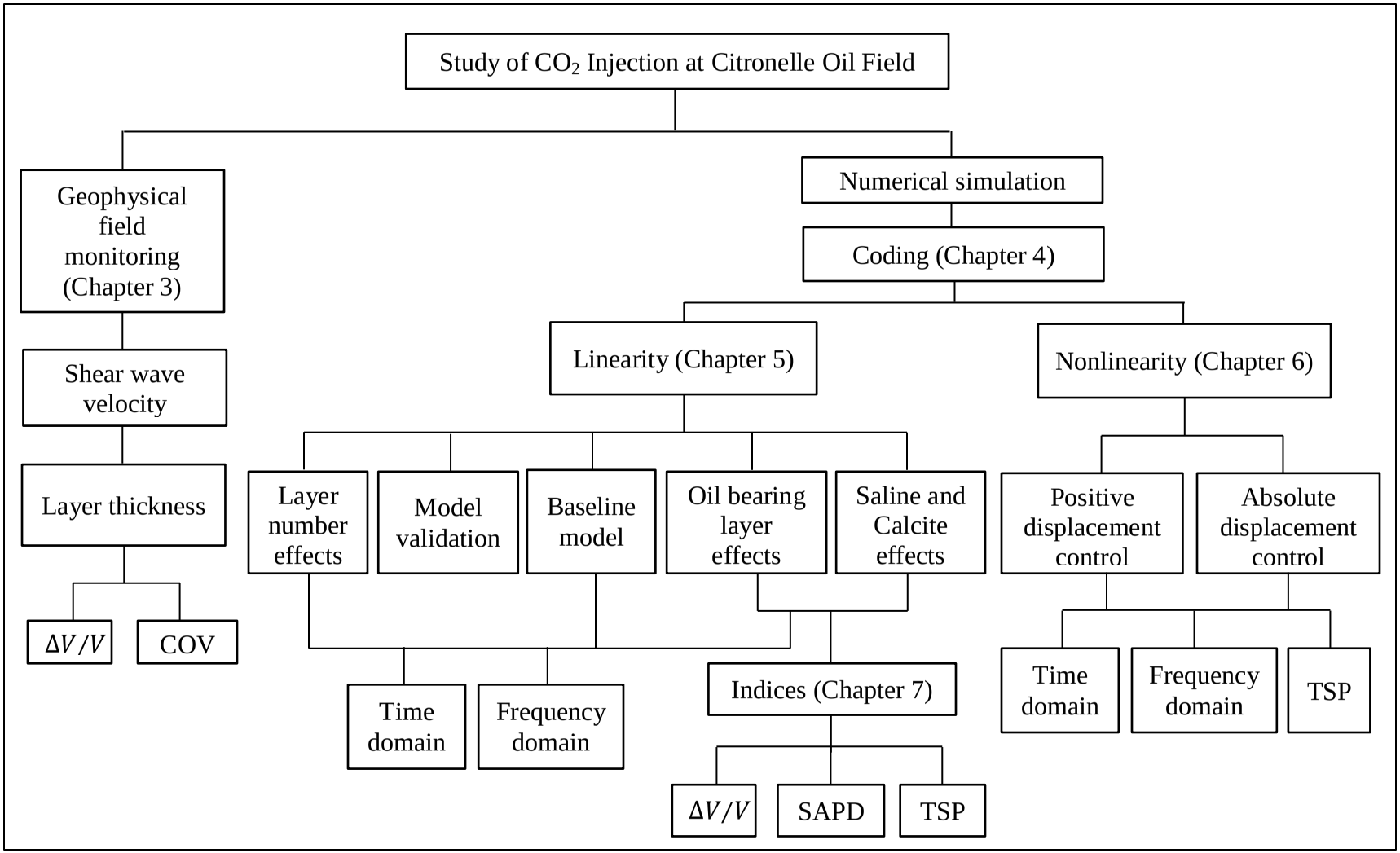

FIGURE 1.3: Structure of dissertation

CHAPTER 2: LITERATURE REVIEW

2.1. Introduction

CO_2-EOR is viable for sequestering CO_2 and increasing oil production at oil fields. However, injection of CO_2 into geological formations may have negative environmental implications. For example, high pressure CO_2 injection may lead to the formation pressure rising over a large area (Mutschler et al. 2009). Stress in the surrounding geological formation may affect the structural stability in a CO_2 reservoir (Hawkins et al. 2007). Therefore, it is necessary to monitor CO_2 storage reservoir before, during and after CO_2 injection. Large-scale geological storage of CO_2 is being monitored at several sites around the world, for example, Sleipner (North Sea), Weyburn (Canada) and In Salah (Algeria) (Chadwick et al. 2009). The geophysical techniques are typically performed to monitor CO_2 movement during sequestration and to determine the potential of possible geological changes that may occur due to the injection of CO_2.

2.2. Geophysical Methods Used in CO_2 Storage Reservoir

Chadwick et al. (2009) showed that several geophysical sensing methods, such as gravity, active seismic, electrical, and electromagnetic methods, can be used to observe changes due to CO_2 migration.

3D surface seismic method is the most powerful geophysical sensing technology in subsurface imaging for oil prospecting and seismic liquefaction prediction, etc (Chadwick et al. 2009). McKenna et al. (2003) found that the method can generate

reasonable seismic data for monitoring CO_2 if the storage reservoir has good injection and storage characteristics. However, the seismic technique is difficult to use to image the location of CO_2 in reservoirs with low porosity and low permeability. Time-lapse 3D (also known as 4D) seismic monitoring surveys were conducted at the Weyburn-Midale field, Canada, from 2000-2007, the monitoring results showed the spread of CO_2 in the reservoir (White 2009). Passive seismic monitoring surveys have also been conducted at the Weyburn-Midale field to detect microseismic events (Verdon 2012; Verdon et al. 2010; White 2011): less than 100 events occurred over 5 years of microseismic monitoring at Weyburn indicated that the location is not undergoing large geomechanical deformation in the reservoir. Similar studies have been performed at the Sleipner West field in the Norwegian North Sea for carbon capture and storage (CCS) in saline aquifers (Arts et al. 2004).

For the passive seismic technique, any small movement near the reservoir can be regarded as a microseismic event, which can be considered as seismic source. These microseismic events can be produced by the creation of new fractures accompanied by the high pressure CO_2 injection within a storage reservoir. These microseismic events can also be influenced by pre-existing faults and structures, and natural seismicity. Passive seismic method uses no active or human controlled excitation source; therefore, it can be performed at any time. Passive seismic monitoring method has been successfully used in the oil and gas industry (Maxwell et al. 2010; Maxwell and Urbancic 2001; Verdon et al. 2010). The Derivative of Refraction Microtremor (DoReMi) geophysical testing method was reported by Qi (2010) for site monitoring at the Citronelle Oil Field in Mobile, Alabama. Subsequent monitoring during CO_2 injection conducted by Chen and Liu

(2011) and (Liu 2012) showed evidence of strata pressurization in the form of increased shear-wave velocity. Other seismic methods include the multicomponent (MC) seismic method, which has been successfully performed to detect CO_2 floods at the Vacuum Field in Texas (Angerer et al. 2002) and at the Weyburn Field in Saskatchewan (Davis et al. 2003).

The basic principle of electromagnetic (EM) method is that an EM field generated by a sender will send through the media, and the conductive material in the ground will produce a secondary EM field which can be detected by a receiver. Because CO_2 is resistive in nature and is displacing the conductive formation waters in the reservoir, the EM method has the potential for monitoring CO_2 storage in saline formations (Chadwick et al. 2009). Cross-hole EM method has been used for monitoring CO_2 migration in an EOR flood in the U.S. (Hoversten et al. 2002). Giese et al. (2009) indicated that the electrical resistivity tomography can be used to track the CO_2 plume between monitoring wells at Ketzin, Germany. Numerical simulation has been performed to simulate borehole-to-surface EM (BSEM) survey (Zhdanov et al. 2013). Research conducted by Vilamajó et al. (2013) show that the a deep EM source provided useful information for monitoring CO_2 storage in the Hontomín storage site.

Gravity method is used for measuring the gravitational acceleration due to mass distribution within the Earth. The CO_2 sequestration and its accumulation in shallow overburden traps may cause surface deformation; therefore, the gravity method offers the potential to detect the gravitational field changes in the CO_2 storage reservoir. Gravity method has been shown to detect the volumes of CO_2 in reservoirs (Gasperikova and Hoversten 2008; Hoversten and Gasperikova 2003; Sherlock et al. 2006). A gravity

response can detect more than 2 million tons (4.41 billion pounds) of injected CO_2 within a shallow storage reservoir (Chadwick et al. 2009). The gravity method will most likely be useful for monitoring CO_2 storage if its depth is on the order of 1 Km (Hoversten and Gasperikova 2003).

Well logging, also known as borehole logging, is most common for recording detailed information for the geologic formations penetrated by a borehole. Well logging is widely conducted in areas of mineral resource, geothermal, oil and gas exploration, and the related environmental and geotechnical studies. The technique can be used to obtain rock properties, through downhole measurements including resistivity, sonic velocity, neutron porosity, pressures, and temperatures. Geophysical logs were conducted prior to, during, and post CO_2 injection at Nagaoka, Japan (Sato et al. 2009). The monitoring results show that the logging method can detect the presence of CO_2 in the injected formation and there are no signs of leakage at the storage reservoir.

2.3. Use of Seismic Sensing Data for Condition Detection

To determine condition changes, various interpretation techniques of seismic monitoring results may be implemented. The most common use of seismic data for CO_2 sequestration studies is the detection of CO_2 “chimney” or “plume” migration. For example, using 3D seismic tomography, Chadwick et al. (2006) detected migration process of CO_2 chimney based on spatial pattern of wave speed. Duncan and Eisner (2010) used multiple geophones and relative amplitude to establish microseismic events for reservoir characterizations. Rutqvist et al. (2010) described the use of seismic moment to quantify the seismic event magnitude.

Geophysical testing has been applied to projects similar to the Citronelle field study for the purposes of determining production induced stress changes (Barkved and Kristiansen 2005; Hatchell et al. 2003; Hawkins et al. 2006) and site anisotropy changes (Herwanger and Horne 2009). These high resolution detections are typically performed with controlled excitations such as explosions or gun shots. The results indicate possible monitoring of the migration of injected fluids. However, interpretations of strata stress changes based on wave speed changes are inherently challenging. Finally, Hatchell et al. (2003) and Hawkins et al. (2007) described the use of wave speed differential ratio ($\Delta V/V$) for detection of stress changes in subterranean materials.

2.4. MDOF Lumped Mass Model

The lumped (or concentrated) mass modeling is widely used to study specific vibration problems in the areas of medical research (Williams 1987), civil structures (Hadid and Afra 2000), marine structures (Driscoll et al. 2000), mechanical systems (Mooi and Huibers 2000), aerospace structures (Abu-Saba et al. 1992) and earthquake effects (Ching and Glaser 2001). The method has also been known to provide reasonable accuracy in modeling of complex problems, such as rail-wheel interactions (Knothe and Grassie 1993).

The theory and application of lumped-mass models of voice speech were reviewed by Erath et al. (2013), who demonstrated that the viscoelastic tissue properties can be simulated as lumped masses, springs and dampers. This approach is the most common modeling conception in voiced speech investigations (Erath et al. 2013).

Driscoll et al. (2000) used a one-dimensional finite-element lumped mass model of a vertically tethered caged remotely operated vehicle (ROV) system to simulate the

motion of the cage and tension in the tether under specific input motions. The lumped mass approach was also used to represent a discretized cable system (Kamman and Huston 2001; Masciola et al. 2011). For dynamic problems, this method is more efficient than finite element derivation, and provides better accuracy (Kamman and Huston 2001).

Lumped mass model was used by Cha and Chen (2011) to study the suitability for quenching vibration along a supported elastic structure during harmonic excitations. Numerical experiments show that it is possible when the excitation frequency of the harmonic system is low.

For pipeline segments, Hadid and Afra (2000) analyzed sensitivity of site effects on dynamic response of buried pipelines. The connections of two pipe segments and soil-pipeline were represented by different springs and damping. The former one is modeled by a joint spring and a joint dashpot, while the latter is represented by a soil spring and a soil damping.

The problem of stability influenced by lumped masses and friction effects in elastically supported pipes conveying fluid has been studied by Chen and Fan (1987). It was found that the lumped masses, fluid pressure and friction have destabilizing effects on the mass transport system, while the elastic support may have stabilizing or destabilizing effect due to its stiffness and location.

The suitability of lumped masses for elastic wave propagation problems in beams was investigated by Belytschko and Mindle (1980). They found that the performance of Euler-Bernoulli lumped mass in flexural wave propagation problems is quite poor when the rotational inertia factor is increased; but when shear correction is included in the element, its performance is quite good.

Smith and Newmark (1958) employed a mass-spring model to study 1D stress wave propagation in soil with different physical properties for axially symmetric problems. The response of the lumped mass system was computed by using β-integration method (Newmark 1952). An idealized layered model can be formed by three assumptions: only vertically propagating shear waves in the earthquake ground motion, soils are horizontal layered media, and soil is homogenous within each layer (Ching and Glaser 2001). Glaser and Baise (2000) used a simple lumped mass model to represent the soil system and estimate soil damping and stiffness at the Lotung earthquake site. It should be mentioned that the soil damping estimated by Glaser and Baise (2000) in this study are greater than the values used by Seed and Idriss (1970) for forward modeling.

Hashash and Park (2001) developed a new non-linear 1-D site response analysis model to study the problem of vertical propagation of horizontal shear waves through horizontally layered soil deposits. In the analysis, the geologic layers of the studied area are considered as horizontal layers and are discretized using a MDOF lumped parameter model as shown in FIGURE 2.1 (Hashash and Park 2001; Matasovic 1993). The soil and rock properties of the geologic material are represented by stiffness and damping.

Kuhlemeyer and Lysmer (1973) found that consistent mass matrix gives a better accuracy than the lumped mass matrix in P-wave propagation problem. The finding is in opposite with a conclusion stated by Clough (1969), who showed that the lumped mass formulation obtained reliable results in any wave propagation problem. The disagreement of the two studies may be related to the different numerical schemes used in solving the differential equation of motion (Kuhlemeyer and Lysmer 1973). For these two kinds of

mass matrixes, Wu (2006) proved that under certain smooth solutions, the displacement, velocity and the energies may have the same convergence rates.

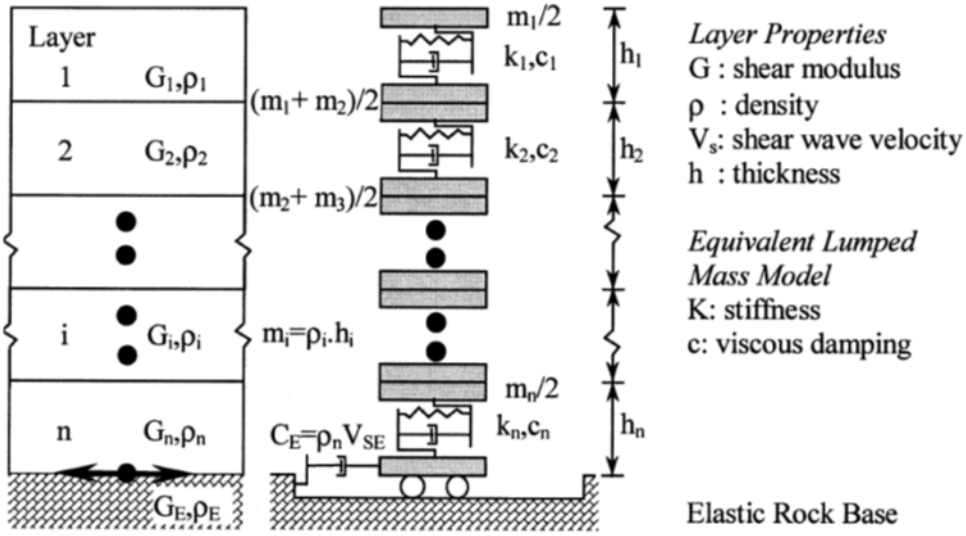

FIGURE 2.1: Multi-degree-of freedom lumped parameter model representation of horizontally layered soil deposit shaken at the base (Hashash and Park 2001; Matasovic 1993)

Lumped mass method was used by Lysmer (1970) to analyze generalized Rayleigh waves in multilayer elastic media system. Velocities of Rayleigh waves obtained by Lysmer (1970) from lumped mass models showed good agreement with a previous study conducted by Stoneley (1955), who obtained group velocities by numerical differentiation of the wave velocities. Seismic body wave propagation problems have been studied by using finite element method (Smith 1975). The finite element results have good agreement with a previous research using finite difference method (Boore 1972).

Methods of analysis of seismic response of horizontal soil layers have been presented by Idriss and Seed (1968b). Several methods including linear elastic analyses (close-form solution and lumped-mass solution), a bilinear analysis and an equivalent

linear analysis have been studied (Idriss and Seed 1967). The assumptions made in adopting these methods are: soil deposits are composed of several horizontal layers, soil or rock properties of any sublayer are constant along horizontal plane, and the seismic excitation is horizontal. In such cases, the deposit may be considered as a one-dimensional shear beam. Analysis of seismic responses at four sites during the 1957 San Francisco earthquake were made by Idriss and Seed (1968a), who utilizing an equivalent linear lumped mass method. They found that several parameters (i.e. the maximum amplitudes of ground motions) for both the computed and recorded ground accelerations have reasonably agreements.

Idriss and Seed (1970) proposed a new analytical procedure to calculate seismic response of horizontal soil deposits: the equivalent linear moduli and damping ratios. They compared its results with the evaluation using a constant damping solution. The comparisons show that the variable damping solution is better than constant damping solution for the analysis of seismic response of soil deposits.

Multi-degree-of-freedom one dimensional lumped parameter soil system model was used by Matasovic (1993) to study seismic response of composite horizontal layered soil deposits, which consists of either (i) layers of sand, (ii) layers of clay or (iii) a combination of layers of sand and clay. The simulation results showed that the simplified models are well able to predict he observed response behavior of the composite horizontal layered soil deposits.

Seed and co-authors (Seed et al. 1986; Seed and Idriss 1970) proposed a simple relationship of the dynamic shear moduli and damping factor for sands and gravels. Shear moduli and damping factors of soils are affected by several factors, the primary factors

are strain amplitude, effective mean principal stress, void ratio, number of cycles of loading, and degree of saturation for cohesive soils (Hardin and Drnevich 1972). They provide a useful guideline for choosing soil characteristics for dynamic response analysis of soil. The research conducted by Seed and Idriss (1969) show that responses of ground surface motion during earthquakes can vary with soil conditions.

Travers and Shepherd (1973) found that the lumped mass model is only be used to calculate the upper level motion from a known base motion and the energy is considered to be lost by internal viscous dampers.

Lumped element models are effective in modeling deformable objects: Provot (1995) used a mass-spring model to study the behavior of deformable cloth objects. Lumped models can also be used in flexible system, for example, robots and space structures are represented by lumped models (O'Connor 2007). Lumped mass model can also be used to estimate responses of a car-to-car collision. An over simplified two-mass-spring model was adopted by Mooi and Huibers (2000) to determine kinetics and dynamics of car-to-car crashes. The lumped mass-spring model of the fracturing specimens can be to analyze dynamic effects in fracture problems (Williams 1987). Abu-Saba et al. (1992) used the lumped mass models to simulate aircraft structures and conduct dynamic analysis for these structures. For the numerical simulation of large-number-of-elements models, the researchers found that the lumped mass system is more efficient than the finite element model.

Lumped mass method was used to analyze the overburden motion during explosive blasting events (Schamaun 1981). In the numerical simulation, the overburden zone was divided into a series of one degree of freedom masses and represented by them.

The simulation results show that the lumped mass method is a useful tool in the experimental blasting studies of oil shales (Schamaun 1981). Lisa and DeCapua (1974) used linear lumped mass modeling techniques to study the rigid body soil-structure interaction and the dynamic response of a buried building in a nuclear blast environment.

At the micro level, lumped-mass method was also used to study the band structure of two-dimensional phononic crystals (Wang et al. 2004). The researchers found that the method is suitable to compute the sharp variation of elastic constants inside the phononic crystals.

Dupac et al. (2002) modeled an electromagnetically levitated (ELM) flexible droplet as a mechanical system with lumped masses, elastic springs, and rigid massless rods. Lumped masses, springs and links were used to model and analyze the levitated droplet in mechanical engineering (Dupac 2005). 2D and 3D systems were studied for the flexible droplet; the results of the study provide more information for the dynamic response of droplet.

Finally, Verdon et al. (2012) described 1D velocity model for down well simulation of wave, it was called the layer lake model. But they did not extend the model to the entire oil field.

2.5. Summary

Lumped mass models are widely used in numerical simulation of dynamic problems; several numerical methods were employed by the past researchers to solve the dynamic equations. Partial applications of lumped mass method are summarized in TABLE 2.1. The application can basically differentiate into modeling and wave motion approximation.

TABLE 2.1: Partial applications of lumped mass method

	Application	References
Structure problems	Quenching vibration along an supported elastic structure	(Cha and Chen 2011)
	Pipe conveying fluid	(Chen and Fan 1987)
	Vertically tethered caged remotely operated vehicle system	(Driscoll et al. 2000; Kamman and Huston 2001; Masciola et al. 2011)
	Medical science, e.g. viscoelastic tissue properties	(Erath et al. 2013)
	Dynamic response of deformable objects	(Mooi and Huibers 2000; O'Connor 2007; Provot 1995)
	Dynamic response of buried pipeline	(Hadid and Afra 2000)
	Mechanical fracture problems	(Williams 1987)
	Band structure of phononic crystals	(Wang et al. 2004)
	Electromagnetically levitated flexible droplet in mechanical engineering	(Dupac 2005; Dupac et al. 2002)
	Aircraft structures	(Abu-Saba et al. 1992)
Wave problems	Elastic wave propagation in beams	(Belytschko and Mindle 1980)
	Seismic ground motion prediction	(Ching and Glaser 2001)
	Wave propagation through soil	(Glaser and Baise 2000)
	Seismic response of horizontal soil layer	(Hashash and Park 2001; Idriss and Seed 1967; Idriss and Seed 1968a; Idriss and Seed 1968b; Idriss and Seed 1970; Matasovic 1993; Seed et al. 1986; Seed and Idriss 1969; Seed and Idriss 1970)
	P-wave propagation	(Clough 1969; Kuhlemeyer and Lysmer 1973; Wu 2006)
	Rayleigh wave	(Lysmer 1970; Stoneley 1955)
	Seismic body wave	(Smith 1975)
	Soil-structure interaction	(Lisa and DeCapua 1974; Newmark 1959; Schamaun 1981; Wolf 1985)

To the best of the writer's knowledge, a detailed study of a P-wave propagating in an oil field using MDOF lumped mass has not been previously attempted. In this dissertation, MDOF models will be used to determine the effect of oil field change on wave propagation in an oil field. The basic observation to be presented herein should be beneficial for performing CO_2-EOR commercial projects.

The lumped mass method is not useful for analyzing the detailed CO_2 migration characteristics, but will provide an approximate solution for wave propagation induced by the input pressure.

CHAPTER 3: CO_2-EOR MONITORING AT CITRONELLE OIL FIELD USING PASSIVE SEISMIC MONITORING

3.1. Background

Denbury Onshore Co. and its partners begun working in CO_2 injection for a pilot study of possible CO_2-EOR for the highly heterogeneous and discontinuous sandstone reservoir of the Citronelle Oil Field since 2007. The Citronelle Oil Field is a mature oil reservoir and an ideal site for CO_2-EOR and sequestration, from both reservoir engineering and geological perspectives (Esposito et al. 2010; Esposito et al. 2008; Kovscek 2002). The Citronelle Oil Field is located about 50 km north of Mobile, Alabama, USA. This domestic giant oil field is located on the crest of the Citronelle Dome, which is a giant salt-cored anticline in the eastern Mississippi Interior Salt Basin (FIGURE 3.1). The field covers an area of 16,400 acres. The Citronelle Dome forms an elliptical, four-way structural closure, which is considered naturally stable for CO_2-EOR and CO_2 sequestration. In 1955, oil was first discovered by the Gulf Oil Company in the Zack Brooks Drilling Company No. 1 Donovan well. Since then, over 500 wells have been drilled and cumulative oil production has exceeded 169 million barrels (Esposito et al. 2008).

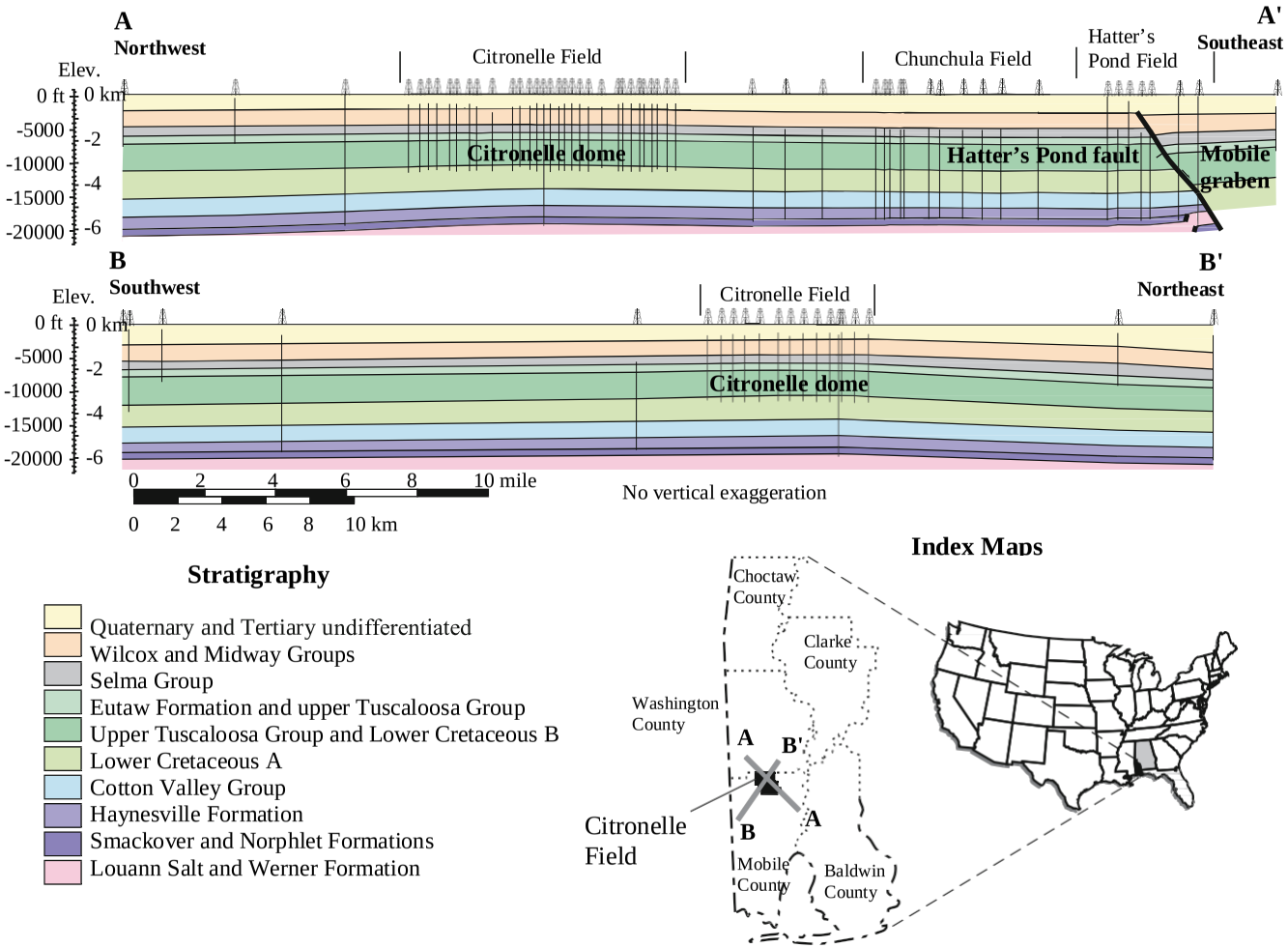

FIGURE 3.1: Structural cross sections showing Citronelle Dome and location of Citronelle Field (Esposito et al. 2010)

This chapter reports the use of a geophysical testing method to monitor the effects of CO_2 injection into the Citronelle Unit B-19-10 #2 well (Permit No. 3232). The goal of the geophysical testing is to monitor the CO_2 injection process, in particular, the detection of possible relationship between shear-wave velocity profiles and the static stress distribution before, during and after the injection. Such relationships may be helpful in understanding the field performance and establishing monitoring criteria for future decision making. To date, ten geophysical tests have been conducted.

3.2. Experimental Methodology and Materials

3.2.1 Geophysical Testing Technique

Passive seismic monitoring is non-intrusive testing method gathering information about the storage reservoir, migration of CO_2, and subsurface geomechanics (Verdon 2012; Verdon et al. 2010). It has been successfully applied to address specific issues in the oil and gas industry (Maxwell et al. 2010; Maxwell and Urbancic 2001; Verdon et al. 2010). The basic principle of passive seismic monitoring is that any small movement can be regarded as microseismic events that can be recorded near the reservoir. Seismic energy can be emitted by movement on preexisting faults and structures; it can also be produced by the creation of new fractures both within and around a reservoir. The main advantage of passive monitoring is that it can be carried out at any time, and it does not require application of an active or controlled excitation source. The disadvantage of passive sensing is the uncertainty introduced due to the lack of controlled energy input, which can result in both poor data sensitivity and detection accuracy.

Citronelle Oil Field has several wells located on private properties, which makes it difficult to perform active seismic investigation (i.e. controlled explosion, seismic

vibrator truck) at the location which is near concentrated population. Therefore, passive sensing is the choice to study the influence of the CO_2 injection, sequestration and oil production in the oil field.

A modified passive sensing Refractive Microtremor (ReMi) technique, DoReMi (Derivative of ReMi), is used at the Citronelle Oil Field, Alabama (Chen and Liu 2011; Chen et al. 2011). To improve mobility and avoid cumbersome wiring, wireless triaxial Micro-Electro-Mechanical System (MEMS) accelerometers from MicroStrain (2007) have been modified for the field study (FIGURE 3.2). The MEMS sensor is encased in a hard metal box and buried at depth into the ground. Coupling of the sensor to the surrounding soil is extremely important. Sensors were buried about 1 ft (0.3 m) at specified locations during monitoring. The wireless sensor unit can record seismic energy in three Cartesian directions (vertical and two horizontal directions). Signals obtained by the wireless accelerometer are acceleration time histories, which have amplitudes in g's and time unit in seconds. The information received from the vertical direction has been used in data processing for this study.

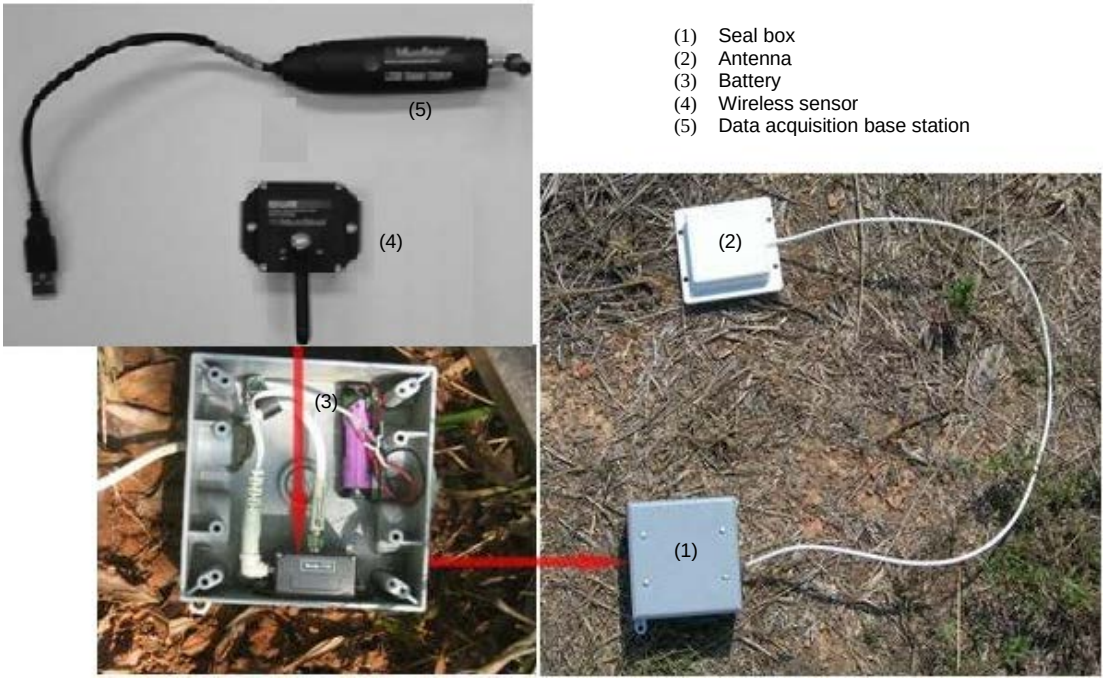

FIGURE 3.2: Wireless sensor used in DoReMi method (Chen et al. 2011)

3.2.2 Monitoring at Citronelle Oil Field

To monitor the response of the reservoir before, during, and after CO_2 injection, two linear arrays with 24 pickup points each were deployed at the Citronelle Oil Field. As shown in FIGURE 3.3, the direction of survey line 1 is from north to south, while survey line 2 is from northeast to southwest. Survey line 1 covered approximately 30,102 ft (9,175 m) span with 1,309 ft (399 m) for typical sensor spacing, while survey line 2 covered approximately 25,603 ft (7,804 m) span with 1,113 ft (339 m) for typical sensor spacing. The CO_2 injection well, B-19-10 #2, is located near the intersection of the two survey lines, in the northeast corner of the Field. The wireless sensor was buried near the well at each well site. A total of six sets were recorded at each point, and the recording duration for each set was set at 39.06 seconds. The sampling frequency is therefore 512 Hz.

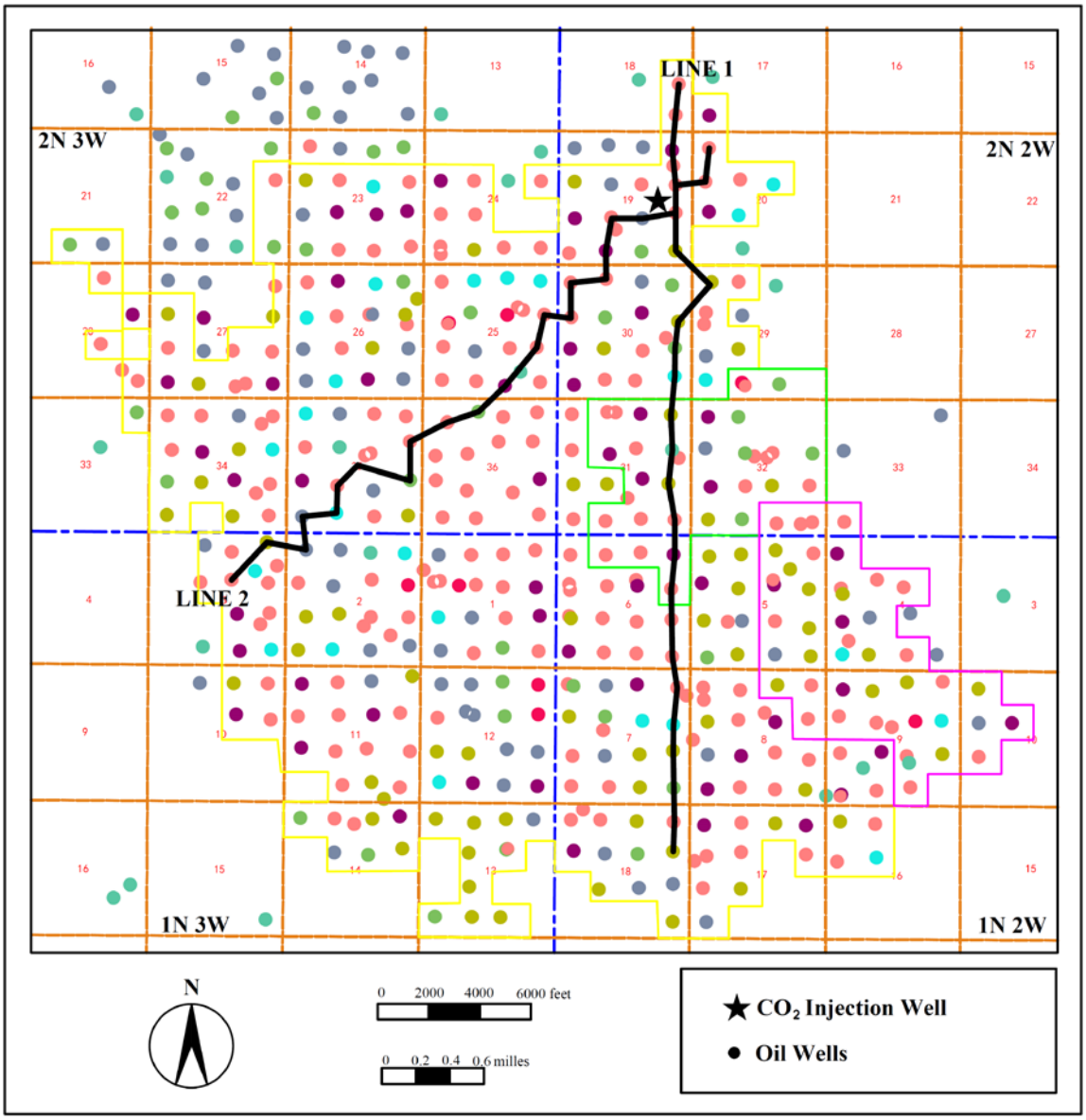

FIGURE 3.3: The testing lines at the Citronelle Oil Field (modified from (Chen and Liu 2011))

Background measurement was deployed in October 2008, January 2009 and June 2009, prior to the start of CO_2 injection in the field. It should be noted that water injection at the well has been conducted since 2007 to restore the pressure in the well to a level suitable for production. CO_2 injection began in December 2009 in well B-19-10 #2 at the

rate of 46.5 tons/day. Injection of CO_2 was stalled between the periods from 30 December 2009 to 26 January 2010, because of some problems with the triplex pump. The average injection rate of CO_2, including maintenance time for equipment, was stabilized at 31.5 tons/day. The history of CO_2 injection, from December 2009 to September 2010, is shown in FIGURE 3.4. A total of 8,036 tons of CO_2 (7,500 tons plus cushion) had been injected into the pilot well at the end of the injection. The record of well head stress at Well B-19-10 #2 from the beginning of CO_2 injection to the end of the injection is shown in FIGURE 3.5.

In the first month of CO_2 injection, the well head pressure increased from 2,400 psig to 3,800 psig. After CO_2 injection was resumed on 27 January 2010, the range of well head is between 3,800 psig and 4,200 psig. Passive tests were conducted at the Citronelle Oil Field in December 2009 with the start of significant CO_2 injection, and during steady CO_2 injection in March 2010, May 2010 and September 2010, respectively. Water injection was switched back on immediately after CO_2 injection finished. In addition, measurements were made after CO_2 injection in November 2010, March 2011 and May 2011, respectively. A summary of the monitoring history at the Citronelle Oil Field is shown in TABLE 3.1. The monitoring results are presented in section 3.3 in the form of shear wave velocity profiles.

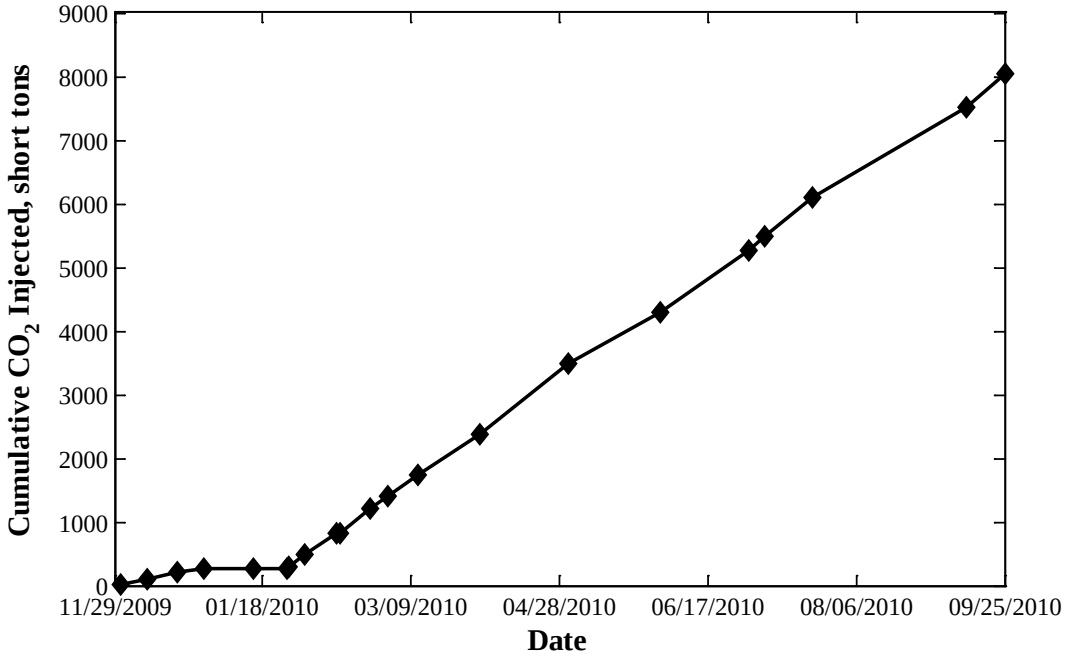

FIGURE 3.4: Record of CO_2 injection during Phase II at Well B-19-10#2.

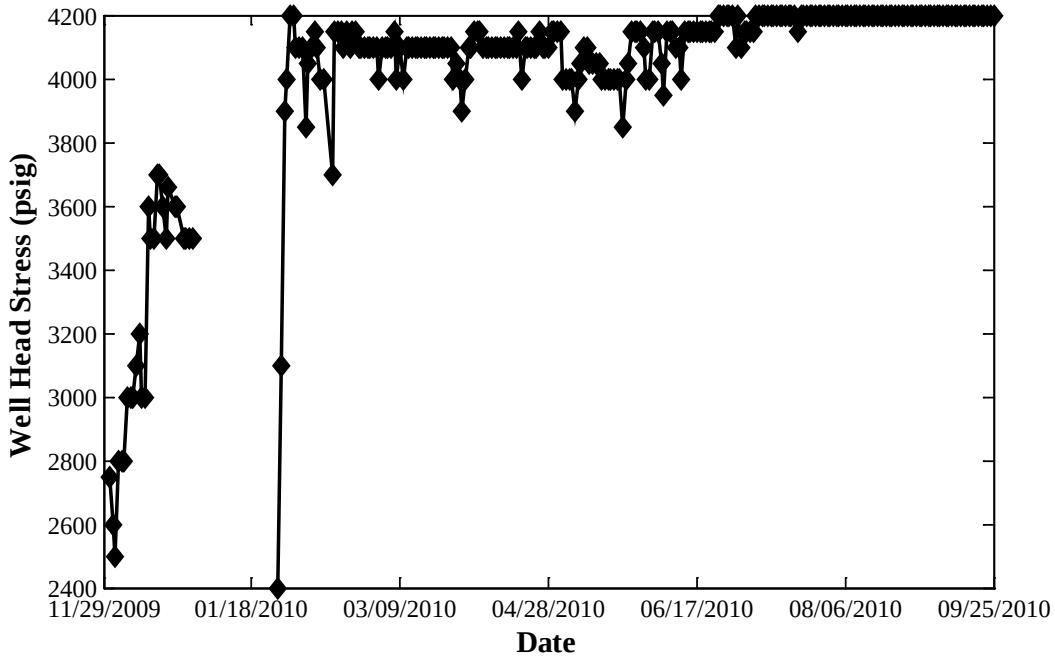

FIGURE 3.5: Well head stress at Well B-19-10#2 during CO_2 injection

TABLE 3.1: Summary of monitoring history at the Citronelle Oil Field

Test No.	Injection	Monitoring Date
1	Water	8-10 October 2008
2	Water	21-22 January 2009
3	Water	15-16 June 2009
4	CO_2	9-10 December 2009
5	CO_2	11-12 March 2010
6	CO_2	18-19 May 2010
7	CO_2	8-9 September 2010
8	Water	17-18 November 2010
9	Water	16-17 March 2011
10	Water	17-18 May 2011

3.2.3 Statistical Analysis Model

Because the monitoring involved all three stages of the injection process, namely, water injection (pressure building), CO_2 injection, and post injection, it is of interest to interpret the results at different stages. For each stage, at least three monitoring tests were performed. For a first order analysis, basic statistical parameters will be used to study the effect of pressure building at the field.

Statistical analysis is conducted by finding the average shear velocities at different depths for each test group along the two test lines. The average values, $\bar{v}$, were determined as (Davis 1986; Rétháti 1988)

$$\bar{v} = \frac{1}{N}\sum_{i=1}^{N} v_i \tag{1}$$

where v_i represents the speed data at the corresponding depth for each test group, and N represents the total number of tests in each group. After calculating the average shear wave velocities, the standard deviations of the corresponding data are given by

$$\sigma = \sqrt{\frac{1}{N}\sum_{i=1}^{N}(v_i - \bar{v})^2} \tag{2}$$

The average and standard deviation values were then used to compute the coefficient of variation (COV):

$$c_v = \frac{\sigma}{\bar{v}} \tag{3}$$

The COV illustrates how far a set of numbers approximate the average value for the statistical distribution between the three tests of data in each group. The lower the COV, the data points at the corresponding depth for each test group tend to be closer to the average value. The entire project represents a continuous pressure building process at the oil field. The pressure built-up will slowly dissipate throughout the oil bearing layer. Due to the presence of an anhydrate layer, the CO_2 remains within the oil bearing rock. As long as the anhydrate retains its integrity, the pressure in the oil layer will be higher than in the strata layers.

3.3. Results and Discussion

3.3.1 Shear-Wave Velocity Determination

Each sensor line has 24 survey points, and is referred to as 24 channels in data processing. The channel number of survey line 1 increases as the position of the wells from north to south, while survey line 2 increases from northeast to southwest. The data collected from each survey line were divided into seven groups: Channel 1 to Channel 18 as Group 1, Channel 2 to Channel 19 as Group 2, Channel 3 to Channel 20 as Group 3, Channel 4 to Channel 21 as Group 4, Channel 5 to Channel 22 as Group 5, Channel 6 to Channel 23 as Group 6, and Channel 7 to Channel 24 as Group 7.

The data of shear wave velocity profiles were computed using SeisOpt ReMi software (Optim 2006): First, wavefield transformation data processing (ReMi Vspect module) was used to process the time domain data acquired in the field. Secondly, an

interactive Rayleigh-wave dispersion-modeling was performed to generate a 1-D model of shear-wave velocity for each set of traces. In data processing, dispersion curves were picked from the p-f results (Louie 2001). The shear-wave velocity curve for each test line was obtained from an averaging of the seven data groups. Typical average shear-wave velocity profile versus depth measured from survey line 1 is shown in FIGURE 3.6. The generated profile has a total of 14 strata. Measurements of shear-wave velocity to depths around 12,500 ft (3,810 m) (oil bearing Donovan Formation) were achieved. As discussed previously, most of the injection pressures were retained within the oil layer around 12,500 ft (3,810 m). If the anhydrite barrier maintained its leak-prevention, a pressurization of the strata above the oil bearing layer may be expected.

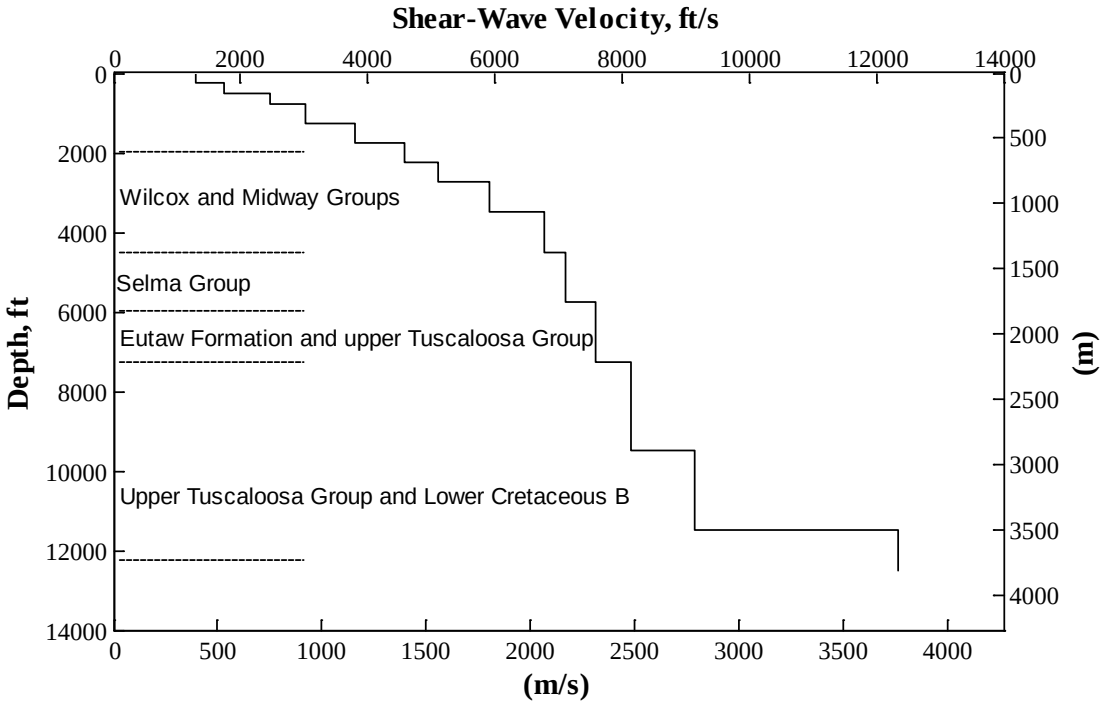

FIGURE 3.6: Average shear-wave velocity profiles versus depth from survey line 1, 8-9 September 2010.

In order to compare the changes of the shear-wave velocity obtained from the geophysical tests, the data were divided into three groups: before CO_2 injection, during

CO_2 injection, and after CO_2 injection. Test results of shear wave velocity versus depth curves along the two survey lines are shown in FIGURE 3.7 through FIGURE 3.12. Error bars were used to indicate the deviation of shear-wave velocity in the measurements. FIGURE 3.7 and FIGURE 3.8 show the test results of average shear-wave velocity versus depth curve between test 1, 2 and 3 for survey line 1 and 2, respectively. FIGURE 3.9 and FIGURE 3.10 show the test results for test 4, 5, 6 and 7, for survey line 1 and 2 respectively. Wave speed results of the last four layers shown in FIGURE 3.9 and FIGURE 3.10 are higher than the corresponding results shown in FIGURE 3.7 and FIGURE 3.8. The increase in shear-wave velocity is associated with CO_2 injection, which caused an increase in the effective stresses in layers above the injection zone (pressurization). Notice that the pressures at the oil layer for tests 4, 5, 6 and 7 are slightly lower than during CO_2 injection. Also note that the pressures at the oil bearing layer in FIGURE 3.11 and FIGURE 3.12 are lower than in FIGURE 3.9 and FIGURE 3.10. This is interpreted as the injection pressure is mobilizing the migration of oil. The deviations on the graphs shown in FIGURE 3.11 and FIGURE 3.12 are significantly smaller indicating that the strata pressurization has stabilized. A reduction of the strata pressure (shear-wave velocity) could mean a likely leak occurring within the system.

The shear wave velocities at the Donovan and the well head stress at CO_2 injection well have been normalized, as shown in FIGURE 3.13. Assuming the shear wave velocity is a good representation of the stress level within the oil bearing stratum. The well-fitting of the two kinds of data represents the shear-wave velocity and stresses within the reservoir have been consistent through the injection process.

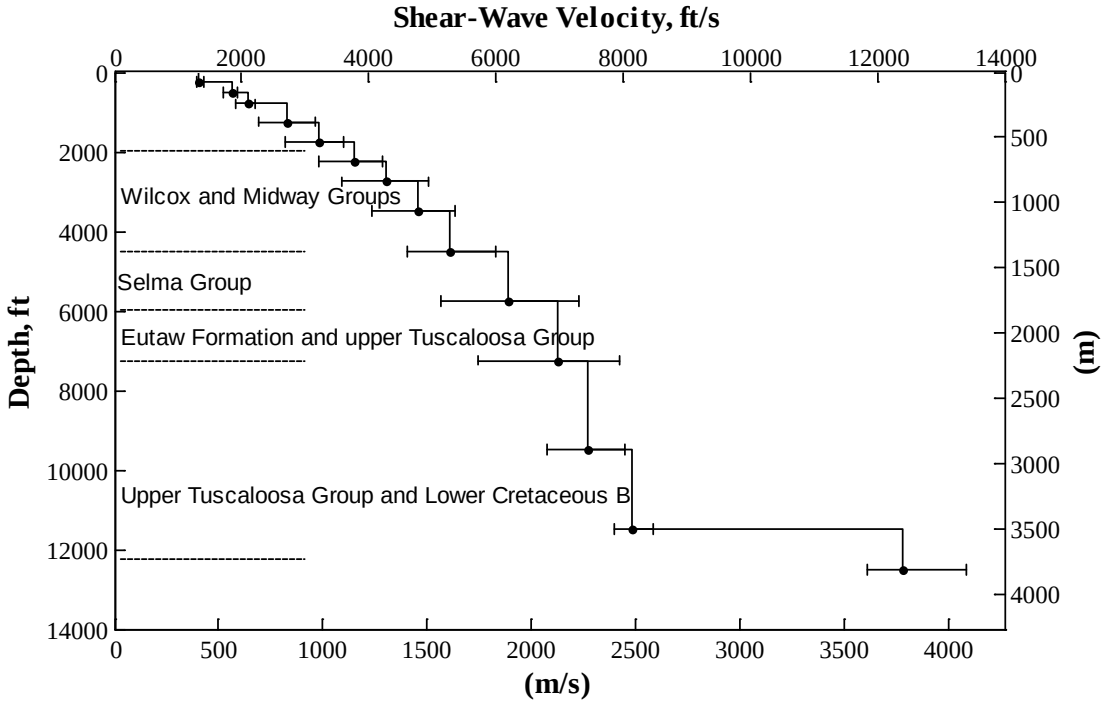

FIGURE 3.7: Average shear-wave velocity profile versus depth from survey line 1 before CO_2 injection, average of test 1, test 2 and test 3.

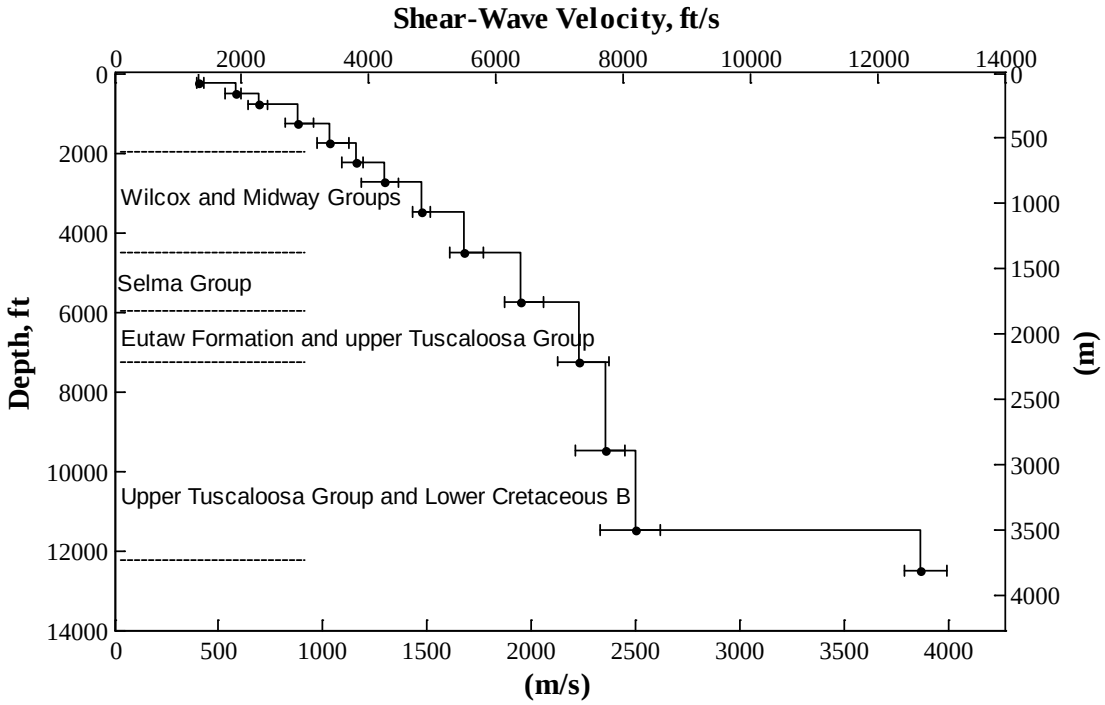

FIGURE 3.8: Average shear-wave velocity profile versus depth from survey line 2 before CO_2 injection, average of test 1, test 2 and test 3**.**

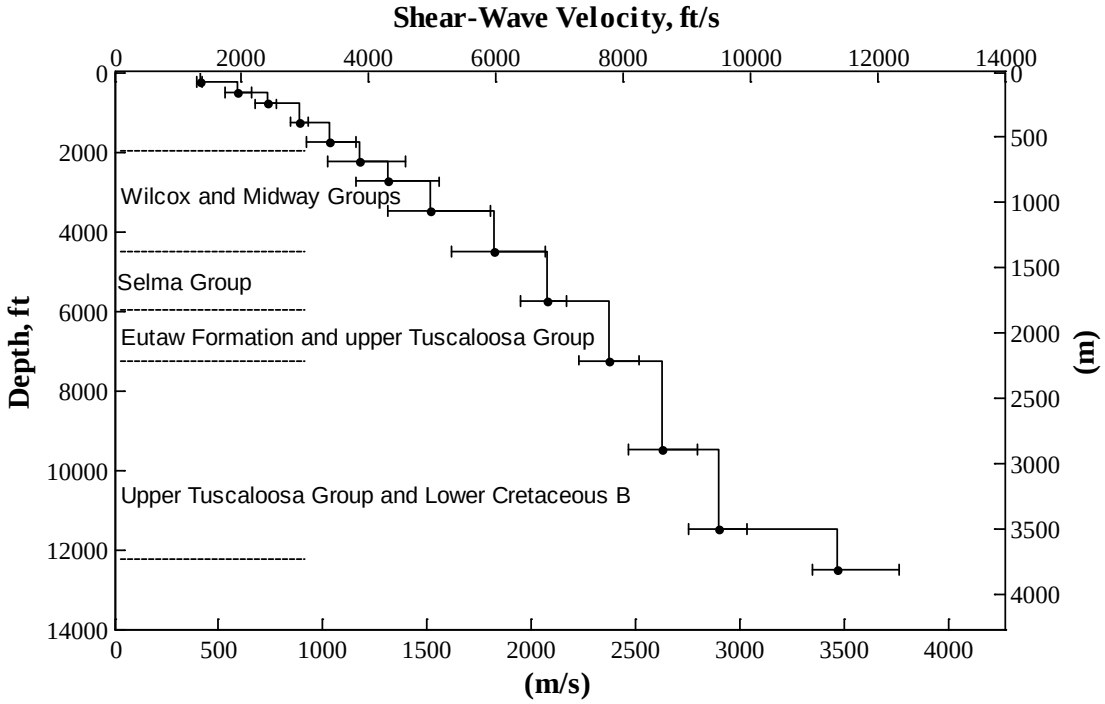

FIGURE 3.9: Average shear-wave velocity profile versus depth from survey line 1 during CO_2 injection, average of test 4, test 5, test 6 and test 7.

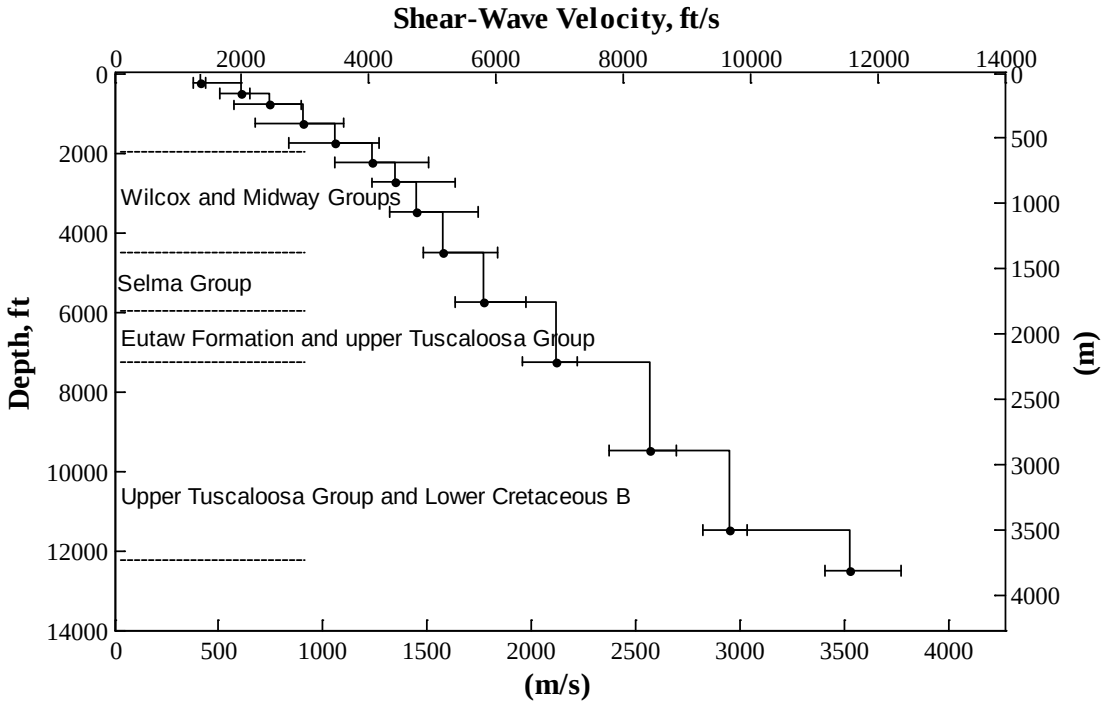

FIGURE 3.10: Average shear-wave velocity profile versus depth from survey line 2 during CO_2 injection, average of test 4, test 5, test 6 and test 7.

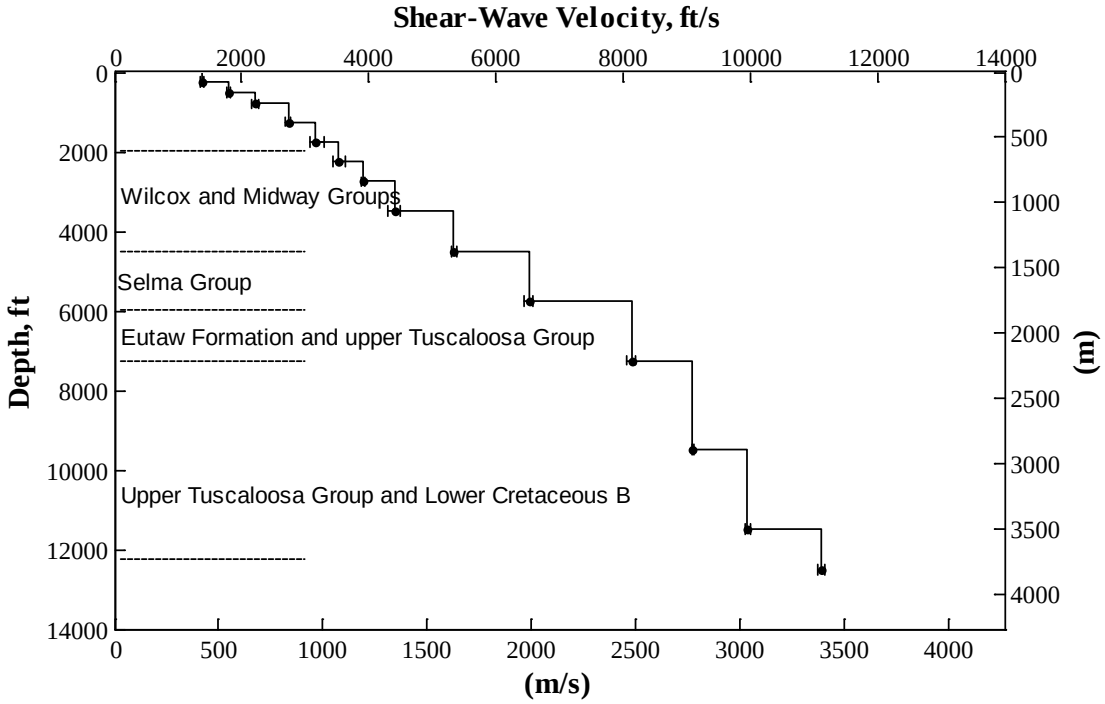

FIGURE 3.11: Average shear-wave velocity profile versus depth from survey line 1 after CO_2 injection, average of test 8, test 9 and test 10.

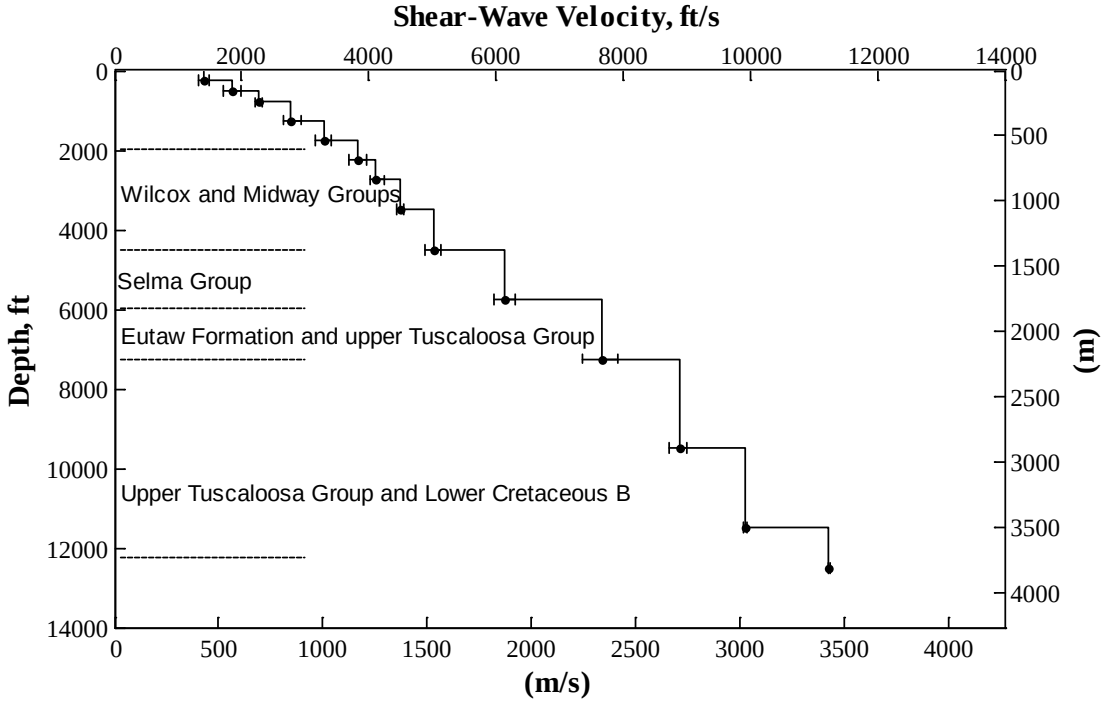

FIGURE 3.12: Average shear-wave velocity profile versus depth from survey line 2 after CO_2 injection, average of test 8, test 9 and test 10.

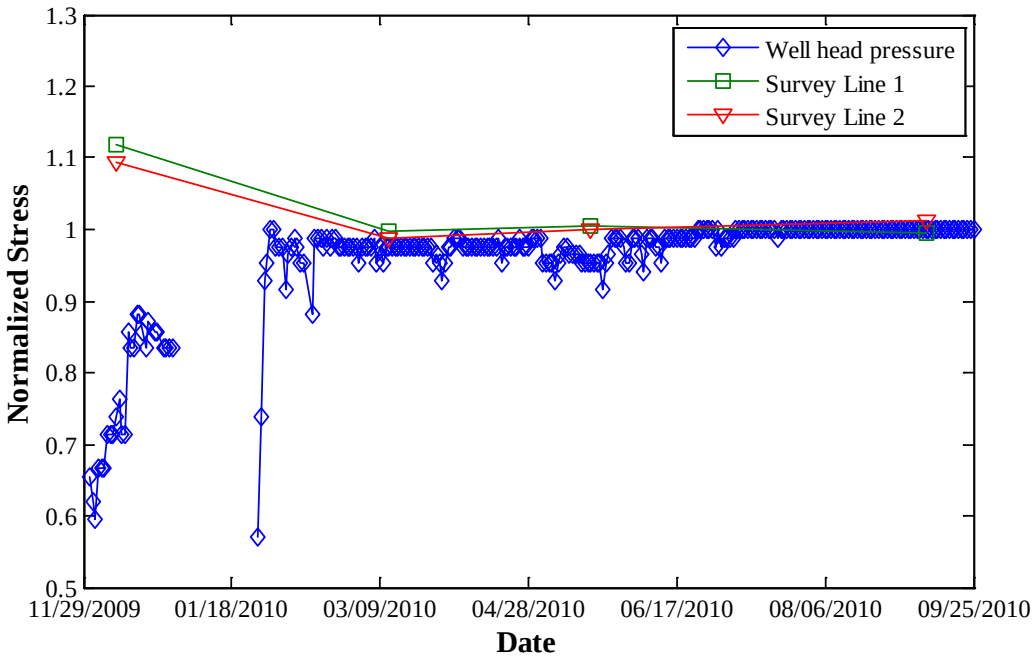

FIGURE 3.13: Normalized well head pressure at well B-19-10#2 during CO_2 injection with geophysical test data.

3.3.2 Statistical Analysis and Interpretation

In order to understand the pressurization history of the Citronelle injection experiment, an evaluation of the statistics of the field geophysics data is performed. The statistics were computed based on results presented in section 3.2.3. The measured well head stresses during CO_2 injection from February to September 2010, were also evaluated by statistical analysis. The COV value of the well head stresses is 0.019.

Before CO_2 injection, average shear-wave velocities for survey line 1 were found ranged from 1,329.8 to 12,392.1 ft/s (405.3 to 3,777.1 m/s). The standard deviations of the data ranged from 70.9 to 1,133.3 ft/s (21.6 to 345.4 m/s). The COV of the recorded velocities varied with depth from 0.04 to 0.17. Before CO_2 injection on survey line 2, the average shear-wave velocities are ranged from 1,334.0 to 12,667.2 ft/s (406.6 to 3,861.0 m/s). The standard deviations of the data ranged from 74.4 to 492.1 ft/s (22.7 to 150.0

m/s). The COV of the recorded velocities varied with depth from 0.03 to 0.08. The statistical data calculated in before CO_2 injection on both survey line 1 and 2 are shown in TABLE 3.2, and graphically presented in FIGURE 3.7 and FIGURE 3.8, respectively.

During CO_2 injection, average shear-wave velocities for survey line 1 were found ranged from 1,339.4 to 11,365.0 ft/s (408.2 to 3,464.1 m/s) and increased with depth. The standard deviations of the data ranged from 38.5 to 755.0 ft/s (11.7 to 230.1 m/s). The COV of the recorded velocities varied with depth from 0.03 to 0.15. During CO_2 injection on survey line 2, the average shear-wave velocities are ranged from 1,338.0 to 11,570.3 ft/s (407.8 to 3,526.6 m/s). The standard deviations of the data ranged from 89.2 to 660.3 ft/s (27.2 to 201.3 m/s). The COV of the recorded velocities varied with depth from 0.03 to 0.20. The statistical data calculated in during CO_2 injection on both survey line 1 and 2 are shown in TABLE 3.3, and presented in FIGURE 3.9 and FIGURE 3.10, respectively.

After CO_2 injection on survey line 1 found average shear-wave velocities that ranged from 1,378.9 to 11,108.8 ft/s (420.3 to 3,386.0 m/s) and increased with depth. The standard deviations of the data ranged from 15.5 to 109.2 ft/s (4.7 to 33.3 m/s). The COV of the recorded velocities varied with depth from 0.002 to 0.03. After CO_2 injection on survey line 2, found average shear-wave velocities ranged from 1,416.6 to 11,235.8 ft/s (431.8 to 3,424.7 m/s). The standard deviations of the data ranged from 15.8 to 289.1 ft/s (4.8 to 88.1 m/s). The COV of the recorded velocities varied with depth from 0.001 to 0.07. The statistical data calculated in after CO_2 injection on both survey line 1 and 2 are shown in TABLE 3.4 and are presented in FIGURE 3.11 and FIGURE 3.12, respectively.

TABLE 3.2: Statistical analysis on shear-wave velocity obtained from field tests before CO_2 injection stage

	Survey Line 1						Survey Line 2					
Layer	Test 1	Test 2	Test 3	$\bar{v}$	σ	COV	Test 1	Test 2	Test 3	$\bar{v}$	σ	COV
1 [a]	1411.0	1280.5	1297.8	1329.8	70.9	0.05	1302.0	1419.0	1281.0	1334.0	74.4	0.06
1 [b]	430.1	390.3	395.6	405.3	21.6		396.8	432.5	390.4	406.6	22.7	
2 [a]	1933.7	1715.8	1901.4	1850.3	117.6	0.06	1752.4	1952.4	1976.2	1893.7	122.9	0.06
2 [b]	589.4	523.0	579.6	564.0	35.9		534.1	595.1	602.3	577.2	37.5	
3 [a]	2199.8	1904.9	2219.0	2107.9	176.1	0.08	2089.1	2323.8	2414.3	2275.7	167.9	0.07
3 [b]	670.5	580.6	676.4	642.5	53.7		636.7	708.3	735.9	693.6	51.2	
4 [a]	3151.2	2280.8	2690.5	2707.5	435.4	0.16	2677.0	3138.1	2823.8	2879.6	235.6	0.08
4 [b]	960.5	695.2	820.1	825.2	132.7		816.0	956.5	860.7	877.7	71.8	
5 [a]	3601.6	2688.7	3333.3	3207.9	469.2	0.15	3189.1	3700.0	3276.2	3388.4	273.3	0.08
5 [b]	1097.8	819.5	1016.0	977.8	143.0		972.0	1127.8	998.6	1032.8	83.3	
6 [a]	4227.5	3224.7	3847.6	3766.6	506.3	0.13	3563.7	3900.0	3904.8	3789.5	195.6	0.05
6 [b]	1288.5	982.9	1172.8	1148.1	154.3		1086.2	1188.7	1190.2	1155.0	59.6	
7 [a]	4937.1	3588.7	4276.2	4267.3	674.2	0.16	3881.3	4338.1	4476.2	4231.9	311.3	0.07
7 [b]	1504.8	1093.8	1303.4	1300.7	205.5		1183.0	1322.3	1364.3	1289.9	94.9	
8 [a]	5370.1	4045.0	4880.8	4765.3	670.1	0.14	4677.9	4823.8	4957.1	4819.6	139.7	0.03
8 [b]	1636.8	1232.9	1487.7	1452.5	204.2		1425.8	1470.3	1510.9	1469.0	42.6	
9 [a]	6010.2	4611.8	5166.7	5262.9	704.2	0.13	5796.9	5452.4	5271.4	5506.9	266.9	0.05
9 [b]	1831.9	1405.7	1574.8	1604.1	214.6		1766.9	1661.9	1606.7	1678.5	81.4	
10 [a]	7304.7	5145.4	6142.9	6197.6	1080.7	0.17	6749.9	6247.6	6138.1	6378.5	326.2	0.05
10 [b]	2226.5	1568.3	1872.3	1889.0	329.4		2057.4	1904.3	1870.9	1944.2	99.4	
11 [a]	7949.5	5729.1	7233.6	6970.7	1133.3	0.16	7134.0	6985.7	7781.0	7300.2	422.9	0.06
11 [b]	2423.0	1746.2	2204.8	2124.7	345.4		2174.4	2129.2	2371.6	2225.1	128.9	
12 [a]	8020.6	6796.3	7547.6	7454.9	617.4	0.08	7868.9	7242.9	8028.6	7713.4	415.3	0.05
12 [b]	2444.7	2071.5	2300.5	2272.2	188.2		2398.4	2207.6	2447.1	2351.1	126.6	
13 [a]	8115.4	7856.4	8461.9	8144.6	303.8	0.04	8589.6	7652.4	8381.0	8207.6	492.1	0.06
13 [b]	2473.6	2394.6	2579.2	2482.5	92.6		2618.1	2332.4	2554.5	2501.7	150.0	
14 [a]	11941.8	11834.4	13400.0	12392.1	874.5	0.07	12425.4	12481.0	13095.2	12667.2	371.7	0.03
14 [b]	3639.9	3607.1	4084.3	3777.1	266.6		3787.3	3804.2	3991.4	3861.0	113.3	

Note: [a] unit is ft/s; [b] unit is m/s.

TABLE 3.3: Statistical analysis on shear-wave velocity obtained from field tests during CO_2 injection stage

	Survey Line 1							Survey Line 2						
Layer	Test 4	Test 5	Test 6	Test 7	$\bar{v}$	σ	COV	Test 4	Test 5	Test 6	Test 7	$\bar{v}$	σ	COV
1 [a]	1296.5	1320.7	1383.7	1356.8	1339.4	38.5	0.03	1282.3	1242.6	1402.4	1424.7	1338.0	89.2	0.07
1 [b]	395.2	402.5	421.7	413.6	408.2	11.7		390.8	378.8	427.5	434.2	407.8	27.2	
2 [a]	1749.4	1961.6	1850.2	2155.1	1929.1	173.8	0.09	2013.7	1653.2	2134.4	2119.6	1980.2	224.5	0.11
2 [b]	533.2	597.9	563.9	656.9	588.0	53.0		613.8	503.9	650.6	646.0	603.6	68.4	
3 [a]	2462.3	2545.0	2213.5	2463.4	2421.1	143.7	0.06	2927.1	1865.0	2433.6	2528.3	2438.5	438.1	0.18
3 [b]	750.5	775.7	674.7	750.8	737.9	43.8		892.2	568.5	741.7	770.6	743.3	133.5	
4 [a]	3013.6	3054.1	2778.6	2775.4	2905.4	149.2	0.05	3612.6	2199.5	2951.9	3119.1	2970.8	585.7	0.20
4 [b]	918.5	930.9	846.9	845.9	885.6	45.5		1101.1	670.4	899.7	950.7	905.5	178.5	
5 [a]	3808.4	3383.0	3291.9	3029.5	3378.2	323.6	0.10	4160.5	2738.3	3407.1	3592.9	3474.7	586.3	0.17
5 [b]	1160.8	1031.1	1003.4	923.4	1029.7	98.6		1268.1	834.6	1038.5	1095.1	1059.1	178.7	
6 [a]	4583.2	3866.0	3585.2	3343.0	3844.4	536.9	0.14	4930.8	3455.4	3895.7	3925.5	4051.8	624.1	0.15
6 [b]	1397.0	1178.4	1092.8	1019.0	1171.8	163.7		1502.9	1053.2	1187.4	1196.5	1235.0	190.2	
7 [a]	5105.7	4371.4	3895.8	3797.8	4292.7	597.1	0.14	5356.5	4055.5	4128.0	4133.6	4418.4	626.4	0.14
7 [b]	1556.2	1332.4	1187.5	1157.6	1308.4	182.0		1632.7	1236.1	1258.2	1259.9	1346.7	190.9	
8 [a]	5912.4	5211.1	4292.1	4417.9	4958.4	755.0	0.15	5722.9	4557.2	4337.9	4356.5	4743.6	660.3	0.14
8 [b]	1802.1	1588.4	1308.2	1346.6	1511.3	230.1		1744.3	1389.0	1322.2	1327.9	1445.9	201.3	
9 [a]	6775.3	6103.0	5306.5	5680.4	5966.3	629.9	0.11	6016.6	4958.5	4863.8	4848.9	5171.9	565.2	0.11
9 [b]	2065.1	1860.2	1617.4	1731.4	1818.5	192.0		1833.8	1511.3	1482.5	1477.9	1576.4	172.3	
10 [a]	7105.1	6753.2	6397.1	6950.4	6801.4	305.6	0.04	6468.6	5400.7	5958.0	5365.4	5798.2	522.9	0.09
10 [b]	2165.6	2058.4	1949.8	2118.5	2073.1	93.1		1971.6	1646.1	1816.0	1635.4	1767.3	159.4	
11 [a]	7575.7	7318.0	8246.4	7960.3	7775.1	410.3	0.05	7204.4	6413.2	7282.7	6831.3	6932.9	398.5	0.06
11 [b]	2309.1	2230.5	2513.5	2426.3	2369.9	125.1		2195.9	1954.8	2219.8	2082.2	2113.2	121.5	
12 [a]	8149.8	8096.5	9160.5	9079.8	8621.6	577.0	0.07	8359.3	7765.8	8687.3	8843.4	8414.0	476.9	0.06
12 [b]	2484.1	2467.8	2792.1	2767.5	2627.9	175.9		2547.9	2367.0	2647.9	2695.5	2564.6	145.4	
13 [a]	9131.9	9023.6	9938.2	9957.9	9512.9	504.4	0.05	9578.8	9257.7	9856.0	9963.7	9664.0	315.7	0.03
13 [b]	2783.4	2750.4	3029.2	3035.2	2899.5	153.8		2919.6	2821.7	3004.1	3036.9	2945.6	96.2	
14 [a]	12350.4	11015.3	11100.6	10993.8	11365.0	658.5	0.06	12371.4	11162.1	11316.3	11431.5	11570.3	545.3	0.05
14 [b]	3764.4	3357.5	3383.5	3350.9	3464.1	200.7		3770.8	3402.2	3449.2	3484.3	3526.6	166.2	

Note: [a] unit is ft/s; [b] unit is m/s.

TABLE 3.4: Statistical analysis on shear-wave velocity obtained from field tests after CO_2 injection stage

	Survey Line 1						Survey Line 2					
Layer	Test 8	Test 9	Test 10	$\bar{v}$	σ	COV	Test 8	Test 9	Test 10	$\bar{v}$	σ	COV
1 [a]	1344.8	1413.6	1378.3	1378.9	34.4	0.02	1331.8	1480.4	1437.7	1416.6	76.5	0.05
1 [b]	409.9	430.9	420.1	420.3	10.5		405.9	451.2	438.2	431.8	23.3	
2 [a]	1824.2	1775.8	1787.0	1795.7	25.3	0.01	1723.8	1976.5	1852.0	1850.8	126.3	0.07
2 [b]	556.0	541.3	544.7	547.3	7.7		525.4	602.4	564.5	564.1	38.5	
3 [a]	2164.2	2273.8	2214.3	2217.4	54.9	0.02	2323.9	2242.2	2199.5	2255.2	63.3	0.03
3 [b]	659.6	693.0	674.9	675.9	16.7		708.3	683.4	670.4	687.4	19.3	
4 [a]	2740.1	2764.3	2688.1	2730.8	38.9	0.01	2944.5	2738.3	2660.2	2781.0	146.9	0.05
4 [b]	835.2	842.5	819.3	832.4	11.9		897.5	834.6	810.8	847.6	44.8	
5 [a]	3293.8	3141.4	3082.0	3172.4	109.2	0.03	3418.3	3277.0	3171.1	3288.8	124.0	0.04
5 [b]	1003.9	957.5	939.4	966.9	33.3		1041.9	998.8	966.6	1002.4	37.8	
6 [a]	3622.6	3477.7	3431.3	3510.5	99.8	0.03	3968.2	3782.4	3693.2	3814.6	140.3	0.04
6 [b]	1104.2	1060.0	1045.8	1070.0	30.4		1209.5	1152.9	1125.7	1162.7	42.8	
7 [a]	3925.5	3903.2	3882.7	3903.8	21.4	0.01	4248.7	4061.1	4027.7	4112.5	119.2	0.03
7 [b]	1196.5	1189.7	1183.5	1189.9	6.5		1295.0	1237.8	1227.6	1253.5	36.3	
8 [a]	4306.3	4425.2	4505.1	4412.2	100.0	0.02	4438.3	4488.4	4560.9	4495.8	61.6	0.01
8 [b]	1312.6	1348.8	1373.2	1344.9	30.5		1352.8	1368.1	1390.2	1370.3	18.8	
9 [a]	5304.0	5296.6	5382.1	5327.6	47.3	0.01	4889.7	5042.1	5140.5	5024.1	126.4	0.03
9 [b]	1616.7	1614.4	1640.5	1623.8	14.4		1490.4	1536.8	1566.8	1531.4	38.5	
10 [a]	6576.7	6437.4	6571.1	6528.4	78.9	0.01	5972.9	6156.8	6311.0	6146.9	169.3	0.03
10 [b]	2004.6	1962.1	2002.9	1989.9	24.0		1820.5	1876.6	1923.6	1873.6	51.6	
11 [a]	8206.1	8061.2	8124.4	8130.6	72.7	0.01	7351.5	7726.8	7920.0	7666.1	289.1	0.04
11 [b]	2501.2	2457.1	2476.3	2478.2	22.1		2240.7	2355.1	2414.0	2336.6	88.1	
12 [a]	9103.5	9081.2	9110.9	9098.5	15.5	0.002	8726.3	8906.0	9006.9	8879.7	142.1	0.02
12 [b]	2774.7	2768.0	2777.0	2773.2	4.7		2659.8	2714.5	2745.3	2706.5	43.3	
13 [a]	9952.6	9928.4	10010.2	9963.7	42.0	0.004	9898.7	9948.9	9960.0	9935.8	32.7	0.003
13 [b]	3033.5	3026.2	3051.1	3036.9	12.8		3017.1	3032.4	3035.8	3028.4	10.0	
14 [a]	11050.6	11098.9	11176.9	11108.8	63.7	0.01	11247.5	11217.8	11242.0	11235.8	15.8	0.001
14 [b]	3368.2	3382.9	3406.7	3386.0	19.4		3428.3	3419.2	3426.6	3424.7	4.8	

Note: [a] unit is ft/s; [b] unit is m/s.

The two monitoring lines performed to help determine possible directional effects at the oil field: the first line indicated likely north-east direction pressurization, and the second line indicated likely northeast-southwest direction pressurization. The direction selection is constrained by available monitoring locations. Comparing the average velocity at the oil bearing layer indicated that it reached 12,392.1 ft/s (3,777.1 m/s) during water injection, 11,365.0 ft/s (3,464.1 m/s) during CO_2 injection, and slightly dropped to 11,108.8 ft/s (3,386.0 m/s) post CO_2 injection. Whereas for survey line 2, the velocity reached 12,667.2 ft/s (3,861.0 m/s) during water injection, 11,570.3 ft/s (3,526.6 m/s) during CO_2 injection and dropped to 11,235.8 ft/s (3,424.7 m/s) post CO_2 injection. The drop in velocity (pressure) may be an indication of possible mobilization of the oil, hence may be an indication of increased oil production. Comparing survey line 1 and 2, it may be concluded that the pressure build ups are almost identical in both directions indicating uniform build-up of pressures at all directions.

The COV value of the wave speed at the oil bearing layer is used as an indication of the stabilization of the strata pressurization process: as the oil bearing layer pressure is building up, a larger COV value is expect. A latter drop in COV indicates stable and sustained pressure in the oil bearing rock. This is shown in FIGURE 3.7 through FIGURE 3.12 for both survey line 1 and 2. It is especially notable for the post CO_2 injection stage, where the COV values are shown to be 0.01 for survey line 1 and 0.001 for survey line 2. This contrasts to initial water injection stage, where COV values are 0.07 for survey line 1 and 0.03 for survey line 2. The COV values for the strata pressures above the oil bearing layer also showed similar behaviors of reduced values due to pressure build up. However, it is also noticed that strata pressure above the oil bearing

layer is increased as contrast to the drop in pressure within the oil bearing layer. For survey line 1, the pressure immediately above the oil bearing layer increased from 8,144.6 ft/s (2,482.5 m/s) initially, to 9,512.9 ft/s (2,899.5 m/s), and finally, to 9,963.7 ft/s (3,036.9 m/s). For survey line 2, the pressure immediately above the oil bearing layer increased from 8,207.6 ft/s (2,501.7 m/s), to 9,664.0 ft/s (2,945.6 m/s), and finally, to 9,935.8 ft/s (3,028.4 m/s). This observation may be an indication that the oil pressure is stressing (possible lifting) the above-strata and resulting in wave speed increase.

COV values for before and after CO_2 injection stages, for both survey line 1 and 2 are not consistent indicating the pressure distribution at Citronelle at the time of injection study is directional. COV values obtained from before and during CO_2 injection are larger than the COV of well head stresses (0.019). The COV values from after CO_2 injection stage are similar as the COV values of well head stresses, indicates the effective stresses inside the reservoir are stabilized during after CO_2 injection.

3.4. Summary

The proposed passive DoReMi technique was shown to detect the strata wave speed changes successfully. Being passive, the method relies on consistent input sources and usually focuses on low frequency band width signals. With only two survey lines, current study does not have the resolution to establish the migration of CO_2 through the oil field, which can be accomplished with additional data pick ups. Steiner et al. (2008) has successfully used synchronized measurement to localize microtremors. The COV value analysis has shown to indicate velocity change at different stages of injection and may further develop into index such as $\Delta v/v$.

Carbon sequestration through injection into Citronelle Oil Field is an effective method to reduce atmospheric CO_2. A proper monitoring technique is necessary to monitoring the CO_2 injection process and to provide information about the geomechanic stability of the storage reservoir.

The ability of the passive DoReMi technique to monitor the CO_2 sequestration process in the heterogeneous oil reservoir, Citronelle Oil Field, has been explained and demonstrated through the wave speed profiles. The technique is a novel and cost-effective surface Rayleigh wave monitoring method and is deemed able to provide information on the pressure response of the reservoir. The shear wave velocities are for before, during, and after CO_2 injection in the field, with notable changes of the shear wave velocity indicating that the reservoir pressure has gradually influenced the Rodessa oil bearing layers. The results can be used to indicate the total stress distribution at Citronelle, which is an important factor to prove significant geomechanical deformation has not occurred.

Finally, the COV value of the shear wave velocity change is observed to drop during the CO_2 injection experiment and can be used as an indication of oil field stability during the CO_2 injection operation. The proposed passive DoReMi and COV value of shear wave velocity changes have the potential for long term monitoring of the strata stress change throughout the field operations.

CHAPTER 4: METHODOLOGY

4.1. Introduction

In this chapter, the MDOF dynamic linear models used to simulate wave propagation in a simulated geo-media are described. The strata profile of the Citronelle Oil Field was divided into several layers of simulated lumped mass-spring-dashpots with assumptions made about the spring constant, mass and damping. The MDOF modeling is shown in FIGURE 4.1 and the experimental design is shown in TABLE 4.1. The excitation source is the vibration of an ESP, which is commonly used in petroleum production. The status of the CO_2 may be a multi-phase blend with in-situ oil-in-place and injection water under certain temperature and pressure at depth. As a result, instead of pure CO_2, the model was assumed multiphase, gas/water/oil mixtures with in-situ pressure, which is simplified into layer stiffness amplification.

TABLE 4.1: Experimental design

Multi-harmonic Excitation		
Material properties	Linearity	Nonlinearity
	Soft Hard Hard Multiphase (K, 1.2K, 1.4K, 1.6K, 1.8K and 2.0K)	Soft Hard Hard Multiphase (K, 1.2K, 1.4K, 1.6K, 1.8K and 2.0K)
Oil bearing phase transition	Gas ↔ Liquid → Solid	

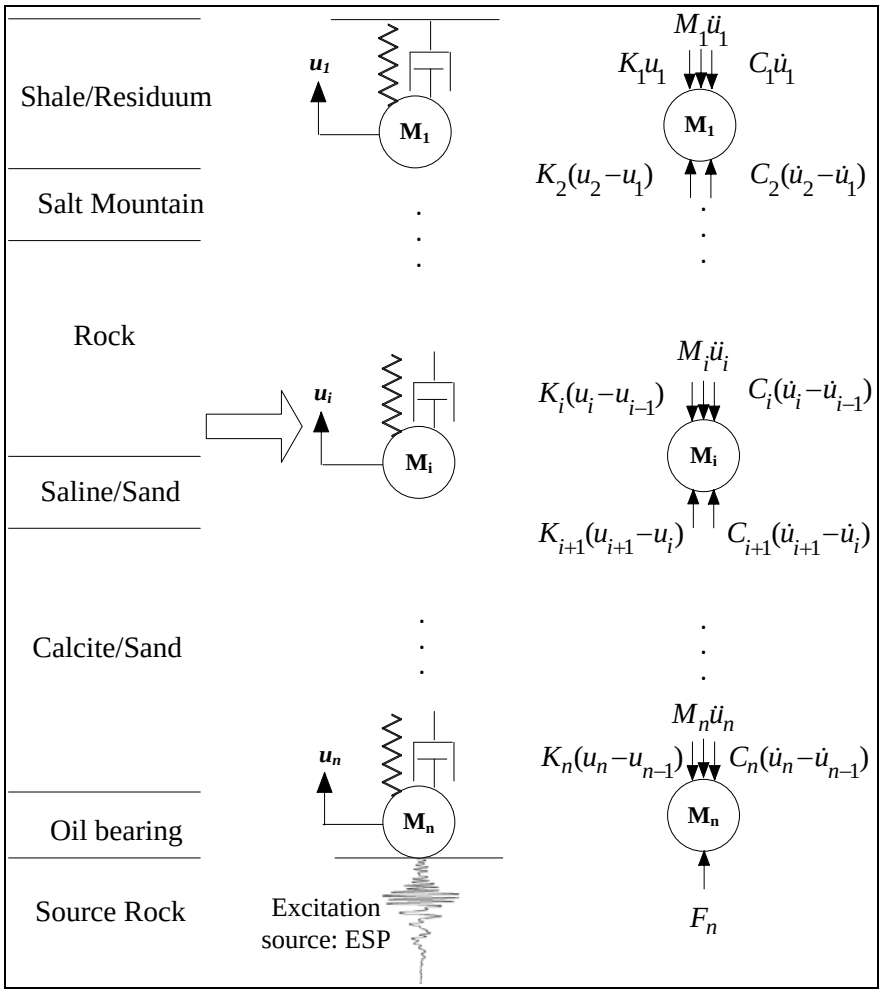

FIGURE 4.1: The MDOF Model and its Free Body Diagrams

Runge-Kutta method was employed to solve the equations of motion for the MDOF model. Commercial software, Matlab, was used to develop the program to conduct numerical simulation and the software structure as shown in FIGURE 1.2. The results of the numerical simulation were analyzed in both time domain and frequency domain.

4.2. Lumped Mass Modeling Assumptions and Algorithm

4.2.1 The Equations of Motion

For the MDOF model shown in FIGURE 4.1, the masses are constrained to move only vertically, and there is no horizontal motion. With the assumption that soil layers can be modeled as concentrated masses, the equations of motion can be established by *Newton's Second Law*. In FIGURE 4.1, the masses are numbered as m_{11}, m_{22}, …, m_{nn} from top to bottom; similarly, the damping coefficients, C_1, C_2, …, C_n, and the layer stiffnesses, K_1, K_2, …, K_n, are also named from top down. The equation of motion for the system in dynamic equilibrium can be written as:

$$F - Q - D = M\ddot{u} \tag{4}$$

where F is the applied external force and Q is the spring force due to the stiffness of the lumped mass and D is the damping force. These forces are acting on the mass M, with resulting acceleration of the mass, $\ddot{u}$. Equations of motion for adjacent layers would be coupled reactions as a result of the layer interactions. For the lumped masses and spring model shown in FIGURE 4.1, the equations of motion for all layers can be written as:

$$\begin{aligned}
M_n\ddot{u}_n + C_n\dot{u}_n - C_n\dot{u}_{n-1} + K_n u_n - K_n u_{n-1} &= F_n(t) \\
M_{n-1}\ddot{u}_{n-1} - C_{n-1}\dot{u}_{n-2} + (C_{n-1} + C_n)\dot{u}_{n-1} - C_n\dot{u}_n - K_{n-1}u_{n-2} + (K_{n-1} + K_n)u_{n-1} - K_n u_n &= 0 \\
&\vdots \\
M_i\ddot{u}_i - C_i\dot{u}_{i-1} + (C_i + C_{i+1})\dot{u}_i - C_{i+1}\dot{u}_{i+1} - K_i u_{i-1} + (K_i + K_{i+1})u_i - K_{i+1}u_{i+1} &= 0 \\
&\vdots \\
M_1\ddot{u}_1 + (C_1 + C_2)\dot{u}_1 - C_2\dot{u}_2 + (K_1 + K_2)u_1 - K_2 u_2 &= 0
\end{aligned} \tag{5}$$

where i denotes the element number and n is the total number of degrees of freedom. K_i is the stiffness coefficient and C_i is the damping coefficient. $F_n(t)$ is the applied external force at layer *n*, which is a time-dependent function. Equation (5) can be rewritten in matrix form:

$$[M]\cdot\{\ddot{u}\}+[C]\cdot\{\dot{u}\}+[K]\cdot\{u\}=\{F\} \tag{6}$$

where

$$[M]=\begin{bmatrix} m_{11} & & \cdots & & 0 \\ & m_{22} & & & \\ & & \ddots & & \\ \vdots & & m_{ii} & & \vdots \\ & & & \ddots & \\ & & & & m_{(n-1)(n-1)} \\ 0 & & \cdots & & m_n \end{bmatrix} \tag{7}$$

$$[C]=\begin{bmatrix} C_1+C_2 & -C_2 & 0 & \cdots & & & 0 \\ -C_2 & C_2+C_3 & -C_3 & & & & \\ & \ddots & \ddots & \ddots & & & \\ \vdots & & -C_i & C_i+C_{i+1} & -C_{i+1} & & \vdots \\ & & & \ddots & \ddots & \ddots & \\ & & & & -C_{n-1} & C_{n-1}+C_n & -C_n \\ 0 & & \cdots & & 0 & -C_n & C_n \end{bmatrix} \tag{8}$$

$$[K]=\begin{bmatrix} K_1+K_2 & -K_2 & 0 & \cdots & & & 0 \\ -K_2 & K_2+K_3 & -K_3 & & & & \\ & \ddots & \ddots & \ddots & & & \\ \vdots & & -K_i & K_i+K_{i+1} & -K_{i+1} & & \vdots \\ & & & \ddots & \ddots & \ddots & \\ & & & & -K_{n-1} & K_{n-1}+K_n & -K_n \\ 0 & & \cdots & & 0 & -K_n & K_n \end{bmatrix} \tag{9}$$

$$[u]=\begin{bmatrix} u_1 \\ \vdots \\ u_i \\ \vdots \\ u_n \end{bmatrix} \tag{10}$$

$$[\dot{u}] = \begin{bmatrix} \dot{u}_1 \\ \vdots \\ \dot{u}_i \\ \vdots \\ \dot{u}_n \end{bmatrix} \tag{11}$$

$$[\ddot{u}] = \begin{bmatrix} \ddot{u}_1 \\ \vdots \\ \ddot{u}_i \\ \vdots \\ \ddot{u}_n \end{bmatrix} \tag{12}$$

$$[F] = \begin{bmatrix} 0 \\ \vdots \\ 0 \\ \vdots \\ F_n(t) \end{bmatrix} \tag{13}$$

where $[M]$, $[C]$ and $[K]$ are the mass matrix, the damping matrix and stiffness matrix, respectively, and they are $n \times n$ matrices; $[u]$, $[\dot{u}]$, $[\ddot{u}]$ and $[F]$ are displacement, velocity, acceleration and external force functions, respectively, and they are vector arrays of n entries.

Equation (5) is a set of simultaneous equations, which can be solved once for each time step using numerical methods (e.g. Runge-Kutta method and Linear-Acceleration method, etc.) and will be presented next.

4.2.2 Numerical Analysis

According to the mathematical treatments of differential equations of motion, the numerical methods for solving such equations can be classified into two types: implicit and explicit. The fundamental differences in explicit and implicit solutions for dynamic

problems are that explicit solvers solve one step at a time and implicit solvers address the entire process simultaneously. As a result, implicit schemes require assemblies of large matrices and can be hard on computation time. In order to make the convergence of the mathematical equations, very small time steps are needed in the explicit methods. Therefore, the explicit methods take longer solution time to solve the problems than the implicit methods. Even though time consumption is the disadvantage of explicit method, the explicit method is more suitable for dealing with partial differential equations that need special treatments.

Several numerical methods for solving the differential equations of motion were introduced in Berg (1989). The methods include the linear-acceleration method, the Adams-Stoermer method, special linear-acceleration method, the Newmark Beta method, Runge-Kutta method, and Milne Predictor-Corrector method. In order to check the size of numerical error, the author examined the solutions of two specific problems by some of the numerical methods and compared them with the exact analytical solutions. It can be shown that Runge-Kutta gives the best accuracy, with maximum error decreasing as h^4, where h is a time step.

Runge-Kutta method is a stable algorithm, very efficient and easy to program, because the main calculation processes of the method are matrix multiplication and addition. The accuracy of the fourth order Runge-Kutta method for solving differential equation depends on the step size used. The local truncation error involved in the fourth order Runge-Kutta method is $\boldsymbol{O}(h^5)$, while the final global error is on the order of $\boldsymbol{O}(h^4)$ (Mathews and Fink 2004). Runge-Kutta method was widely used in numerical simulations (Rezaiguia et al. 2010; Smith 1975; Tu et al. 2001).

Runge-Kutta Method, which is an explicit method based on step-by-step direct integration, may be adopted in solving the differential equations of motion for the dynamic problems (Berg, 1989). The number of simultaneously solved equations is proportional to the degrees of model. The equation of motion for each layer can be expressed by its acceleration as:

$$\ddot{u}_i = f(u_i, \dot{u}_i, t) \tag{14}$$

Equation (14) shows that the acceleration is a function of the velocity and the displacement of each mass. Because the equations of the two adjacent masses are ordinarily coupled, these equations for MDOF model must be assembled and solved simultaneously. The detailed form of Equation (14) is written as,

$$\ddot{u}_{i,t} = \frac{F_{i,t} - K_{i,t}u_{i-1,t} + (K_{i,t} + K_{i+1,t})u_{i,t} - K_{i+1,t}u_{i+1,t} - C_{i,t}\dot{u}_{i-1,t} + (C_{i,t} + C_{i+1,t})\dot{u}_{i,t} - C_{i+1,t}\dot{u}_{i+1,t}}{M_i} \tag{15}$$

Equation (15) shows that the acceleration of the lumped mass can be determined by its resultant force divided by its mass. $F_{i,t}$ is the total applied force acting on each mass, and the stiffness coefficient and the damping coefficients of the lumped masses are time-dependent parameters in Equation (14), which is simplified as:

$$\ddot{u}_i = \frac{F_i - Q_i - D_i}{M_i} \tag{16}$$

The procedure of Runge-Kutta method is to determine the weighted averages of acceleration through trial calculation at each time step. The fourth-order Runge Kutta method is employed and four evaluations of the function $\boldsymbol{f}$ per time step are needed. The calculation of the Fourth-Order Runge Kutta Method in each time step is as follows:

1. Compute four trial changes in velocity:

$$
\begin{aligned}
k_1 &= h\, f(u_{i,p}, \dot{u}_{i,p}, t_p) \\
k_2 &= h\, f(u_{i,p} + \frac{h\dot{u}_{i,p}}{2} + \frac{hk_1}{8}, \dot{u}_{i,p} + \frac{k_1}{2}, t_p + \frac{h}{2}) \\
k_3 &= h\, f(u_{i,p} + \frac{h\dot{u}_{i,p}}{2} + \frac{hk_1}{8}, \dot{u}_{i,p} + \frac{k_2}{2}, t_p + \frac{h}{2}) \\
k_4 &= h\, f(u_{i,p} + h\dot{u}_{i,p} + \frac{hk_3}{2}, \dot{u}_{i,p} + k_3, t_p + h)
\end{aligned}
\tag{17}
$$

where h is the time step. Trial stages k_1, k_2, k_3 and k_4 will be used as average factors to project the displacement and velocity at the end of each time interval.

2. Compute displacement at a subsequent time:

$$u_{i,p+1} = u_{i,p} + h(\dot{u}_{i,p} + \frac{k_1 + k_2 + k_3}{6}) \tag{18}$$

(Subscript p represents each time step)

3. Compute velocity at the subsequent time:

$$\dot{u}_{i,p+1} = \dot{u}_{i,p} + \frac{k_1 + 2\left(k_2 + k_3\right) + k_4}{6} \tag{19}$$

4. Compute acceleration at subsequent time using Equation (5).

The fourth-order Runge-Kutta method flow chart is shown in FIGURE 4.2:

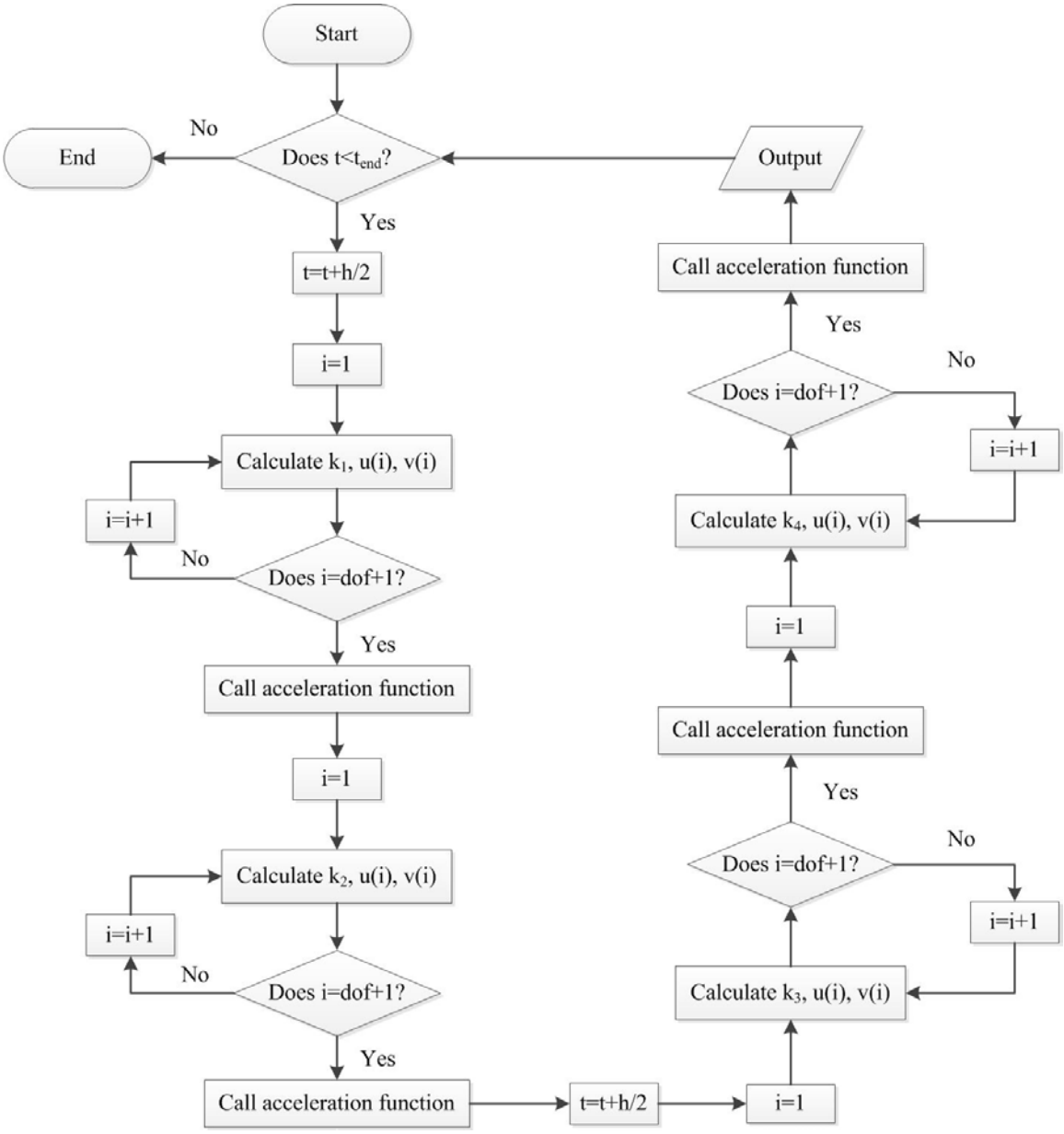

FIGURE 4.2: Fourth-order Runge-Kutta method flow chart

4.2.3 Mass, Stiffness and Damping for Each Layer

FIGURE 4.3 shows an example of idealized horizontal layered soil profile, consists of n sublayers having different material properties. The soil profile is composed of a series of lumped masses and connected by springs and dashpots.

E_1, ρ_1, h_1	1^{st} layer
E_2, ρ_2, h_2	2^{nd} layer
⋮	
E_i, ρ_i, h_i	i^{th} layer
⋮	
E_n, ρ_n, h_n	n^{th} layer

FIGURE 4.3: Idealized horizontal layer soil profile

For an element in the assumed MDOF model, the cross-sectional area of the element is assumed to be unity, then, the axial stiffness of the i^{th} layer is

$$k_i = E_i / h_i \tag{20}$$

where E_i is the elastic modulus of the i^{th} layer; h_i is the thickness of the i^{th} layer.

Similarly, for an element in the assumed MDOF model, the mass of the i^{th} layer is

$$m_i = \rho_i h_i = \gamma_i h_i / g \tag{21}$$

where ρ_i is the density of the i^{th} layer; γ_i is the unit weight of the i^{th} layer.

Damping of each layer in the lumped mass model is typically related to the mass and stiffness of the corresponding layer. Rayleigh damping was first proposed by Rayleigh in 1877 (1945, reprint) and later expanded for damped linear and nonlinear dynamic systems (Caughey 1960; Caughey and O'Kelly 1965; Hashash and Park 2002; Idriss and Seed 1970; Park and Hashash 2004; Phillips and Hashash 2009). The general formulation of traditional damping matrix is given as:

$$[C] = a_0[M] + a_1[K] \tag{22}$$

where a_0 and a_1 are damping coefficients.

Considering the radial energy dissipation, in our model, the damping coefficient of each layer is expressed as:

$$c_i = \rho_i v_i = \rho_i \sqrt{\frac{E_i}{\rho_i}} = \sqrt{\rho_i E_i} = \sqrt{M_i k_i} \tag{23}$$

where c_i is the damping coefficient of layer i; v_i is the longitudinal wave velocity of the i^{th} layer. The general formulation of damping matrix is given as:

$$[C] = c_i \tag{24}$$

When a P-wave ray is incident on an interface with acoustic impedance contrasts, reflected and refracted P-waves are generated. Additionally, some of the energy of P-wave is converted into reflected and transmitted S-wave rays, the detail introduction can be found in Kearey et al. (2002). In our model, the reflection and refraction of waves are ignored and are truncated by reduced sampling time.

In summary, once the geometry and material properties of the rock layers are known, the mass and stiffness of each layer can be obtained by using Equations (20) and (21). Then, according to the details of the equations of motion, the mass, stiffness and damping coefficient matrices of the lumped mass system can be determined. When the input motion at the bottom are known, and the evaluation of the dynamic response of the MDOF lumped model can be solved by the Runge-Kutta method.

4.2.4 Time Domain and Spectral Domain Analyses

Since time domain analysis is conducted in the MDOF model, we can simulate the sequence of wave propagating through the rock layers. In general, the frequency of

the wave may change when it crosses different mass media. However, the changes of the frequencies are not easily identifiable in time domain. In order to obtain the frequency response of signal received on the ground, Fourier transformation should be conducted on the time domain signals.

An algorithm of Fast Fourier Transformation (FFT) is used to compute the Discrete Fourier Transform (DFT) and its inverse, and the FFT will be employed for frequency spectrum analyses. The DFT of a finite discrete signal $x(n)$, $n = 0,1,\ldots,N-1$ is defined as:

$$X\left(k\right) = \sum_{n=0}^{N-1} x(n) e^{-j2\pi kn/N} \tag{25}$$

where $k = 0,1,\ldots,N-1$, $x(n)$ is the displacement versus time obtained from the MDOF model, and $X\left(k\right)$ is the transformed frequency spectrum of the $x(n)$.

Frequency spectra of the signals received on the ground surface were obtained from the Fourier transform. The frequency range of the simulation can be used to guide the sensor selection in actual geophysical testing in oil field. Spectral analysis of stress wave propagations is conducted to delineate wave components and at the same time, establish the spectral amplitude ratios.

4.2.5 Sensitivity Effects of the MDOF Model

First of all, the influence of the layer number of the MDOF model was studied. The sensitivity analysis was performed by using the same parameters of rocks and changing the number of layers. A best suitable layer number for the proposed model was determined.

We define sensitivity as the amplitude ratio between the vibration level at the excitation source layer and the top layer, where sensor is placed. The amplitude ratio represents sensitivity requirement and the value is then used to establish the required geophone sensitivity requirement.

A result of the assumption about field condition change is that the acceleration/velocity/displacement correlations may change during CO_2 injection as a result of rock stress and pore fluid pressure change. To demonstrate this effect, different variables are derived from the spectral data and observed for possible correlations to condition changes. Numerical sensitivity analysis of the MDOF model on dynamic response of input motion, for different CO_2 injection phases and oil bearing layer's parameters, will be presented in Chapter 5.

4.3. Condition Change Using Dynamic Modeling and Micro-Seismic Measurements

For a single degree of freedom (SDOF) model, the frequency of the model is influenced by the mass and elastic modulus. FIGURE 4.4 show the frequency increases of SDOF model due to the increases of stiffness (all parameters normalized). This phenomenon forms the basis of this study where the geomedia is assumed to be made up of layers of different rock formations. The interactions between the injected CO_2 flow, the porous rock matrix, residual oil and fluid resulted from previous water flood during secondary production, are assumed to be reflected in the stiffness change. There may be a chance that the interactions may change the damping effect of the material, however, damping is a very complex phenomenon and material damping changes will not be considered in this study. The effects of stiffness change for MDOF system are more

complex than the SDOF system, the simulation results should reflect on the overall property changes of the propagating waves.

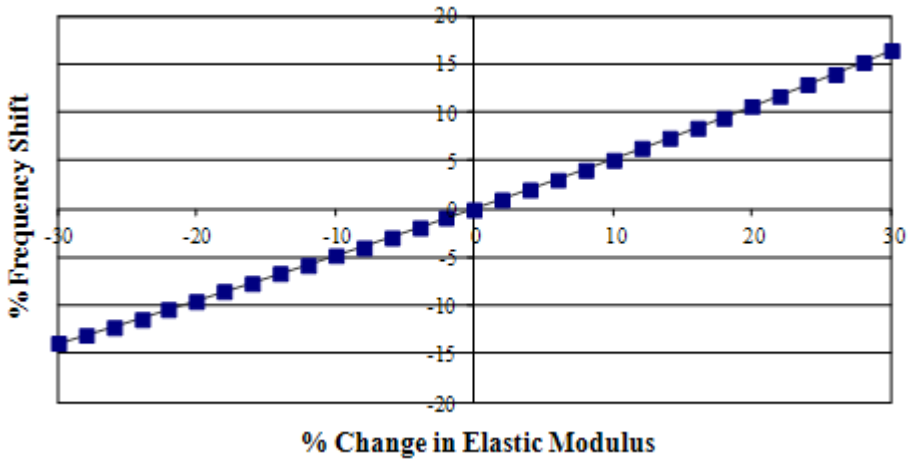

FIGURE 4.4: Frequency shift due to stiffness reduction

As CO_2 injected into oil bearing layer, the pump vibration can be considered as a vibrator. Wave caused by the vibration will propagate through geo-media in all directions. One direction is along the well body; these kinds of waves are not studied, because they are relatively high frequency and do not carry the information of overburden strata. Hence, during the field study, the sensors were placed away from the well head (larger than 10 ft or 3 m) and collected information about the ground vibration.

Due to the dense hard rock, the oil may migrate or may not migrate in the oil bearing layer. When the oil migrates in the oil layer, pressure at the producing layer will decrease slightly resulting in the stiffness of oil bearing layer decrease. When no oil migrates in the oil bearing layer, the stress of the oil bearing layer and the overburden layers will increase. Therefore, the numerical MDOF model will simulate the changing stiffness of both oil bearing layer and overburden strata.

The simulated strata formation of Citronelle Oil Field is shown in TABLE 4.2. The corresponding parameters, including elastic modulus, density and thickness of layer, of MDOF model for the site are also summarized in the table.

TABLE 4.2: Parameters of the strata formation

Part #	Thickness (m)	# of Layers	Type	Mass Density (kg/m^3)	Modulus of Elasticity (kN/m^2)	Stiffness (kN/m)
1	609.6	10*	Shale/Residuum	2701	3275332	4992*
2	304.8	5*	Salt Mountain	2701	10921900	16645*
3	914.4	15*	Rock	2701	22289592	33969*
4	304.8	5*	Saline/Sand	2501.5	28098195	42822*
5	1097.28	18*	Calcite/Sand	2501.5	34887636	53169*
6	243.84	4	Oil bearing	2501.5	38557605	58762*
7	…	…	Source Rock	…	…	…

* Considered variable in parametric study.

The nodes of the MDOF model are named from top to bottom, respectively. The vibration time of the input signal (FIGURE 4.5) is 1 second with sampling time at 0.0005 second and is applied at the last node. The computation time of the numerical simulation is 10 seconds. The input signal is composed of 20 sinusoids with different frequencies, including 1, 1.5, 3, 7, 9, 11, 15, 19, 28.5, 29, 31, 34, 38, 43, 45, 53, 57, 58, 58.5 and 60 Hz. The frequencies are randomly selected. The magnitude of applied force is assumed in the range of ± 675 lb (3,000 N) (This is established based on the assumption that the ESP pump stroke and its fixity with the surrounding rock resulted in a vertical motion that generates a cyclic force). Typical ESP provides consistent pump speed of around 60 Hz. The frequency domain of the input signal was obtained by taking FFT, as shown in FIGURE 4.6. Due to several frequency values closely spaced, only sixteen peaks are observed in this figure.

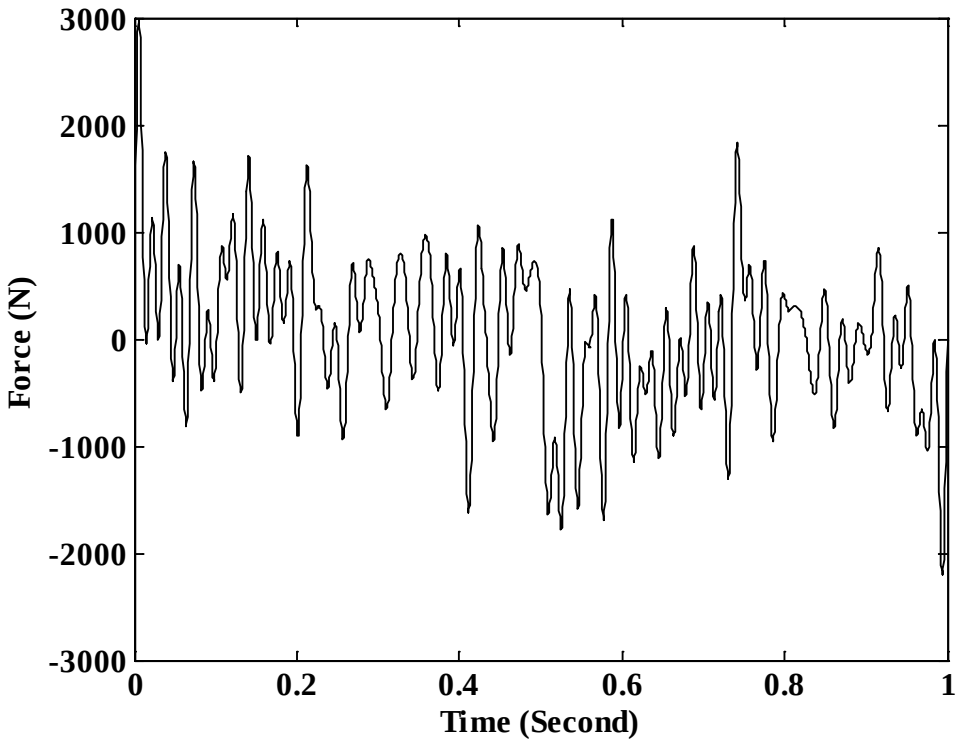

FIGURE 4.5: Time history of input signal

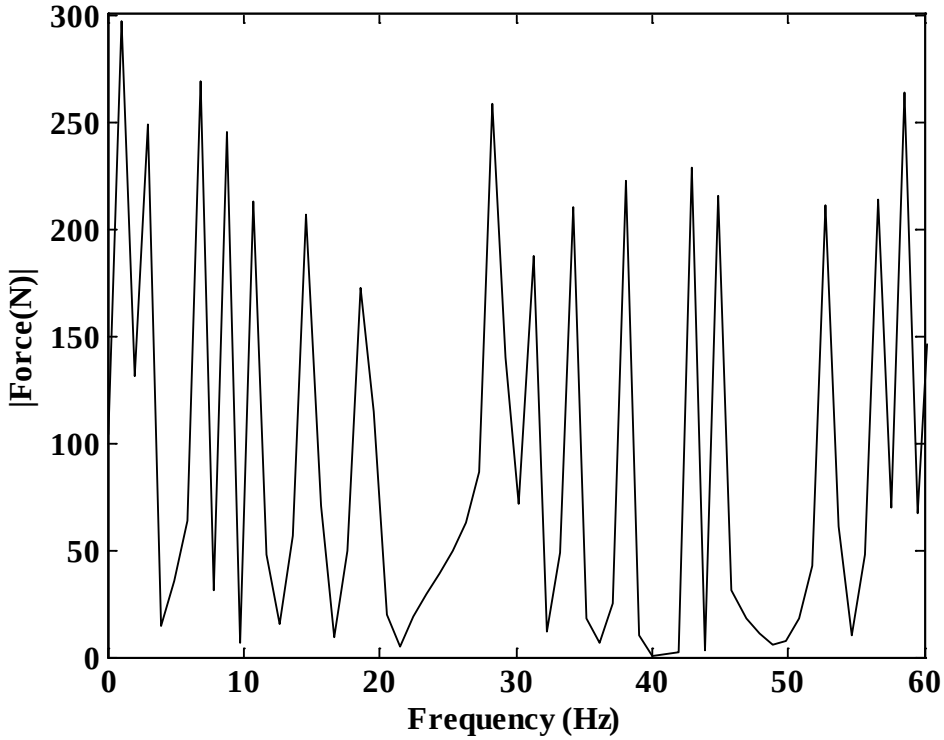

FIGURE 4.6: Frequency domain of input signal

CHAPTER 5: SIMULATION RESULTS IN LINEAR CONDITION

5.1. Introduction

In the oil bearing injection scenario, it is critical to recognize that high fluid pressure (5 ksi or 34.5 MPa) is typically used, hence, we can simulate the stiffening of the layer due to pressurization. Prior geostability analysis indicated that field test results are consistent with the effective stress model, which is influenced by the injection pressure in the porous media (Chen and Qi 2009). When oil is displaced by water or gas, the mass of the layer will decrease only slightly. This is the basis of the Biot (1956a, 1956b) condition. In numerical simulation, we will use stiffness changes for different combination of gas/solid/liquid phases.

The physical properties of each layer may be changed due to CO_2 injection and oil production, which will affect the wave propagating through the geomedia. The change of conditions will be modeled by effective stiffness change using a decoupled stiffness term

$$K_{effective} = K_{martix} + K_{fluid} \tag{26}$$

where K_{matrix} accounts for the change in rock matrix, and K_{fluid} will account for the pore fluid pressure.

A very important observation in Biot's reports is the presence of the low frequency and high frequency waves. Even though the MDOF model does not model directly the two waves, the two stiffness terms effectively includes two separate

conditions (the pore fluid pressure and the rock matrix changes) on the propagating waves.

This chapter reports the observations of a series of numerical simulations using the proposed MDOF model in linear conditions only. To demonstrate the effect of parameter changes, we also propose to present the results in the form of tripartite spectral plots (TSP). The results of numerical simulation will be presented in the following forms:

(1) Top nodes displacement, velocity and acceleration time series;

(2) Top nodes spectral spectra; and

(3) Top nodes TSP;

5.2. Layer Assumption (Discretization Effect) Analysis

In order to study the effect of layer number on the MDOF model, the model layer number was varied consistently from which 57 to 534, which represents layer thickness ranging from 200 ft (60.96 m) to 20 ft (6.096 m). 20 ft (6.096 m) is smaller than most microseismic wave lengths. The detailed information is summarized in TABLE 5.1. The total effective stiffnesses of the different layer models were kept constant, and the detailed derivation of the effective stiffness is discussed in Appendix A. The input signal used in the linear model is described in previous chapter (shown in FIGURE 4.5). The plots of time histories of displacement, velocity and acceleration at Node 1 for the simulation models with ten different layers are shown in FIGURE 5.1, FIGURE 5.2, and FIGURE 5.3, respectively. The time history plots at Node 1 showed that the arrival time of the 534 layers model is longer than the 57 layers model. The frequency domains of the corresponding figures are shown in FIGURE 5.4, FIGURE 5.5 and FIGURE 5.6,

respectively, which showed that the higher frequencies were received at Node 1 when the thickness of the layer decreases.

Twelve modes were selected from the frequency domain of displacement (FIGURE 5.7); the magnitude of different modes is plot with the layer numbers of MDOF model in FIGURE 5.7, which showed the displacement amplitude is converging when the layer number exceeds 300. Similar results were obtained from the frequency domain of both velocity and acceleration plots (FIGURE 5.8 and FIGURE 5.9). Therefore, the 534 layer model will be used for conducting the numerical simulation in both linear and nonlinear conditions. In this model, the thickness of sublayer for oil bearing layer is 200 ft (60.96 m), while 20 ft (6.096 m) for other sublayers.

TABLE 5.1: Layer numbers of MDOF model

Case #	1	2	3	4	5	6	7	8	9	10
Total layers	57	110	163	216	269	322	375	428	481	534
Thickness of sublayer (m)	60.96	30.48	20.32	15.24	12.192	10.16	8.709	7.62	6.773	6.096

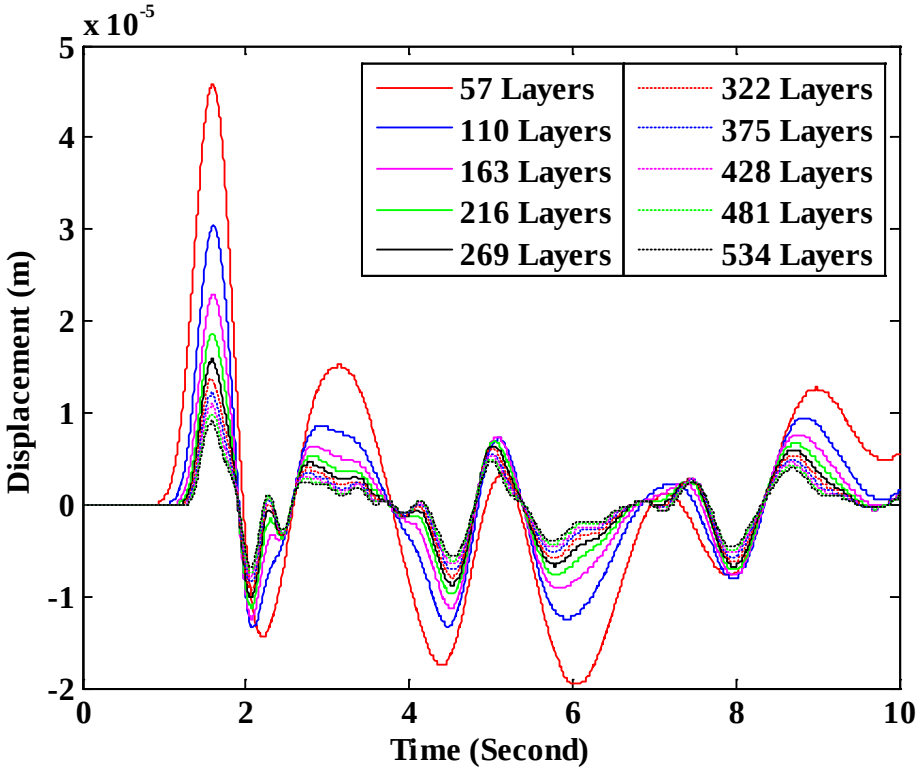

FIGURE 5.1: Displacement time histories of Node 1 for models of different layer numbers

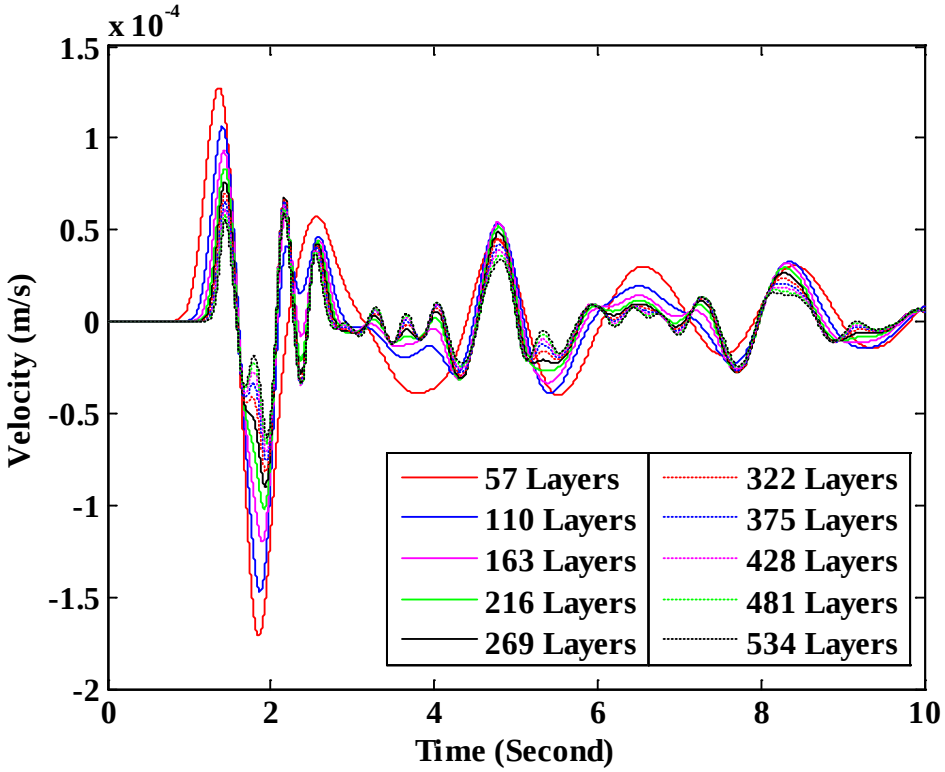

FIGURE 5.2: Velocity time histories of Node 1 for models of different layer numbers

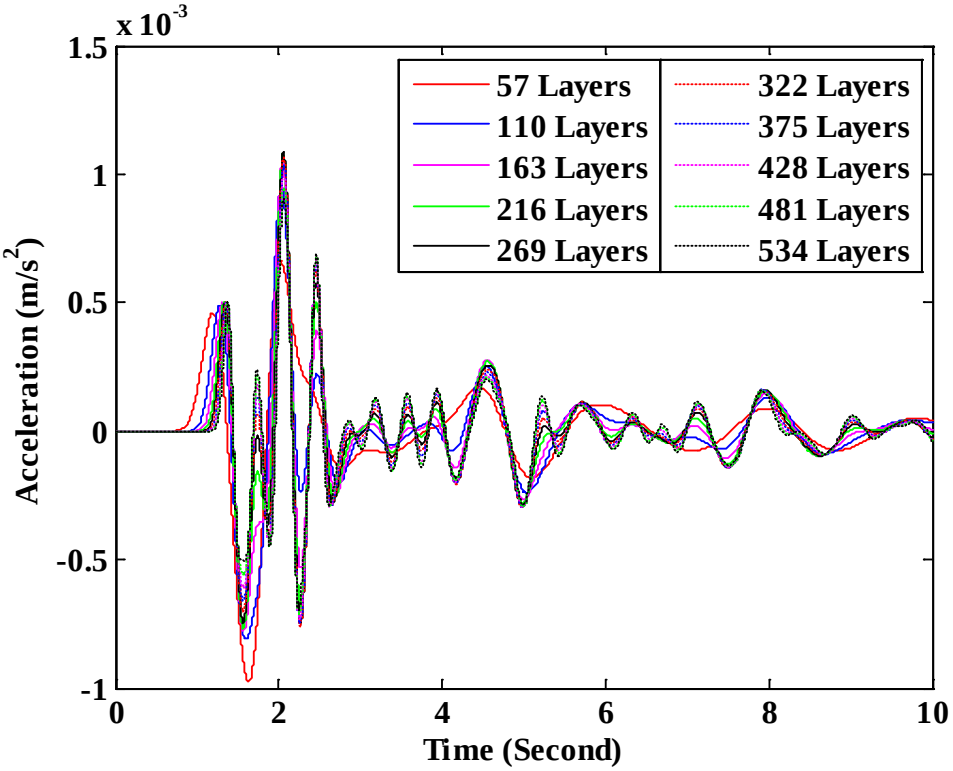

FIGURE 5.3: Acceleration time histories of Node 1 for models of different layer numbers

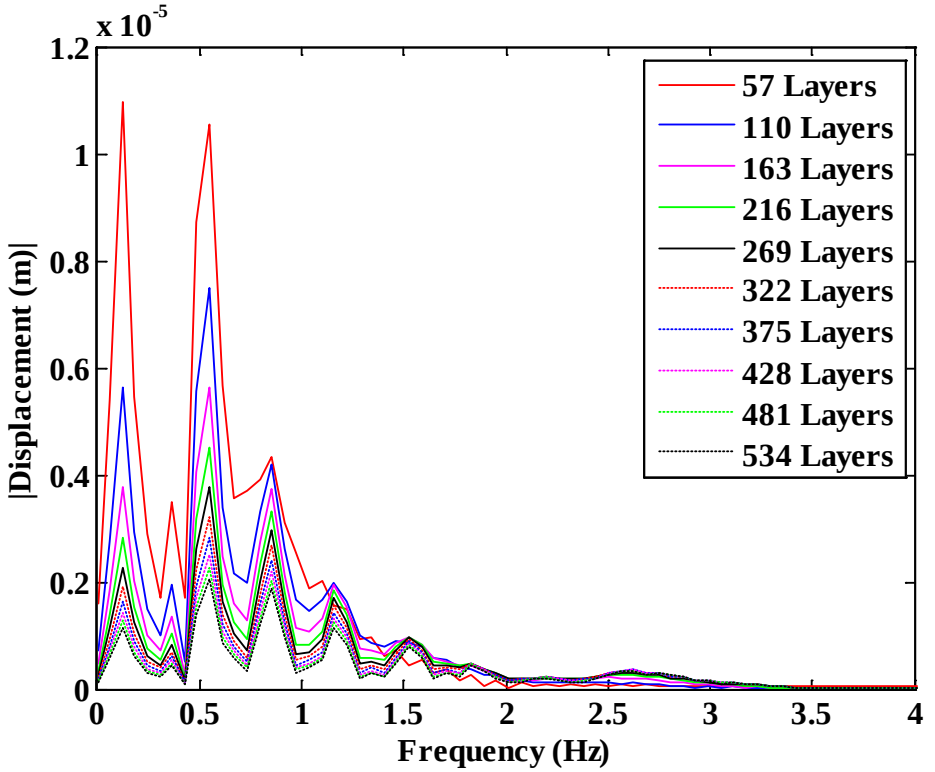

FIGURE 5.4: Frequency domain of Node 1 displacement (corresponding to FIGURE 5.1)

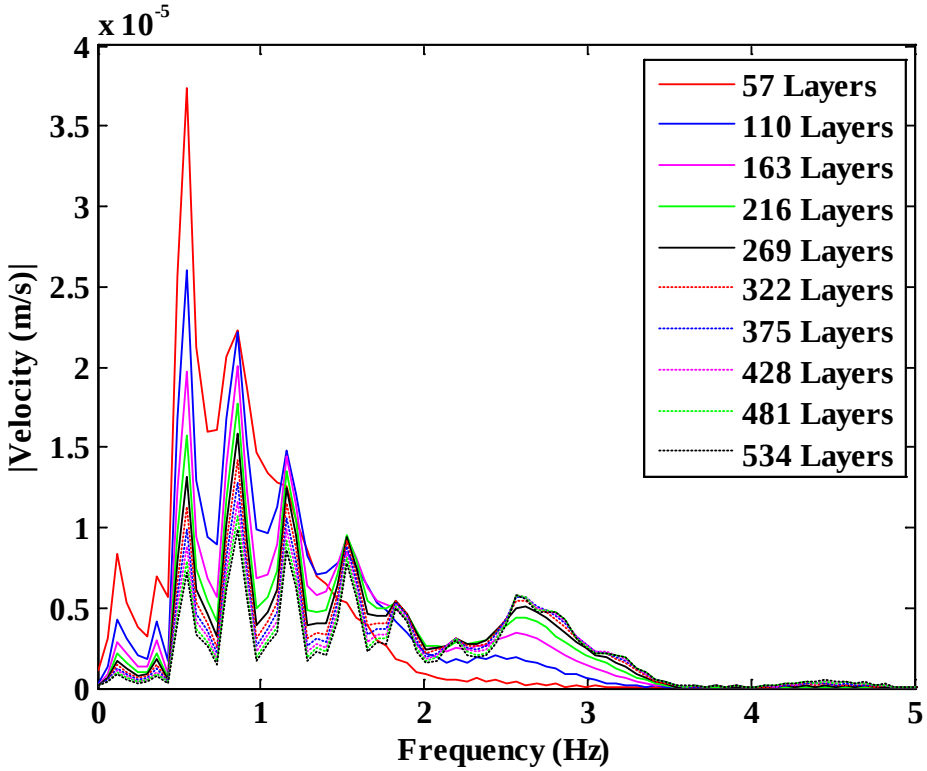

FIGURE 5.5: Frequency domain of Node 1 velocity (corresponding to FIGURE 5.2)

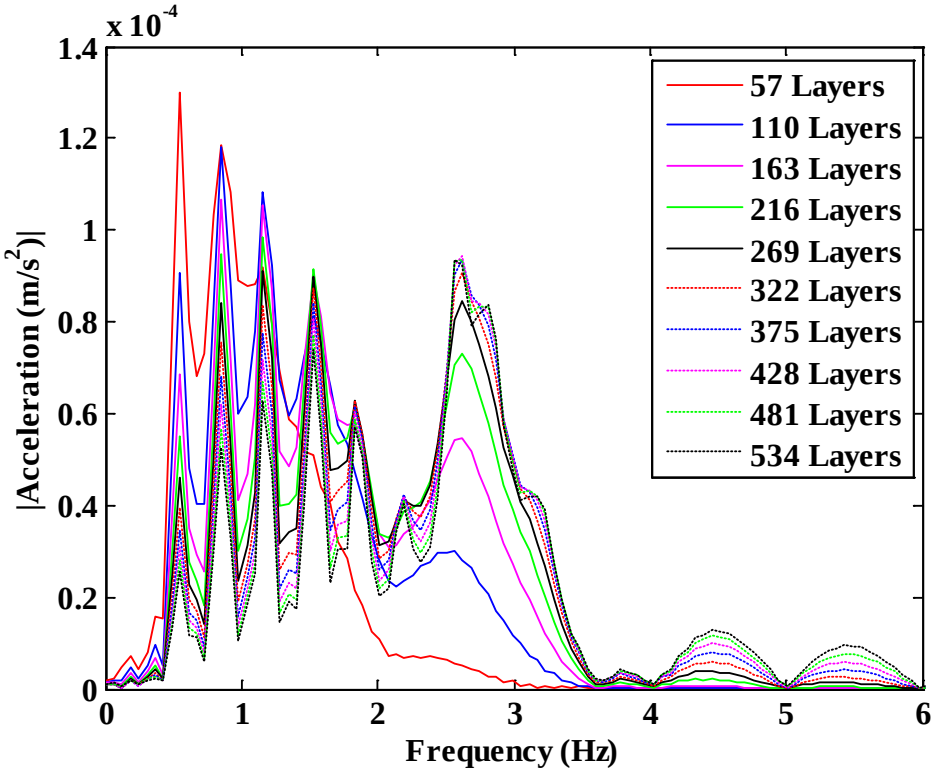

FIGURE 5.6: Frequency domain of Node 1 acceleration (corresponding to FIGURE 5.3)

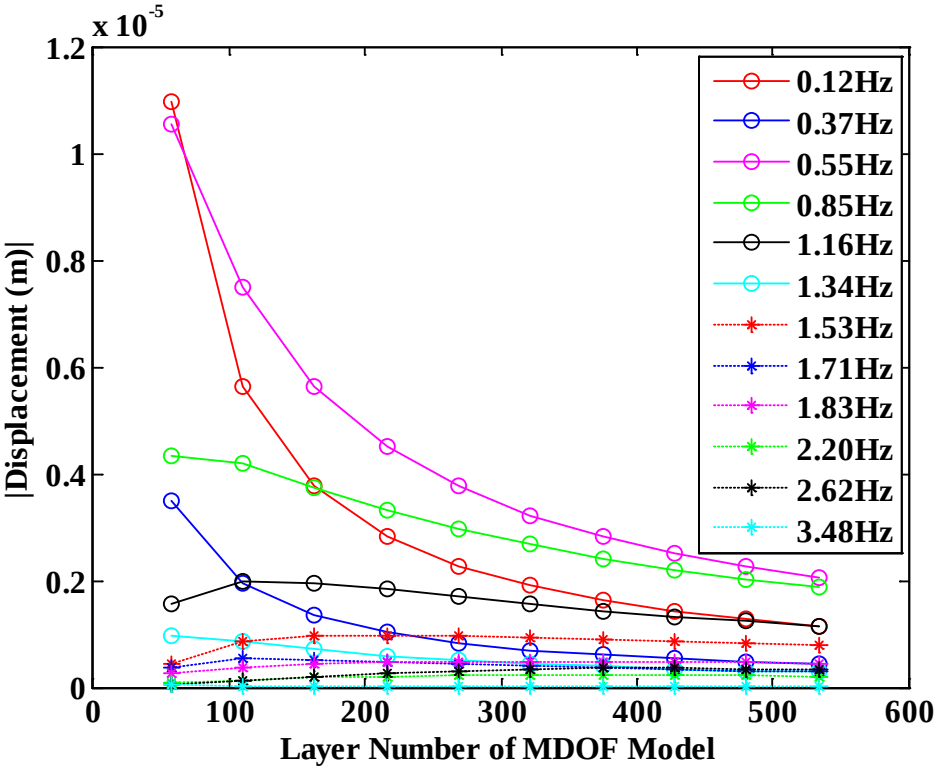

FIGURE 5.7: Displacement amplitude of selected frequency modes for different layer numbers

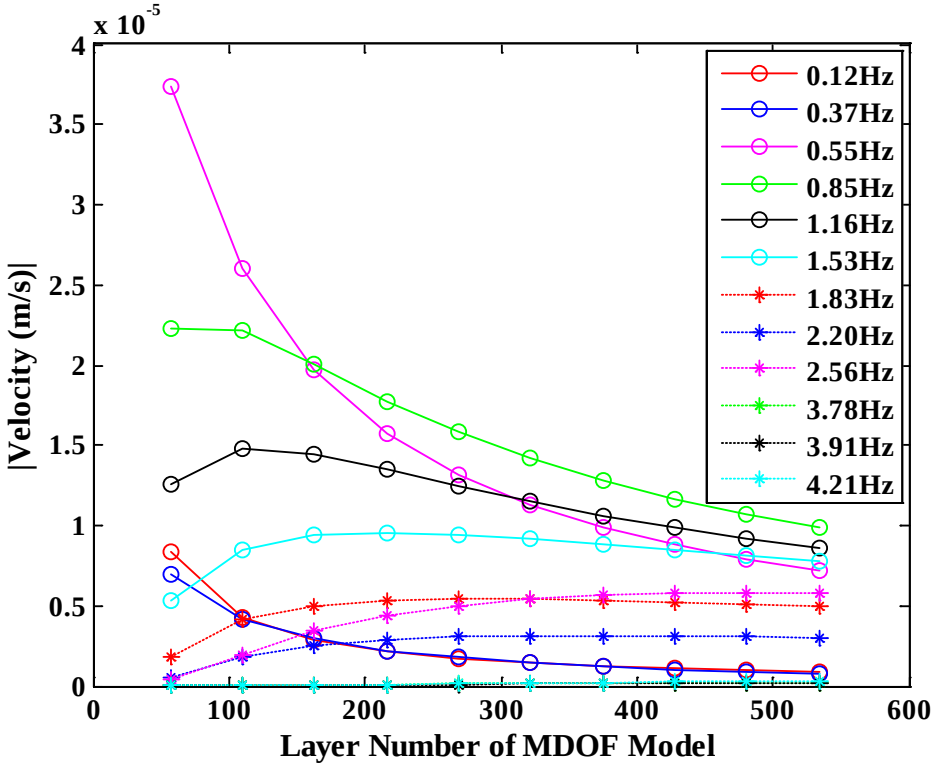

FIGURE 5.8: Velocity amplitude of selected frequency modes for different layer numbers

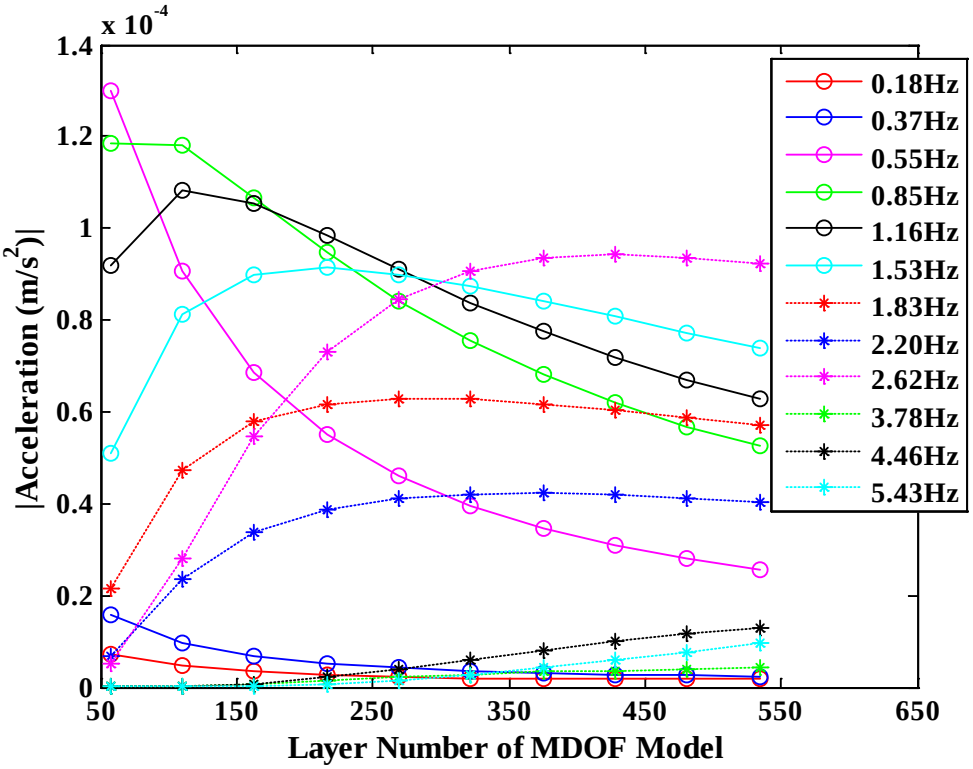

FIGURE 5.9: Acceleration amplitude of selected frequency modes for different layer numbers

5.3. Model Validation

534 layers MDOF model selected from previous section was used to study the model in linear condition. In the linear model, the maximum displacement amplitude of Node 1 of each model is expected to increase with increasing loading magnitude. Seven loading amplitudes ranging from 675 lb (3,000 N) to 1,350 lb (6,000 N) were applied to the model and denoted as Case I through Case VII respectively. The design parameters of the numerical simulation are shown in TABLE 5.2.

TABLE 5.2: Cases of MDOF models with different loading amplitudes

Case #	I	II	III	IV	V	VI	VII
Unit (lb)	675	787.5	900	1,012.5	1,125	1,237.5	1,350
Unit (N)	3,000	3,500	4,000	4,500	5,000	5,500	6,000

The displacement time histories of Node 1 are plotted in FIGURE 5.10, which indicated that as the loading force increases, the absolute amplitudes of displacement also increase. It is especially true for the absolute peak amplitudes. The maximum displacement amplitudes of the seven models in FIGURE 5.10 were selected to plot against the loading magnitudes shown in FIGURE 5.11, which shows that as the loading magnitude increases, the maximum displacement amplitude increases linearly. It indicates the MDOF model is good to perform numerical simulation in linear condition. Loading magnitude of 675 lb (3,000 N) was used for all model studies in later sections.

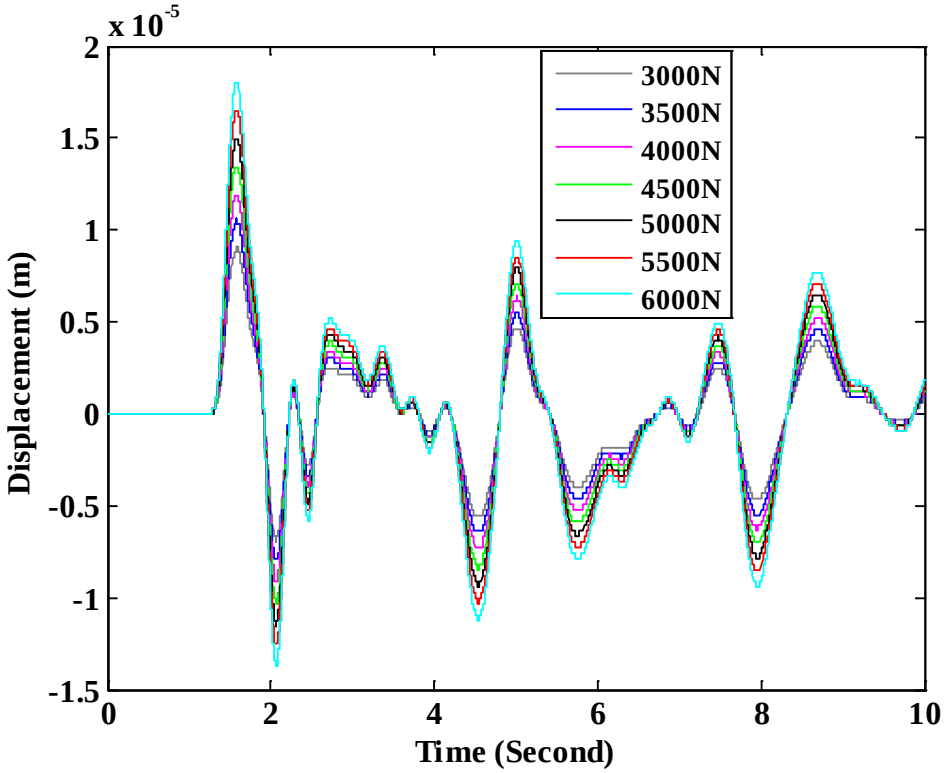

FIGURE 5.10: Displacement time histories of Node 1 of Cases I to VII

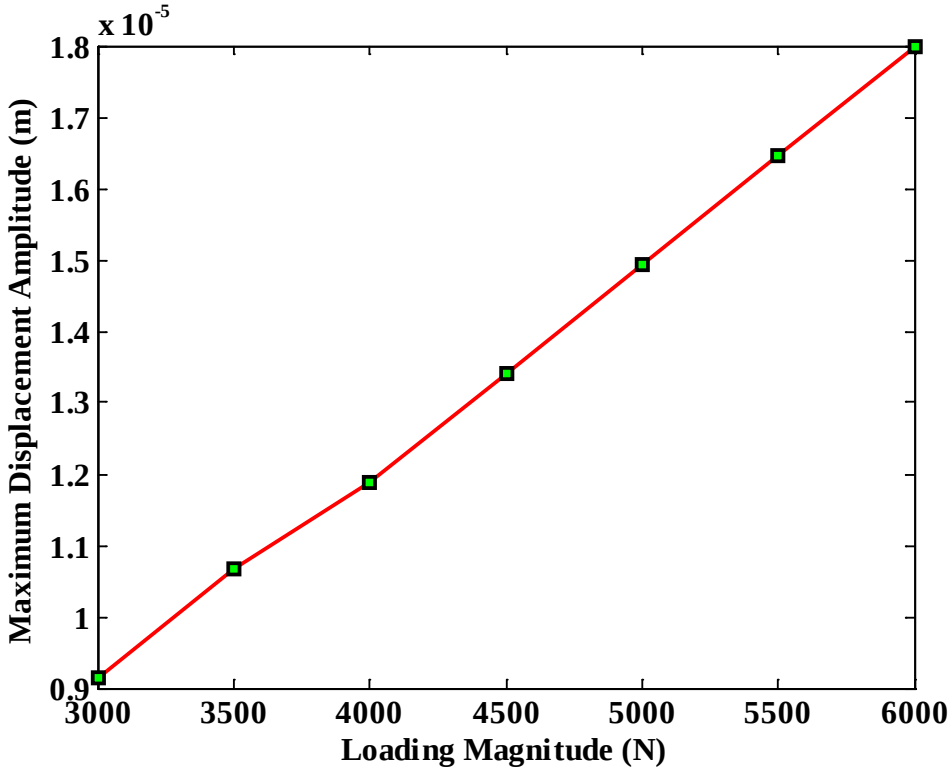

FIGURE 5.11: Maximum displacement amplitude versus loading in linear MDOF model

5.4. Baseline MDOF Model

A Matlab script has been developed to compute the time domain response of the MDOF model. In the analysis of the 534 layer MDOF model, we establish the baseline response by using the parameters provided in TABLE 4.2. FIGURE 5.12 shows the displacement response of selected nodes from the model.

The frequency domain of the corresponding plot shown in FIGURE 5.12 was computed by FFT and is shown in FIGURE 5.13 (up to 5 Hz). FIGURE 5.13 indicates that most high frequency signals have died out and only waves up to 4 Hz are transmitted to the top layer. The velocity and acceleration time histories of Node 1 of the baseline MDOF model are shown in FIGURE 5.14 and FIGURE 5.16, respectively. Frequency

domain responses of selected nodal velocity and acceleration time histories of the baseline MDOF model are shown in FIGURE 5.15 and FIGURE 5.17, respectively.

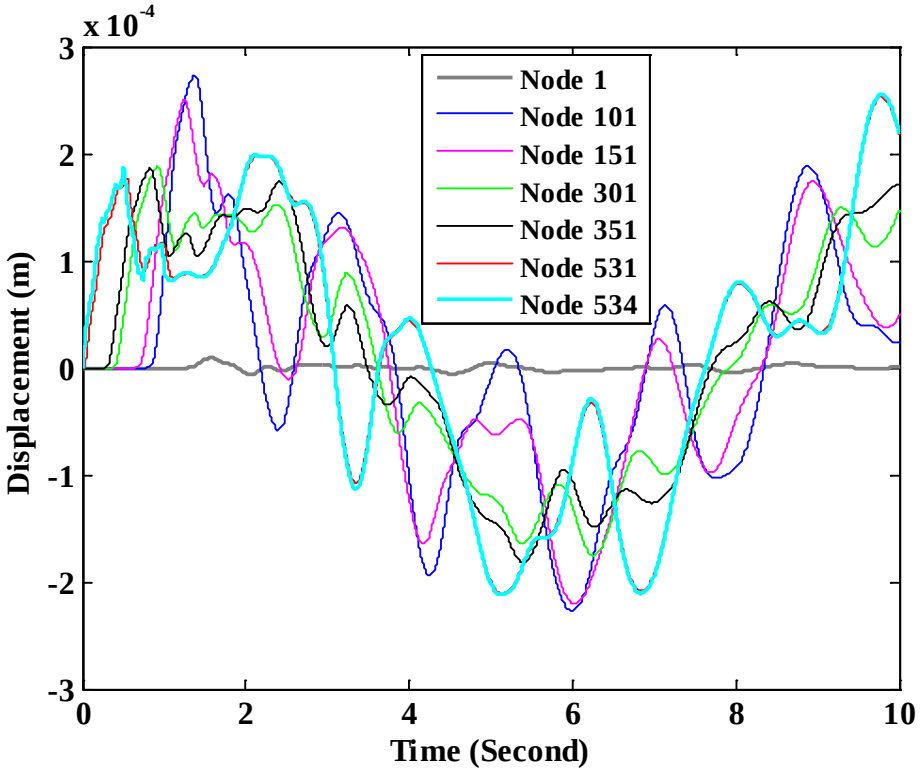

FIGURE 5.12: Displacement time histories of selected nodes of baseline model

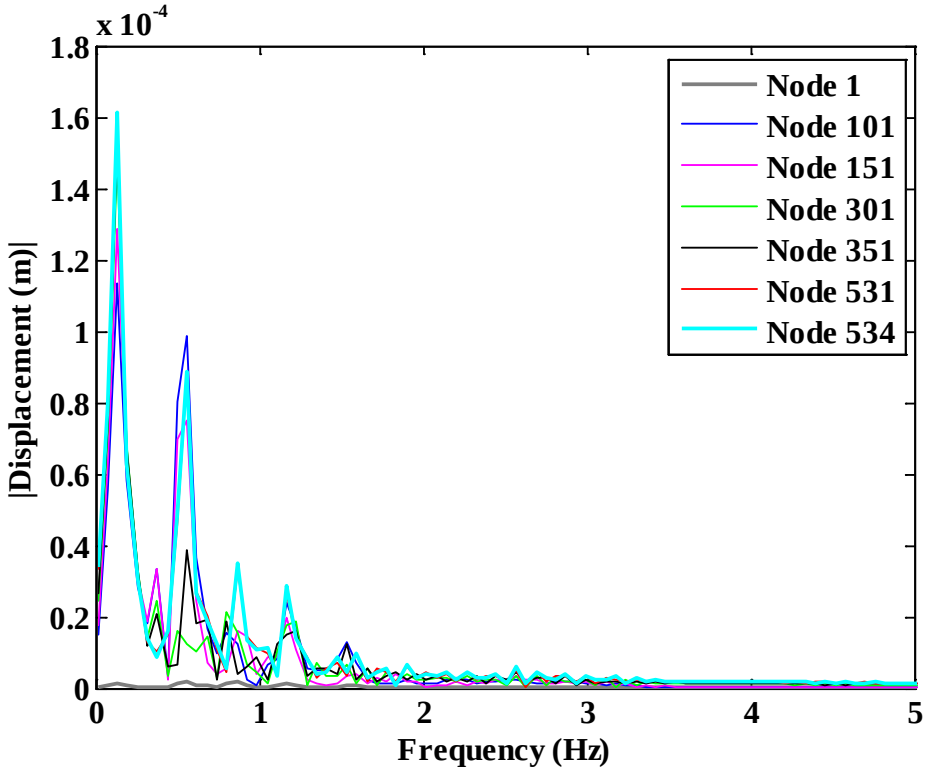

FIGURE 5.13: Frequency domain of selected nodes displacement (corresponding to FIGURE 5.12)

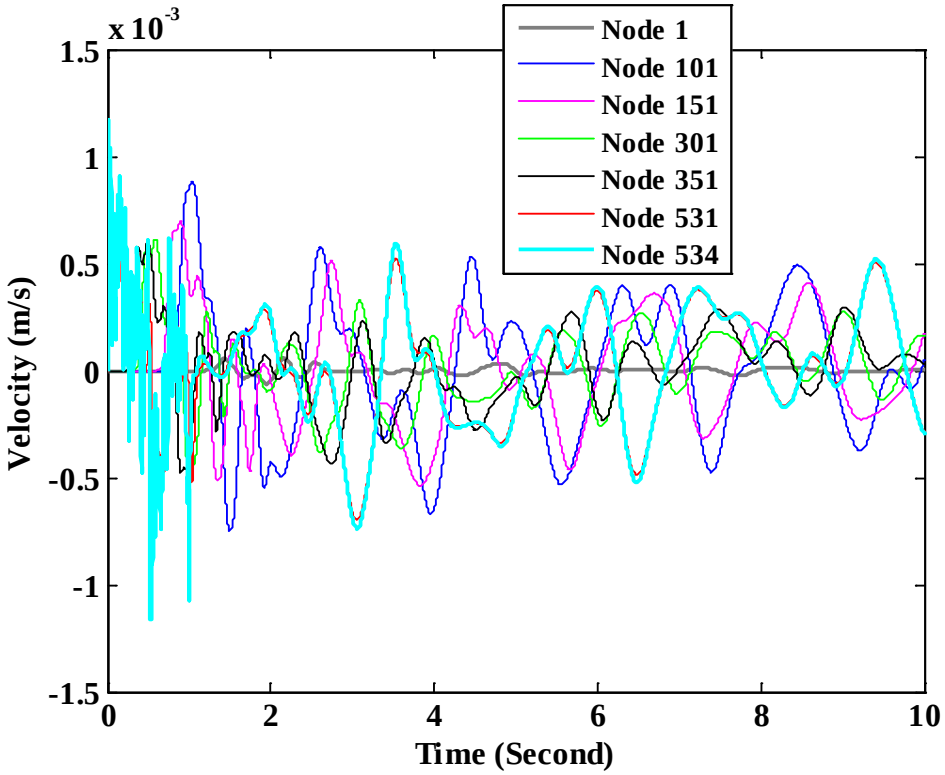

FIGURE 5.14: Velocity time histories of selected nodes of baseline model

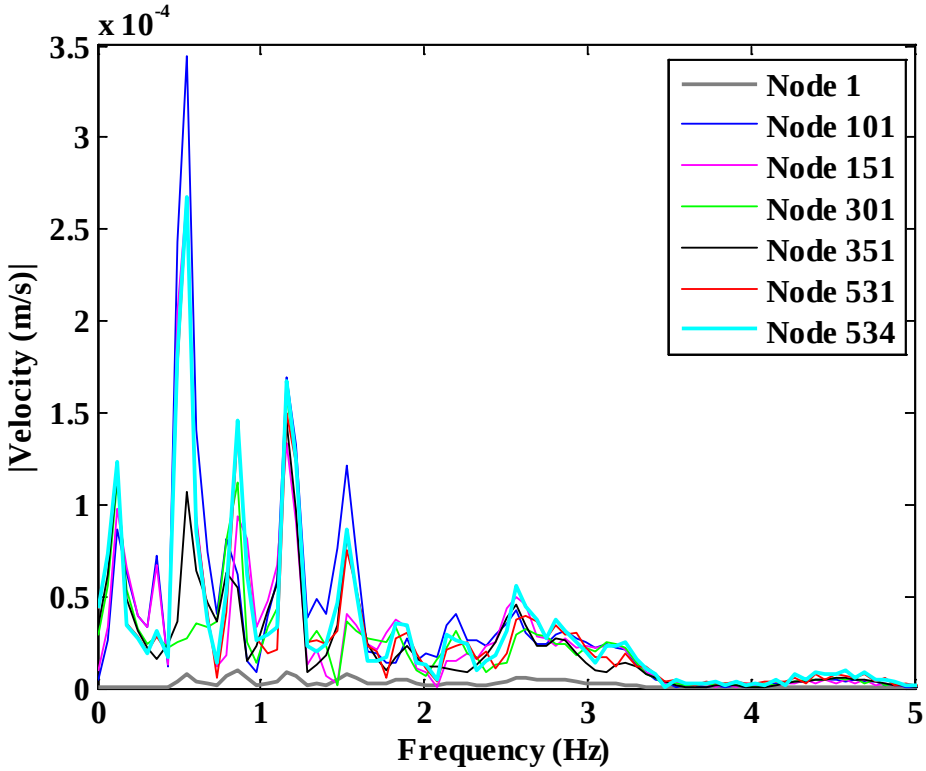

FIGURE 5.15: Frequency domain of selected nodes velocity (corresponding to FIGURE 5.14)

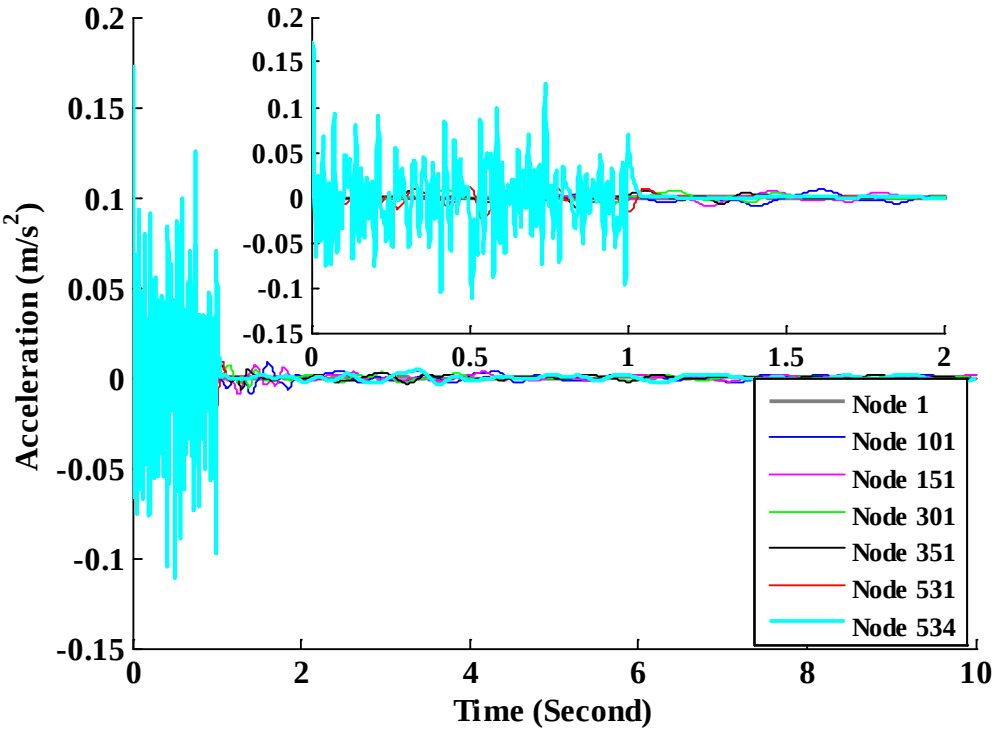

FIGURE 5.16: Acceleration time histories of selected nodes of baseline model

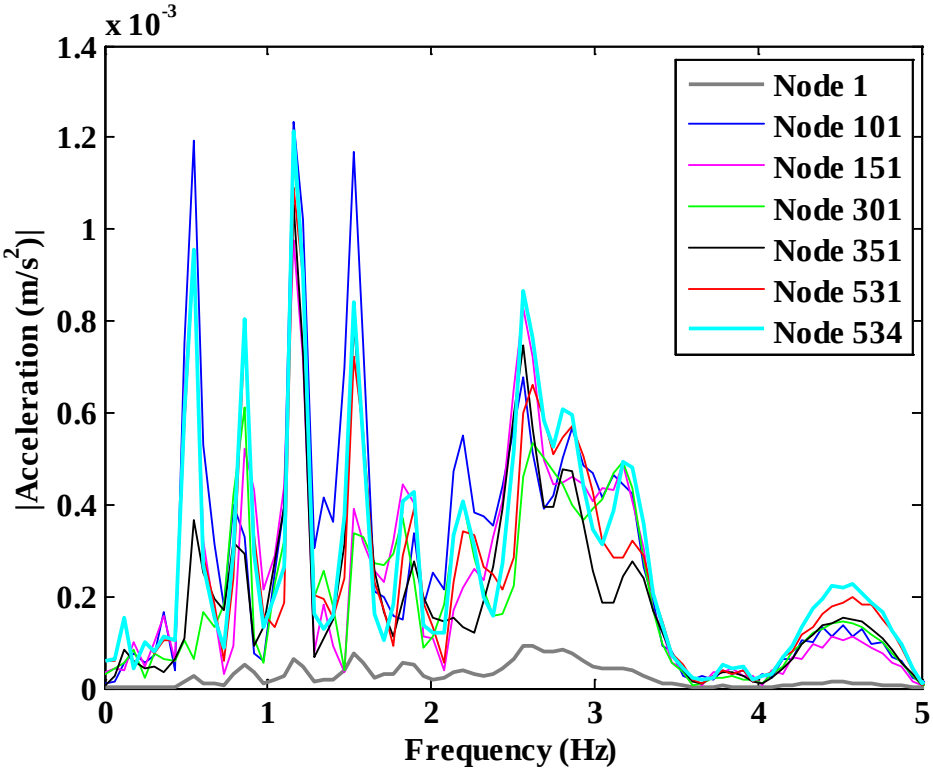

FIGURE 5.17: Frequency domain of selected nodes acceleration (corresponding to FIGURE 5.16)

5.5. Oil Bearing Layer Effects

5.5.1 Sensitivity to Oil Bearing Layer Stress Changes

As CO_2 is injected into the oil bearing layer, oil may not migrate resulting an stress increase in the oil bearing layer. The multi-physical phase change at the oil bearing layer is simplified into stiffness increase in the MDOF model. In order to study the influence of effective stiffness changes at the oil bearing layer, the term K_{matrix} in Equation (26) has been kept as constant, while the term K_{fluid} in Equation (26) has been increased to 0%, 20%, 40%, 60%, 80% and 100% of original stiffness of K_{matrix}. The corresponding simulations are defined as L Cases I-0 to I-5, respectively. This is a

significant simplification of the actual oil-water-gas-rock-pore pressure interactions, which is too complex to capture using the lumped massed model.

The displacement time histories of Node 1 in the model are shown in FIGURE 5.18. The corresponding frequency domain is shown in FIGURE 5.19 (up to 4 Hz). Frequency amplitude is used to indicate the effect of stiffness change. Spectral amplitude percentage difference (SAPD) is defined as:

$$\frac{A_{Case\ I-i} - A_{Case\ I-0}}{A_{Case\ I-0}} \times 100\% \tag{27}$$

where $A_{Case\ I-i}$ represents the frequency amplitude in i^{th} cases, $A_{Case\ I-0}$ represents the frequency amplitude in the baseline model.

The SAPD for Node 1 displacement data due to the five stiffness increase scenarios are shown in TABLE 5.3. The SAPD represents the effect of stiffness increase at oil layer on the wave components at different frequencies. FIGURE 5.19 shows that as the oil bearing layer increases its stiffness, the displacement amplitude reduces for different frequency components. This is especially true for modes at 0.55, 0.85, 1.16, 1.34, 1.53, 1.71, 1.83, 2.56 and 2.81 Hz.

The velocity and acceleration time histories of Node 1 in the MDOF model are shown in FIGURE 5.20 and FIGURE 5.22, respectively, with the corresponding frequency spectra shown in FIGURE 5.21 and FIGURE 5.23, respectively. It is noted that there are some differences in the frequency domain, especially for the frequency signals ranged from 2.5 Hz to 3 Hz. The exact differences of the corresponding amplitude are shown in TABLE 5.4 and TABLE 5.5, for Node 1 velocity and acceleration data, respectively.

It is noted that the energy distribution is not consistent throughout all frequencies, indicates SAPD changes are frequency dependent. In general, the SAPD difference of higher frequency is larger than the difference of lower frequency, which means the higher mode frequencies are being attenuated more than the lower frequencies. This observation is consistent with our understanding of wave propagation phenomenon.

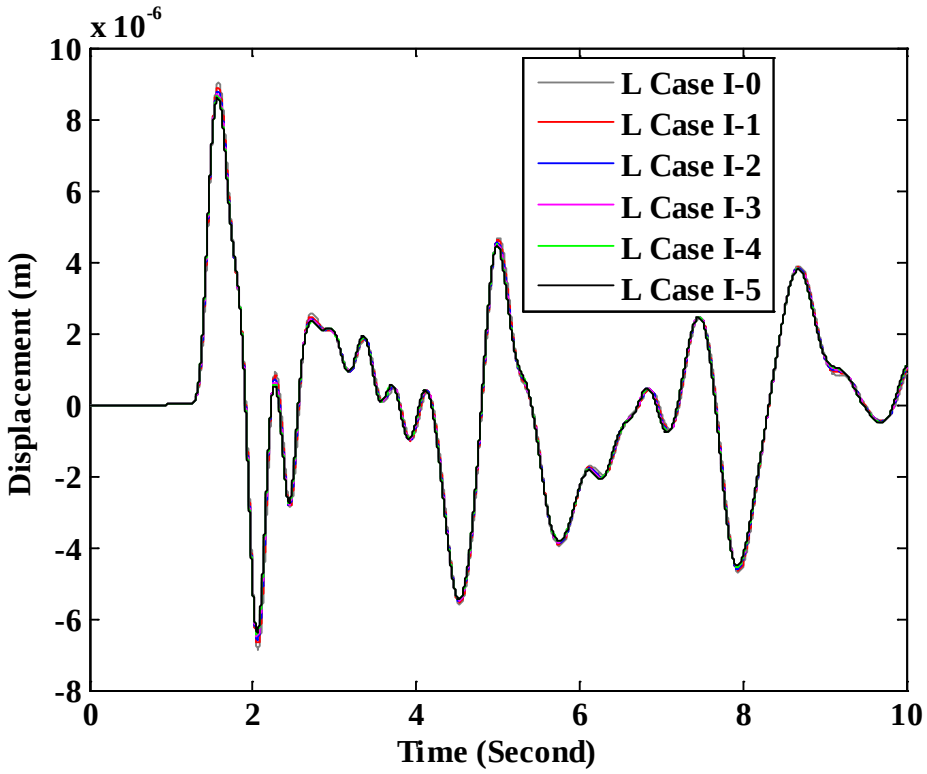

FIGURE 5.18: Displacement time histories of Node 1 of L Cases I-0 to I-5

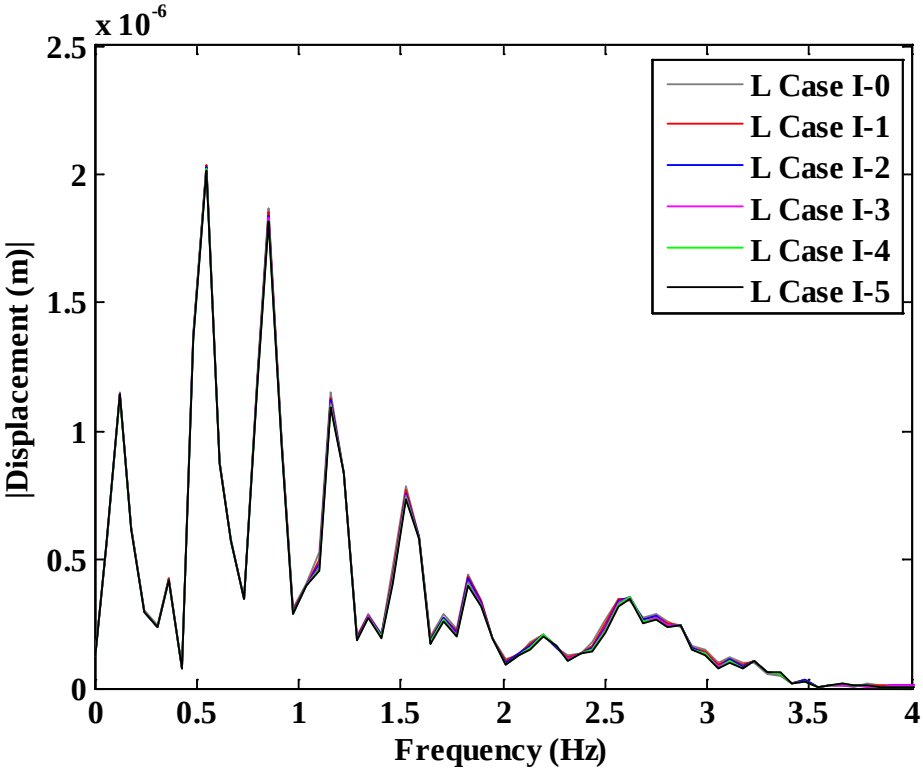

FIGURE 5.19: Frequency domain of Node 1 displacement (corresponding to FIGURE 5.18)

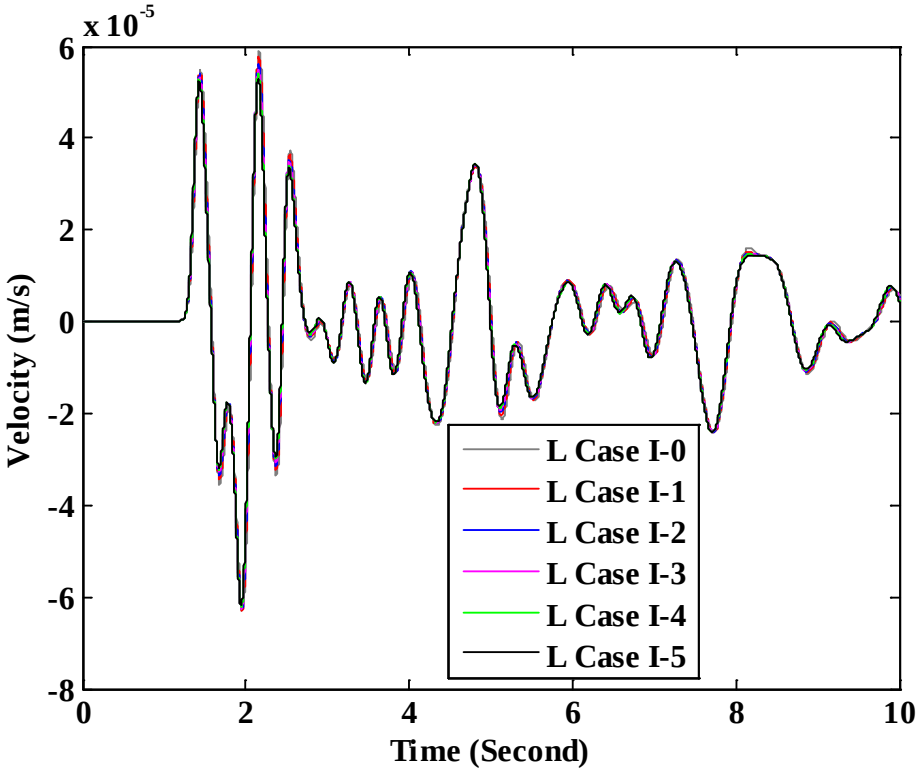

FIGURE 5.20: Velocity time histories of Node 1 of L Cases I-0 to I-5

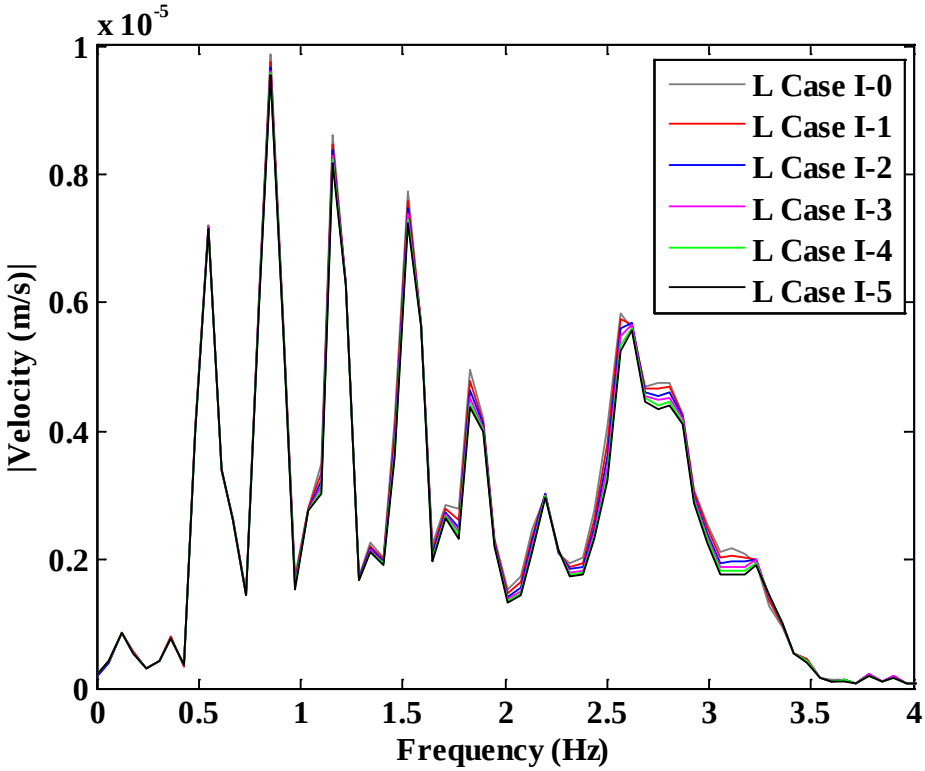

FIGURE 5.21: Frequency domain of Node 1 velocity (corresponding to FIGURE 5.20)

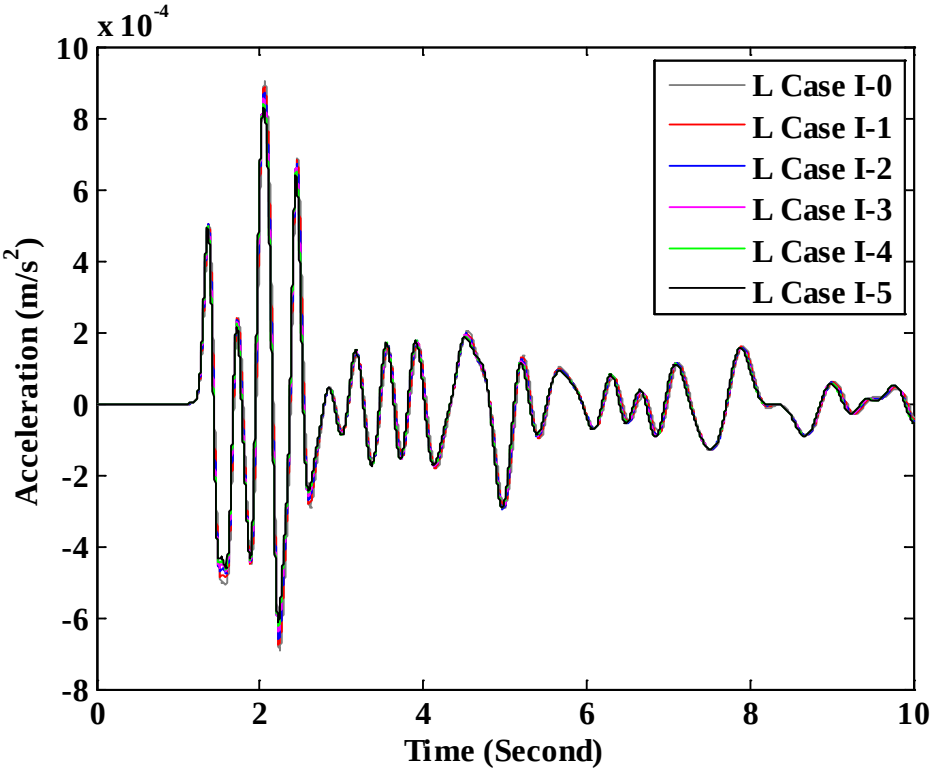

FIGURE 5.22: Acceleration time histories of Node 1 of L Cases I-0 to I-5

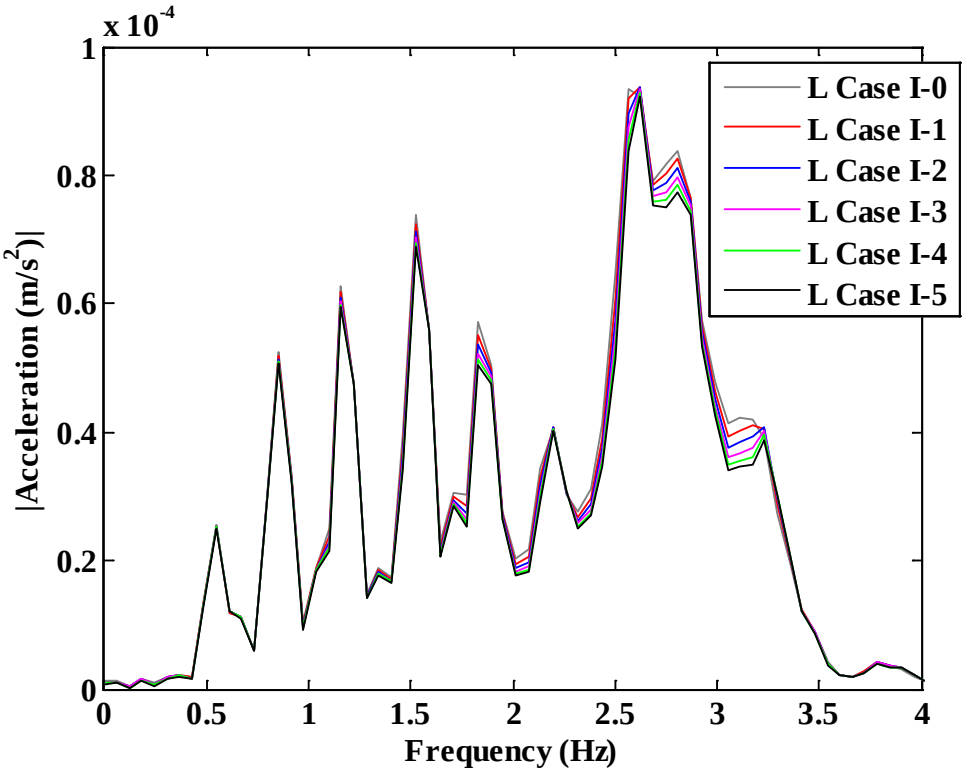

FIGURE 5.23: Frequency domain of Node 1 acceleration (corresponding to FIGURE 5.22)

TABLE 5.3: SAPD for Node 1 displacement signal of L Cases I-0 to I-5

Case #	Stiffness of oil bearing	Frequency (Hz)										
		0.37	0.55	0.85	1.16	1.34	1.53	1.71	1.83	2.20	2.56	2.81
L Case I-0	100%	0.00	0.00	0.00	0.00	0.00	0.00	0.00	0.00	0.00	0.00	0.00
L Case I-1	120%	-0.97	-0.23	-0.81	-1.68	-2.15	-1.84	-3.79	-1.52	0.62	-0.94	-1.68
L Case I-2	140%	-1.69	-0.35	-1.40	-2.81	-3.96	-3.25	-5.98	-3.61	-0.33	-3.44	-3.30
L Case I-3	160%	-2.28	-0.66	-2.02	-3.77	-4.36	-4.28	-7.11	-6.12	0.47	-5.16	-5.32
L Case I-4	180%	-2.40	-0.90	-2.54	-4.54	-4.46	-5.28	-8.40	-8.24	-0.17	-6.70	-6.53
L Case I-5	200%	-2.36	-1.02	-2.89	-5.21	-4.70	-6.24	-8.67	-9.81	-0.76	-8.81	-7.65

TABLE 5.4: SAPD for Node 1 velocity signal of L Cases I-0 to I-5

Case #	Stiffness of oil bearing	Frequency (Hz)										
		0.37	0.55	0.85	1.16	1.34	1.53	1.71	1.83	2.20	2.56	2.81
L Case I-0	100%	0.00	0.00	0.00	0.00	0.00	0.00	0.00	0.00	0.00	0.00	0.00
L Case I-1	120%	-2.51	-0.20	-1.18	-1.52	-2.23	-1.94	-2.03	-3.71	0.80	-1.53	-1.27
L Case I-2	140%	-3.98	-0.36	-1.95	-2.63	-3.90	-3.47	-3.62	-6.51	0.75	-3.85	-2.98
L Case I-3	160%	-5.08	-0.48	-2.56	-3.58	-5.03	-4.75	-4.92	-8.74	0.24	-6.19	-4.60
L Case I-4	180%	-5.71	-0.62	-2.99	-4.31	-5.93	-5.79	-5.89	-10.43	-0.32	-8.36	-6.15
L Case I-5	200%	-6.12	-0.69	-3.37	-4.91	-6.51	-6.62	-6.60	-11.89	-1.06	-10.20	-7.51

TABLE 5.5: SAPD for Node 1 acceleration signal of L Cases I-0 to I-5

Case #	Stiffness of oil bearing	Frequency (Hz)										
		0.37	0.55	0.85	1.16	1.34	1.53	1.71	1.83	2.20	2.56	2.81
L Case I-0	100%	0.00	0.00	0.00	0.00	0.00	0.00	0.00	0.00	0.00	0.00	0.00
L Case I-1	120%	-3.44	-0.36	-1.08	-1.55	-2.23	-1.98	-2.00	-3.60	0.88	-1.64	-1.40
L Case I-2	140%	-6.35	-0.69	-1.82	-2.75	-3.78	-3.56	-3.55	-6.39	0.85	-4.03	-3.17
L Case I-3	160%	-8.63	-0.97	-2.36	-3.69	-4.90	-4.82	-4.75	-8.56	0.45	-6.41	-4.89
L Case I-4	180%	-10.39	-1.20	-2.76	-4.45	-5.74	-5.84	-5.70	-10.28	-0.08	-8.57	-6.45
L Case I-5	200%	-11.76	-1.39	-3.08	-5.06	-6.40	-6.68	-6.47	-11.67	-0.65	-10.46	-7.81

The lumped mass model provides an approximate solution for wave propagation induced by the assumed input signal in the CO_2-EOR project and also demonstrated that the change in condition due to carbon injection can be detected using surface wave monitoring technique.

5.5.2 Influence of Oil Producer Stiffness Reduction

As CO_2 injected into oil bearing layer, oil may migrate, it means the stress of the oil bearing layer may decrease slightly, and resulting in decreased stiffness. To simulate the effect, stiffness has been decreased by 50% of its original stiffness. The corresponding simulations are described as L Case 50. We also present the result of stiffness increase by 50% and denote as L Case 150. The first case is used to simulate the oil migration in the oil bearing layer, the stress and stiffness of the oil bearing layer is decrease; the second case is used to simulate where no oil migration in the oil bearing layer and the stress and stiffness of the oil bearing layer are increased.

Time histories of displacement, velocity and acceleration at Node 1 are shown in FIGURE 5.24, FIGURE 5.26 and FIGURE 5.28, respectively. The corresponding frequency domains are shown in FIGURE 5.25, FIGURE 5.27 and FIGURE 5.29, respectively, which show the differences of spectral amplitudes at higher frequencies are

more obvious for velocity and acceleration plots than the displacement plot. This observation is significant because it implies the sensor type selection is important, at least in theory.

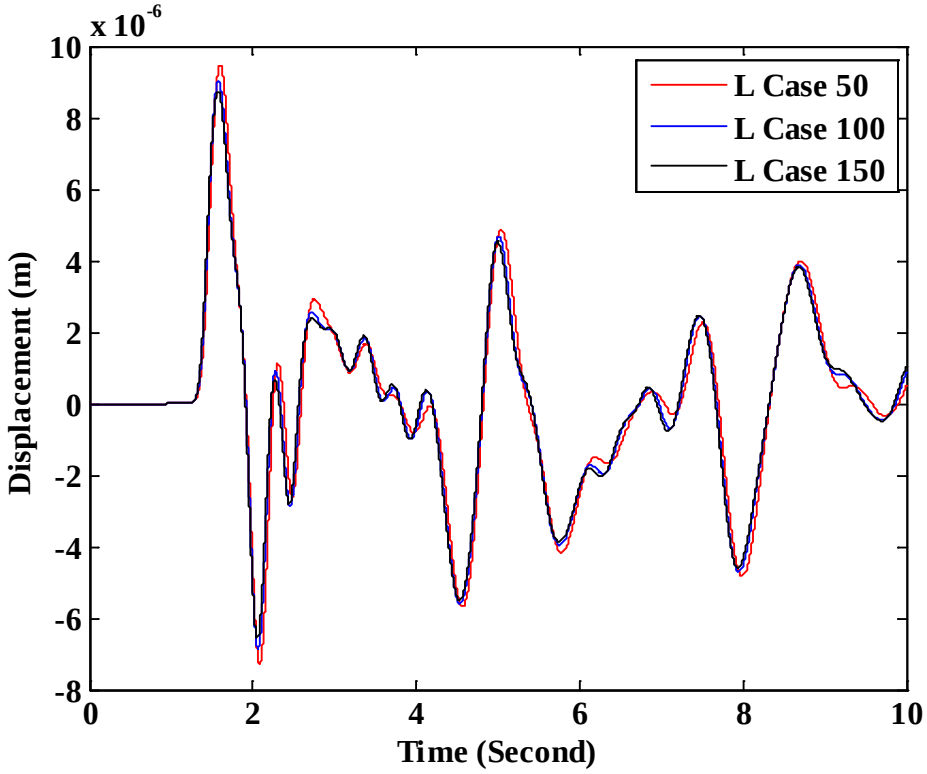

FIGURE 5.24: Displacement time histories of Node 1 of L Cases 50 to 150

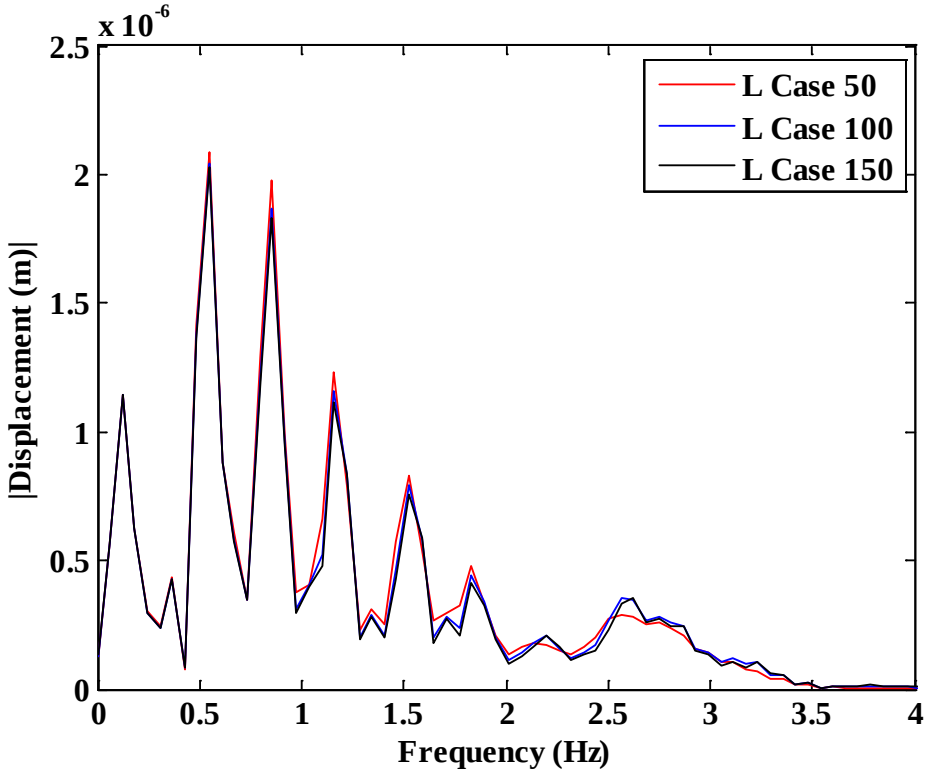

FIGURE 5.25: Frequency domain of Node 1 displacement (corresponding to FIGURE 5.24)

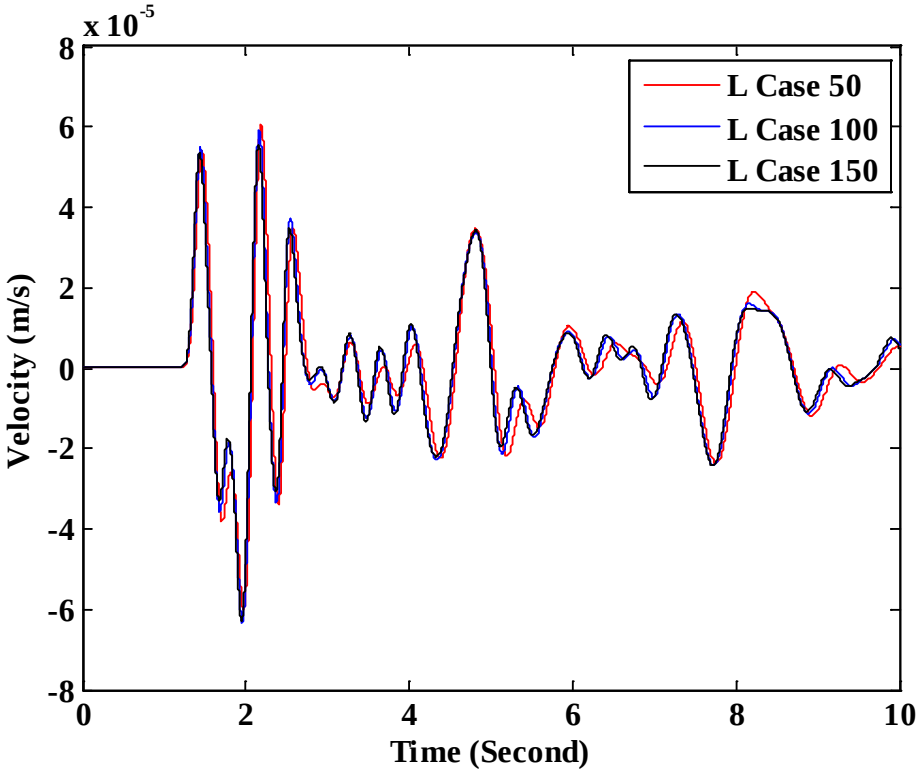

FIGURE 5.26: Velocity time histories of Node 1 of L Cases 50 to 150

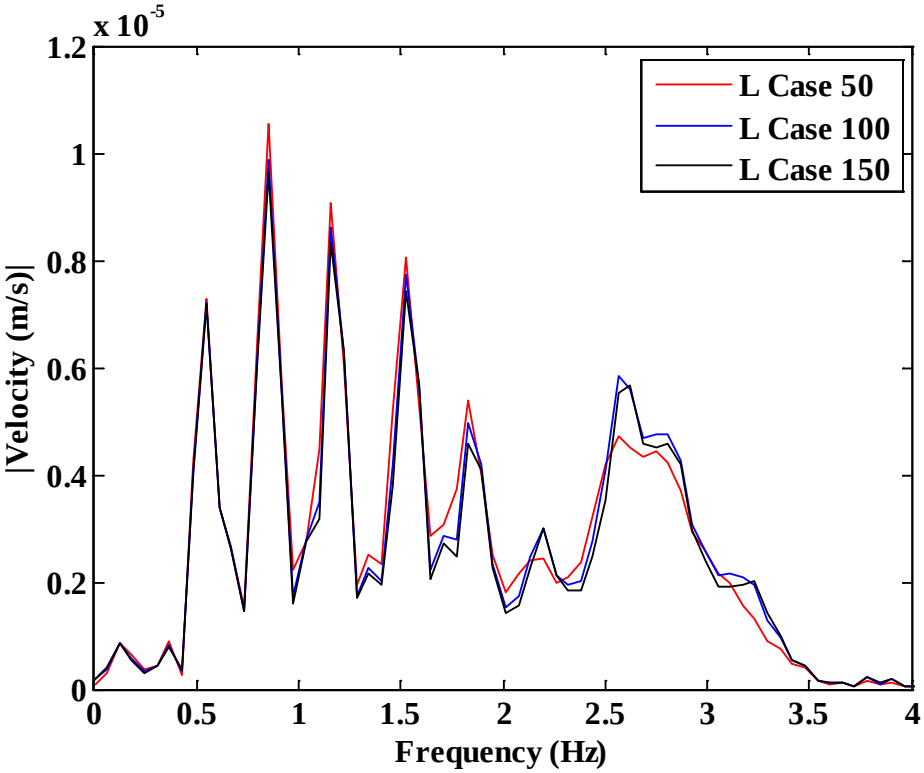

FIGURE 5.27: Frequency domain of Node 1 velocity (corresponding to FIGURE 5.26)

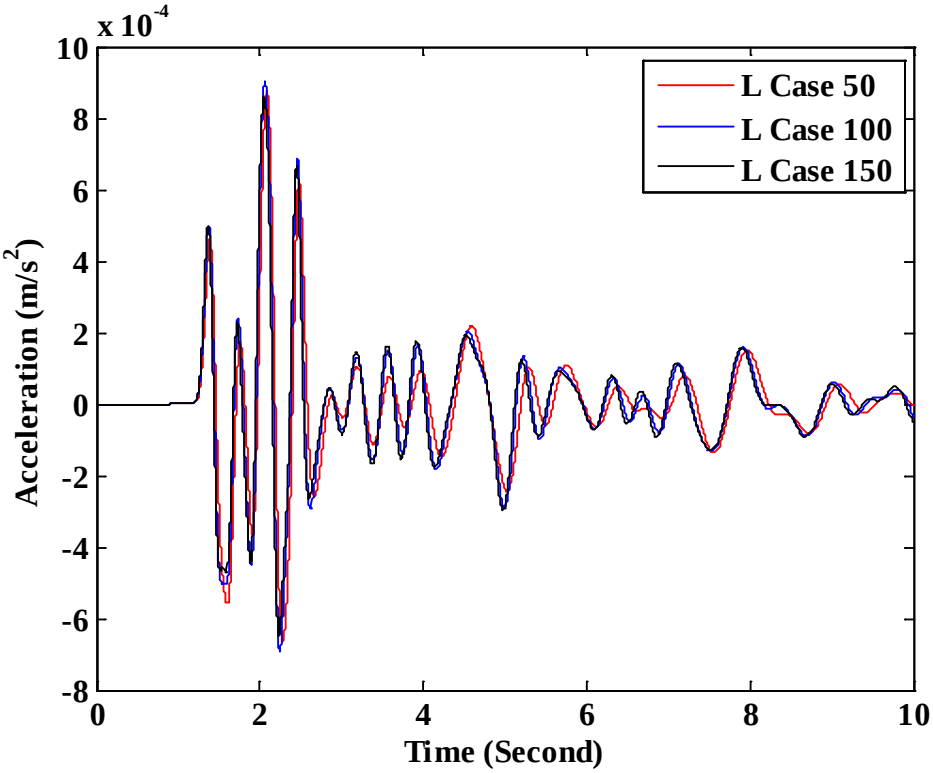

FIGURE 5.28: Acceleration time histories of Node 1 of L Cases 50 to 150

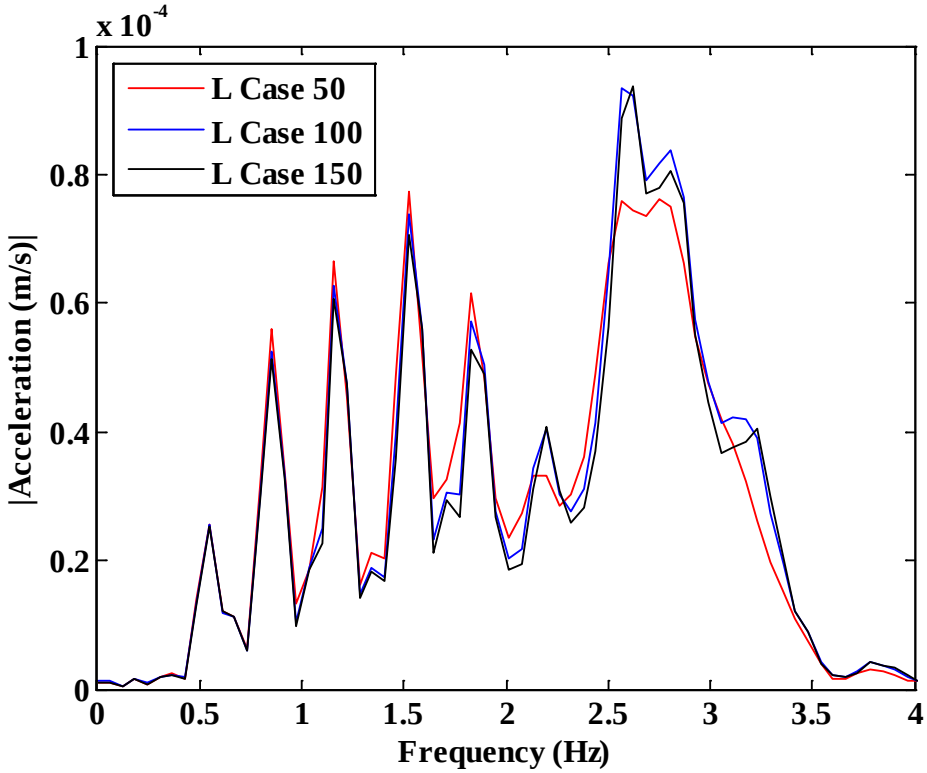

FIGURE 5.29: Frequency domain of Node 1 acceleration (corresponding to FIGURE 5.28)

5.6. Influence of the Saline and Calcite Layers

An important observation made at the Citronelle field study is the significant effect of CO_2 injection to the stress changes in the above oil producing strata. In order to study the influence of stiffness changes of the Saline and Calcite layers, stiffness of Nodes 301 to 530 have been increased from 100%, 120%, 140%, 160%, 180% and 200% of its original stiffness. The corresponding simulations are defined as L Cases II-0, II-1, II-2, II-3, II-4 and II-5, respectively.

The displacement, velocity and acceleration time histories of Node 1 are plotted in FIGURE 5.30, FIGURE 5.32 and FIGURE 5.34, respectively, which show as the stiffness of the Saline and Calcite layers increased, there is a general time shift to the

overall waveform. This is interpreted as the stiffness changes in the Saline and Calcite layers resulted in overall attenuation. The corresponding frequency domains are shown in FIGURE 5.31, FIGURE 5.33 and FIGURE 5.35, respectively, which show that the frequency modes of each case are different with one another, it is especially true when the frequency modes greater than 1 Hz. Due to the frequency modes are not consistent for different cases, SAPD for Node 1 displacement, velocity and acceleration signals were not computed.

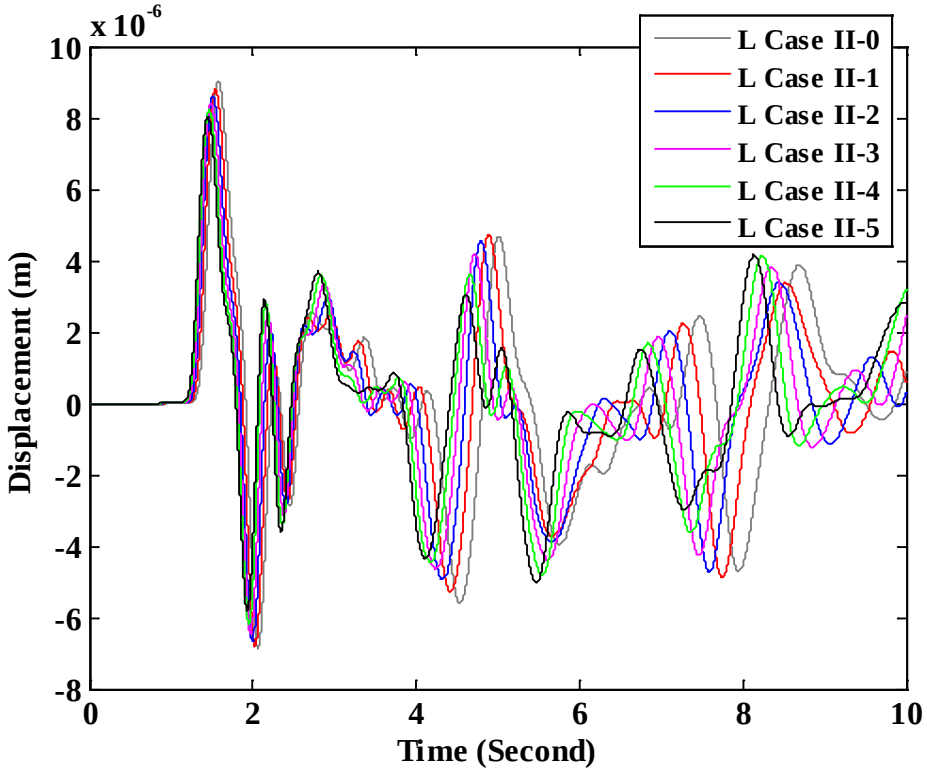

FIGURE 5.30: Displacement time histories of Node 1 of L Cases II-0 to II-5

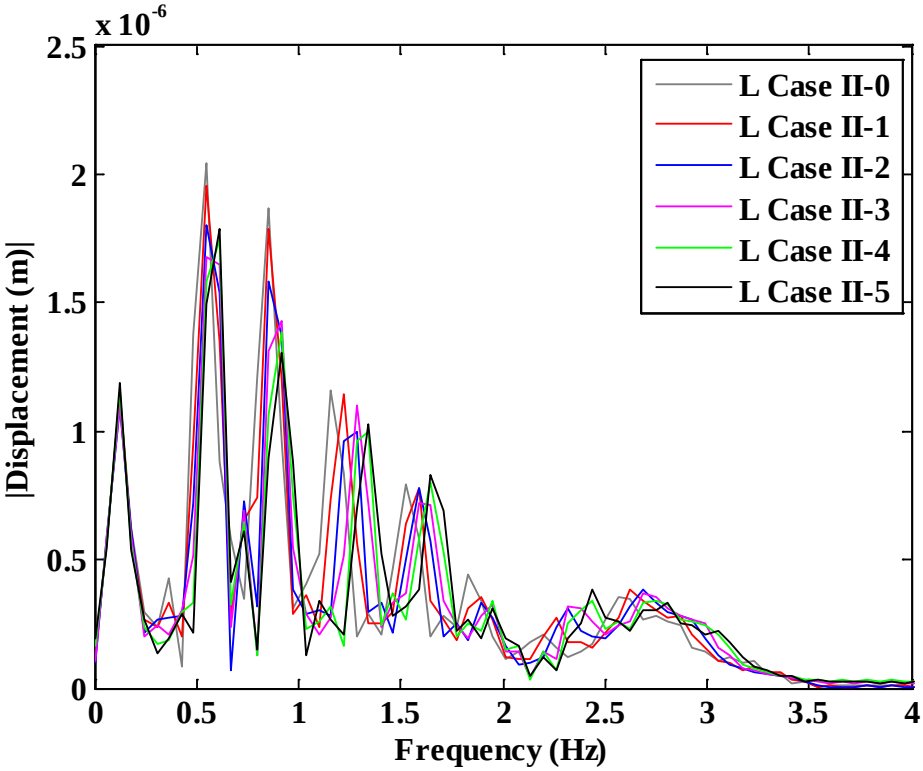

FIGURE 5.31: Frequency domain of Node 1 displacement (corresponding to FIGURE 5.30)

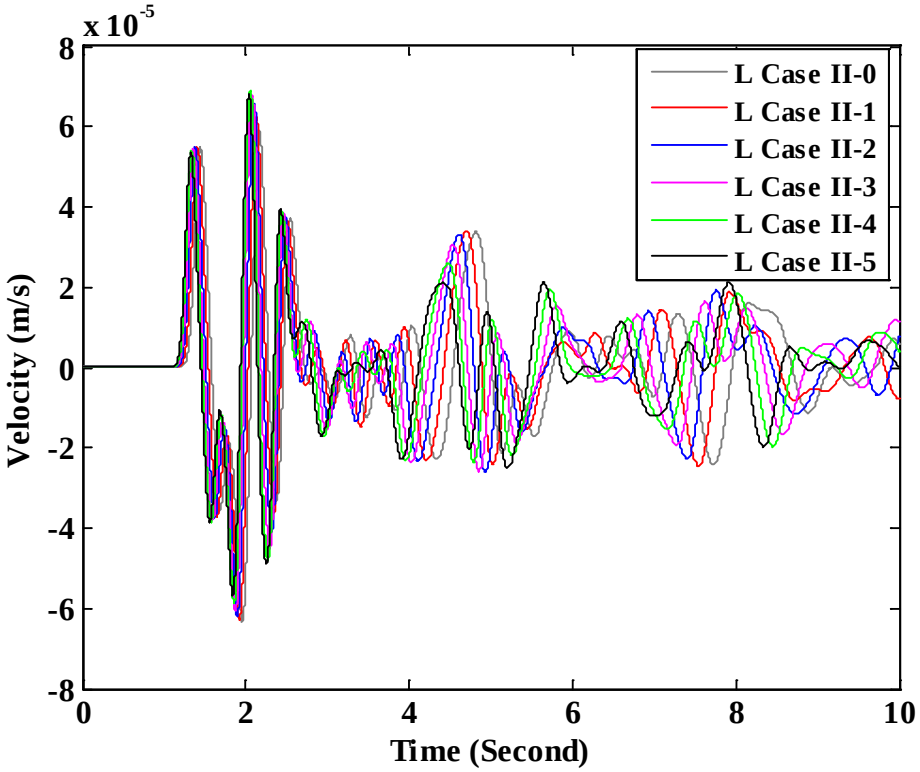

FIGURE 5.32: Velocity time histories of Node 1 of L Cases II-0 to II-5

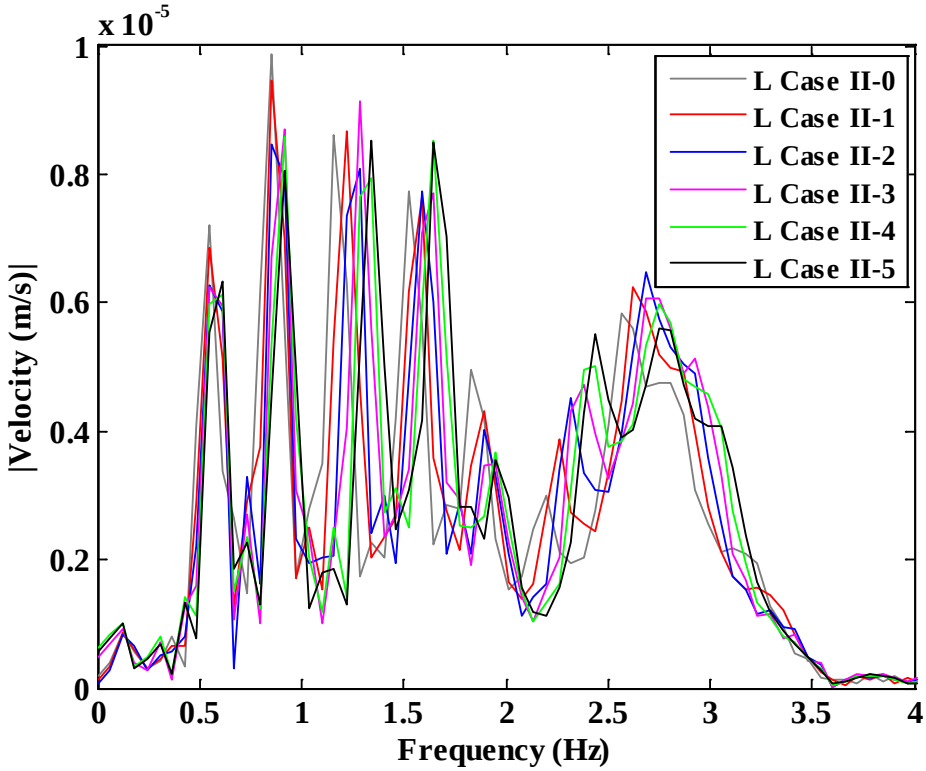

FIGURE 5.33: Frequency domain of Node 1 velocity (corresponding to FIGURE 5.32)

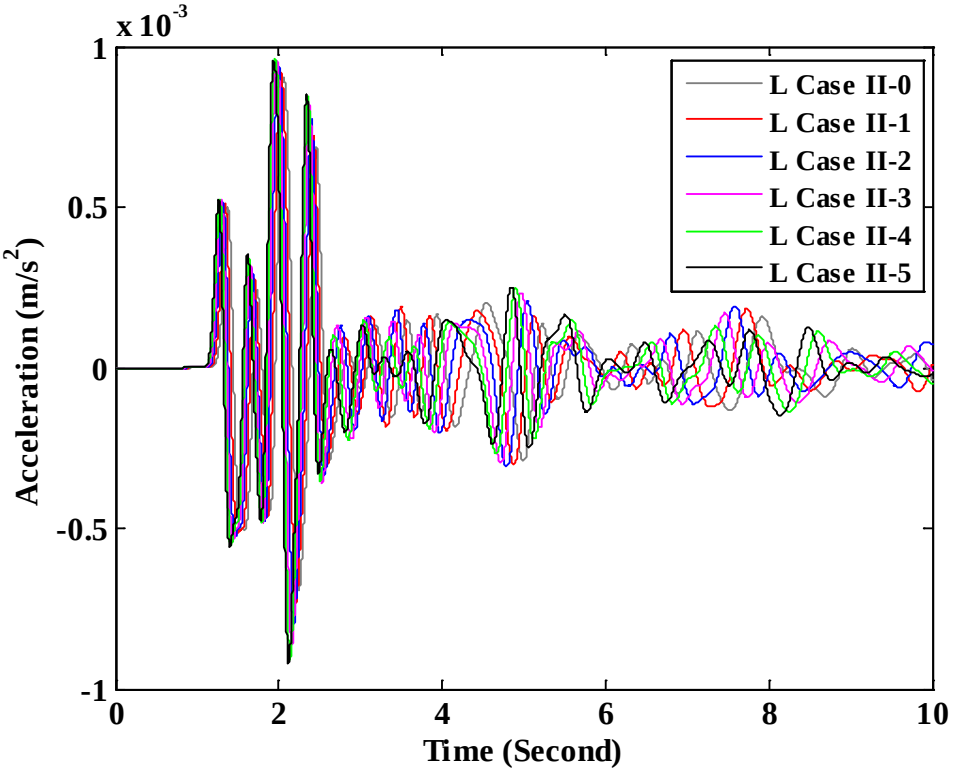

FIGURE 5.34: Acceleration time histories of Node 1 of L Cases II-0 to II-5

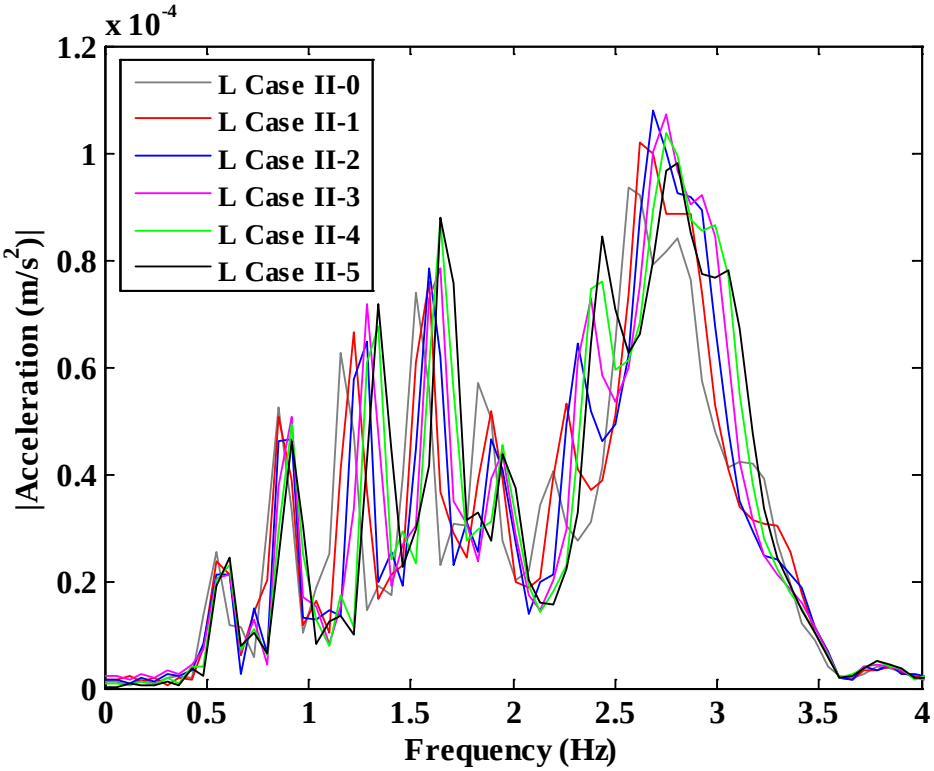

FIGURE 5.35: Frequency domain of Node 1 acceleration (corresponding to FIGURE 5.34)

5.7. Results of Tripartite Spectral Plots

The response spectrum method is commonly used for specifying the earthquake loading in earthquake engineering (Gupta 1992). Response spectra give the maximum response values of a SDOF system based on a given vibration accelerogram; it also indicates the frequency distribution of the vibration energy of a given vibration signal. The response of the SDOF system is typically amplified when the vibration energy is close to its natural frequency. The response spectrum represents the response of an actual dynamic motion of a structure or machine; it shows the correlation between displacement, velocity and acceleration spectral data.

The tripartite spectrum is proposed as a means to compare simultaneously the spectral acceleration/velocity/displacement. The vertices of each case shown in FIGURE

5.21 and FIGURE 5.33 are connected to obtain tripartite response spectrum for the data of Nodes 1 for L Cases I-0 to I-5 and L Cases II-0 to II-5, as shown in FIGURE 5.36 and FIGURE 5.37, respectively. These figures show interesting deviation of different frequency components as wave propagates to the ground surface. The response spectrums of Node 1 of L Cases I-0 to I-5 almost coincide with each other, except the differences at vertices of each plot. FIGURE 5.36 also shows the differences of the cases increased as the frequency modes increased (greater than 5 Hz). The response spectrums in FIGURE 5.37 have obvious differences due to stress changes in Saline and Calcite layers.

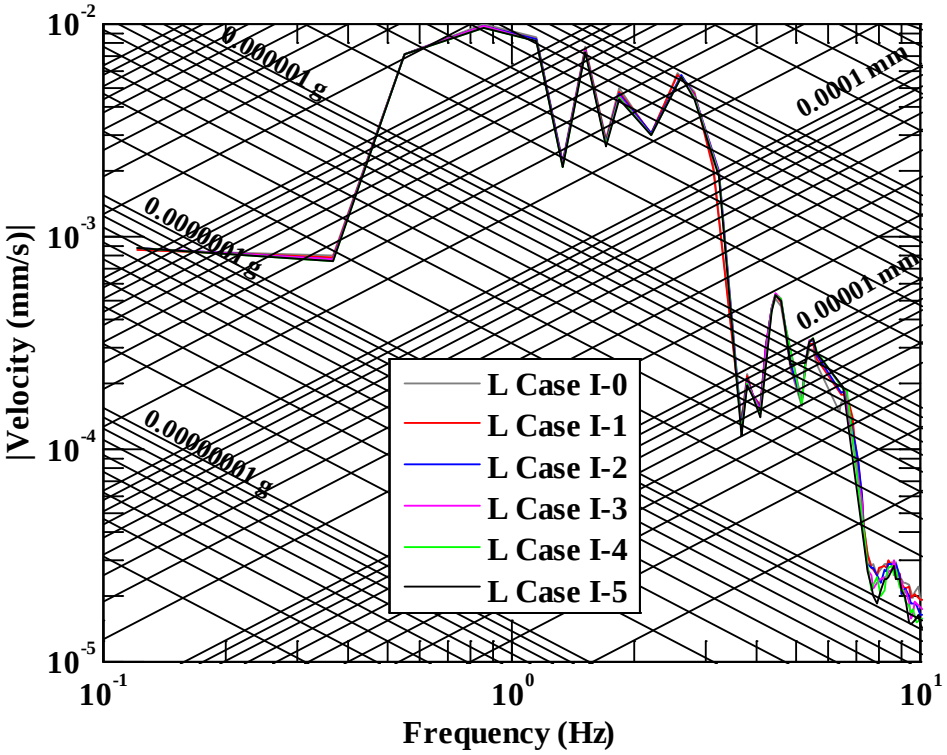

FIGURE 5.36: Response spectrum of velocity at Node 1 of L Case I-0 to I-5

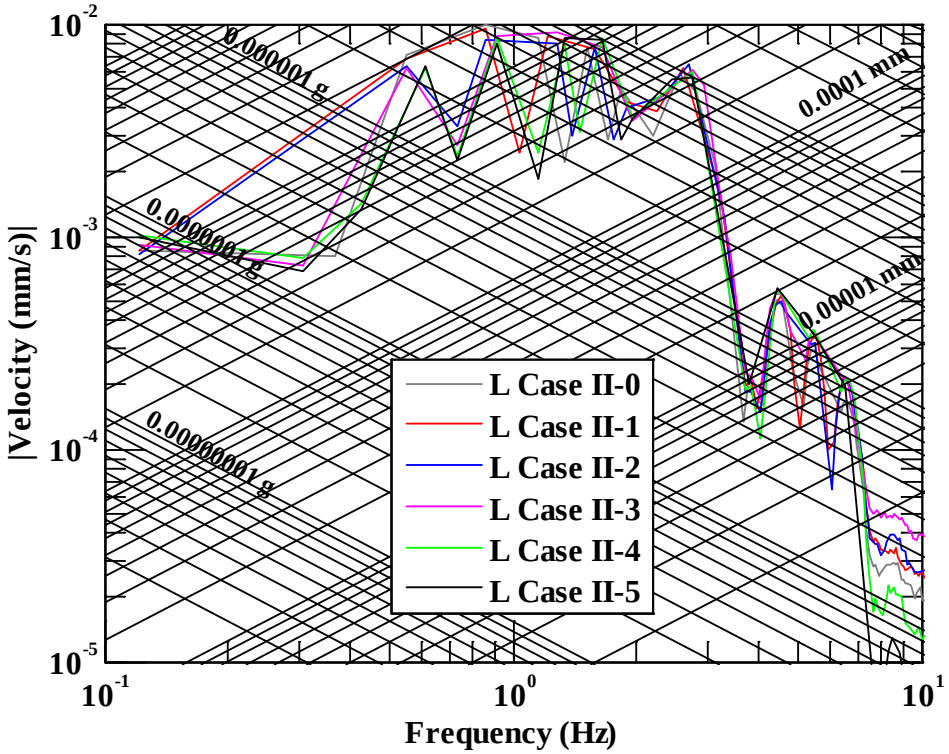

FIGURE 5.37: Response spectrum of velocity at Node 1 of L Case II-0 to II-5

CHAPTER 6: SIMULATION RESULTS IN NONLINEAR CONDITION

As the injection pressure at oil bearing layer increases, at some point, the rock may fracture and result in significant change in stiffness. However, effect of rock fracture on pressurized porous material is uncertain; hence, this study is largely based on the following assumption: In the nonlinear model, the effective stiffness ($K_{effective}$) value is composed of stiffness caused by pore pressure (K_{fluid}) and stiffness of rock properties (K_{matrix}). The effective stiffness is given by Equation (26). K_{fluid} is controlled by velocity of node in the nonlinear model, while K_{matrix} is controlled by displacement of node. Hence, the nonlinear condition is defined as:

For Nodes 531 to 534, $K_{effective} = K_{matrix} = K$ and $K_{fluid} = 0$;

If $u(531{:}534) > 0.0006\,ft$, $K_{effective} = (1+k)K$, while $K_{matrix} = K$ and $K_{fluid} = kK$;

where $u(531{:}534)$ is the displacement of Nodes 531 to 534, $k = 0.2, 0.4, 0.6, 0.8\ or\ 1.0$.

The control displacement is 0.0006 ft (0.00018 m), because it is close to the limitation of rock fracture. Two cases will be studied in nonlinear condition: one case is the positive displacement of the oil bearing layer controlled by its stiffness change; another case is absolute displacement values controlled by its stiffness change.

6.1. Positive Displacement Control Influence of Oil Bearing Layer's Stiffness

The displacement time history of selected nodes in baseline MDOF model is shown in FIGURE 6.1, which shows that the maximum of displacement of the selected nodes in 10 seconds is about 0.0009 ft (0.00027 m).

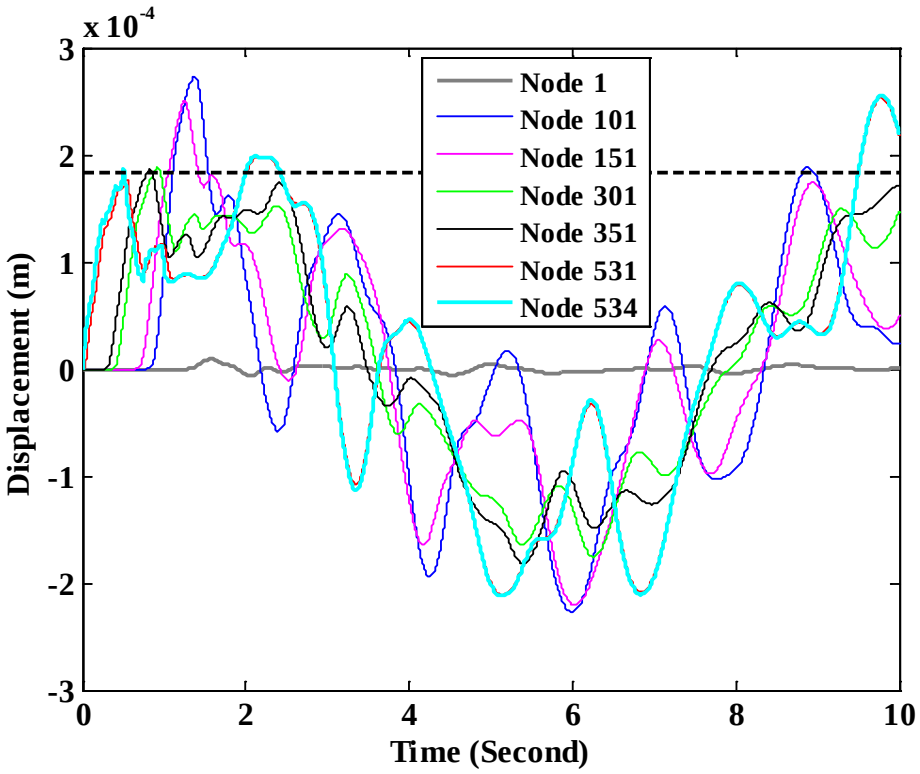

FIGURE 6.1: Displacement time histories of selected nodes of baseline model

In the nonlinear model, the displacement value of Nodes 531 to 534 was considered to control the stiffness value of the layer. Assume the effective stiffness value of layers 531 to 534 in the baseline MDOF model is K, the effective stiffness value is changed by 20%, 40%, 60%, 80% and 100% of its original stiffness, respectively, when nonlinear condition is met. Those cases are named as NL Case I-0 to I-5, respectively, as shown in TABLE 6.1.

TABLE 6.1: Parameters of effective stiffness in nonlinear model

Nodes	NL Case I-0	NL Case I-1	NL Case I-2	NL Case I-3	NL Case I-4	NL Case I-5
531:534	K	$1.2K$	$1.4K$	$1.6K$	$1.8K$	$2.0K$

The displacement, velocity, and acceleration time histories of Node 1 of NL Case I-0 to I-5 are shown in FIGURE 6.2, FIGURE 6.4 and FIGURE 6.6, respectively. The corresponding frequency spectra for the displacement, velocity, and acceleration time histories are shown in FIGURE 6.3, FIGURE 6.5 and FIGURE 6.7, respectively. These figures show that it is easy to distinguish the plot of NL Case I-0 from other cases in both time domain and frequency domain. However, it is difficult to distinguish NL Cases I-1 to I-5 from one another. The simulation results in frequency domain show that there are several frequencies are sensitive to nonlinear condition.

SAPD is another parameter introduced to show the effect of different assumptions of K increase. The percentage differences of displacement, velocity and acceleration of NL Cases I-1 to I-5 to NL Case I-0 are shown in TABLE 6.2, TABLE 6.3 and TABLE 6.4, respectively, which show the changes of percentage difference to NL Case I-0 at eleven frequency modes. TABLE 6.2, TABLE 6.3 and TABLE 6.4 also show that the percentage differences of six frequency modes (1.16 Hz, 1.34 Hz, 1.53 Hz, 1.71 Hz, 1.83 Hz and 2.20 Hz) exceeding 10% indicating that these six frequency modes are more sensitivity than other five frequency modes.

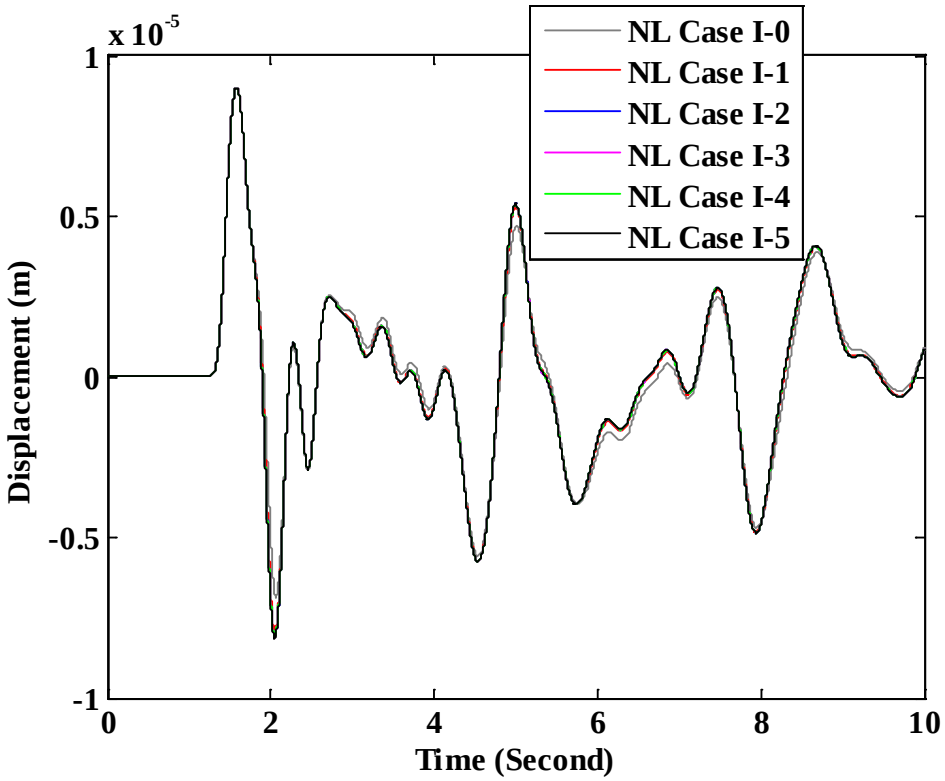

FIGURE 6.2: Displacement time histories of Node 1 of NL Cases I-0 to I-5

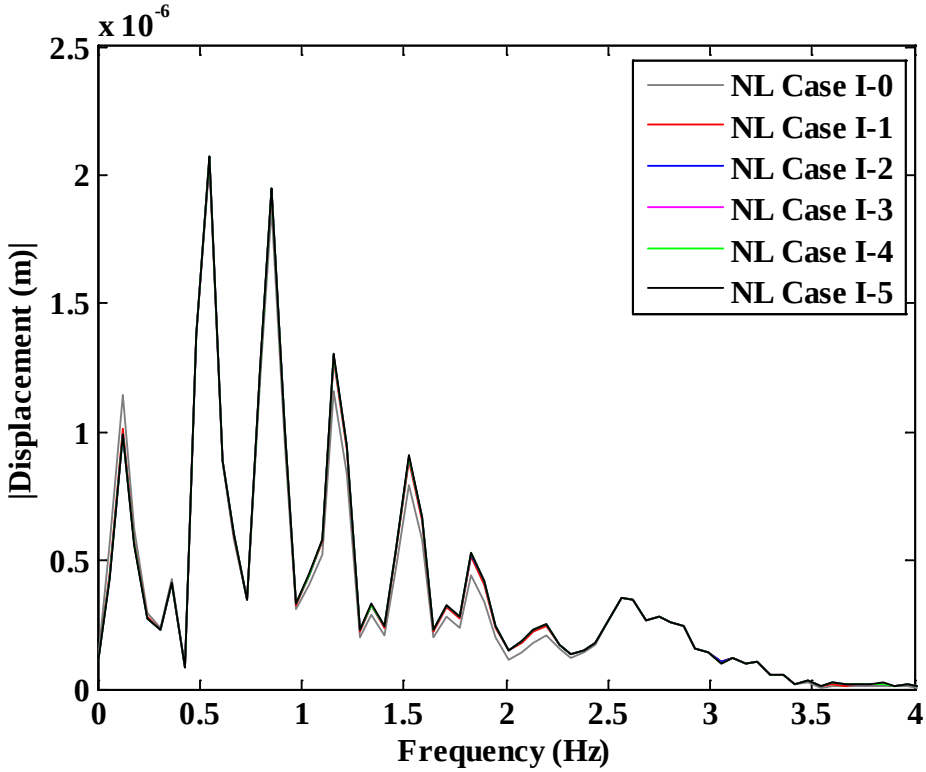

FIGURE 6.3: Frequency domain of Node 1 displacement (corresponding to FIGURE 6.2)

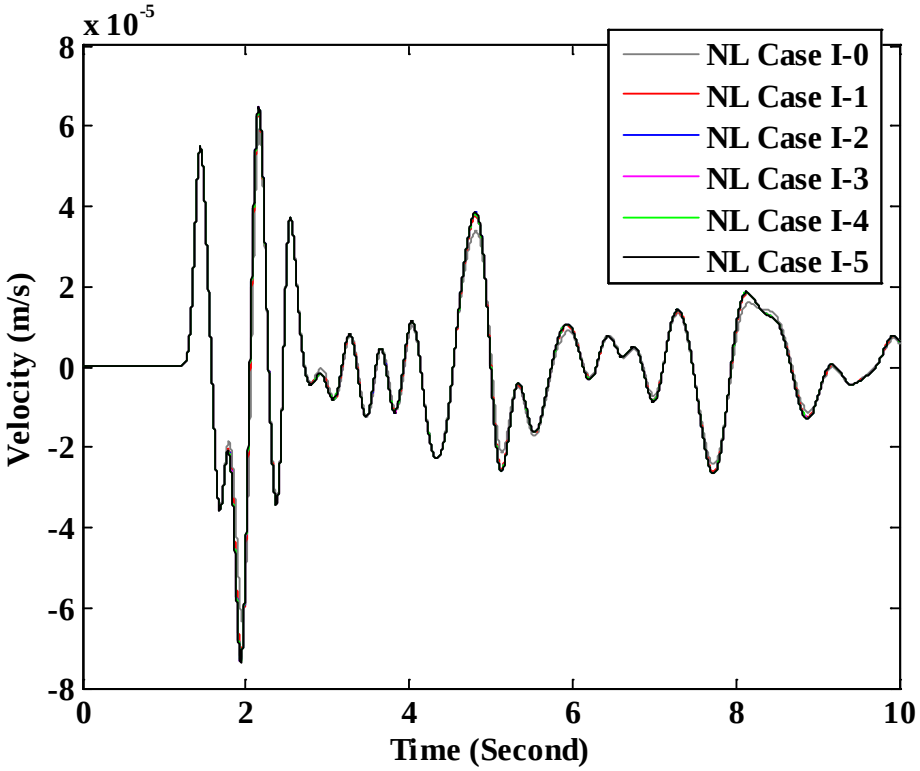

FIGURE 6.4: Velocity time histories of Node 1 of NL Cases I-0 to I-5

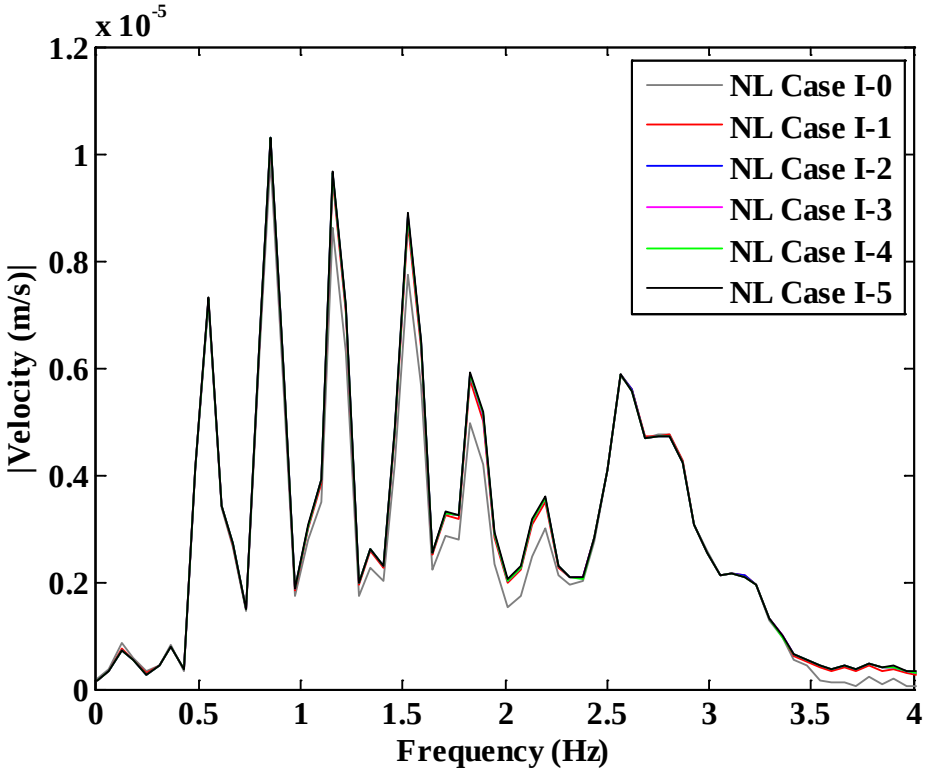

FIGURE 6.5: Frequency domain of Node 1 velocity (corresponding to FIGURE 6.4)

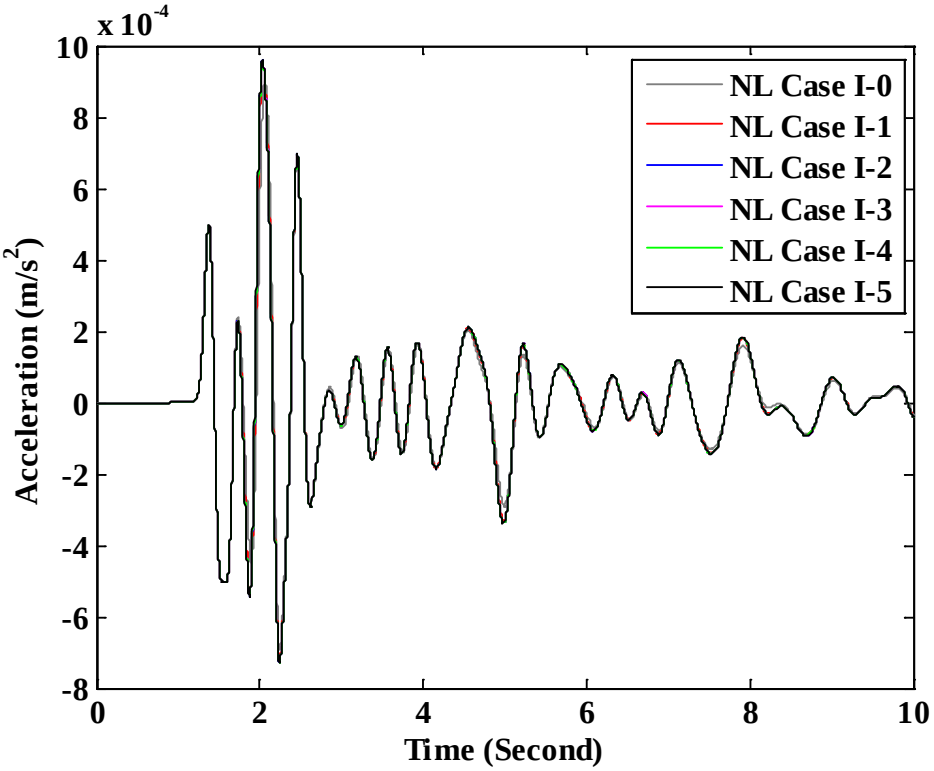

FIGURE 6.6: Acceleration time histories of Node 1 of NL Cases I-0 to I-5

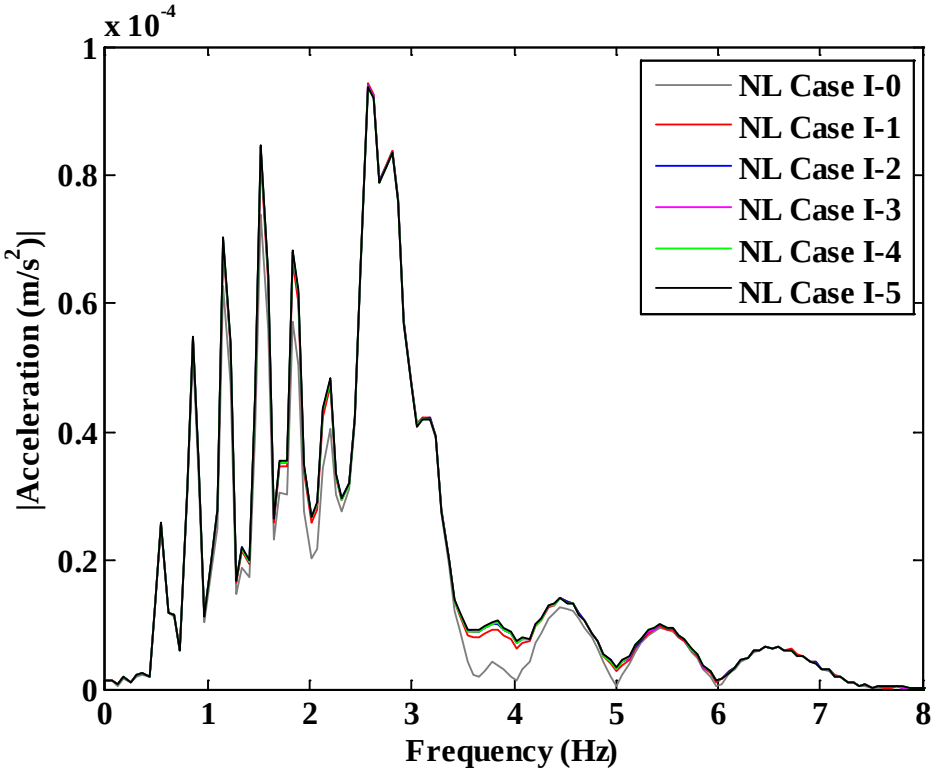

FIGURE 6.7: Frequency domain of Node 1 acceleration (corresponding to FIGURE 6.6)

TABLE 6.2: SAPD for Node 1 displacement signal of NL Cases I-0 to I-5

Case #	Frequency (Hz)										
	0.37	0.55	0.85	1.16	1.34	1.53	1.71	1.83	2.20	2.56	2.81
NL Case I-0	0.00	0.00	0.00	0.00	0.00	0.00	0.00	0.00	0.00	0.00	0.00
NL Case I-1	-2.78	1.09	3.85	10.93	12.19	12.68	12.74	15.81	18.52	1.20	-0.28
NL Case I-2	-3.12	1.26	4.36	12.42	13.89	14.53	14.62	18.14	20.95	1.15	-0.54
NL Case I-3	-3.14	1.23	4.33	12.39	13.87	14.54	14.64	18.17	20.75	1.00	-0.68
NL Case I-4	-3.15	1.22	4.31	12.37	13.86	14.55	14.65	18.18	20.65	0.92	-0.74
NL Case I-5	-3.25	1.29	4.50	12.88	14.43	15.16	15.27	18.95	21.55	0.96	-0.78

TABLE 6.3: SAPD for Node 1 velocity signal of NL Cases I-0 to I-5

Case #	Frequency (Hz)										
	0.37	0.55	0.85	1.16	1.34	1.53	1.71	1.83	2.20	2.56	2.81
NL Case I-0	0.00	0.00	0.00	0.00	0.00	0.00	0.00	0.00	0.00	0.00	0.00
NL Case I-1	-2.16	1.08	3.91	10.62	13.45	12.35	13.79	16.48	16.87	0.88	0.02
NL Case I-2	-2.40	1.24	4.43	12.07	15.32	14.14	15.81	18.91	19.08	0.79	-0.21
NL Case I-3	-2.43	1.22	4.39	12.04	15.29	14.16	15.83	18.94	18.88	0.65	-0.36
NL Case I-4	-2.45	1.21	4.38	12.02	15.28	14.16	15.84	18.95	18.78	0.57	-0.44
NL Case I-5	-2.51	1.27	4.57	12.52	15.91	14.76	16.51	19.76	19.60	0.60	-0.46

TABLE 6.4: SAPD for Node 1 acceleration signal of NL Cases I-0 to I-5

Case #	Frequency (Hz)										
	0.37	0.55	0.85	1.16	1.34	1.53	1.71	1.83	2.20	2.56	2.81
NL Case I-0	0.00	0.00	0.00	0.00	0.00	0.00	0.00	0.00	0.00	0.00	0.00
NL Case I-1	6.37	0.90	4.04	10.52	13.56	12.42	13.58	16.34	16.75	0.70	-0.13
NL Case I-2	7.29	1.03	4.59	11.95	15.45	14.23	15.59	18.75	18.95	0.58	-0.38
NL Case I-3	7.25	1.00	4.55	11.91	15.43	14.24	15.62	18.78	18.74	0.43	-0.54
NL Case I-4	7.22	0.99	4.53	11.90	15.42	14.24	15.63	18.80	18.64	0.36	-0.61
NL Case I-5	7.55	1.05	4.73	12.39	16.06	14.84	16.29	19.59	19.46	0.38	-0.64

6.2. Absolute Displacement Control Influence of Oil Bearing Layer's Stiffness

Section 6.1 discussed the case of rock fracture is influenced by compression only; however, rock fracture can also be influenced by tension. Simulation of displacement responses due to absolute displacement control is shown in FIGURE 6.8.

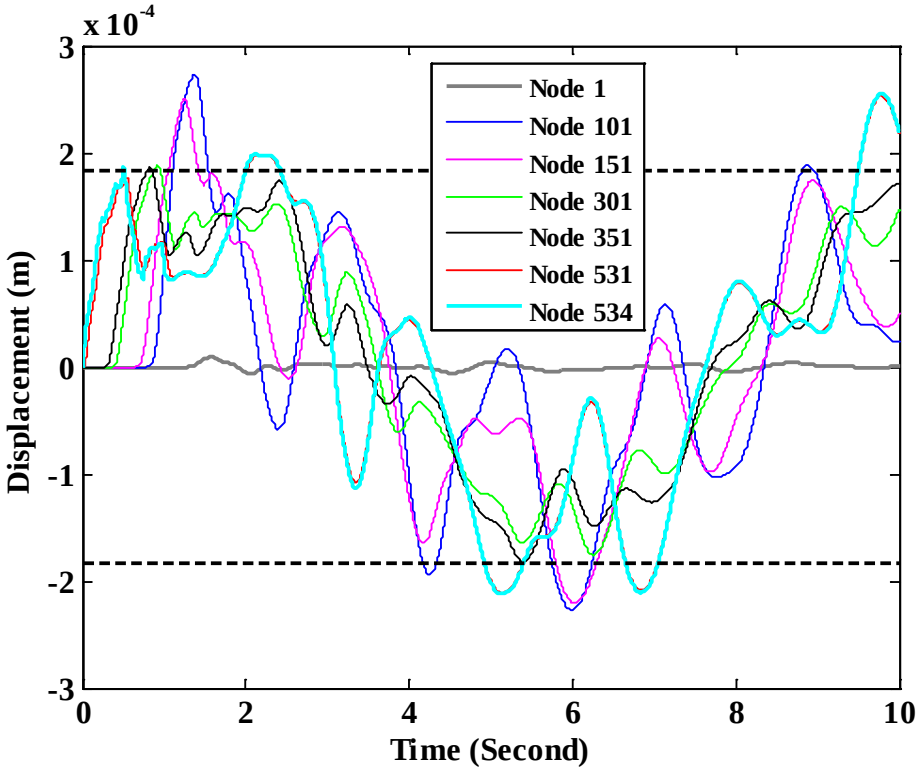

FIGURE 6.8: Displacement time histories of selected nodes of baseline Model

In second consideration of nonlinearity, the absolute amplitudes of displacement value of Nodes ranged from 531 to 534 were considered to control the stiffness value of the layer. Assume the stiffness value of the oil bearing layer in the linear model is changed by 20%, 40%, 60%, 80% and 100% of its original stiffness when the absolute amplitude of displacement value of corresponding oil bearing layer exceeds 0.0006 ft (0.00018 m). Those cases are named as NL Case II-0 to II-5, respectively, as shown in TABLE 6.5.

TABLE 6.5: Parameters of stiffness in nonlinear model

Nodes	NL Case II-0	NL Case II-1	NL Case II-2	NL Case II-3	NL Case II-4	NL Case II-5
531:534	K	$1.2K$	$1.4K$	$1.6K$	$1.8K$	$2.0K$

The displacement, velocity, and acceleration time histories of Node 1 of NL Cases II-0 to II-5 are shown in FIGURE 6.9, FIGURE 6.11 and FIGURE 6.13, respectively. The corresponding frequency domain for the displacement, velocity, and acceleration time histories are shown in FIGURE 6.10, FIGURE 6.12 and FIGURE 6.14, respectively, which show that nonlinear cases can be distinguished. The detailed differences will be discussed in terms of SAPD in the following paragraph.

The SAPD values of displacement, velocity and acceleration of NL Cases II-1 to II-5 to NL Case II-0 are shown in TABLE 6.6, TABLE 6.7 and TABLE 6.8. Notably, different frequencies have different sensitivities to the nonlinear condition. The most sensitive frequencies are different between displacement, velocity and acceleration SAPDs.

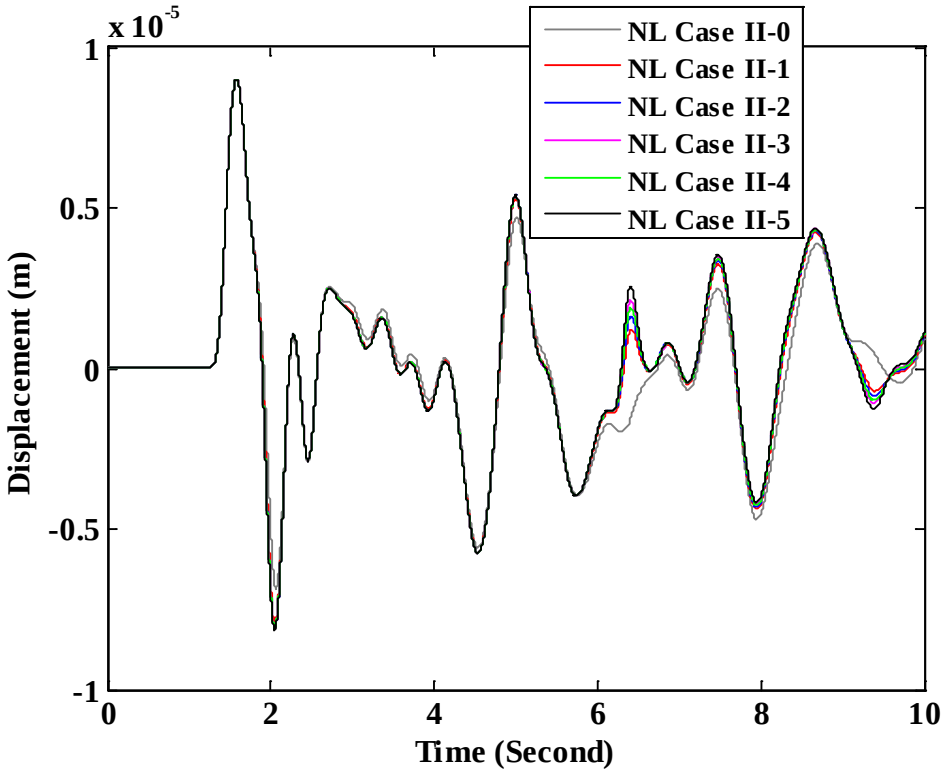

FIGURE 6.9: Displacement time histories of Node 1 of NL Cases II-0 to II-5

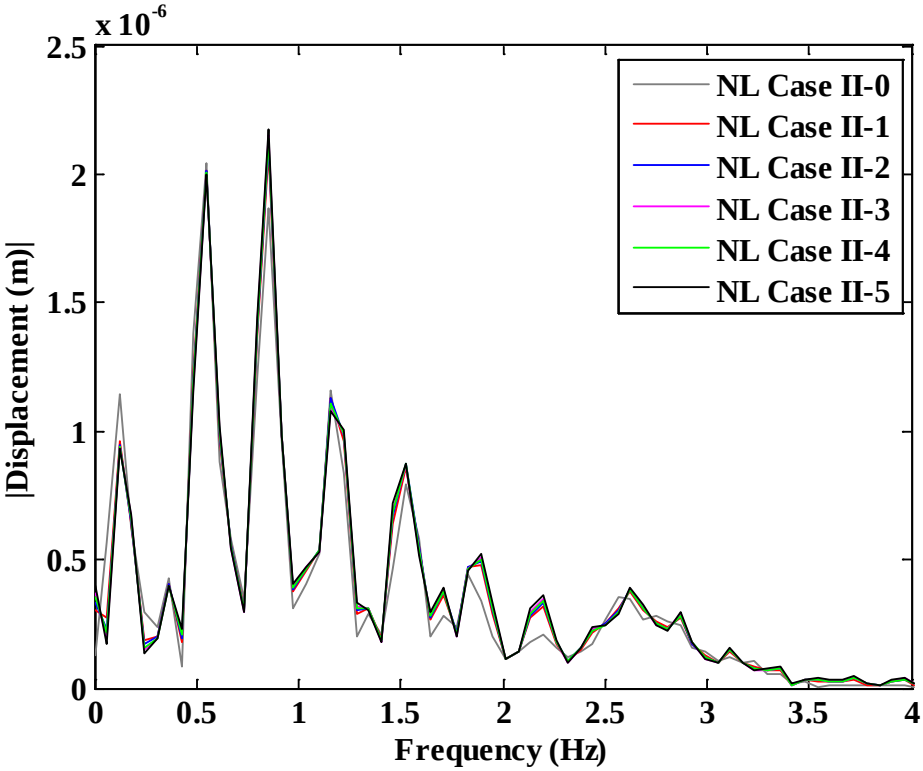

FIGURE 6.10: Frequency domain of Node 1 displacement (corresponding to FIGURE 6.9)

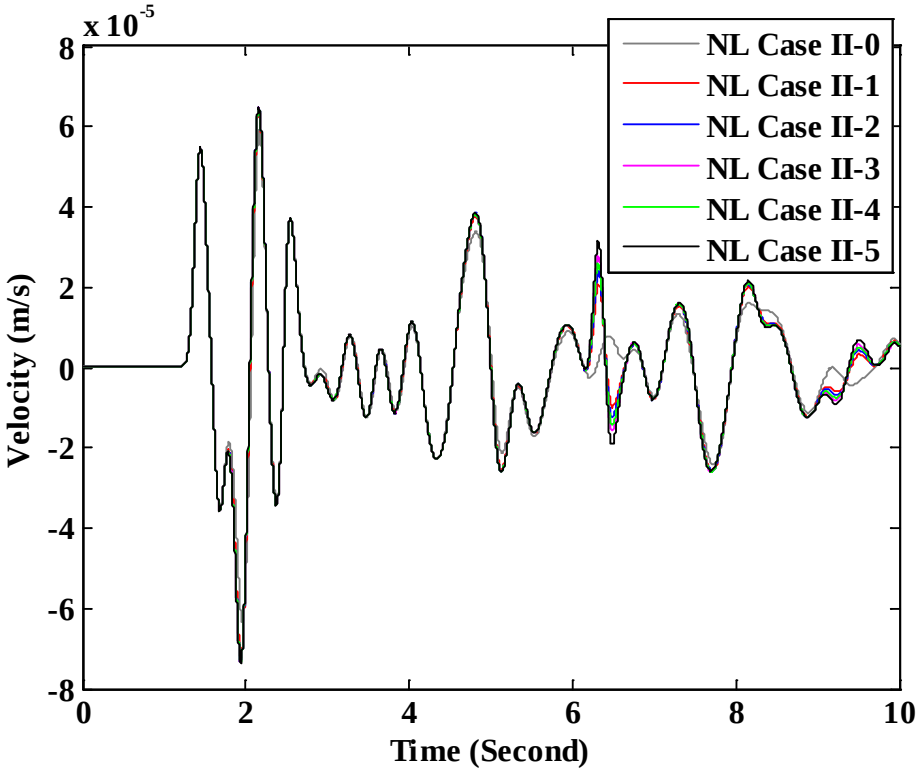

FIGURE 6.11: Velocity time histories of Node 1 of NL Cases II-0 to II-5

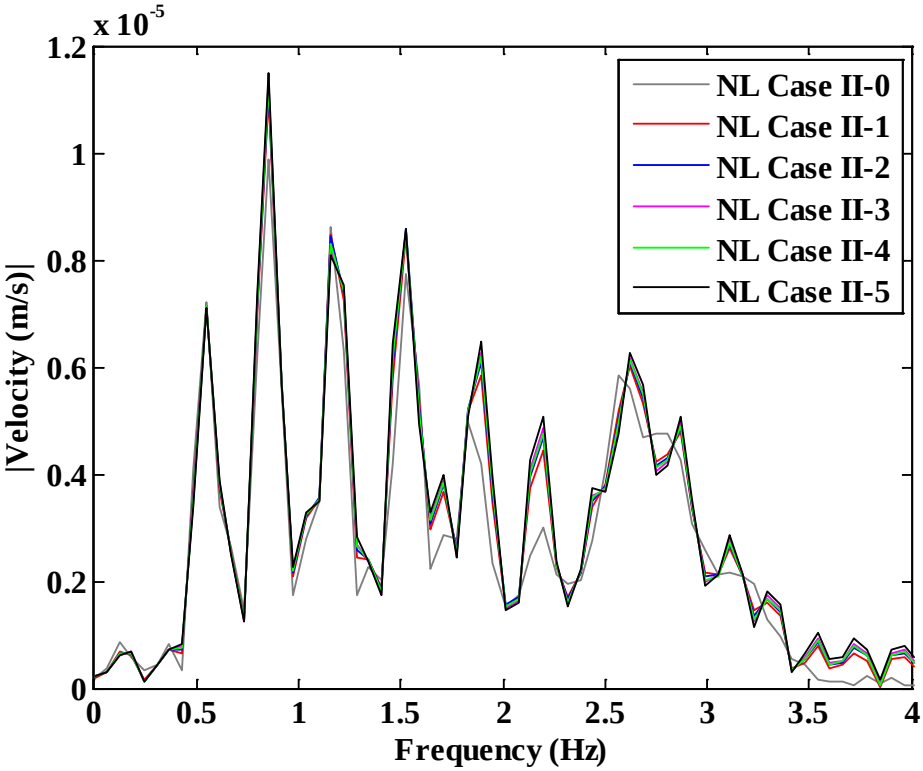

FIGURE 6.12: Frequency domain of Node 1 velocity (corresponding to FIGURE 6.11)

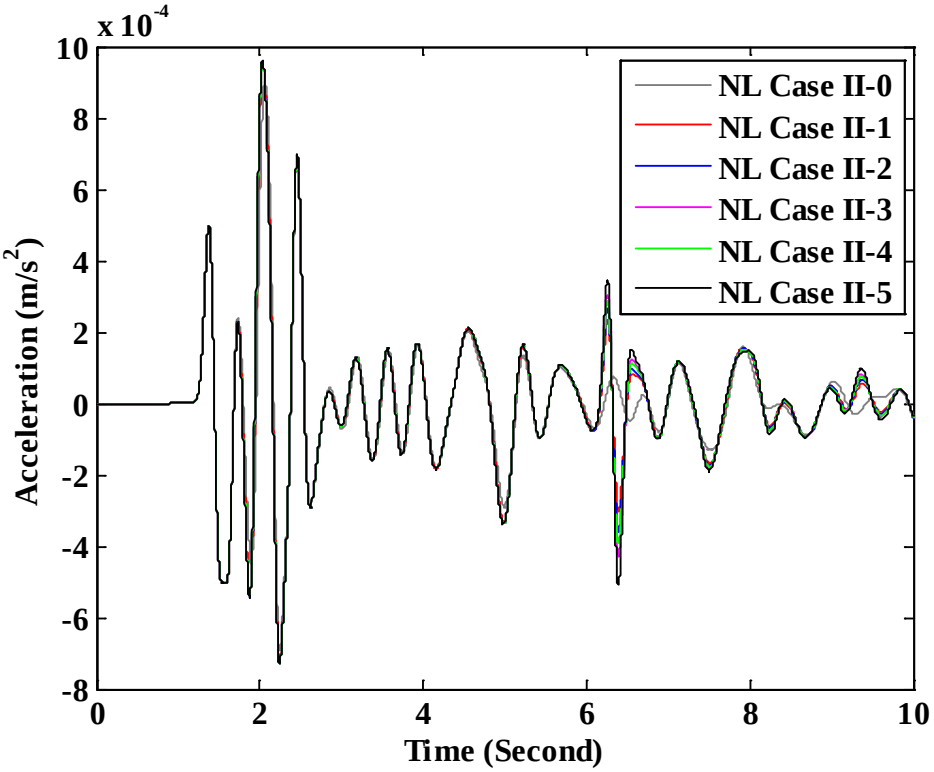

FIGURE 6.13: Acceleration time histories of Node 1 of NL Cases II-0 to II-5

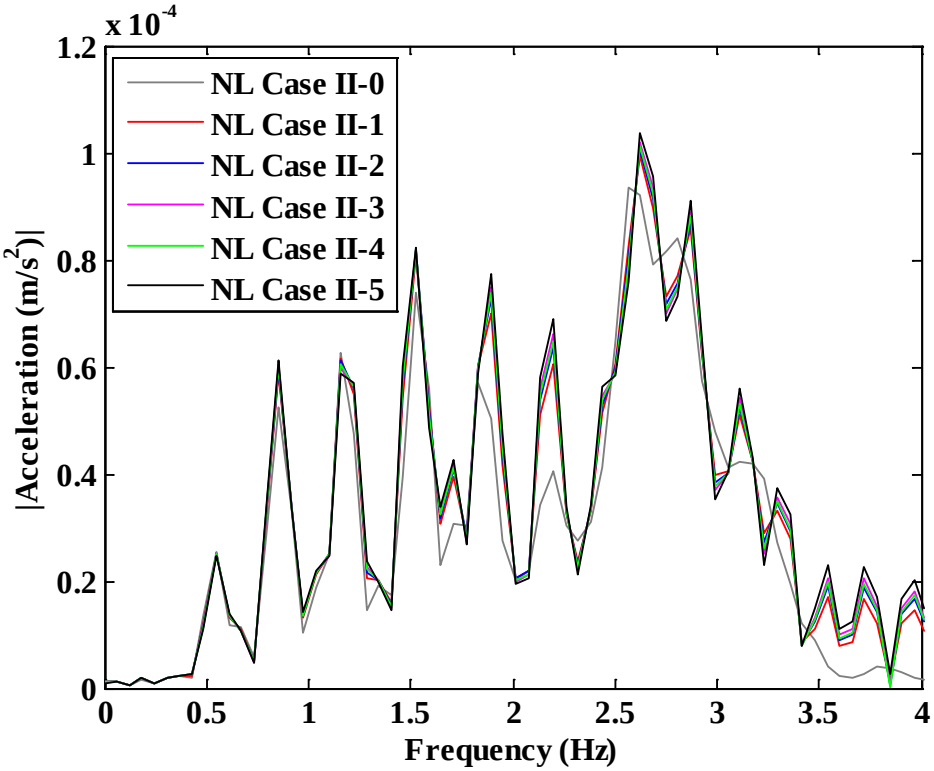

FIGURE 6.14: Frequency domain of Node 1 acceleration (corresponding to FIGURE 6.13)

TABLE 6.6: SAPD for Node 1 displacement signal of NL Cases II-0 to II-5

Case #	Frequency (Hz)										
	0.37	0.55	0.85	1.16	1.34	1.53	1.71	1.83	2.20	2.56	2.81
NL Case II-0	0.00	0.00	0.00	0.00	0.00	0.00	0.00	0.00	0.00	0.00	0.00
NL Case II-1	-5.42	-1.50	11.81	-1.97	6.80	8.74	28.32	5.12	50.58	-11.76	-9.47
NL Case II-2	-6.02	-1.62	13.55	-2.46	7.64	10.46	32.69	5.60	58.17	-13.87	-11.04
NL Case II-3	-6.47	-2.07	15.20	-5.15	6.52	9.96	35.95	4.04	64.49	-16.41	-12.84
NL Case II-4	-6.30	-1.90	14.46	-4.02	6.99	10.18	34.53	4.74	61.41	-15.41	-12.08
NL Case II-5	-6.88	-2.33	16.67	-6.76	6.14	10.58	39.34	3.04	71.53	-18.87	-14.59

TABLE 6.7: SAPD for Node 1 velocity signal of NL Cases II-0 to II-5

Case #	Frequency (Hz)										
	0.37	0.55	0.85	1.16	1.34	1.53	1.71	1.83	2.20	2.56	2.81
NL Case II-0	0.00	0.00	0.00	0.00	0.00	0.00	0.00	0.00	0.00	0.00	0.00
NL Case II-1	-9.19	-0.91	11.71	-1.60	6.02	9.03	29.07	4.85	48.75	-11.41	-7.85
NL Case II-2	-10.18	-0.95	13.42	-2.03	6.73	10.77	33.57	5.28	56.06	-13.48	-9.34
NL Case II-3	-11.46	-1.28	15.04	-4.58	5.17	10.39	36.75	3.58	62.34	-15.91	-10.74
NL Case II-4	-10.95	-1.16	14.31	-3.50	5.83	10.56	35.35	4.34	59.28	-14.94	-10.28
NL Case II-5	-12.30	-1.45	16.50	-6.10	4.55	11.06	40.19	2.51	69.21	-18.32	-12.20

TABLE 6.8: SAPD for Node 1 acceleration signal of NL Cases II-0 to II-5

Case #	Frequency (Hz)										
	0.37	0.55	0.85	1.16	1.34	1.53	1.71	1.83	2.20	2.56	2.81
NL Case II-0	0.00	0.00	0.00	0.00	0.00	0.00	0.00	0.00	0.00	0.00	0.00
NL Case II-1	0.31	-1.64	11.96	-1.77	6.27	9.36	28.74	5.05	49.82	-11.65	-8.17
NL Case II-2	0.47	-1.79	13.71	-2.22	7.01	11.15	33.22	5.51	57.29	-13.75	-9.70
NL Case II-3	-0.83	-2.22	15.36	-4.78	5.48	10.81	36.38	3.87	63.81	-16.19	-11.13
NL Case II-4	-0.34	-2.07	14.61	-3.70	6.13	10.96	35.00	4.61	60.64	-15.22	-10.65
NL Case II-5	-1.22	-2.48	16.84	-6.32	4.88	11.53	39.81	2.85	70.87	-18.63	-12.63

6.3. Results of Tripartite Spectral Plots

The time history of velocity at Nodes 1 of NL Case I-0 to I-5 is shown in FIGURE 6.4. The detail frequency content of obtained signal at Node 1 can be presented by conducting FFT, as shown in FIGURE 6.5. The corresponding tripartite response spectrum of Nodes 1 of NL Case I-0 to I-5 is shown in FIGURE 6.15. The plot of Node 1 of NL Case I-0 can be distinguished from the other four plots. The plots of Node 1 of NL Case I-1 to I-5 are almost coincide with each other, indicates little differences of the obtained signal between the four cases.

The tripartite response spectrum derived from the time history of velocity at Nodes 1 of NL Case II-0 to II-5 is shown in FIGURE 6.16. The plots of Node 1 of NL Case II-0 to II-5 can be distinguished from one another, especially in the vertices of the plots.

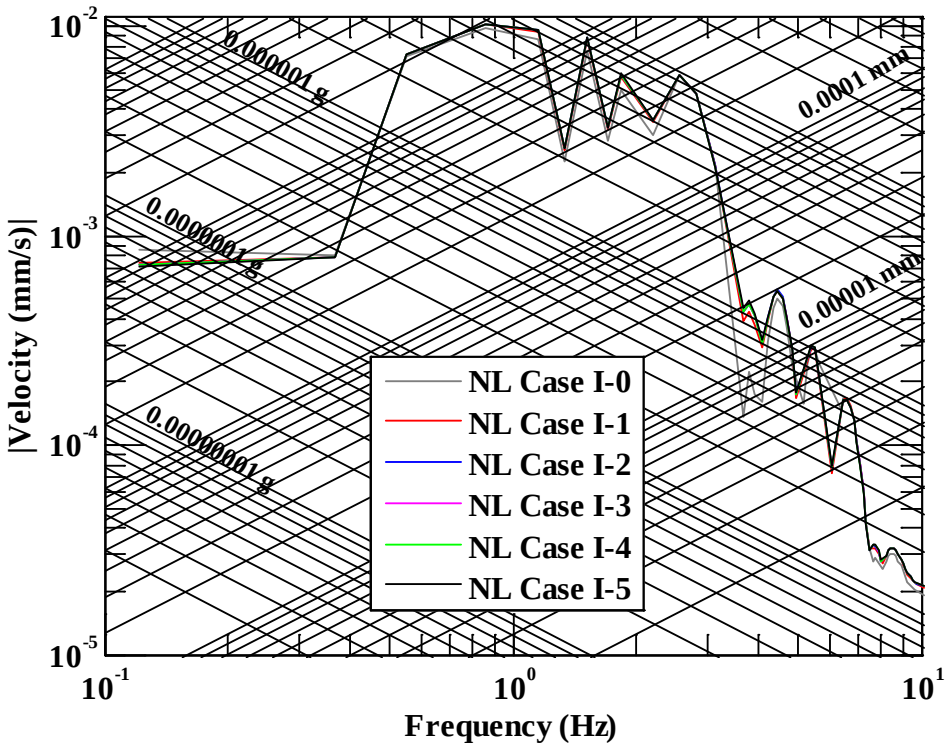

FIGURE 6.15: Response spectrum of velocity at Node 1 of NL Case I-0 to I-5

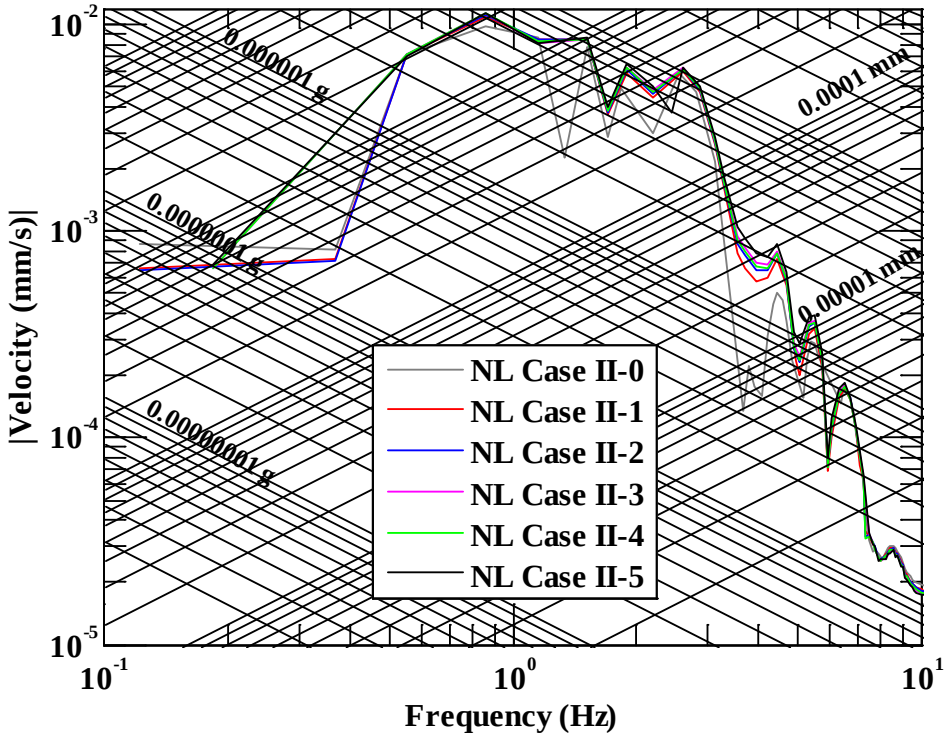

FIGURE 6.16: Response spectrum of velocity at Node 1 of NL Case II-0 to II-5

CHAPTER 7: ANALYSIS AND DISCUSSION

7.1. Introduction

CO_2 is a greenhouse gas, and the relationship between global warming and greenhouse gases has become more and more of concerns to the scientific community (Balat et al. 2003; Halmann and Steinberg 1999; Zhong and Haigh 2013). Carbon capture and geologic storage is a promising method for reducing the concentration of CO_2 in the atmosphere (Bachu 2008; Holloway 2005; Plasynski et al. 2009; Reichle et al. 1999; Webre 2012; White et al. 2003). The process usually involves injecting supercritical CO_2 at high pressure into the storage reservoir, which must meet stringent geological requirements including anticline, porosity, permeability, void volume, pressure limits, neighboring groundwater aquifers, seepage characteristics and cap rock characteristics. Using underground oil reservoirs as CO_2 storage sites may have the additional benefits of EOR, which provides the economic incentives for CO_2 sequestration (Blunt et al. 1993; Esposito et al. 2008; Gaspar Ravagnani et al. 2009; Lake 1989). Currently there are several hundreds of oil field injection sites worldwide and in the US (Hosa et al. 2011; OGJ 2010).

The ability of the passive seismic testing technique to monitor the injection and storage process at Citronelle Oil Field has been demonstrated in detail. 1-D MDOF lumped mass model was used to simulate wave propagation in an assumed layered model.

7.2. Application of Seismic Monitoring for Various Geologic, Mineral Extraction and Environmental Studies

The seismic technique introduced in this study not only can be used to monitor the CO_2 sequestration process in an oil reservoir, but also can be used in many other environmental and engineering investigations, including compressed air energy storage (CAES), earthquake potential, ground water breakthrough in land void, underground gas leak, land void subsidence (i.e. sinkhole), tidal wave effect on coastal ground water fluctuation, foundation problems and underground waste storage. Stress wave detected by seismic technique can be generated actively by using an impact source (i.e. sledgehammer) or passively by natural (i.e. winds and tidal motion) and anthropogenic (i.e. traffic) activities.

The basic principle of the geophysical techniques is to find the response signature differences from the site geological or geotechnical properties of the subsurface. Therefore, an accurate subsurface model is very important to study any related problems.

7.3. Model Validation against Field Results

To study the wave propagation in the MDOF model and compare the simulation results with geophysical tests, several rock layers are considered. The depth of each layer is considered from the top of the layer. P-wave speed of the selected layers can be determined by calculating the distance between two adjacent layers and the travel time of the wave. The wave velocity V_p is determined by $V_p = L/t$, where L is the distance between adjacent layers and t is the travel time of the wave from one layer to another layer. Then, the shear wave velocity can be determined by assuming $V_s = V_p/1.73$. The

relationship between V_s and V_p may vary slightly when waves across different materials, however, the coefficient is simplified to 1.73 in this study.

In the 534 layer MDOF model, the vertical distance between two adjacent layers is determined. The key is to determine the arrival time for the selected layers. There are several methods for determining wave arrival time, such as first arrival time and first peak to peak time. First arrival time (t_0) of the wave is defined as the first major deflection of the received signal. There are different viewpoints regarding how to determine the first arrival point: some researchers determined first arrival time by first deflection point of output signal, while others determined first arrival using first reversal point of the output signal.

In this study, first arrival time is determined by point A, as shown in FIGURE 7.1. The corresponding shear wave velocity can be computed using the first arrival time. The data of displacement, velocity and acceleration time history obtained from the numerical simulation will be used to determine wave's travel time of the adjacent layers.

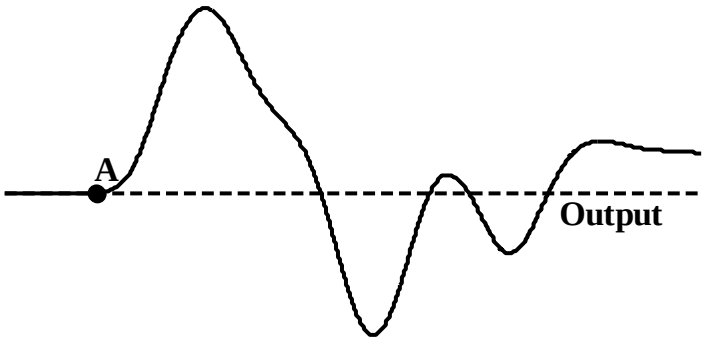

FIGURE 7.1: First arrival time method

The plots of computed shear wave velocity from the baseline MDOF model and average shear wave velocity from geophysical tests are plotted together in FIGURE 7.2. The curve represents closeness of fit between the simulation results and the experimental

data. Shear wave velocity computed from the data of displacement time history ranged from 1,671.4 to 10,343.8 ft/s (509.4 to 3,152.8 m/s) and increased with depth. Shear wave velocity computed from the data of velocity time history ranged from 1,981.8 to 13,648.0 ft/s (604.1 to 4,159.9 m/s) and increased with depth. Shear wave velocity computed from the data of acceleration time history ranged from 2,134.3 to 17,239.6 ft/s (650.5 to 5,254.6 m/s) and increased with depth. The simulation results also show that wave speed obtained from acceleration data is highest among the three data group, the second highest wave speed is obtained from velocity data and the lowest speed obtained from displacement data. The velocity difference obtained from the three different data group increased with depth.

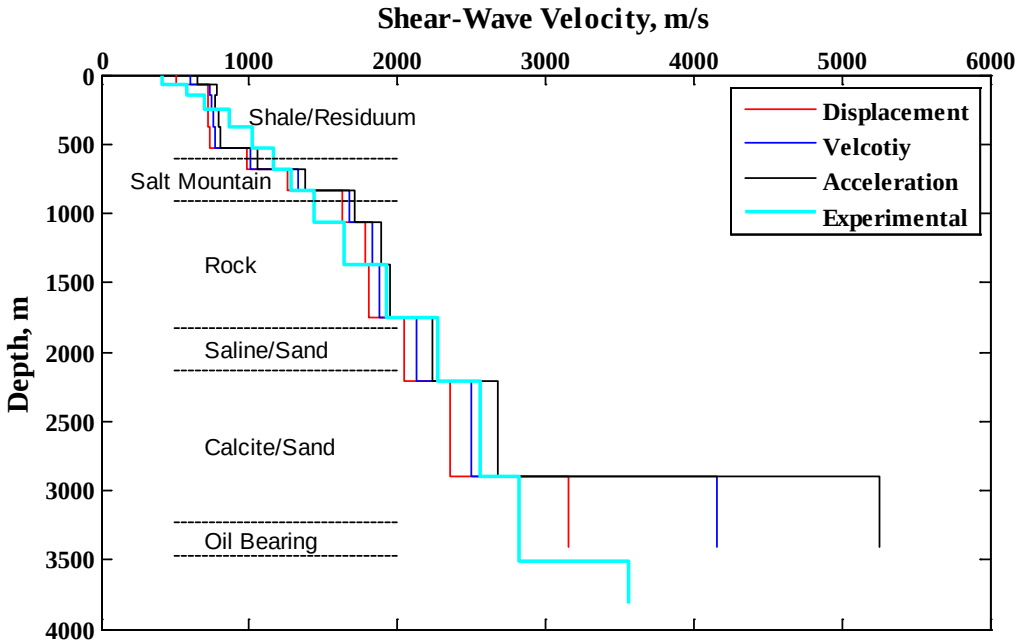

FIGURE 7.2: Comparison of shear wave velocity obtained from the baseline simulation data and averaged experimental tests

Velocity changes, $\Delta v/v$, has been used by several researchers (Hatchell et al. 2003; Hawkins et al. 2006) as condition index to estimate geomechanical model and to

explain the stress changes. Hence, if different sensors were used other than the velocimeter (geophone), then the data can be transformed to velocity.

$\Delta v/v$ can be defined differently, in this case it is defined as:

$$(\frac{\Delta v}{v})_i = \frac{(v_{simulation\ result})_i - (v_{experimental\ data})_i}{(v_{experimental\ data})_i} \quad (28)$$

where i denotes i^{th} layer of the rock profile, $v_{experimental\ data}$ represents average shear wave velocity obtained from geophysical tests, $v_{simulation\ result}$ represents shear wave velocity obtained from the baseline MDOF model, including displacement, velocity and acceleration time histories.

$\Delta v/v$ of simulation data are compared with the average value from experimental results and are plotted in bar chart, as shown in FIGURE 7.3. $\Delta v/v$ for simulation displacement data and averaged experimental results varied with depth from -0.28 to 0.24. $\Delta v/v$ for simulation velocity data and averaged experimental results varied with depth from -0.24 to 0.47. $\Delta v/v$ for simulation acceleration data and averaged experimental results varied with depth from -0.21 to 0.86. $\Delta v/v$ values for simulation data and average experimental results are also summarized in TABLE 7.1.

The acceleration curves introduced the highest errors, than velocity and followed by the displacement. This is especially true because of the skew at the last layer. The theoretical wave speed value would be significant depending on the sensor type: accelerometer, velocimeter or displacement sensors. But this has no bearing to the interpretation of the results, because velocity is directly related to stiffness of a layer.

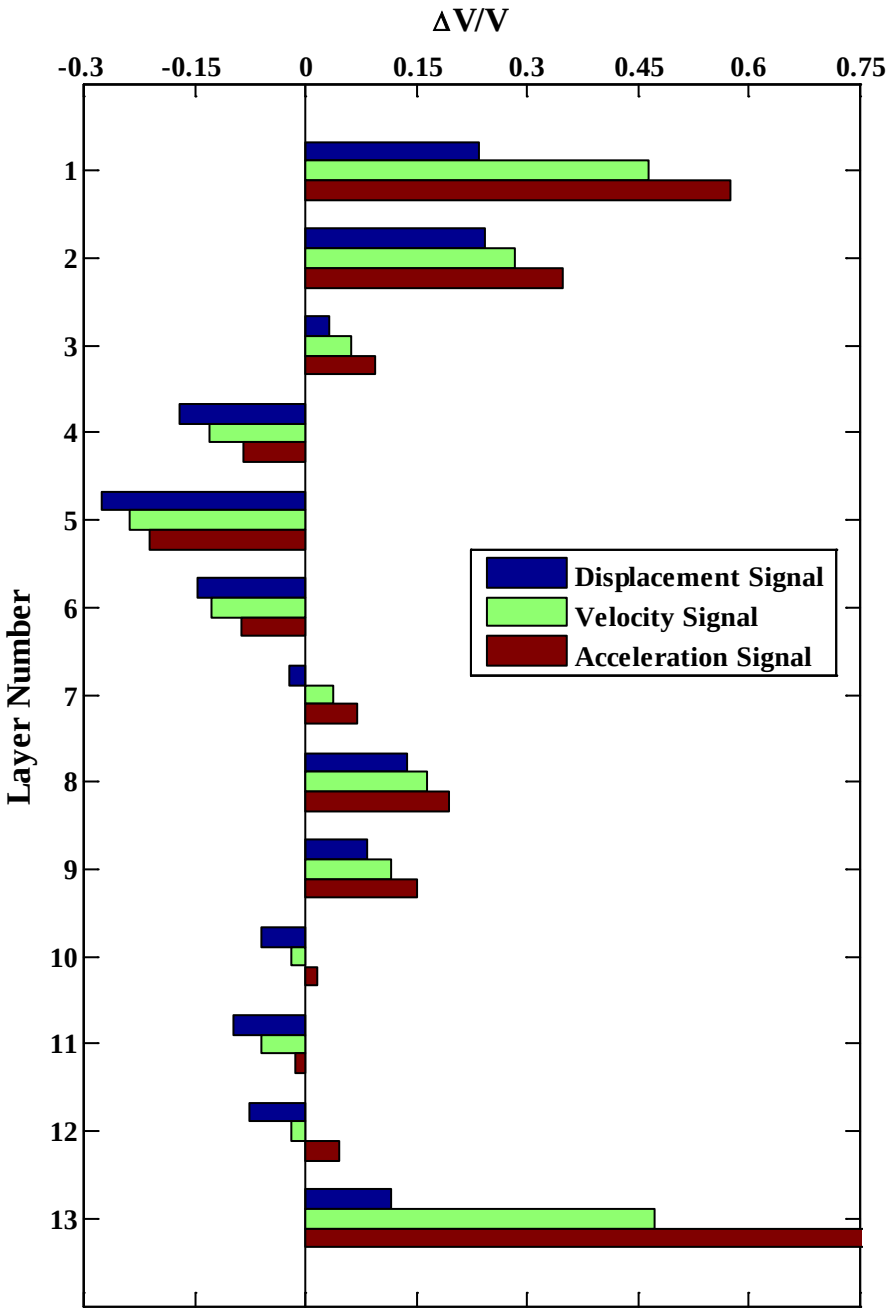

FIGURE 7.3: $\Delta V/V$ computed from the baseline simulation data and averaged experimental tests

TABLE 7.1: $\Delta V/V$ values for the baseline simulation data and averaged experimental data

Layer	Thickness, ft (m)	$\Delta V/V$		
		Displacement	Velocity	Acceleration
1	240 (73.15)	0.23	0.46	0.58
2	260 (79.25)	0.24	0.28	0.35
3	300 (91.44)	0.03	0.06	0.09
4	440 (134.11)	-0.17	-0.13	-0.09
5	500 (152.40)	-0.28	-0.24	-0.21
6	500 (152.40)	-0.15	-0.13	-0.09
7	500 (152.40)	-0.02	0.04	0.07
8	760 (231.65)	0.14	0.16	0.19
9	1000 (304.80)	0.08	0.12	0.15
10	1240 (377.95)	-0.06	-0.02	0.01
11	1500 (457.20)	-0.10	-0.06	-0.01
12	2260 (688.85)	-0.08	-0.02	0.05
13	1700 (518.16)	0.12	0.47	0.86

In order to demonstrate the changes of velocity in the actual field tests, $\Delta v/v$ is employed to compute their differences. As mentioned in Chapter 3, the experimental tests in the Citronelle Oil Field can be categorized into three groups: before, during and after CO_2 injection. The average shear wave velocities from the three corresponding groups were used to compute velocity changes.

The procedures of the computation as follows: the wave speed of the before CO_2 injection is used as base velocity, the comparisons with the velocities of during and after CO_2 injection are then performed separately. Here, we define $\Delta v/v$ as

$$(\frac{\Delta v}{v})_i = \frac{(v_{During})_i - (v_{Before})_i}{(v_{Before})_i} \tag{29}$$

$$(\frac{\Delta v}{v})_i = \frac{(v_{After})_i - (v_{Before})_i}{(v_{Before})_i} \tag{30}$$

where i denotes i^{th} layer of the soil profile, v_{Before}, v_{During} and v_{After} represents average shear wave velocity of before, during and after CO_2 injection, respectively.

The wave speed of the during CO_2 injection is also used as base velocity, then a comparison with the velocity of after CO_2 injection is given by

$$(\frac{\Delta v}{v})_i = \frac{(v_{After})_i - (v_{During})_i}{(v_{During})_i} \tag{31}$$

where i denotes i^{th} layer of the soil profile, v_{During} and v_{After} represents average shear wave velocity of during and after CO_2 injection, respectively.

$\Delta v/v$ of the experimental data of before, during and after CO_2 injection are plotted in bar charts, as shown in FIGURE 7.4 and FIGURE 7.5, for both survey line 1 and 2, respectively. FIGURE 7.6 shows the velocity changes of during versus after CO_2 injection. $\Delta v/v$ for survey line 1 of before versus during CO_2 injection varied with depth from -0.08 to 0.17. $\Delta v/v$ for survey line 1 of before versus after CO_2 injection varied with depth from -0.10 to 0.22. $\Delta v/v$ for survey line 2 of before versus during CO_2 injection varied with depth from -0.09 to 0.18. $\Delta v/v$ for survey line 2 of before versus after CO_2 injection varied with depth from -0.11 to 0.21. $\Delta v/v$ for survey line 1 of during versus after CO_2 injection varied with depth from -0.11 to 0.06. $\Delta v/v$ for survey line 2 of during versus after CO_2 injection varied with depth from -0.08 to 0.11. $\Delta v/v$ values for experimental data of before, during and after CO_2 injection are shown in TABLE 7.2.

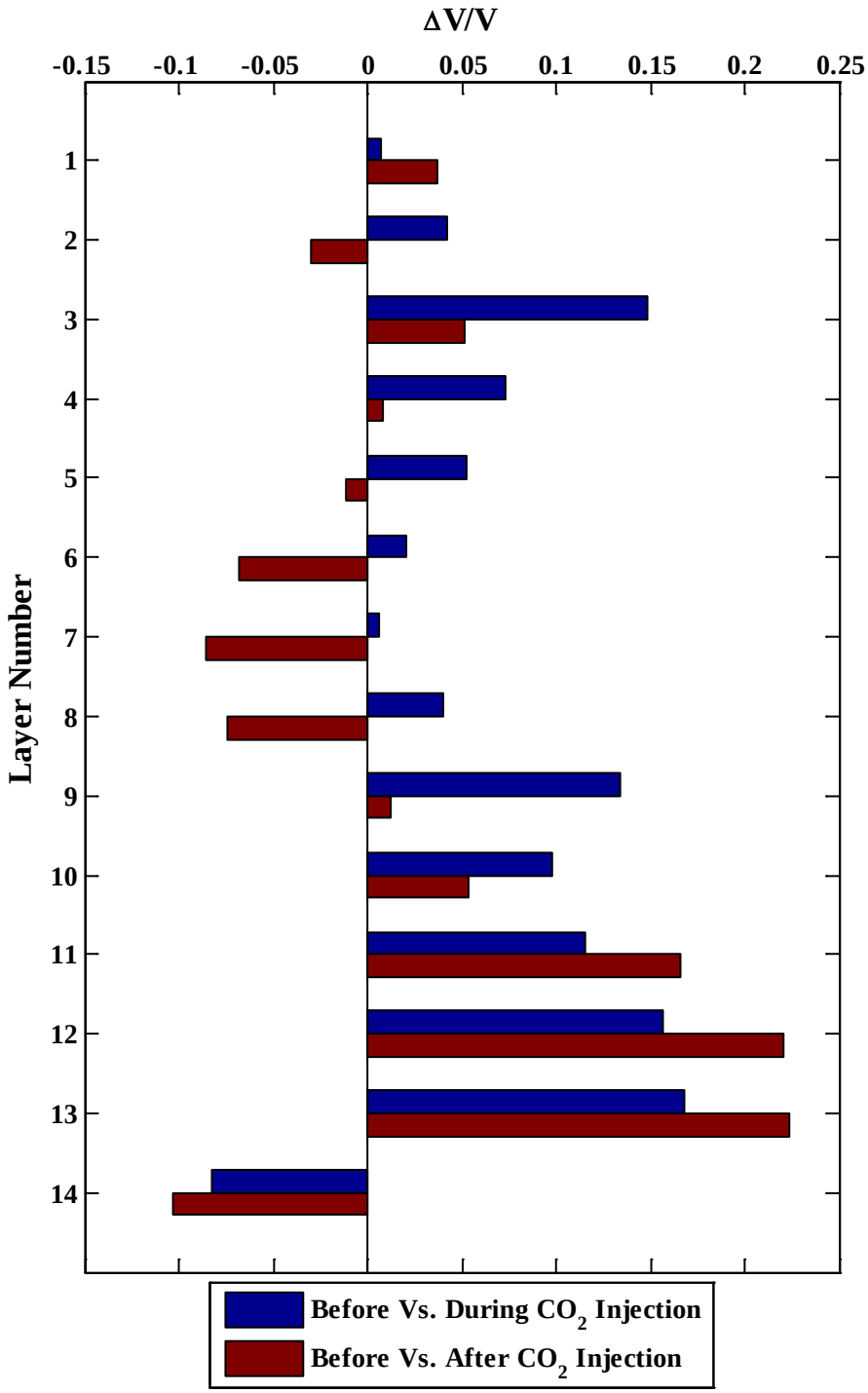

FIGURE 7.4: $\Delta V/V$ computed from the shear wave velocity of survey line 1 of before, during and after CO_2 injection.

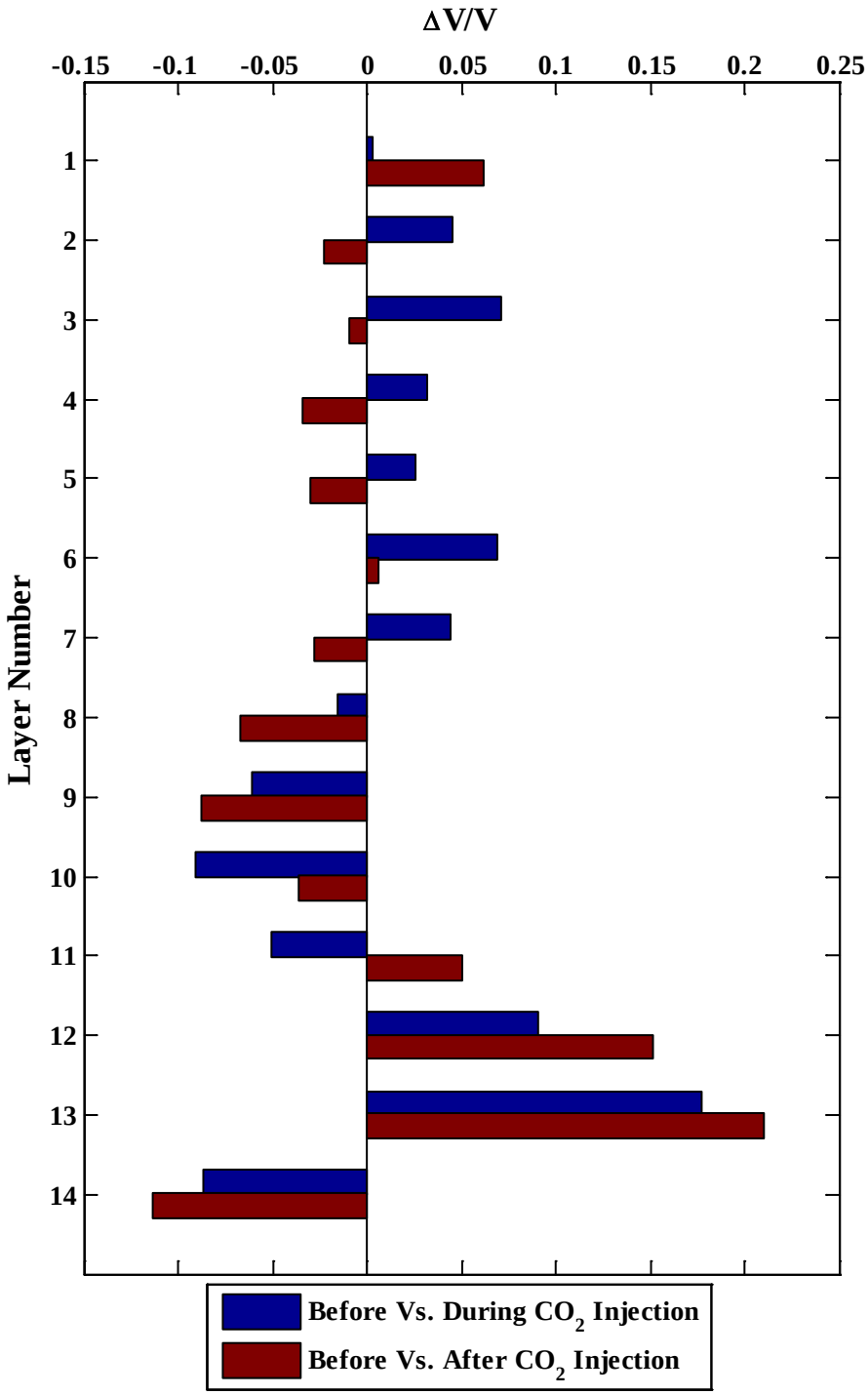

FIGURE 7.5: $\Delta V/V$ computed from the shear wave velocity of survey line 2 of before, during and after CO_2 injection.

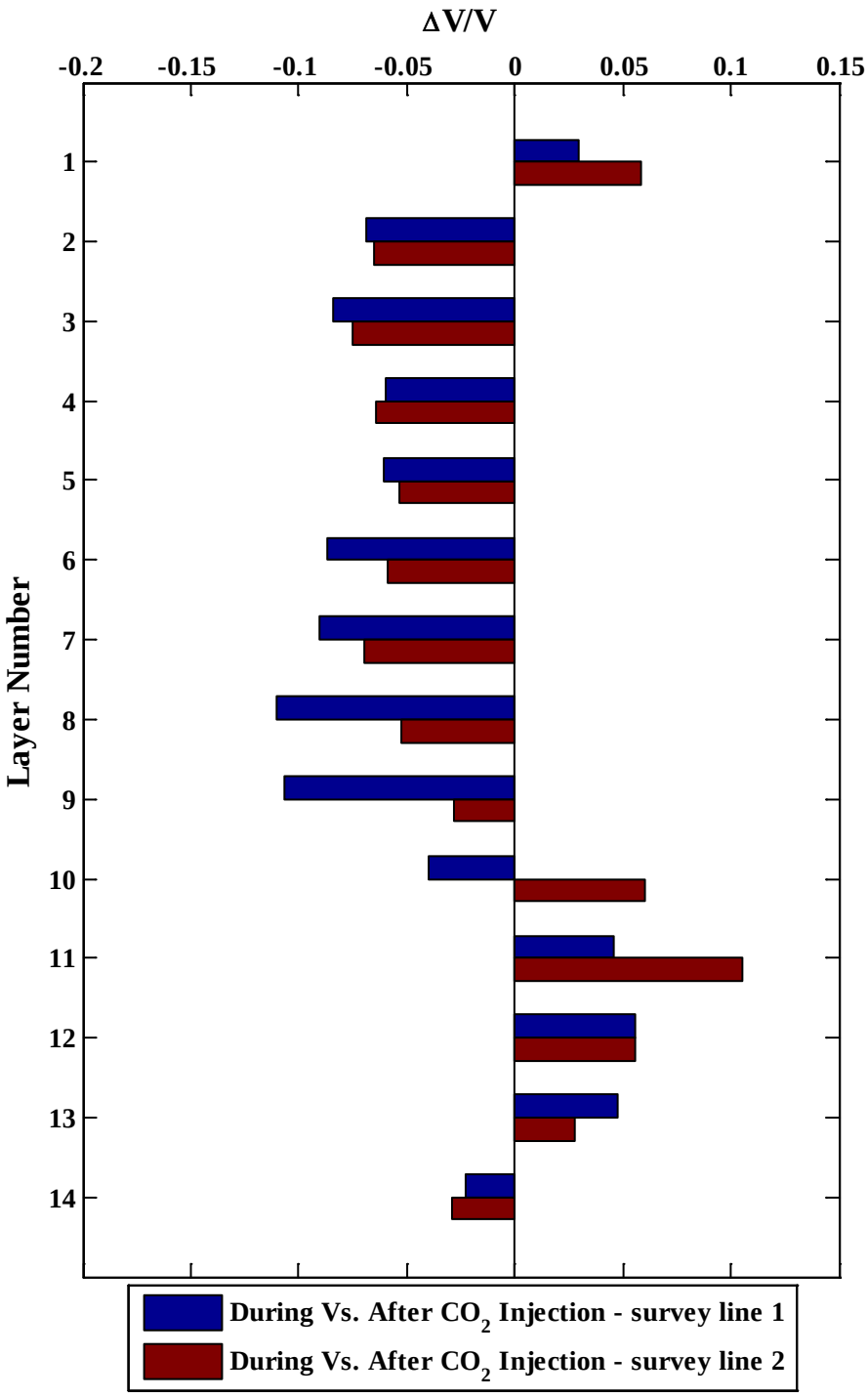

FIGURE 7.6: $\Delta V/V$ computed from the shear wave velocity of survey line 1 and 2 of during and after CO_2 injection.

TABLE 7.2: $\Delta V/V$ values for experimental tests of before, during and after CO_2 injection

Layer	Thickness, ft (m)	Before Vs. During		Before Vs. After		During Vs. After	
		survey line 1	survey line 2	survey line 1	survey line 2	survey line 1	survey line 2
1	250 (76.20)	0.01	0.00	0.04	0.06	0.03	0.06
2	250 (76.20)	0.04	0.05	-0.03	-0.02	-0.07	-0.07
3	300 (91.44)	0.15	0.07	0.05	-0.01	-0.08	-0.08
4	450 (137.16)	0.07	0.03	0.01	-0.03	-0.06	-0.06
5	500 (152.40)	0.05	0.03	-0.01	-0.03	-0.06	-0.05
6	500 (152.40)	0.02	0.07	-0.07	0.01	-0.09	-0.06
7	500 (152.40)	0.01	0.04	-0.09	-0.03	-0.09	-0.07
8	750 (228.60)	0.04	-0.02	-0.07	-0.07	-0.11	-0.05
9	1000 (304.80)	0.13	-0.06	0.01	-0.09	-0.11	-0.03
10	1250 (381.00)	0.10	-0.09	0.05	-0.04	-0.04	0.06
11	1500 (457.20)	0.12	-0.05	0.17	0.05	0.05	0.11
12	2250 (685.80)	0.16	0.09	0.22	0.15	0.06	0.06
13	2000 (609.60)	0.17	0.18	0.22	0.21	0.05	0.03
14	1000 (304.80)	-0.08	-0.09	-0.10	-0.11	-0.02	-0.03

7.4. Shear-Wave Velocity Profiles Influenced by Oil Bearing Layer Change

7.4.1 Sensitivity to Oil Bearing Layer Stress Changes

The pressure in the oil bearing layer will slowly built up during the CO_2 injection. The MDOF model influenced by the oil bearing layer was discussed in section 5.5. The shear wave velocity profiles derived from displacement, velocity and acceleration signal of the simulation results and averaged experimental data are shown in FIGURE 7.7 through FIGURE 7.9. The MDOF shear wave velocity plots indicated that the wave speeds increased consistently as the pressure at the oil bearing layers are increasing. It is especially true in the layers of Calcite and oil bearing. It should be noted that the shear wave velocity plots derived from displacement, velocity and acceleration time histories yield slight different results, the last layer effect is more pronounced for velocity and acceleration derived shear wave velocity plots than for displacement derived plots.

The wave speeds of the L Case I-0 as base velocity, the comparisons with the velocity of L Cases I-1 to I-5 are performed respectively. The equation of $\Delta v/v$ in this case is given by

$$(\frac{\Delta v}{v})_{i,j} = \frac{(v_{L\ \text{Case I-j}})_i - (v_{L\ \text{Case I-0}})_i}{(v_{L\ \text{Case I-0}})_i} \tag{32}$$

where i denotes i^{th} layer of the rock profile, j denotes j^{th} simulation case. $v_{L\ Case\ I-j}$ represents shear wave velocity obtained from j^{th} simulation case, $v_{L\ Case\ I-0}$ represents shear wave velocity obtained from the baseline MDOF model.

$\Delta v/v$ of the simulation results of L Cases I-0 to I-5 are plotted in bar charts, as shown in FIGURE 7.10, FIGURE 7.11 and FIGURE 7.12, for displacement, velocity and acceleration signal, respectively. The magnitude of $\Delta v/v$ is in the order of 0.03, hence, change is not obvious, but detectable. The $\Delta v/v$ values for displacement, velocity and acceleration signal of L Cases I-0 to I-5 are shown in TABLE 7.3, TABLE 7.4 and TABLE 7.5, respectively.

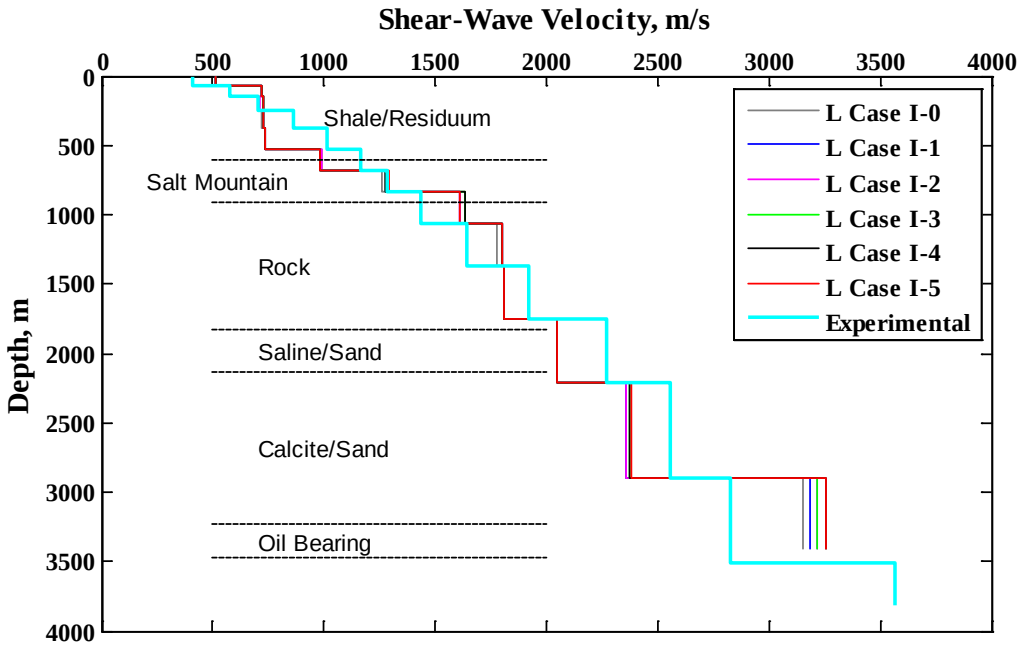

FIGURE 7.7: Shear wave velocity derived from displacement signal of simulation results and experimental data

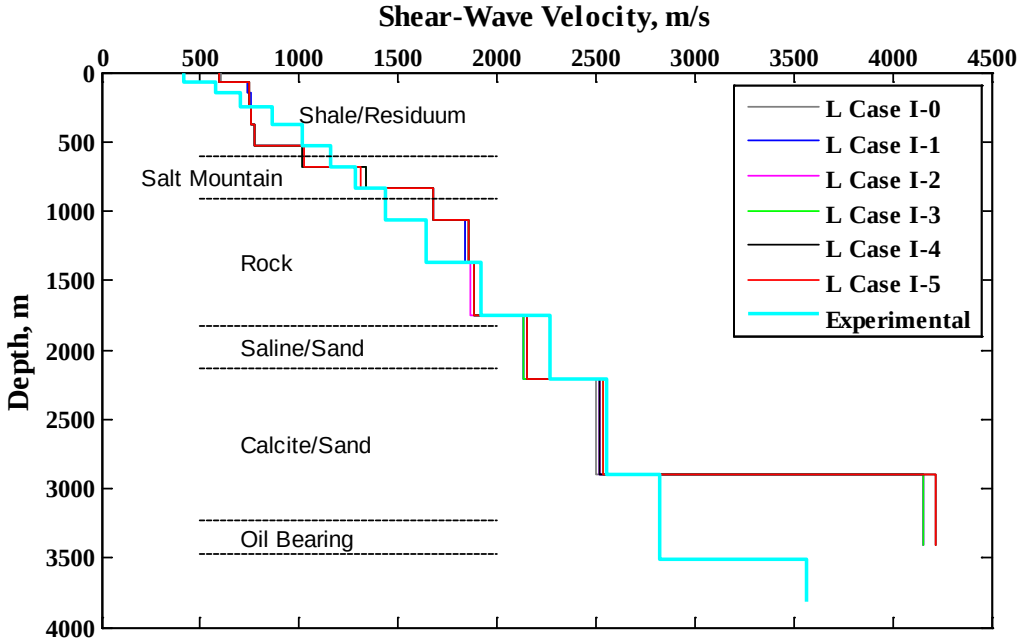

FIGURE 7.8: Shear wave velocity derived from velocity signal of simulation results and experimental data

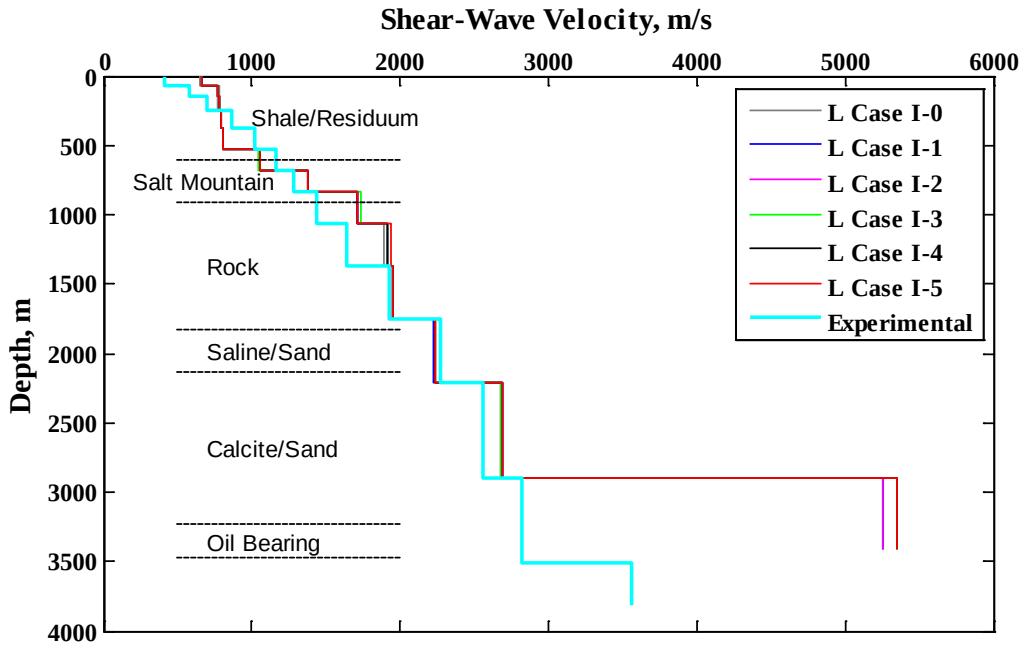

FIGURE 7.9: Shear wave velocity derived from acceleration signal of simulation results and experimental data

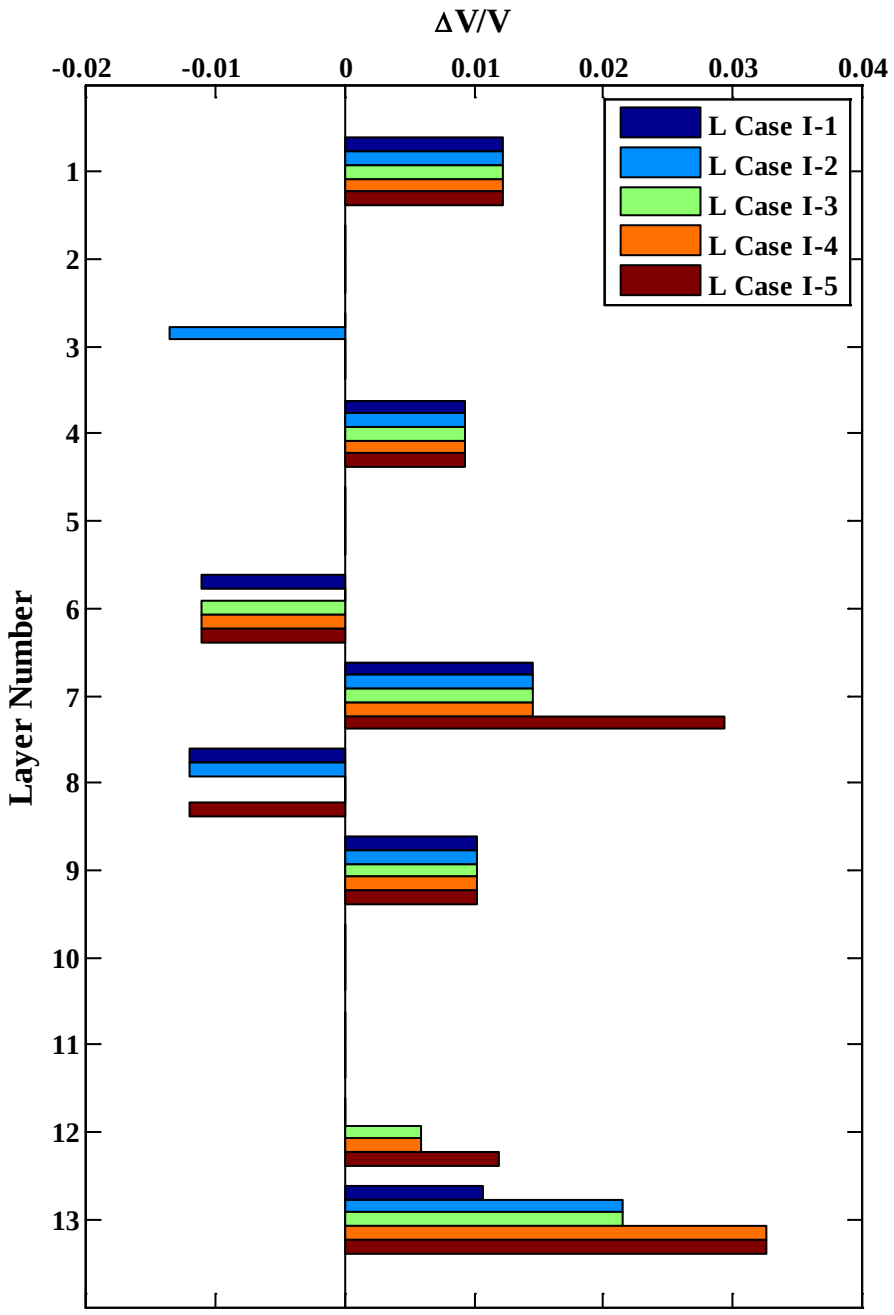

FIGURE 7.10: $\Delta V/V$ computed from shear wave velocity derived from displacement signal of L Cases I-0 to I-5

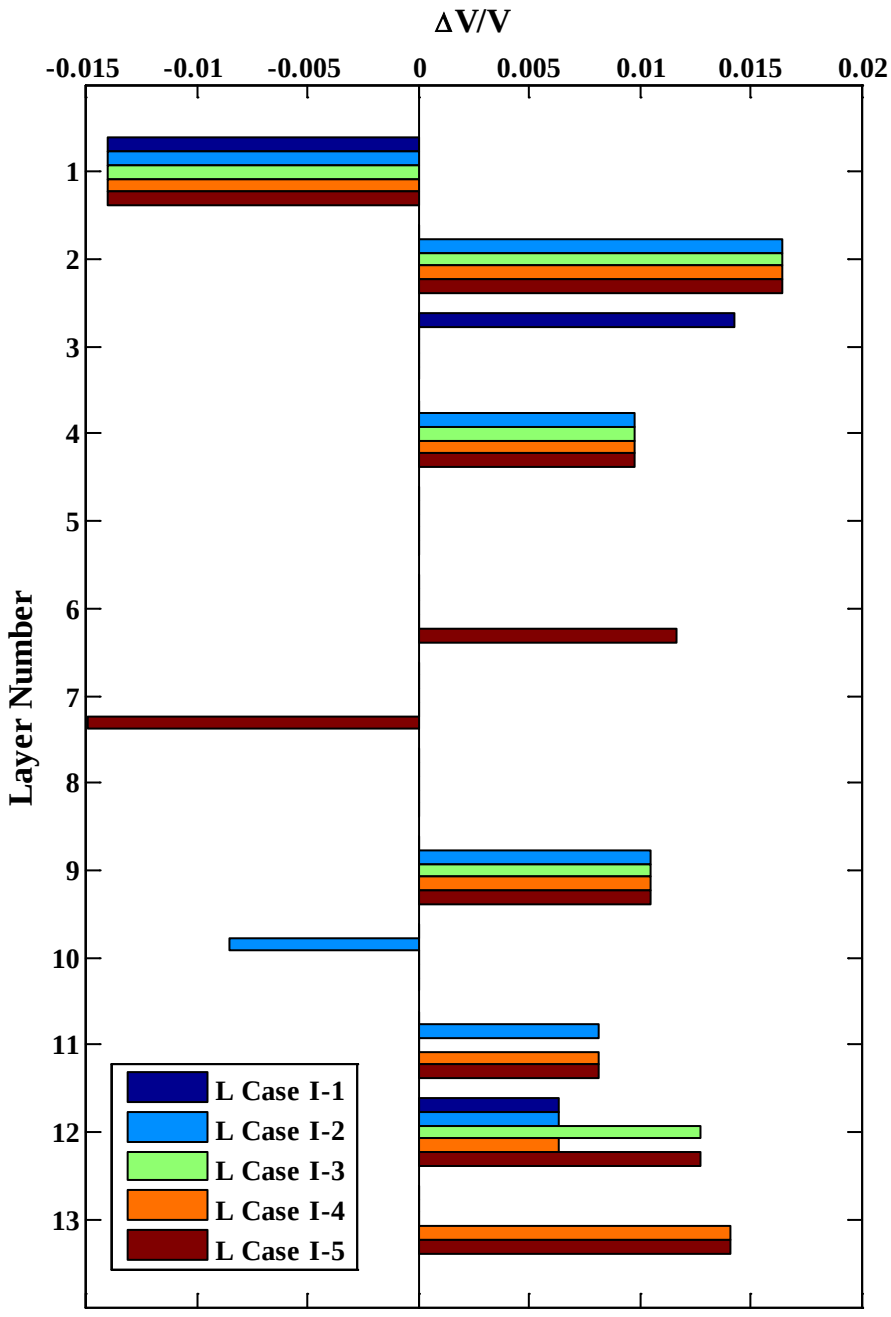

FIGURE 7.11: $\Delta V/V$ computed from shear wave velocity derived from velocity signal of L Cases I-0 to I-5

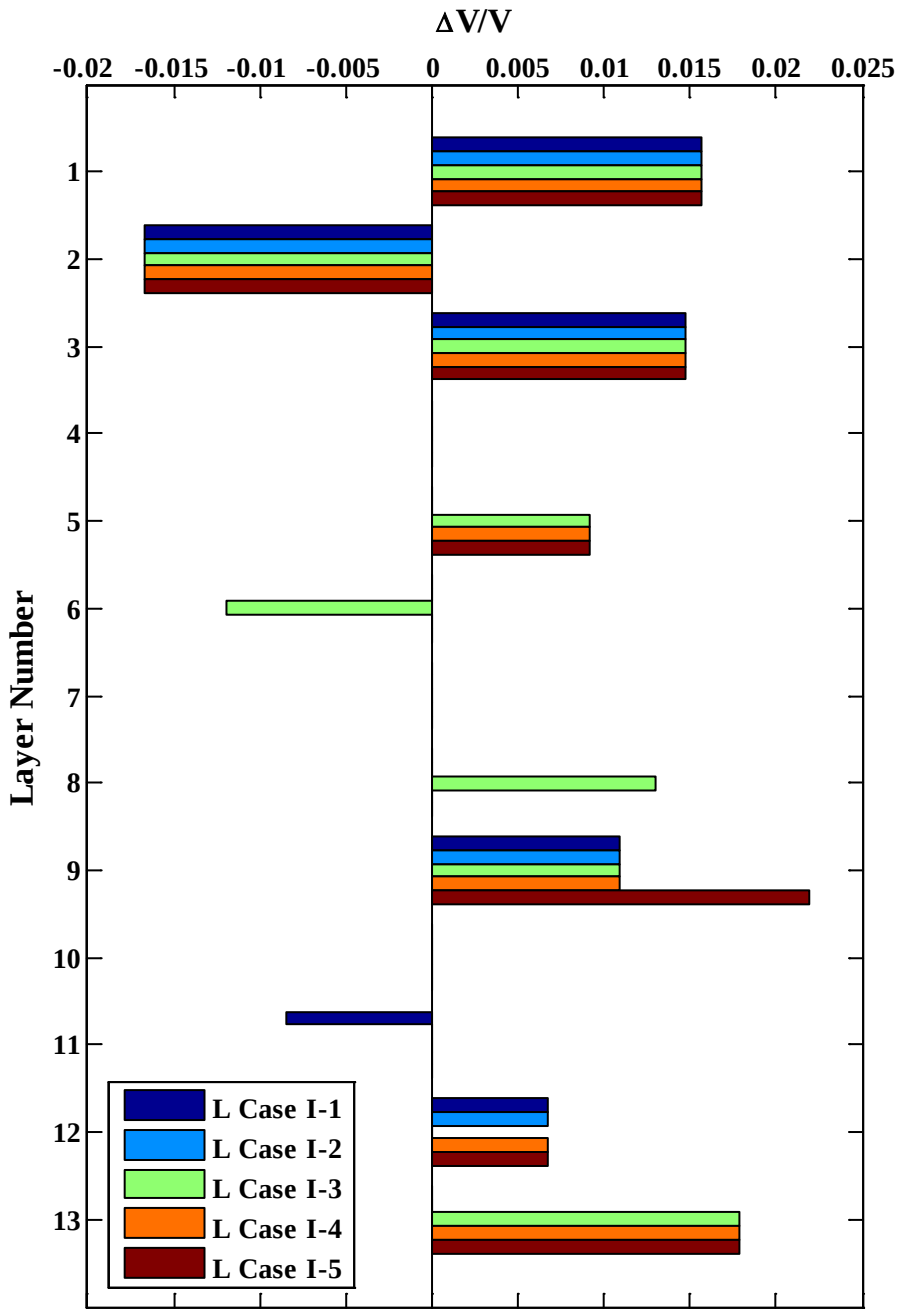

FIGURE 7.12: $\Delta V/V$ computed from shear wave velocity derived from acceleration signal of L Cases I-0 to I-5

TABLE 7.3: $\Delta V/V$ values for displacement signal of L Cases I-0 to I-5

Layer	Thickness, ft (m)	Displacement Signal				
		L Case I-1	L Case I-2	L Case I-3	L Case I-4	L Case I-5
1	240 (73.15)	0.012	0.012	0.012	0.012	0.012
2	260 (79.25)	0.000	0.000	0.000	0.000	0.000
3	300 (91.44)	0.000	-0.014	0.000	0.000	0.000
4	440 (134.11)	0.009	0.009	0.009	0.009	0.009
5	500 (152.40)	0.000	0.000	0.000	0.000	0.000
6	500 (152.40)	-0.011	0.000	-0.011	-0.011	-0.011
7	500 (152.40)	0.014	0.014	0.014	0.014	0.029
8	760 (231.65)	-0.012	-0.012	0.000	0.000	-0.012
9	1000 (304.80)	0.010	0.010	0.010	0.010	0.010
10	1240 (377.95)	0.000	0.000	0.000	0.000	0.000
11	1500 (457.20)	0.000	0.000	0.000	0.000	0.000
12	2260 (688.85)	0.000	0.000	0.006	0.006	0.012
13	1700 (518.16)	0.011	0.022	0.022	0.033	0.033

TABLE 7.4: $\Delta V/V$ values for velocity signal of L Cases I-0 to I-5

Layer	Thickness, ft (m)	Velocity Signal				
		L Case I-1	L Case I-2	L Case I-3	L Case I-4	L Case I-5
1	240 (73.15)	-0.014	-0.014	-0.014	-0.014	-0.014
2	260 (79.25)	0.000	0.016	0.016	0.016	0.016
3	300 (91.44)	0.014	0.000	0.000	0.000	0.000
4	440 (134.11)	0.000	0.010	0.010	0.010	0.010
5	500 (152.40)	0.000	0.000	0.000	0.000	0.000
6	500 (152.40)	0.000	0.000	0.000	0.000	0.012
7	500 (152.40)	0.000	0.000	0.000	0.000	-0.015
8	760 (231.65)	0.000	0.000	0.000	0.000	0.000
9	1000 (304.80)	0.000	0.011	0.011	0.011	0.011
10	1240 (377.95)	0.000	-0.009	0.000	0.000	0.000
11	1500 (457.20)	0.000	0.008	0.000	0.008	0.008
12	2260 (688.85)	0.006	0.006	0.013	0.006	0.013
13	1700 (518.16)	0.000	0.000	0.000	0.014	0.014

TABLE 7.5: $\Delta V/V$ values for acceleration signal of L Cases I-0 to I-5

Layer	Thickness, ft (m)	Acceleration Signal				
		L Case I-1	L Case I-2	L Case I-3	L Case I-4	L Case I-5
1	240 (73.15)	0.016	0.016	0.016	0.016	0.016
2	260 (79.25)	-0.017	-0.017	-0.017	-0.017	-0.017
3	300 (91.44)	0.015	0.015	0.015	0.015	0.015
4	440 (134.11)	0.000	0.000	0.000	0.000	0.000
5	500 (152.40)	0.000	0.000	0.009	0.009	0.009
6	500 (152.40)	0.000	0.000	-0.012	0.000	0.000
7	500 (152.40)	0.000	0.000	0.000	0.000	0.000
8	760 (231.65)	0.000	0.000	0.013	0.000	0.000
9	1000 (304.80)	0.011	0.011	0.011	0.011	0.022
10	1240 (377.95)	0.000	0.000	0.000	0.000	0.000
11	1500 (457.20)	-0.008	0.000	0.000	0.000	0.000
12	2260 (688.85)	0.007	0.007	0.000	0.007	0.007
13	1700 (518.16)	0.000	0.000	0.018	0.018	0.018

7.4.2 Influence of Oil Producer Stiffness Reduction

When CO_2 injected into oil bearing layer, the oil may migrate and result in stress decrease in the oil bearing layer. Section 5.5.2 describes the simulation of stiffness of the oil bearing layer decreased by 50% and increased by 50% of its original stiffness. The former is to simulate oil migration in the oil bearing layer resulting in the stiffness of the oil bearing layer decreased; the latter is to simulate no oil migration in the oil bearing layer, stiffness of the oil bearing layer is increased with CO_2 injection. Shear wave velocity profiles derived from displacement, velocity and acceleration signal of the simulation results are shown in FIGURE 7.13, FIGURE 7.14 and FIGURE 7.15, respectively. The results of L Cases 50, 100 and 150 are consistent with the simulation results of L Cases I-0 to I-5 discussed in Section 7.4.1.

The wave speeds of the L Case 100 as base velocity, the comparisons with the velocity of L Cases 50 and 150 are performed respectively. The equations of $\Delta v/v$ in this case are defined as:

$$(\frac{\Delta v}{v})_i = \frac{(v_{L\ \text{Case 50}})_i - (v_{L\ \text{Case 100}})_i}{(v_{L\ \text{Case 100}})_i} \tag{33}$$

$$(\frac{\Delta v}{v})_i = \frac{(v_{L\ \text{Case 150}})_i - (v_{L\ \text{Case 100}})_i}{(v_{L\ \text{Case 100}})_i} \tag{34}$$

where i denotes i^{th} layer of the rock profile, $v_{L\ Case\ 50}$, $v_{L\ Case\ 100}$ and $v_{L\ Case\ 150}$ represent shear wave velocity obtained from L Case 50, baseline MDOF model, and L Case 150, including data of displacement, velocity and acceleration time histories.

$\Delta v/v$ of the simulation results of L Cases 50 and 150 are plotted in bar charts, as shown in FIGURE 7.16, FIGURE 7.17 and FIGURE 7.18, for displacement, velocity and acceleration signal, respectively. The simulation results are consistent with the discussion in Section 7.4.1. The magnitude of $\Delta v/v$ is in the order of 0.03, hence, change is not obvious, but detectable. The $\Delta v/v$ values for displacement, velocity and acceleration signal of L Cases I-0 to I-5 are shown in TABLE 7.6.

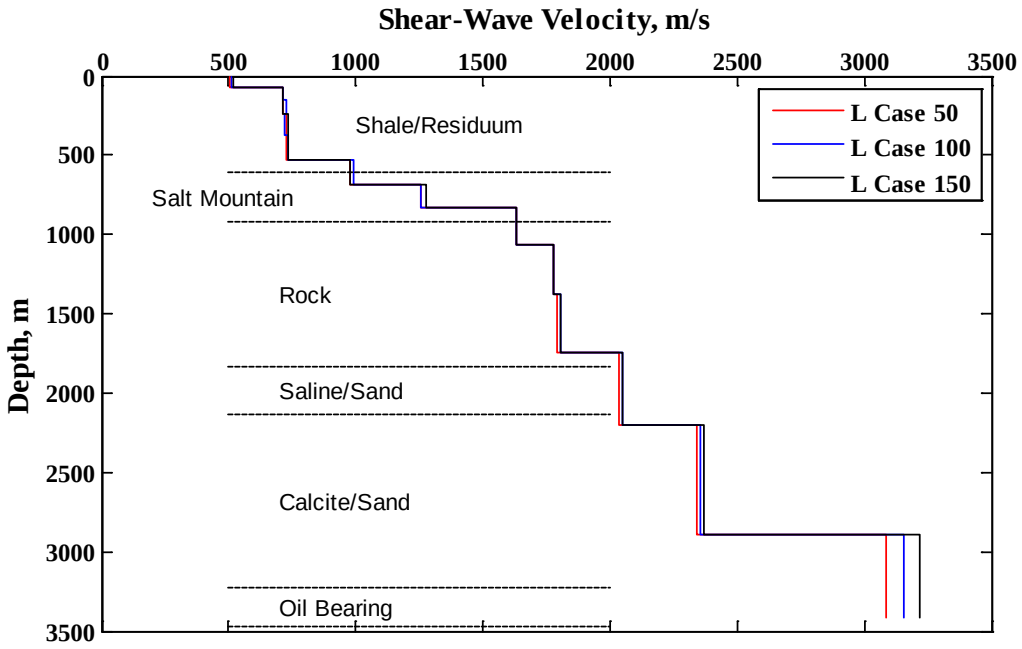

FIGURE 7.13: Shear wave velocity derived from displacement signal of L Cases 50, 100 and 150

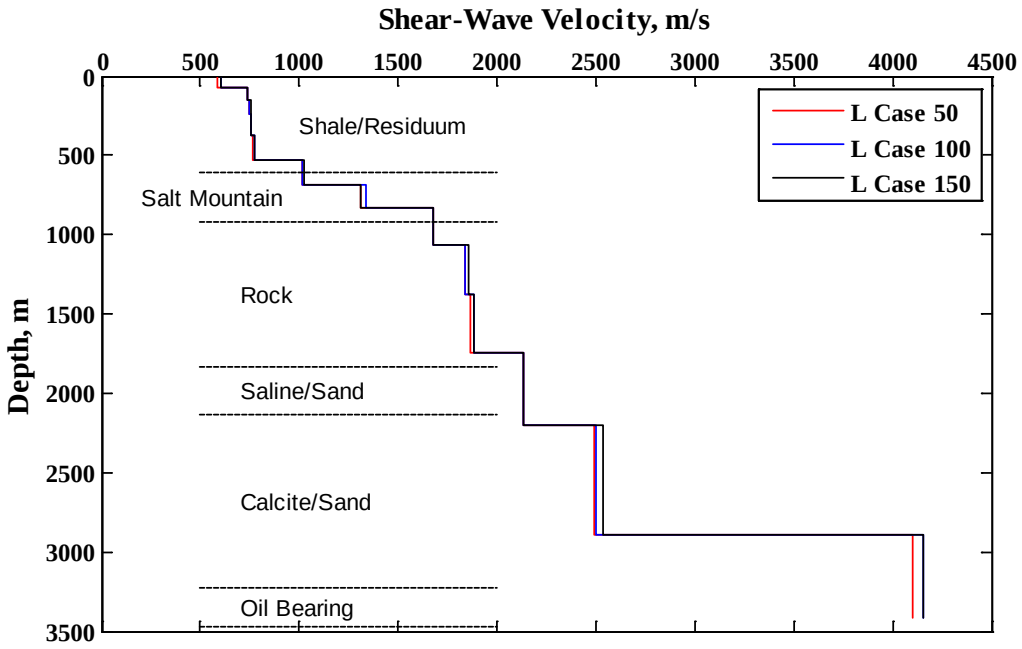

FIGURE 7.14: Shear wave velocity derived from velocity signal of L Cases 50, 100 and 150

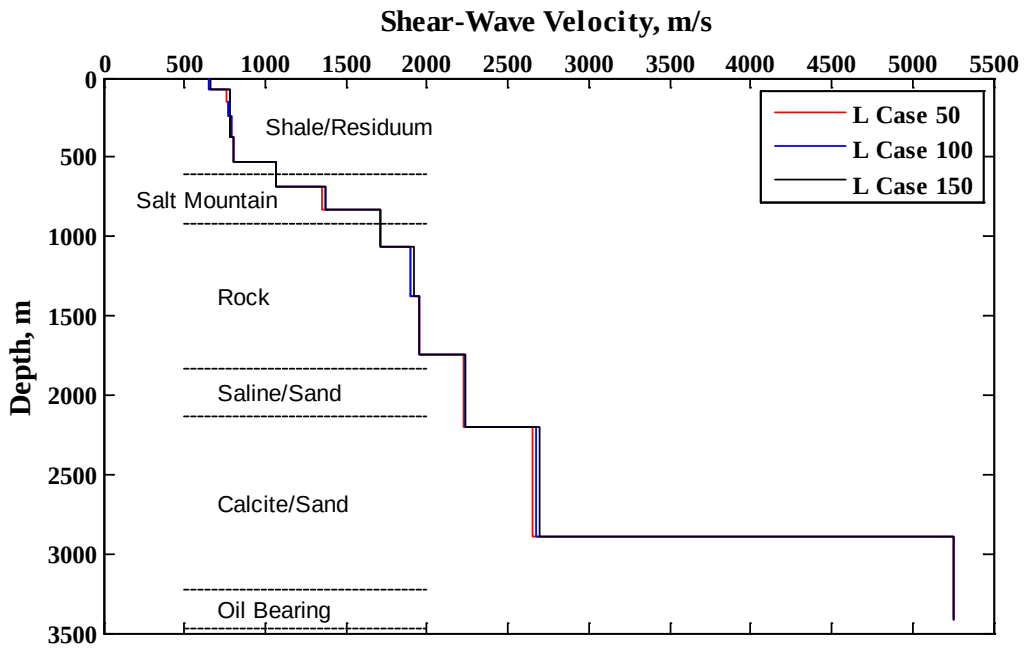

FIGURE 7.15: Shear wave velocity derived from acceleration signal of L Cases 50, 100 and 150

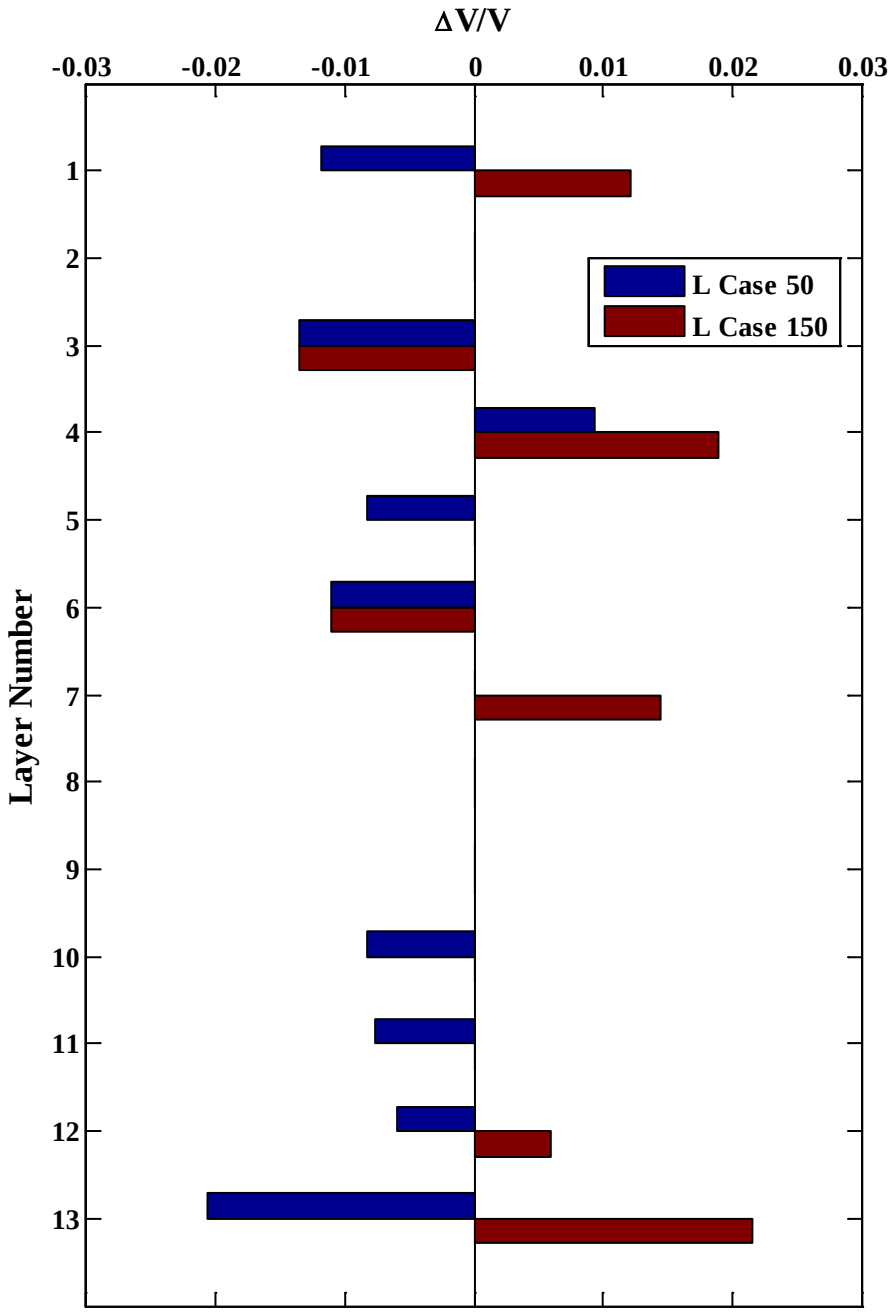

FIGURE 7.16: $\Delta V/V$ computed from shear wave velocity derived from displacement signal of L Cases 50, 100 and 150

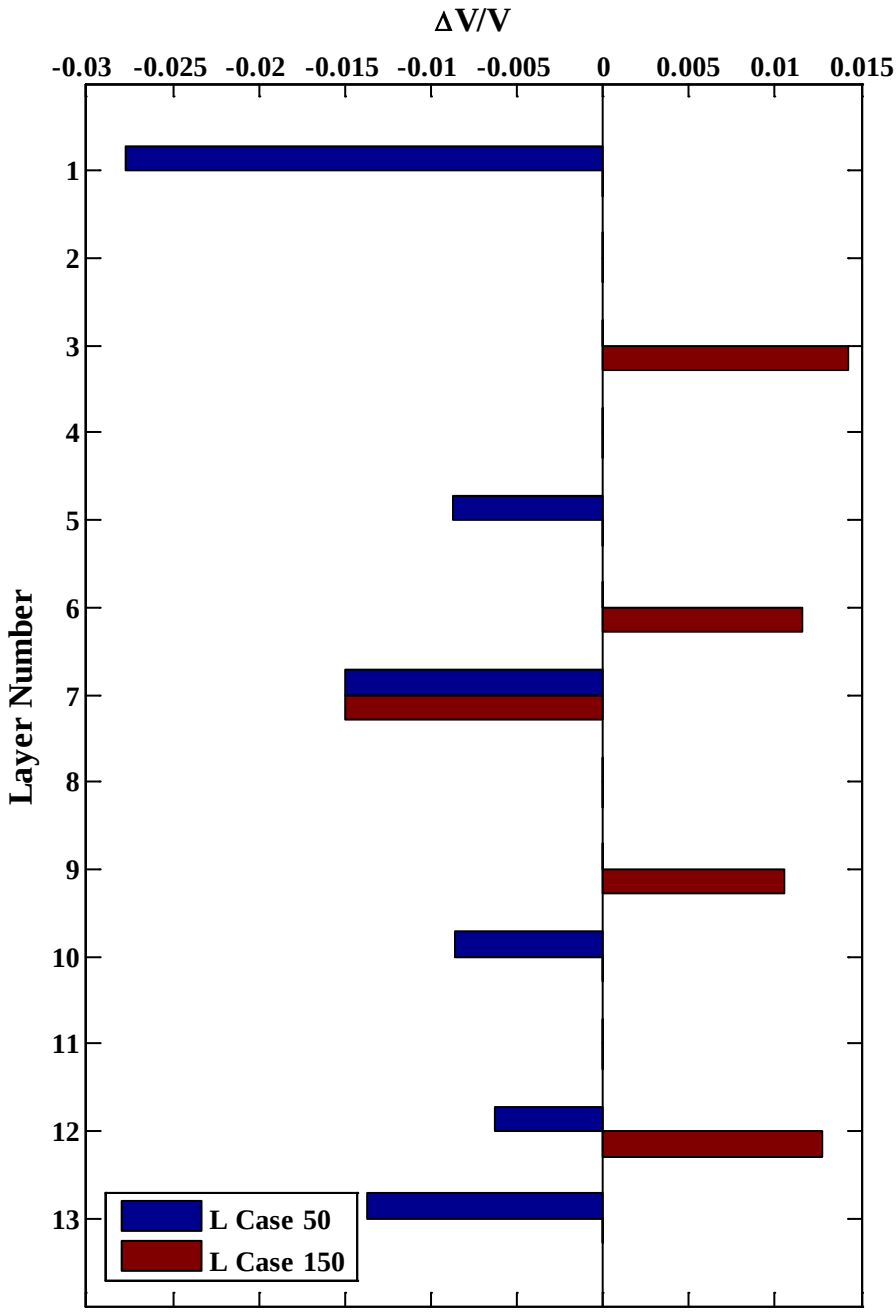

FIGURE 7.17: $\Delta V/V$ computed from shear wave velocity derived from velocity signal of L Cases 50, 100 and 150

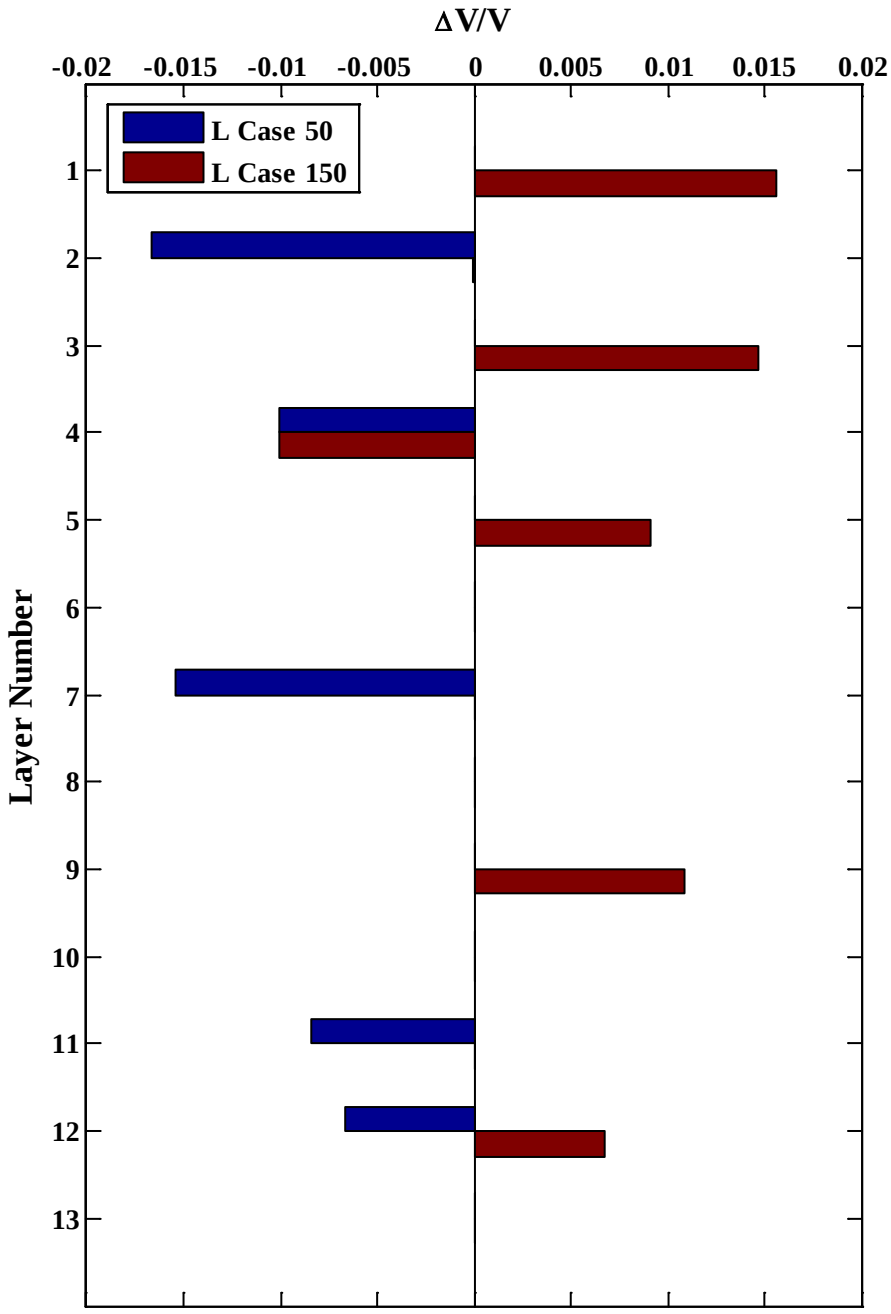

FIGURE 7.18: $\Delta V/V$ computed from shear wave velocity derived from acceleration signal of L Cases 50, 100 and 150

TABLE 7.6: $\Delta V/V$ values for displacement, velocity and acceleration signal of L Cases 50, 100 and 150

Layer	Thickness, ft (m)	Displacement		Velocity		Acceleration	
		L Case 50	L Case 150	L Case 50	L Case 150	L Case 50	L Case 150
1	240 (73.15)	-0.012	0.012	-0.028	0.000	0.000	0.016
2	260 (79.25)	0.000	0.000	0.000	0.000	-0.017	0.000
3	300 (91.44)	-0.014	-0.014	0.000	0.014	0.000	0.015
4	440 (134.11)	0.009	0.019	0.000	0.000	-0.010	-0.010
5	500 (152.40)	-0.008	0.000	-0.009	0.000	0.000	0.009
6	500 (152.40)	-0.011	-0.011	0.000	0.012	0.000	0.000
7	500 (152.40)	0.000	0.014	-0.015	-0.015	-0.015	0.000
8	760 (231.65)	0.000	0.000	0.000	0.000	0.000	0.000
9	1000 (304.80)	0.000	0.000	0.000	0.011	0.000	0.011
10	1240 (377.95)	-0.008	0.000	-0.009	0.000	0.000	0.000
11	1500 (457.20)	-0.008	0.000	0.000	0.000	-0.008	0.000
12	2260 (688.85)	-0.006	0.006	-0.006	0.013	-0.007	0.007
13	1700 (518.16)	-0.021	0.022	-0.028	0.000	0.000	0.000

7.5. Shear-Wave Velocity Profiles Influenced by the Saline and Calcite Layers Change

When CO_2 is injected into the oil bearing layer, the pressure will slowly built up in the oil bearing layer. If the oil production is limited by porosity of the rock, then the pressurization may result in elastic deformation of the rock formation. However, depending on the overbearing material weight and rigidity, the deformation may be constrained.

The MDOF model influenced by the Saline and Calcite layers was discussed in Section 5.6. The shear wave velocity profiles derived from displacement, velocity and acceleration signal of the simulation results and experimental data are shown in FIGURE 7.19 through FIGURE 7.21.

Recent observations of land uplift at CO_2 injection sites indicated that the effect of overbearing material may be critical to the containment of CO_2 underground. In the

Citronelle field study, we also observed likely pressurization of the Saline and Calcite layers above the oil bearing layer.

To study the stiffening of the Saline and Calcite layers due to pressurization of oil bearing layer, it is assumed that the spring constants at these layers are modeled as increasing. The reconstructed shear wave velocity plots indicate that the wave speeds consistently increased as the pressure at these layers are increasing.

Nonetheless, the derived shear wave speed is higher for acceleration measurements than velocity measurements, and finally displacement measurements. This observation may indicate the sensor type appropriate for detection.

The wave speeds of the L Case II-0 as base velocity, the comparisons with the velocity of L Cases II-1 to II-5 are performed respectively. The equation of $\Delta v/v$ in this case is given by

$$\left(\frac{\Delta v}{v}\right)_{i,j} = \frac{(v_{L\ \text{Case II-j}})_i - (v_{L\ \text{Case II-0}})_i}{(v_{L\ \text{Case II-0}})_i} \tag{35}$$

where i denotes i^{th} layer of the rock profile, j denotes j^{th} case of the simulation. $v_{L\ Case\ II-j}$ represents shear wave velocity obtained from j^{th} case of the simulation, $v_{L\ Case\ II-0}$ represents shear wave velocity obtained from the baseline MDOF model, including data of displacement, velocity and acceleration time histories.

$\Delta v/v$ of the simulation results of L Cases II-0 to II-5 are plotted in bar charts, as shown in FIGURE 7.22, FIGURE 7.23 and FIGURE 7.24, for displacement, velocity and acceleration signal, respectively. The magnitude of $\Delta v/v$ is in the order of 0.35, hence, change is obvious. The observation is similar as the results of $\Delta v/v$ derived from experimental data; the magnitude of $\Delta v/v$ is in the order of 0.25, discussed in Section

7.3. The $\Delta v/v$ values for displacement, velocity and acceleration signal of L Cases I-0 to I-5 are shown in TABLE 7.7, TABLE 7.8 and TABLE 7.9, respectively.

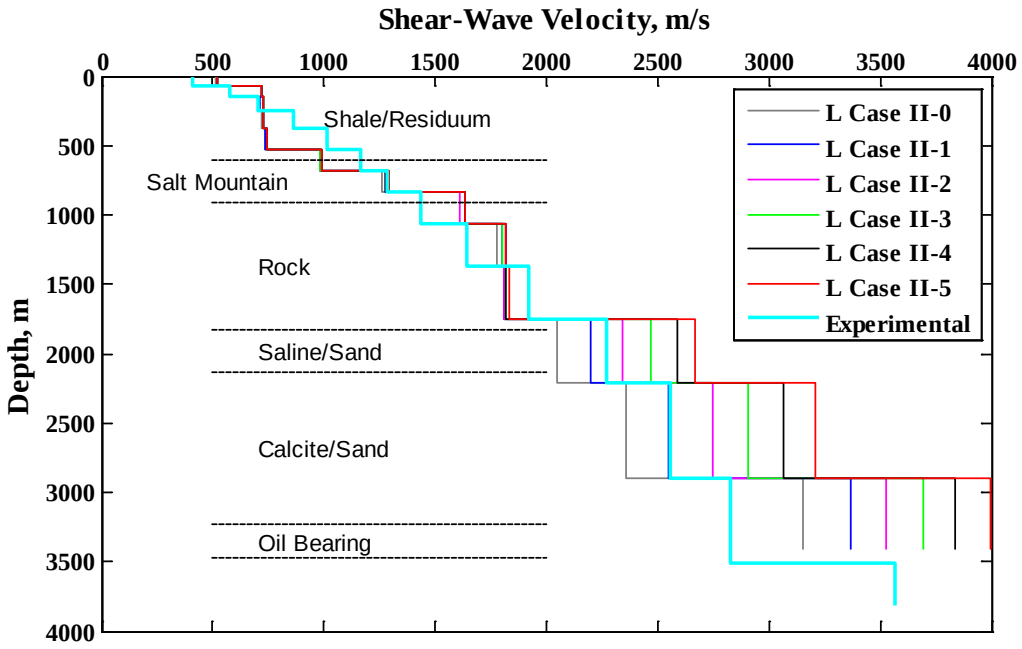

FIGURE 7.19: Shear wave velocity derived from displacement signal of simulation results and experimental data

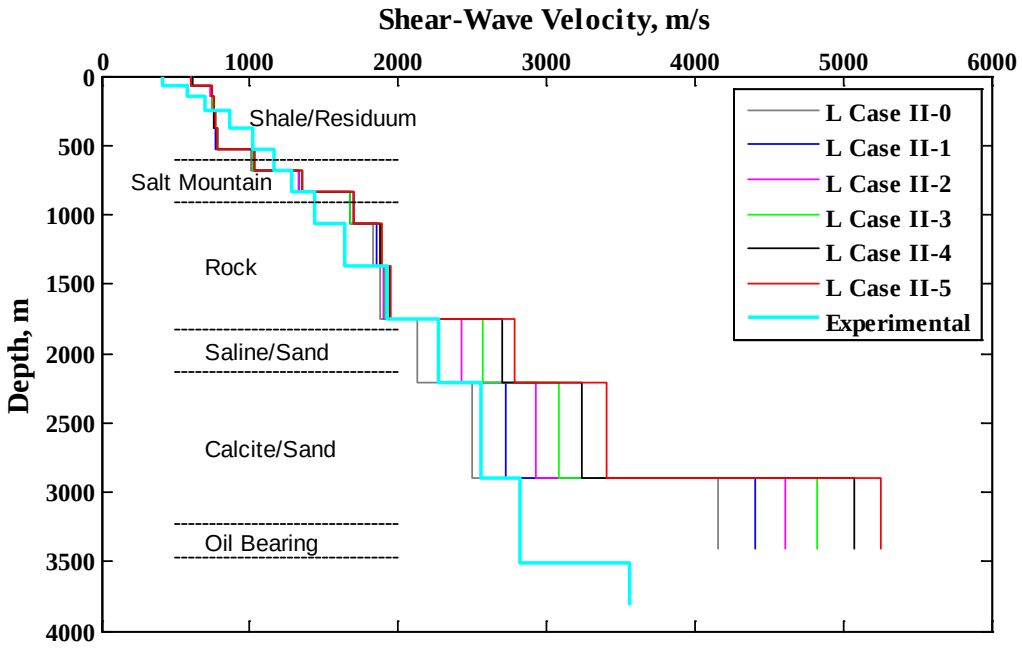

FIGURE 7.20: Shear wave velocity derived from velocity signal of simulation results and experimental data

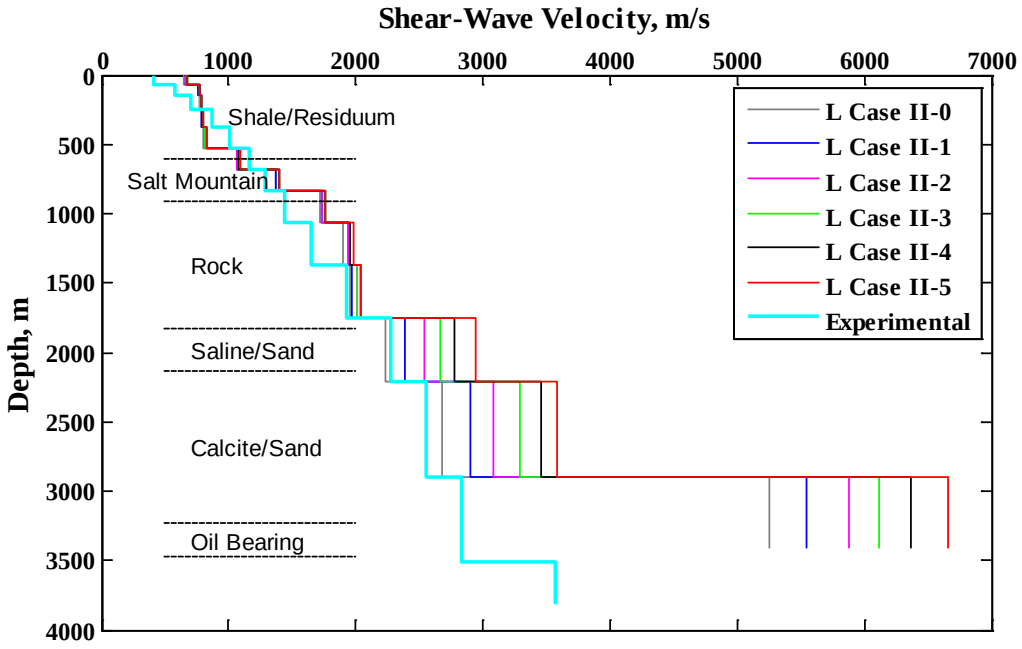

FIGURE 7.21: Shear wave velocity derived from acceleration signal of simulation results and experimental data

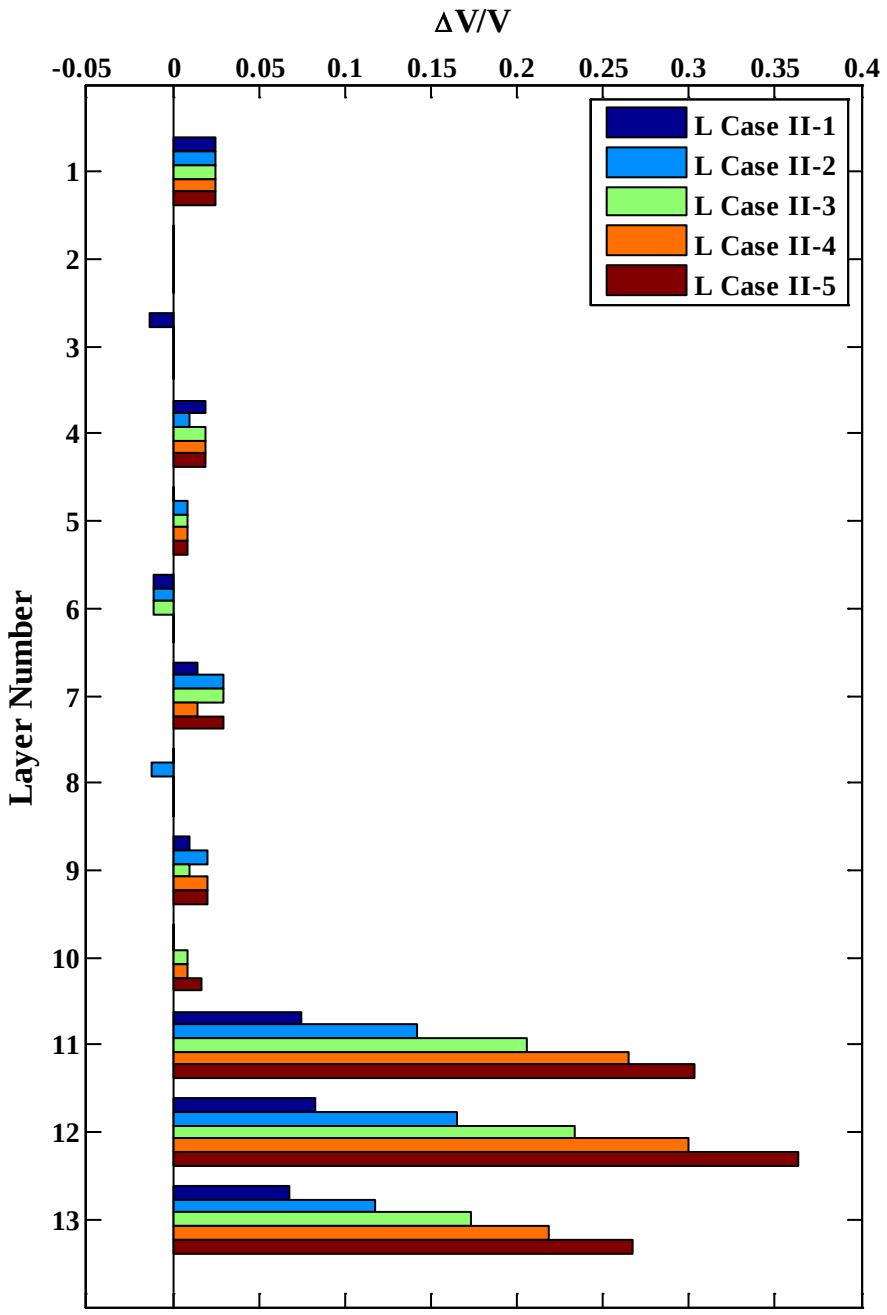

FIGURE 7.22: $\Delta V/V$ computed from shear wave velocity derived from displacement signal of L Cases II-0 to II-5

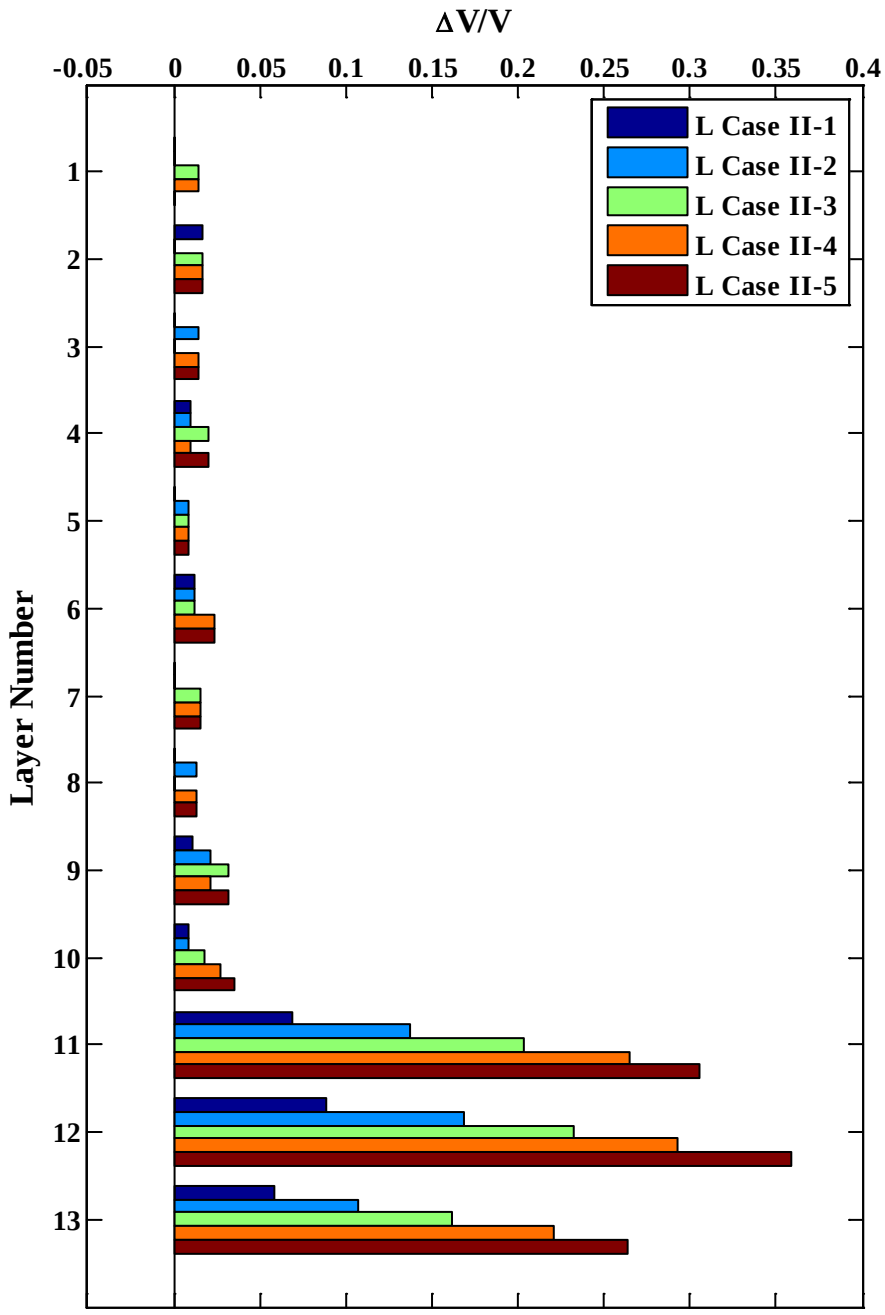

FIGURE 7.23: $\Delta V/V$ computed from shear wave velocity derived from velocity signal of L Cases II-0 to II-5

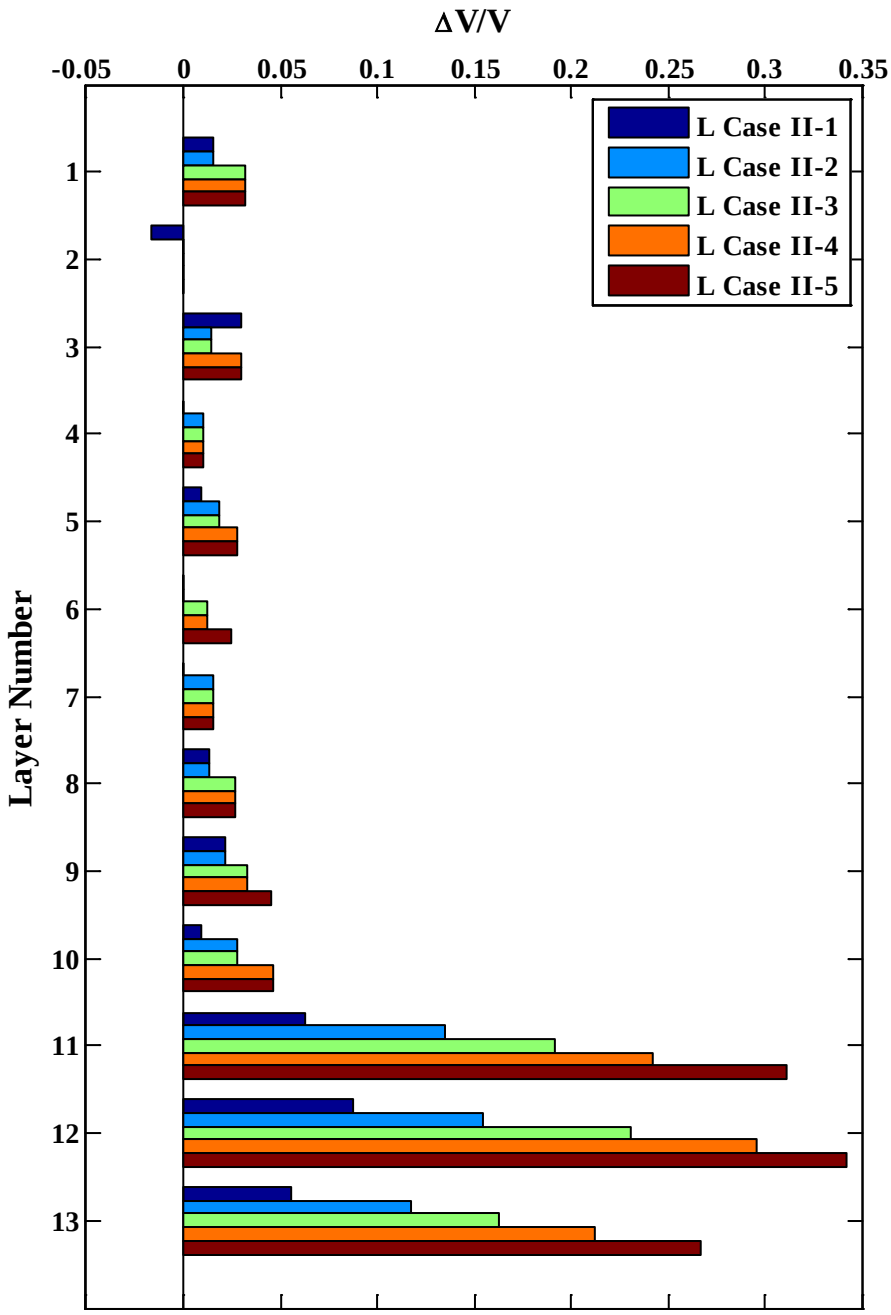

FIGURE 7.24: $\Delta V/V$ computed from shear wave velocity derived from acceleration signal of L Cases II-0 to II-5

TABLE 7.7: $\Delta V/V$ values for displacement signal of L Cases II-0 to II-5

Layer	Thickness, ft (m)	Displacement Signal				
		L Case II-1	L Case II-2	L Case II-3	L Case II-4	L Case II-5
1	240 (73.15)	0.025	0.025	0.025	0.025	0.025
2	260 (79.25)	0.000	0.000	0.000	0.000	0.000
3	300 (91.44)	-0.014	0.000	0.000	0.000	0.000
4	440 (134.11)	0.019	0.009	0.019	0.019	0.019
5	500 (152.40)	0.000	0.008	0.008	0.008	0.008
6	500 (152.40)	-0.011	-0.011	-0.011	0.000	0.000
7	500 (152.40)	0.014	0.029	0.029	0.014	0.029
8	760 (231.65)	0.000	-0.012	0.000	0.000	0.000
9	1000 (304.80)	0.010	0.021	0.010	0.021	0.021
10	1240 (377.95)	0.000	0.000	0.008	0.008	0.017
11	1500 (457.20)	0.075	0.142	0.206	0.265	0.303
12	2260 (688.85)	0.083	0.166	0.234	0.300	0.363
13	1700 (518.16)	0.067	0.118	0.173	0.218	0.267

TABLE 7.8: $\Delta V/V$ values for velocity signal of L Cases II-0 to II-5

Layer	Thickness, ft (m)	Velocity Signal				
		L Case II-1	L Case II-2	L Case II-3	L Case II-4	L Case II-5
1	240 (73.15)	0.000	0.000	0.014	0.014	0.000
2	260 (79.25)	0.016	0.000	0.016	0.016	0.016
3	300 (91.44)	0.000	0.014	0.000	0.014	0.014
4	440 (134.11)	0.010	0.010	0.020	0.010	0.020
5	500 (152.40)	0.000	0.009	0.009	0.009	0.009
6	500 (152.40)	0.012	0.012	0.012	0.024	0.024
7	500 (152.40)	0.000	0.000	0.015	0.015	0.015
8	760 (231.65)	0.000	0.013	0.000	0.013	0.013
9	1000 (304.80)	0.011	0.021	0.032	0.021	0.032
10	1240 (377.95)	0.009	0.009	0.018	0.027	0.036
11	1500 (457.20)	0.069	0.138	0.204	0.265	0.305
12	2260 (688.85)	0.089	0.169	0.233	0.293	0.359
13	1700 (518.16)	0.059	0.108	0.161	0.220	0.263

TABLE 7.9: $\Delta V/V$ values for acceleration signal of L Cases II-0 to II-5

Layer	Thickness, ft (m)	Acceleration Signal				
		L Case II-1	L Case II-2	L Case II-3	L Case II-4	L Case II-5
1	240 (73.15)	0.016	0.016	0.032	0.032	0.032
2	260 (79.25)	-0.017	0.000	0.000	0.000	0.000
3	300 (91.44)	0.030	0.015	0.015	0.030	0.030
4	440 (134.11)	0.000	0.010	0.010	0.010	0.010
5	500 (152.40)	0.009	0.019	0.019	0.028	0.028
6	500 (152.40)	0.000	0.000	0.012	0.012	0.025
7	500 (152.40)	0.000	0.016	0.016	0.016	0.016
8	760 (231.65)	0.013	0.013	0.026	0.026	0.026
9	1000 (304.80)	0.022	0.022	0.033	0.033	0.045
10	1240 (377.95)	0.009	0.028	0.028	0.047	0.047
11	1500 (457.20)	0.063	0.135	0.192	0.242	0.311
12	2260 (688.85)	0.088	0.155	0.231	0.296	0.342
13	1700 (518.16)	0.056	0.118	0.163	0.213	0.267

CHAPTER 8: CONCLUSION

The following are conclusions from the study:

- The outcomes of the DoReMi monitoring at the Citronelle Oil Field are shear-wave velocity profiles that are correlated to the static stress distribution at different injection stages. It is noticed that the pressures in the oil production layer and overburden strata at the time of water injection and CO_2 injection have already been built up in the entire monitored region. Injection history interpretation using the stress wave monitoring indicates that CO_2 injection resulted in the stressing of the overbearing strata. The changes of COV value, obtained by a closer evaluation of the statistics of the experimental data, indicate that shear wave velocity change at different stages of injection at Citronelle Oil Field. The results of the geophysical monitoring for the pilot injection will aid oil field operators in decision making for the future commercial-scale reservoir management strategies.

- COV of the shear wave speed has been computed for field data and observations are:

  - Survey line 1, $COV_{before} > COV_{during} > COV_{after}$
  - Survey line 2, $COV_{during} > COV_{before} > COV_{after}$

This means the pressure distribution at Citronelle at the time of injection study is directionally differentiable.

● COV of before and during CO_2 injection is larger than COV of well head pressure which means the DoReMi method is capable of detecting site condition change.

● COV of after CO_2 injection is very similar to COV of well head pressure, indicate stable pressure in the reservoir.

● $\Delta V/V$ has been used for all studies and is most complete, $\Delta V/V$ for field data shows order of magnitude between -0.15 to 0.25, which is in the same order with the simulation of Saline and Calcite layer stress change.

● In linear and nonlinear modeling, the MDOF lumped-mass model was used to simulate the propagation of P-wave during static phase change during CO_2 injection in a multilayered elastic media. When no oil migrates at the oil bearing layer, the multi-physical phase change at the layer is simplified into stiffness increase in the model. Studies were performed with the stiffness of oil bearing layer increased by 20%, 40%, 60%, 80% and 100% of its original stiffness. When oil migrates at the oil bearing layer, the multi-physical phase change at the layer was simplified into stiffness decrease by 50% of its original stiffness. The simulation results show that higher mode frequencies are being attenuated more than the lower frequencies and the energy distribution is not consistent throughout all frequencies. This indicates that vertical wave responses can be used for monitoring of condition changes at the oil bearing layer and time frequency analysis can be used to detect the changes in wave signals.

● The responses of the MDOF model confirmed that it can reflect changes in both oil bearing and Saline and Calcite layer changes. As the stiffness of oil bearing layer increases, shear wave velocities of the Calcite and oil bearing layer are also increased. Likewise the stiffness of Saline and Calcite layer increased while the stiffness of the oil

bearing layer are kept as constant: Shear wave velocities of the Saline, Calcite and the oil bearing layer are also strongly influenced by these layer changes.

● Because signal changes are amplitude based, TSP is suggested as an indicator to present the signal changes obtained from different MDOF models in both linear and nonlinear conditions. The results show interesting deviation of different frequency components as wave propagates to the ground surface. TSP represents an effective approach to present the multi-frequency response deviations and may be able to project multi-layer stress changes. TSP data can provide good visual differences for site condition changes, but is too complicated to interpret.

● The index method of $\Delta V/V$ (commonly used in oil production geophysical monitoring) is also discussed and is used to express stress changes by comparing simulation results with the averaged experimental data. The bar charts of the $\Delta V/V$ obtained from displacement, velocity and acceleration time histories, and averaged experimental data show that shear wave velocity obtained from acceleration time history demonstrated the highest errors, then velocity and followed by the displacement results. This may indicate possible sensitivity of acceleration-based sensing units can be more effective in monitoring site condition changes for seismic methods.

● For the simulation of sensitivity to oil bearing layer stress changes, SAPD value change is frequency dependent and higher frequency experienced larger changes than lower frequency amplitudes.

● For the simulation of sensitivity to oil bearing layer stress changes, $\Delta V/V$ is in the order of 0.03 (displacement) and 0.02 (velocity and acceleration), hence the change is detectable.

● When oil migrates in oil bearing layer, both pressure and stiffness of the layer are decreased. When oil not migrates in oil bearing layer, both stress and stiffness of the layer are increased. But the layer responses are not uniform.

● For the simulation of Saline and Calcite layer stress change (stiffness increase), $\Delta V/V$ has significant changes on the magnitude order as large as 0.35 (displacement, velocity and acceleration).

● In this study, the effects of oil bearing layer stress change and the above strata (Saline and Calcite layers) are decoupled in the numerical simulation.

● Finally, this study show that MDOF lumped mass modeling can replicate field conditions and can represent oil bearing layer stress change and Saline and Calcite strata stress change. In actual study, $\Delta V/V$ and COV seem to be good indicators of stress changes in layers. $\Delta V/V$ and COV are layer sensitive but not frequency dependent. On the other hand, SAPD and TSP can show changes in frequency domain, because they are frequency dependent.

In conclusion, this study presents a simple yet effective theoretical model to demonstrate the stress (velocity) changes during CO_2 injection processes in an oil field. Comparisons to actual experimental data indicate that the passive seismic sensing method can be used for field monitoring of CO_2-EOR process in deep formations (circa 12,000 ft).

CHAPTER 9: FUTURE STUDIES

DoReMi technique was employed to monitor CO_2 storage at Citronelle Oil Field before, during and after CO_2 injection along two linear arrays running from north - south and from northeast - southwest. The monitoring points are too limited to acquire the whole site information from the reservoir. It is suggested to perform three dimensional explorations by using the DoReMi technique with a reasonable sensor layout for monitoring CO_2 storage at Citronelle Oil Field. This may replicate the 4D seismic measurements and can detect CO_2 plume movements.

Physical model experiment is another method to check the accuracy of the application of the DoReMi method. We can construct certain scaled physical models with different layer properties, and obtain the responses of the DoReMi method. Then, compare the experimental results with the actual properties of the model.

In the current numerical simulation study, the lumped mass method was employed to study wave propagation problem in one-dimensional model. The physical condition changes of the whole CO_2 storage reservoir during CO_2 injection is very complex. The condition changes would be very helpful to determine the CO_2 storage and avoid geomechanical hazards in and around the reservoir. It is recommended that future studies be expended to two or three-dimensional model.

Another issue in the current numerical simulation study is that the physical parameters of soil layers are assumed based on general information for soils and rocks.

Further studies on the parameters selection is recommended to do more field work in the research area, for example, get more soil and rock samples through drilling in different depths and obtained their physical properties (e.g. density, Young's Modules, etc.) by performing laboratory tests.

Nonlinear phenomenon is not fully understood and need further investigation.

REFERENCES

Abu-Saba, E. G., Shen, J. Y., Mcginley, W. M., and Montgomery, R. C. (1992). "Lumped Mass Modeling for the Dynamic Analysis of Aircraft Structures." National Aeronautics and Space Administration.

Angerer, E., Crampin, S., Li, X.-Y., and Davis, T. L. (2002). "Processing, modelling and predicting time-lapse effects of overpressured fluid-injection in a fractured reservoir." *Geophysical Journal International*, 149(2): 267-280.

Arts, R., Eiken, O., Chadwick, A., Zweigel, P., Van Der Meer, L., and Zinszner, B. (2004). "Monitoring of CO_2 injected at Sleipner using time lapse seismic data." *Energy*, 29(9-10): 1383-1392.

Bachu, S. (2008). "CO_2 storage in geological media: Role, means, status and barriers to deployment." *Progress in Energy and Combustion Science*, 34(2): 254-273.

Balat, M., Balat, H., and Acici, N. (2003). "Environmental issues relating to greenhouse carbon dioxide emissions in the world." *Energy Exploration & Exploitation*, 21(5-6): 457-473.

Barkved, O., and Kristiansen, T. (2005). "Seismic time-lapse effects and stress changes: Examples from a compacting reservoir." *The Leading Edge*, 24(12): 1244-1248.

Belytschko, T., and Mindle, W. L. (1980). "Flexural wave propagation behavior of lumped mass approximations." *Computers & Structures*, 12(6): 805-812.

Berg, G. V. (1989). *Elements of Structural Dynamics*, Prentice Hall, Englewood Cliffs, N.J.

Biot, M. A. (1956a). "Theory of propagation of elastic waves in a fluid-saturated porous solid.1. Low-frequency range." Journal of the Acoustical Society of America, 28(2): 168-178.

Biot, M. A. (1956b). "Theory of propagation of elastic waves in a fluid-saturated porous solid. 2. Higher frequency range." Journal of the Acoustical Society of America, 28(2): 179-191.

Blunt, M., Fayers, F. J., and Orr Jr, F. M. (1993). "Carbon dioxide in enhanced oil recovery." *Energy Conversion and Management*, 34(9–11): 1197-1204.

Boore, D. M. (1972). "A note on the effect of simple topography on seismic SH waves." *Bulletin of the Seismological Society of America*, 62(1): 275-284.

Caughey, T. K. (1960). "Classical normal modes in damped linear dynamic systems." *Journal of Applied Mechanics*, 27(2): 269-271.

Caughey, T. K., and O'Kelly, M. E. J. (1965). "Classical normal modes in damped linear dynamic systems." *Journal of Applied Mechanics*, 32(3): 583-588.

Cha, P. D., and Chen, C.-Y. (2011). "Quenching vibration along a harmonically excited linear structure using lumped masses." *Journal of Vibration and Control*, 17(4): 527-539.

Chadwick, A., Arts, R., Eiken, O., Williamson, P., and Williams, G. (2006). "Geophysical monitoring of the CO_2 plume at Sleipner, North Sea : an outline review." *Advances in the Geological Storage of Carbon Dioxide*, S. Lombardi, L. K. Altunina, and S. E. Beaubien, eds., Springer Netherlands, 303-314.

Chadwick, R. A., Arts, R., Bentham, M., Eiken, O., Holloway, S., Kirby, G. A., Pearce, J. M., Williamson, J. P., and Zweigel, P. (2009). "Review of monitoring issues and technologies associated with the long-term underground storage of carbon dioxide." *Geological Society, London, Special Publications*, 313(1): 257-275.

Chen, S.-E., and Liu, Y. (2011). "Geophysical sensing for CO_2 sequestration and enhanced oil recovery." *2011 GeoHunan International Conference - Contemporary Topics on Testing, Modeling, and Case Studies of Geomaterials, Pavements, and Tunnels, June 9, 2011 - June 11, 2011*, American Society of Civil Engineers (ASCE), Hunan, China, 41-48.

Chen, S.-E., Liu, Y., and Wang, P. (2011). "DoReMi-A passive geophysical monitoring technique for CO_2 injection." *Society of Petroleum Engineers Eastern Regional Meeting 2011, August 17, 2011 - August 19, 2011*, Society of Petroleum Engineers (SPE), Columbus, OH, United states, 254-266.

Chen, S.-E., and Qi, W. (2009). "Carbon dioxide enhanced oil production from the Citronelle Oil Field in the Rodessa Formation, South Alabama, Geostability Analysis." Technical Report, The University of North Carolina at Charlotte.

Chen, W. H., and Fan, C. N. (1987). "Stability analysis with lumped mass and friction effects in elastically supported pipes conveying fluid." *Journal of Sound and Vibration*, 119(3): 429-442.

Ching, J., and Glaser, S. (2001). "1D time-domain solution for seismic ground motion prediction." *Journal of Geotechnical and Geoenvironmental Engineering*, 127(1): 36-47.

Clough, R. W. (1969). "Analysis of structural vibrations and dynamic response " *Japan-U.S. Seminar on Matrix Methods of Structural Analysis and Design*, Tokyo, Japan.

Davis, J. C. (1986). *Statistics and Data Analysis in Geology*, Wiley, New York.

Davis, T. L., Terrell, M. J., Benson, R. D., Cardona, R., Kendall, R. R., and Winarsky, R. (2003). "Multicomponent seismic characterization and monitoring of the CO_2 flood at Weyburn Field, Saskatchewan." *The Leading Edge*, 22(7): 696-697.

Driscoll, F. R., Lueck, R. G., and Nahon, M. (2000). "Development and validation of a lumped-mass dynamics model of a deep-sea ROV system." *Applied Ocean Research*, 22(3): 169-182.

Duncan, P. M., and Eisner, L. (2010). "Reservoir characterization using surface microseismic monitoring." *Geophysics*, 75(5): 75A139-175A146.

Dupac, M. (2005). "Modeling and Analysis of a Levitated Droplet using Lumped Masses." Ph.D. Dissertation, Auburn University, Ann Arbor.

Dupac, M., Marghitu, D., and Beale, D. (2002). "Lumped mass modelling and chaotic behavior of an elastic levitated droplet." *Nonlinear Dynamics*, 27(4): 311-326.

EIA (2014). "International Energy Statistics." *U.S. Energy Information Administration*, <http://www.eia.gov/cfapps/ipdbproject/iedindex3.cfm?tid=90&pid=44&aid=8&cid=regions,&syid=1980&eyid=2011&unit=MMTCD>. (March 22, 2014).

Erath, B. D., Zañartu, M., Stewart, K. C., Plesniak, M. W., Sommer, D. E., and Peterson, S. D. (2013). "A review of lumped-element models of voiced speech." *Speech Communication*, 55(5): 667-690.

Esposito, R., Pashin, J., Hills, D., and Walsh, P. (2010). "Geologic assessment and injection design for a pilot CO_2-enhanced oil recovery and sequestration demonstration in a heterogeneous oil reservoir: Citronelle Field, Alabama, USA." *Environmental Earth Sciences*, 60(2): 431-444.

Esposito, R. A., Pashin, J. C., and Walsh, P. M. (2008). "Citronelle Dome: A giant opportunity for multizone carbon storage and enhanced oil recovery in the Mississippi Interior Salt Basin of Alabama." *Environmental Geosciences*, 15(2): 53-62.

Gaspar Ravagnani, A. T. F. S., Ligero, E. L., and Suslick, S. B. (2009). "CO_2 sequestration through enhanced oil recovery in a Mature Oil Field." *Journal of Petroleum Science and Engineering*, 65(3–4): 129-138.

Gasperikova, E., and Hoversten, G. M. (2008). "Gravity monitoring of CO_2 movement during sequestration: Model studies." *Geophysics*, 73(6): WA105-WA112.

Giese, R., Henninges, J., Lüth, S., Morozova, D., Schmidt-Hattenberger, C., Würdemann, H., Zimmer, M., Cosma, C., and Juhlin, C. (2009). "Monitoring at the CO_2 SINK site: A concept integrating geophysics, geochemistry and microbiology." *Energy Procedia*, 1(1): 2251-2259.

Glaser, S. D., and Baise, L. G. (2000). "System identification estimation of soil properties at the Lotung site." *Soil Dynamics and Earthquake Engineering*, 19(7): 521-531.

Gupta, A. K. (1992). *Response Spectrum Method in Seismic Analysis and Design of Structures*, CRC Press, Boca Raton, FL.

Hadid, M., and Afra, H. (2000). "Sensitivity analysis of site effects on response spectra of pipelines." *Soil Dynamics and Earthquake Engineering*, 20(1–4): 249-260.

Halmann, M. M., and Steinberg, M. (1999). *Greenhouse Gas Carbon Dioxide Mitigation : Science and Technology*, Lewis Publishers, Boca Raton, FL.

Hardin, B. O., and Drnevich, V. P. (1972). "Shear modulus and damping in soils: measurement and parameter effects." *Journal of the Soil Mechanics and Foundations Division*, 98(6): 603-624.

Hashash, Y., and Park, D. (2002). "Viscous damping formulation and high frequency motion propagation in non-linear site response analysis." *Soil Dynamics and Earthquake Engineering*, 22(7): 611-624.

Hashash, Y. M. A., and Park, D. (2001). "Non-linear one-dimensional seismic ground motion propagation in the Mississippi Embayment." *Engineering Geology*, 62(1–3): 185-206.

Hatchell, P., Van Den Beukel, A., Molenaar, M., Maron, K., Kenter, C., Stammeijer, J., Van Der Velde, J., and Sayers, C. (2003). "Whole earth 4D: Reservoir monitoring geomechanics." *73rd SEG Meeting, Dallas, USA, Expanded Abstracts*, 1330-1333.

Hawkins, K., Harris, P. E., and Conroy, G. R. (2006). "Estimating production induced stress changes from 4D finite offset timeshifts." *Society of Petroleum Engineers, 68th European Association of Geoscientists and Engineers Conference and Exhibition, incorporating SPE EUROPEC 2006, EAGE 2006: Opportunities in Mature Areas, June 12, 2006 - June 15, 2006*, Society of Petroleum Engineers, Vienna, Austria, 3014-3018.

Hawkins, K., Howe, S., Hollingworth, S., Conroy, G., Ben-Brahim, L., Tindle, C., Taylor, N., Joffroy, G., and Onaisi, A. (2007). "Production-induced stresses from time-lapse time shifts: A geomechanics case study from Franklin and Elgin Fields." *The Leading Edge*, 26(5): 655-662.

Herwanger, J. V., and Horne, S. A. (2009). "Linking reservoir geomechanics and time-lapse seismics: Predicting anisotropic velocity changes and seismic attributes." *Geophysics*, 74(4): W13-W33.

Holloway, S. (2005). "Underground sequestration of carbon dioxide - a viable greenhouse gas mitigation option." *Energy*, 30(11-12): 2318-2333.

Hosa, A., Esentia, M., Stewart, J., and Haszeldine, S. (2011). "Injection of CO_2 into saline formations: Benchmarking worldwide projects." *Chemical Engineering Research & Design*, 89(9): 1855-1864.

Hoversten, G. M., and Gasperikova, E. (2003). "Investigation of Novel Geophysical Techniques for Monitoring CO_2 Movement during Sequestration."Lawrence Berkeley National Laboratory, Bekeley, CA:2003. LBNL-54110.

Hoversten, G. M., Gritto, R., Daley, T. M., Majer, E. L., and Myer, L. R. (2002). "Crosswell seismic and electromagnetic monitoring of CO_2 sequestration." *Sixth International Conference on Greenhouse Gas Control Technologies*, J. Gale, and Y. Kaya, eds.Kyoto, Japan, 371-376.

Idriss, I. M., and Seed, H. B. (1967). "Response of Horizontal Soil Layers during Earthquakes." Soil Mechanics and Bituminous Materials Laboratory, University of California, Berkeley, California.

Idriss, I. M., and Seed, H. B. (1968a). "An analysis of ground motions during the 1957 San Francisco earthquake." *Bulletin of the Seismological Society of America*, 58(6): 2013-2032.

Idriss, I. M., and Seed, H. B. (1968b). "Seismic response of horizontal soil layers." *Journal of the Soil Mechanics and Foundations Division*, 94(4): 1003-1034.

Idriss, I. M., and Seed, H. B. (1970). "Seismic response of soil deposits." *Journal of the Soil Mechanics and Foundations Division*, 96(2): 631-638.

Kamman, J., and Huston, R. (2001). "Multibody dynamics modeling of variable length cable systems." *Multibody System Dynamics*, 5(3): 211-221.

Kearey, P., Brooks, M., and Hill, I. (2002). *An Introduction to Geophysical Exploration*, Blackwell Science Ltd.

Kirby, H., Paes, R., and Flores, J. (2005). "Speed control of electric submersible pumps - the "Current" approach." *2005 IEEE Industry Applications Conference, Fourtieth IAS Annual Meeting*Hong Kong, 1908-1918.

Knothe, K. L., and Grassie, S. L. (1993). "Modelling of railway track and vehicle/track interaction at high frequencies." *Vehicle System Dynamics*, 22(3-4): 209-262.

Kovscek, A. R. (2002). "Screening criteria for CO_2 storage in oil reservoirs." *Petroleum Science & Technology*, 20(7/8): 841.

Kuhlemeyer, R. L., and Lysmer, J. (1973). "Finite element method accuracy for wave propagation problems." *Journal of Soil Mechanics and Foundations Division*, 99(5): 421-427.

Lake, L. W. (1989). *Enhanced Oil Recovery*, Prentice Hall, Englewood Cliffs, N.J.

Lisa, W., and DeCapua, N. (1974). "Linear lumped-mass modeling techniques for blast loaded structures." *The shock and vibration bulletin. Part 2. Invited papers, structural dynamics*, Naval Research Laboratory, Washington D.C., 111.

Liu, Y. (2012). "DoReMi- A Passive Geophysical Technique and Development of Bilinear Model for CO_2 Injection."M.S. Thesis, University of North Carolina at Charlotte, Charlotte.

Louie, J. N. (2001). "Faster, better: Shear-wave velocity to 100 meters depth from refraction microtremor arrays." *Bulletin of the Seismological Society of America*, 91(2): 347-364.

Lysmer, J. (1970). "Lumped mass method for Rayleigh waves." *Bulletin of the Seismological Society of America*, 60(1): 89-104.

Masciola, M. D., Nahon, M., and Driscoll, F. R. (2011). "Static analysis of the lumped mass cable model using a shooting algorithm." *Journal of Waterway, Port, Coastal, and Ocean Engineering*, 138(2): 164-171.

Matasovic, N. (1993). "Seismic Response of Composite Horizontally-Layered Soil Deposits." Ph.D. Dissertation, University of California, Los Angeles, Los Angeles, California.

Mathews, J. H., and Fink, K. D. (2004). *Numerical Methods using MATLAB*, Pearson, Upper Saddle River, N.J.

Maxwell, S. C., Rutledge, J., Jones, R., and Fehler, M. (2010). "Petroleum reservoir characterization using downhole microseismic monitoring." *Geophysics*, 75(5): 75A129-175A137.

Maxwell, S. C., and Urbancic, T. I. (2001). "The role of passive microseismic monitoring in the instrumented oil field." *The Leading Edge*, 20(6): 636-639.

McKenna, J. J., Gurevich, B., Urosevic, M., and Evans, B. J. (2003). "Rock Physics – Application to Geological Storage of CO_2." *Journal of the Australian Petroleum Production and Exploration Association*, 43(1): 567-576.

MicroStrain (2007). "G-Link Wireless Accelerometer Node, User's Manual, Version 4.0.3." MicroStrain, Williston, VT.

Mooi, H. G., and Huibers, J. H. A. M. (2000). "Simple and effective lumped mass models for determining kinetics and dynamics of car-to-car crashes." *International Journal of Crashworthiness*, 5(1): 7-24.

Morris, J. P., Hao, Y., Foxall, W., and McNab, W. (2011). "In salah CO_2 storage JIP: hydromechanical simulations of surface uplift due to CO_2 injection at in salah." *Energy Procedia*, 4(0): 3269-3275.

Mutschler, T., Triantafyllidis, T., and Balthasar, K. (2009). "Geotechnical investigations of cap rocks above CO_2-resevoirs." *Energy Procedia*, 1(1): 3375-3382.

Newmark, N. M. (1952). *Computation of Dynamic Structural Response in the Range Approaching Failure*, Department of Civil Engineering, University of Illinois.

Newmark, N. M. (1959). "A method of computation for structural dynamics." *Journal of the Engineering Mechanics Division*, 85(3): 67-94.

O'Connor, W. J. (2007). "Theory of wave analysis of lumped flexible systems." *American Control Conference, 2007. ACC '07*New York, NY, 4215-4220.

OGJ (2010). "2010 worldwide EOR survey." *Oil and Gas Journal*: 41-53.

Onuma, T., Okada, K., and Otsubo, A. (2011). "Time series analysis of surface deformation related with CO_2 injection by satellite-borne SAR interferometry at In Salah, Algeria." *Energy Procedia*, 4(0): 3428-3434.

Optim (2006). "User's Manual: SeisOpt ReMi version 4.0." Optim, Inc., Reno, NV.

Park, D., and Hashash, Y. M. A. (2004). "Soil damping formulation in nonlinear time domain site response analysis." *Journal of Earthquake Engineering*, 08(02): 249-274.

Phillips, C., and Hashash, Y. (2009). "Damping formulation for nonlinear 1D site response analyses." *Soil Dynamics and Earthquake Engineering*, 29(7): 1143-1158.

Pielke, R., Gratz, J., Landsea, C., Collins, D., Saunders, M., and Musulin, R. (2008). "Normalized hurricane damage in the United States: 1900–2005." *Natural Hazards Review*, 9(1): 29-42.

Plasynski, S. I., Litynski, J. T., McIlvried, H. G., and Srivastava, R. D. (2009). "Progress and new developments in carbon capture and storage." *Critical Reviews in Plant Sciences*, 28(3): 123-138.

Provot, X. (1995). "Deformation constraints in a mass-spring model to describe rigid cloth behaviour." *Graphics interface*, Canadian Information Processing Society, 147-154.

Qi, W. (2010). "Preliminary Studies and Baseline Results for the Development of DoReMi for CO_2 Injection Monitoring at Citronelle, Alabama."M.S. Thesis, University of North Carolina at Charlotte, Charlotte.

Ranger, N., and Niehörster, F. (2012). "Deep uncertainty in long-term hurricane risk: Scenario generation and implications for future climate experiments." *Global Environmental Change*, 22(3): 703-712.

Rayleigh, L. (1945, reprint). *Theory of Sound, Vol. I.*, Dover Publications, New York.

Reichle, D., Houghton, J., Kane, B., and Ekmann, J. (1999). "Carbon Sequestration Research and Development." Oak Ridge National Lab., TN (US); National Energy Technology Lab., Pittsburgh, PA (US); National Energy Technology Lab., Morgantown, WV (US).

Rétháti, L. (1988). *Probabilistic Solutions in Geotechnics*, Elsevier Science.

Rezaiguia, I., Mahfoud, K., Kamel, T., Belghar, N., and Saouli, S. (2010). "Numerical simulation of the entropy generation in a fluid in forced convection on a plane surface while using the method of Runge-Kutta." *European Journal of Scientific Research*, 42(4): 637-643.

Rutqvist, J., Vasco, D. W., and Myer, L. (2010). "Coupled reservoir-geomechanical analysis of CO_2 injection and ground deformations at In Salah, Algeria." *International Journal of Greenhouse Gas Control*, 4(2): 225-230.

Sato, K., Mito, S., Horie, T., Ohkuma, H., Saito, H., Watanabe, J., and Yoshimura, T. (2009). "A monitoring framework for assessing underground migration and containment of carbon dioxide sequestered in an onshore aquifer." *Energy Procedia*, 1(1): 2261-2268.

Schamaun, J. T. (1981). *Lumped Mass Modeling of Overburden Motion during Explosive Blasting*, Sandia National Laboratories, Albuquerque, N.M.

Seed, H., Wong, R., Idriss, I., and Tokimatsu, K. (1986). "Moduli and damping factors for dynamic analyses of cohesionless soils." *Journal of Geotechnical Engineering*, 112(11): 1016-1032.

Seed, H. B., and Idriss, I. M. (1969). "Influence of soil conditions on ground motions during earthquakes." *Journal of the Soil Mechanics and Foundations Division*, 95(1): 99-137.

Seed, H. B., and Idriss, I. M. (1970). "Soil Moduli and Damping Factors for Dynamic Response Analyses." *Technical report EERC 70-10*, Earthquake Engineering Research Center, University of California, Berkeley.

Sherlock, D., Toomey, A., Hoversten, M., Gasperikova, E., and Dodds, K. (2006). "Gravity monitoring of CO_2 storage in a depleted gas field: A sensitivity study." *Exploration Geophysics*, 37(1): 37-43.

Smith, R. H., and Newmark, N. M. (1958). "Numerical Integration for One-Dimensional Stress Waves." College of Engineering. University of Illinois at Urbana-Champaign., Champaign, IL.

Smith, W. D. (1975). "The application of finite element analysis to body wave propagation problems." *Geophysical Journal of the Royal Astronomical Society*, 42(2): 747-768.

Steiner, B., Saenger, E. H., and Schmalholz, S. M. (2008). "Time reverse modeling of low-frequency microtremors: Application to hydrocarbon reservoir localization." *Geophysical Research Letters*, 35(3): L03307.

Stoneley, R. (1955). "Rayleigh waves in a medium with two surface layers (Second Paper)." *Geophysical Supplements to the Monthly Notices of the Royal Astronomical Society*, 7(2): 71-75.

Travers, J., and Shepherd, R. (1973). "Wave propagation and lumped mass analysis techniques applied to the determination of the response of multiple layered systems to sinusoidal and seismic excitation." *Proceedings, Fifth World Conference on Earthquake Engineering, Rome*, 314-318.

Tu, Z. H., Lim, C. T., and Shim, V. P. W. (2001). "A lumped mass numerical model for cellular materials deformed by impact." *International Journal for Numerical Methods in Engineering*, 50(11): 2459-2488.

Verdon, J. P. (2012). "Microseismic Monitoring and Geomechanical Modelling of CO_2 Storage in Subsurface Reservoirs." Ph.D. Dissertation, University of Bristol, Bristol, UK.

Verdon, J. P., Kendall, J.-M., and White, D. J. (2012). "Monitoring carbon dioxide storage using passive seismic techniques." *Proceedings of the ICE-Energy*, 165(2): 85-96.

Verdon, J. P., Kendall, J.-M., White, D. J., Angus, D. A., Fisher, Q. J., and Urbancic, T. (2010). "Passive seismic monitoring of carbon dioxide storage at Weyburn." *The Leading Edge*, 29(2): 200-206.

Vilamajó, E., Queralt, P., Ledo, J., and Marcuello, A. (2013). "Feasibility of monitoring the Hontomín (Burgos, Spain) CO_2 storage site using a deep EM source." *Surveys in Geophysics*, 34(4): 441-461.

Wang, G., Wen, J., Liu, Y., and Wen, X. (2004). "Lumped-mass method for the study of band structure in two-dimensional phononic crystals." *Physical Review B*, 69(18): 184302.

Webre, P. (2012). "Federal Efforts to Reduce the Cost of Capturing and Storing Carbon Dioxide." Congress of the United States, Congressional Budget Office, Washington, D.C.

White, C. M., Strazisar, B. R., Granite, E. J., Hoffman, J. S., and Pennline, H. W. (2003). "Separation and capture of CO_2 from large stationary sources and sequestration in geological gormations—Coalbeds and deep saline aquifers." *Journal of the Air & Waste Management Association*, 53(6): 645-715.

White, D. (2009). "Monitoring CO_2 storage during EOR at the Weyburn-Midale Field." *The Leading Edge*, 28(7): 838-842.

White, D. J. (2011). "Geophysical monitoring of the Weyburn CO_2 flood: Results during 10 years of injection." *Energy Procedia*, 4(0): 3628-3635.

Williams, J. G. (1987). "The analysis of dynamic fracture using lumped mass-spring models." *International Journal of Fracture*, 33(1): 47-59.

Wolf, J. P. (1985). *Dynamic Soil-Structure Interaction*, Prentice-Hall Englewood Cliffs, NJ.

Wu, S. R. (2006). "Lumped mass matrix in explicit finite element method for transient dynamics of elasticity." *Computer Methods in Applied Mechanics and Engineering*, 195(44–47): 5983-5994.

Zhdanov, M. S., Endo, M., Black, N., Spangler, L., Fairweather, S., Hibbs, A., Eiskamp, G., and Will, R. (2013). "Electromagnetic monitoring of CO_2 sequestration in deep reservoirs." *First Break*, 31(2): 71-78.

Zhong, W. Y., and Haigh, J. D. (2013). "The greenhouse effect and carbon dioxide." *Weather*, 68(4): 100-105.

APPENDIX A: EFFECTIVE STIFFNESS

For an idealized horizontal layer soil profile, assume the elastic modulus of a certain layer is *E*, the thickness of the layer is *H*. In the study of the influence of the layer changes, the layer was divided into N^{th} sublayers with equal thickness.

The thickness of the sublayer is given by

$$h = h_i = \frac{H}{N}$$

where $i = 1, 2, \cdots, N$.

The stiffness of the sublayer is given by

$$k_i = \frac{E}{h_i}$$

or

$$k = k_i = \frac{NE}{H}$$

The effective stiffness of the layer:

$$k_{effective} = \frac{1}{\sum_{i=1}^{N} \frac{1}{k_i}} = \frac{1}{\frac{N}{k}} = \frac{k}{N} = \frac{E}{H}$$

The above equation shows that no matter how many sublayers with equal thickness were divided, the effective stiffness of the layer is a constant.

APPENDIX B: MATLAB CODES

A.1 Linear MDOF Program

```
clc; clear all;
tic
gravity = 32.2; % ft/s2

load('inputsignal.mat') % input signal, 20 sinusoid
A = 0.675; % Loading magnitude, kips - 3000 N
tend = 10; % The end time of computation
t1 = 1; % The end time of the force
h = 0.001; % Time step
kFactor = 1.0; % kFactor = 1.0,1.2,1.4,1.6, 1.8 or 2.0
indexNum = [1 13 26 41 63 88 113 138 176 226 288 363 476 534];
matrixDisp = zeros(10001,length(indexNum)+1);
matrixDisp(:,1) = 0:h:tend;
matrixVel = matrixDisp;
matrixAcc = matrixDisp;
thickness = 20;
thicknessSubLayer = [thickness thickness thickness thickness thickness 200];
% thickness of sublayer, ft
thicknessLayer = [2000 1000 3000 1000 3600 800]; % thickness of main layer, ft
elasticModulusLayer = [68421680 228158494 465629580  ...
                                586971294 728802725 805468363]; % unit is psf
unitWeightLayer = [168.6153 168.6153 168.6153 168.6153 156.16356 156.16356]; % unit is pcf
nLayer = round(thicknessLayer./thicknessSubLayer);
dof = sum(nLayer);
 stiValue = elasticModulusLayer./thicknessSubLayer/1000;
massValue = unitWeightLayer.*thicknessSubLayer/1000;
sti = [stiValue(1)*ones([1,nLayer(1)]) ...
    stiValue(2)*ones([1,nLayer(2)]) ...
    stiValue(3)*ones([1,nLayer(3)]) ...
    stiValue(4)*ones([1,nLayer(4)]) ...
    stiValue(5)*ones([1,nLayer(5)]) ...
    stiValue(6)*ones([1,nLayer(6)])];

mass = [massValue(1)*ones([1,nLayer(1)]) ...
    massValue(2)*ones([1,nLayer(2)]) ...
    massValue(3)*ones([1,nLayer(3)]) ...
    massValue(4)*ones([1,nLayer(4)]) ...
    massValue(5)*ones([1,nLayer(5)]) ...
    massValue(6)*ones([1,nLayer(6)])];

dam = ones([1,dof]); % Each layer's damping force is assumed to 1 kips/(ft/sec)

for i = 1:dof
    dam(i) = sqrt(sti(i)*mass(i)/gravity); %Damping Coefficient of each layer, kips/(ft/sec)
end
```

```
 sti(531:534) = kFactor*sti(531:534); % Stiffness of the oil bearing layer

stiff = zeros(dof);
damp = zeros(dof);

t = 0;
u = zeros([1,dof]);
v = zeros([1,dof]);
k = zeros([4,dof]);
   damp(1,1) = dam(1)+dam(2);
   damp(1,2) = - dam(2);
   for j = 2:dof-1
      damp(j,j) = dam(j) + dam(j+1);
      damp(j,j-1) = - dam(j);
      damp(j,j+1) = - dam(j+1);
   end
   damp(dof,dof-1) = - dam(dof);
   damp(dof,dof) = dam(dof);

   stiff(1,1) = sti(1) + sti(2);
   stiff(1,2) = - sti(2);
   for j = 2:dof-1
      stiff(j,j) = sti(j) + sti(j+1);
      stiff(j,j-1) = - sti(j);
      stiff(j,j+1) = - sti(j+1);
   end
   stiff(dof,dof-1) = - sti(dof);
   stiff(dof,dof) = sti(dof);

[acc,applied_force] = acceleration_L(dam,damp,sti,stiff,v,u,gravity,mass,dof,...
   t,t1,A,inputsignal,h);
[acc,u,v,matrixDisp,matrixVel,matrixAcc] = runge_kutta_L(dof,t,t1,tend,h,u,v,k,dam,damp,...

sti,stiff,gravity,mass,acc,A,applied_force,inputsignal,nLayer,matrixDisp,matrixVel,matrixAcc,ind
exNum);

toc


function [ acc,u,v,matrixDisp,matrixVel,matrixAcc ] =
runge_kutta_L(dof,t,t1,tend,h,u,v,k,dam,damp,sti,stiff,gravity,mass,acc,...
   A,applied_force,inputsignal,nLayer,matrixDisp,matrixVel,matrixAcc,indexNum)

oldu = zeros(1,dof);
oldv = zeros(1,dof);

num = 1;
while t <= tend
   num = num + 1;
   t = t + h/2.0;
```

```
    % Step 1
    for i = 1:dof
        oldu(i) = u(i);
        oldv(i) = v(i);
        k(1,i) = acc(i) * h;
        u(i) = oldu(i) + h*(oldv(i)/2.0 + k(1,i)/8.0);
        v(i) = oldv(i) + k(1,i)/2.0;
    end
    [acc,applied_force] =
acceleration_L(dam,damp,sti,stiff,v,u,gravity,mass,dof,t,t1,A,inputsignal,h);
    % Step 2
    for i = 1:dof
        k(2,i) = acc(i) * h;
        v(i) = oldv(i) + k(2,i)/2.0;
    end
    [acc,applied_force] =
acceleration_L(dam,damp,sti,stiff,v,u,gravity,mass,dof,t,t1,A,inputsignal,h);
    % Step 3
    t = t + h/2.0;
    for i = 1:dof
        k(3,i) = acc(i) * h;
        u(i) = oldu(i) + h*(oldv(i) + k(3,i)/2.0);
        v(i) = oldv(i) + k(3,i);
    end
    [acc,applied_force] =
acceleration_L(dam,damp,sti,stiff,v,u,gravity,mass,dof,t,t1,A,inputsignal,h);
    % Step 4
    for i = 1:dof
        k(4,i) = acc(i) * h;
        u(i) = oldu(i) + h*(oldv(i) + (k(1,i) + k(2,i) + k(3,i))/6.0);
        v(i) = oldv(i) + (k(1,i)+2*(k(2,i) + k(3,i)) + k(4,i))/6.0;
    end
    [acc,applied_force] =
acceleration_L(dam,damp,sti,stiff,v,u,gravity,mass,dof,t,t1,A,inputsignal,h);

    matrixDisp(num,2:end) = u(indexNum);
    matrixVel(num,2:end) = v(indexNum);
    matrixAcc(num,2:end) = acc(indexNum);

end

    xlswrite('Disp_Time_History.xlsx', matrixDisp)
    xlswrite('Vel_Time_History.xlsx', matrixVel)
    xlswrite('Acc_Time_History.xlsx', matrixAcc)
end


function [acc,applied_force] =
acceleration_L(dam,damp,sti,stiff,v,u,gravity,mass,dof,t,t1,A,inputsignal,h)
```

```
acc = zeros(1,dof);
applied_force = zeros(1,dof);

for i = 1:dof
   if (i == dof && t <= t1)
      value = int64(2*t/h + 1);
      f = A*inputsignal(value);
   else
      f = 0;
   end

   d =0.0;
   q = 0.0;

   for j = 1:dof
      d = d + damp(i,j) * v(j);
      q = q + stiff(i,j) * u(j);
   end

   acc(i) = (f - d - q) * gravity / mass(i);
end

end
```

A.2. Nonlinear MDOF Program

```
clc; clear all;
tic
gravity = 32.2; % ft/s2

load('inputsignal.mat') % input signal, 20 sinusoid
A = 0.675; % Loading magnitude, kips - 3000 N
tend = 10; % The end time of computation
t1 = 1; % The end time of the force
h = 0.001; % Time step

indexNum = [1 13 26 41 63 88 113 138 176 226 288 363 476 534];
matrixDisp = zeros(10001,length(indexNum)+1);
matrixDisp(:,1) = 0:h:tend;
matrixVel = matrixDisp;
matrixAcc = matrixDisp;

thickness = 20;
thicknessSubLayer = [thickness thickness thickness thickness thickness 200];
% thickness of sublayer, ft
thicknessLayer = [2000 1000 3000 1000 3600 800]; % thickness of main layer, ft
elasticModulusLayer = [68421680 228158494 465629580 586971294  ...
                       728802725 805468363]; % unit is psf
unitWeightLayer = [168.6153 168.6153 168.6153 168.6153 156.16356 156.16356]; % unit is pcf
```

```
nLayer = round(thicknessLayer./thicknessSubLayer);
dof = sum(nLayer);
stiValue = elasticModulusLayer./thicknessSubLayer/1000;
massValue = unitWeightLayer.*thicknessSubLayer/1000;
sti = [stiValue(1)*ones([1,nLayer(1)]) ...
   stiValue(2)*ones([1,nLayer(2)]) ...
   stiValue(3)*ones([1,nLayer(3)]) ...
   stiValue(4)*ones([1,nLayer(4)]) ...
   stiValue(5)*ones([1,nLayer(5)]) ...
   stiValue(6)*ones([1,nLayer(6)])];

mass = [massValue(1)*ones([1,nLayer(1)]) ...
   massValue(2)*ones([1,nLayer(2)]) ...
   massValue(3)*ones([1,nLayer(3)]) ...
   massValue(4)*ones([1,nLayer(4)]) ...
   massValue(5)*ones([1,nLayer(5)]) ...
   massValue(6)*ones([1,nLayer(6)])];

dam = ones([1,dof]); % Each layer's damping force is assumped to 1 kips/(ft/sec)

for i = 1:dof
   dam(i) = sqrt(sti(i)*mass(i)/gravity); %Damping Coefficient of each layer, kips/(ft/sec)
end

stiff = zeros(dof);
damp = zeros(dof);

t = 0;
u = zeros([1,dof]);
v = zeros([1,dof]);
k = zeros([4,dof]);

   damp(1,1) = dam(1)+dam(2);
   damp(1,2) = - dam(2);
   for j = 2:dof-1
      damp(j,j) = dam(j) + dam(j+1);
      damp(j,j-1) = - dam(j);
      damp(j,j+1) = - dam(j+1);
   end
   damp(dof,dof-1) = - dam(dof);
   damp(dof,dof) = dam(dof);

[acc,applied_force] =
acceleration_NL(dam,damp,sti,stiff,v,u,gravity,mass,dof,t,t1,A,inputsignal,h);

[acc,u,v,matrixDisp,matrixVel,matrixAcc] = runge_kutta_NL(dof,t,t1,tend,h,u,v,k,dam,damp,...

sti,stiff,gravity,mass,acc,A,applied_force,inputsignal,nLayer,matrixDisp,matrixVel,matrixAcc,ind
exNum);
```

```
    xlswrite('Disp_Time_History.xlsx', matrixDisp)
    xlswrite('Vel_Time_History.xlsx', matrixVel)
    xlswrite('Acc_Time_History.xlsx', matrixAcc)

toc


function [ acc,u,v,matrixDisp,matrixVel,matrixAcc ] =
runge_kutta_NL(dof,t,t1,tend,h,u,v,k,dam,damp,sti,stiff,gravity,mass,acc,...
    A,applied_force,inputsignal,nLayer,matrixDisp,matrixVel,matrixAcc,indexNum)

oldu = zeros(1,dof);
oldv = zeros(1,dof);

num = 1;
while t <= tend
    num = num + 1;
    t = t + h/2.0;
    % Step 1
    for i = 1:dof
        oldu(i) = u(i);
        oldv(i) = v(i);
        k(1,i) = acc(i) * h;
        u(i) = oldu(i) + h*(oldv(i)/2.0 + k(1,i)/8.0);
        v(i) = oldv(i) + k(1,i)/2.0;
    end
    [acc,applied_force] =
acceleration_NL(dam,damp,sti,stiff,v,u,gravity,mass,dof,t,t1,A,inputsignal,h);
    % Step 2
    for i = 1:dof
        k(2,i) = acc(i) * h;
        v(i) = oldv(i) + k(2,i)/2.0;
    end
    [acc,applied_force] =
acceleration_NL(dam,damp,sti,stiff,v,u,gravity,mass,dof,t,t1,A,inputsignal,h);
    % Step 3
    t = t + h/2.0;
    for i = 1:dof
        k(3,i) = acc(i) * h;
        u(i) = oldu(i) + h*(oldv(i) + k(3,i)/2.0);
        v(i) = oldv(i) + k(3,i);
    end
    [acc,applied_force] =
acceleration_NL(dam,damp,sti,stiff,v,u,gravity,mass,dof,t,t1,A,inputsignal,h);
    % Step 4
    for i = 1:dof
        k(4,i) = acc(i) * h;
        u(i) = oldu(i) + h*(oldv(i) + (k(1,i) + k(2,i) + k(3,i))/6.0);
        v(i) = oldv(i) + (k(1,i)+2*(k(2,i) + k(3,i)) + k(4,i))/6.0;
    end
```

```
   [acc,applied_force] =
acceleration_NL(dam,damp,sti,stiff,v,u,gravity,mass,dof,t,t1,A,inputsignal,h);

   matrixDisp(num,2:end) = u(indexNum);
   matrixVel(num,2:end) = v(indexNum);
   matrixAcc(num,2:end) = acc(indexNum);

end
end

function [acc,applied_force] =
acceleration_NL(dam,damp,sti,stiff,v,u,gravity,mass,dof,t,t1,A,inputsignal,h)

acc = zeros(1,dof);
applied_force = zeros(1,dof);
kFactor = 1.0; % kFactor = 1.0,1.2,1.4,1.6, 1.8 or 2.0
for i = 1:dof
   if (i == dof && t <= t1)
      value = int64(2*t/h + 1);
      f = A*inputsignal(value);
   else
      f = 0;
   end

   d =0.0;
   q = 0.0;

      stiff(dof,dof) = sti(dof);
      stiff(dof,dof-1) = -sti(dof);

   for j = 2:dof-1
      stiff(j,j) = sti(j) + sti(j+1);
      stiff(j,j-1) = - sti(j);
      stiff(j,j+1) = - sti(j+1);
   end

      stiff(1,1) = sti(1) + sti(2);
      stiff(1,2) = - sti(2);

   for j = dof-3:dof
      if u(j)*100 >= 0.06 %Displacement control
      stiff(j,j) = stiff(j,j)*kFactor;
      end
   end

   for j = 1:dof
      d = d + damp(i,j) * v(j);
      q = q + stiff(i,j) * u(j);
   end
```

```
    acc(i) = (f - d - q) * gravity / mass(i);
end

end
```

B.3. Time histories, frequency domain, spectral amplitude percentage difference, and tripartite spectral plot

```
clear all;clc;

node1Case10 = xlsread('Vel_Time_History_WholeOilBearingLayer_1.0.xlsx');
% Case I-0: Linear
node1Case11 = xlsread('Vel_Time_History_WholeOilBearingLayer_1.2.xlsx');
% Case I-1: 1.2stiff
node1Case12 = xlsread('Vel_Time_History_WholeOilBearingLayer_1.4.xlsx');
% Case I-2: 1.4stiff
node1Case13 = xlsread('Vel_Time_History_WholeOilBearingLayer_1.6.xlsx');
% Case I-3: 1.6stiff
node1Case14 = xlsread('Vel_Time_History_WholeOilBearingLayer_1.8.xlsx');
% Case I-4: 1.8stiff
node1Case15 = xlsread('Vel_Time_History_WholeOilBearingLayer_2.0.xlsx');
% Case I-5: 2.0stiff
ft2m_factor = 0.3048; % Convert ft to meter
%%%%%%%%%%% Velocity time histories of Node 1 %%%%%%%%%%%%
figure;
plot(node1Case11(:,1),ft2m_factor*node1Case10(:,2),'color', [0.5 0.5 0.5]); hold on
plot(node1Case11(:,1),ft2m_factor*node1Case11(:,2),'r');
plot(node1Case11(:,1),ft2m_factor*node1Case12(:,2));
plot(node1Case11(:,1),ft2m_factor*node1Case13(:,2),'m');
plot(node1Case11(:,1),ft2m_factor*node1Case14(:,2),'g');
plot(node1Case11(:,1),ft2m_factor*node1Case15(:,2),'k');
set(gca,'FontName','Times New Roman','FontSize',12,'FontWeight','bold')
xlim([0 10])
xlabel('Time (Second)','FontName','Times New Roman','FontSize',12,'FontWeight','bold')
ylabel('Velocity (m/s)','FontName','Times New Roman','FontSize',12,'FontWeight','bold')
legend('NL Case I-0','NL Case I-1','NL Case I-2','NL Case I-3','NL Case I-4','NL Case I-5')
%%
%%%%%% Frequency domain of Node 1 velocity %%%%%%%%
T = 0.001;   % Sample time
Fs = 1/T;     % Sampling frequency
L = length(node1Case11(:,1));   % Length of signal
t = (0:L-1)*T;% Time vector

NFFT = 2^nextpow2(L); % Next power of 2 from length of y
f = Fs/2*linspace(0,1,NFFT/2+1);
Ycase0 = fft(ft2m_factor*node1Case10(:,2),NFFT)/L;
ycase0 = 2*abs(Ycase0(1:NFFT/2+1));
Ycase1 = fft(ft2m_factor*node1Case11(:,2),NFFT)/L;
ycase1 = 2*abs(Ycase1(1:NFFT/2+1));
```

```
Ycase2 = fft(ft2m_factor*node1Case12(:,2),NFFT)/L;
ycase2 = 2*abs(Ycase2(1:NFFT/2+1));
Ycase3 = fft(ft2m_factor*node1Case13(:,2),NFFT)/L;
ycase3 = 2*abs(Ycase3(1:NFFT/2+1));
Ycase4 = fft(ft2m_factor*node1Case14(:,2),NFFT)/L;
ycase4 = 2*abs(Ycase4(1:NFFT/2+1));
Ycase5 = fft(ft2m_factor*node1Case15(:,2),NFFT)/L;
ycase5 = 2*abs(Ycase5(1:NFFT/2+1));

figure;
plot(f,ycase0,'color', [0.5 0.5 0.5]); hold on
plot(f,ycase1,'r');
plot(f,ycase2);
plot(f,ycase3,'m');
plot(f,ycase4,'g');
plot(f,ycase5,'k');
set(gca,'FontName','Times New Roman','FontSize',12,'FontWeight','bold')
legend('NL Case I-0','NL Case I-1','NL Case I-2','NL Case I-3','NL Case I-4','NL Case I-5')
xlabel('Frequency (Hz)','FontName','Times New Roman','FontSize',12,'FontWeight','bold')
ylabel('|Velocity (m/s)|','FontName','Times New Roman','FontSize',12,'FontWeight','bold')
xlim([0 4])

%%
%%%%%%%%%% Spectral Amplitude Percentage Difference %%%%%%%%%%
hp = peakLocation(ycase0);
freq = f(hp(1:12));
ycase0Amplitude = ycase0(hp(1:12));
ycase1Amplitude = ycase1(hp(1:12));
ycase2Amplitude = ycase2(hp(1:12));
ycase3Amplitude = ycase3(hp(1:12));
ycase4Amplitude = ycase4(hp(1:12));
ycase5Amplitude = ycase5(hp(1:12));

AmplitudeDifference = zeros(5, 12);
AmplitudeDifference(1,:) = 100*(ycase1Amplitude-ycase0Amplitude)./ycase0Amplitude;
AmplitudeDifference(2,:) = 100*(ycase2Amplitude-ycase0Amplitude)./ycase0Amplitude;
AmplitudeDifference(3,:) = 100*(ycase3Amplitude-ycase0Amplitude)./ycase0Amplitude;
AmplitudeDifference(4,:) = 100*(ycase4Amplitude-ycase0Amplitude)./ycase0Amplitude;
AmplitudeDifference(5,:) = 100*(ycase5Amplitude-ycase0Amplitude)./ycase0Amplitude;

xlswrite('AmplitudeData_velocity_diff_SI.xlsx', AmplitudeDifference)

%%
%%%%%%%% Tripartite Response Spectrum %%%%%%%%%%%%%%%%%%
hpcase0 = peakLocation(ycase0);
hpcase1 = peakLocation(ycase1);
hpcase2 = peakLocation(ycase2);
hpcase3 = peakLocation(ycase3);
hpcase4 = peakLocation(ycase4);
hpcase5 = peakLocation(ycase5);
```

```
freqcase0 = f(hpcase0);
freqcase1 = f(hpcase1);
freqcase2 = f(hpcase2);
freqcase3 = f(hpcase3);
freqcase4 = f(hpcase4);
freqcase5 = f(hpcase5);
ycase0Amplitude = ycase0(hpcase0);
ycase1Amplitude = ycase1(hpcase1);
ycase2Amplitude = ycase2(hpcase2);
ycase3Amplitude = ycase3(hpcase3);
ycase4Amplitude = ycase4(hpcase4);
ycase5Amplitude = ycase5(hpcase5);

figure;
loglog(freqcase0,ycase0Amplitude,'color', [0.5 0.5 0.5]); hold on
loglog(freqcase1,ycase1Amplitude,'r');
loglog(freqcase2,ycase2Amplitude);
loglog(freqcase3,ycase3Amplitude,'m');
loglog(freqcase4,ycase4Amplitude,'g');
loglog(freqcase5,ycase5Amplitude,'k');

set(gca,'FontName','Times New Roman','FontSize',12,'FontWeight','bold')
legend('L Case I-0','L Case I-1','L Case I-2','L Case I-3','L Case I-4','L Case I-5')
xlabel('Frequency (Hz)','FontName','Times New Roman','FontSize',12,'FontWeight','bold')
ylabel('|Velocity (mm/s)|','FontName','Times New Roman','FontSize',12,'FontWeight','bold')
xlim([0.1 10])

function [ NewLocation ] = peakLocation( input_vector )

A = input_vector;
Len = length(A);
Location = zeros(1,Len);

if A(1) > A(2)
Location(1) = 1;
end

for i = 2:Len-1
   if A(i)>A(i-1) && A(i)>A(i+1)
      Location(i) = i;
   end
end

if A(Len) > A(Len-1)
Location(Len) = Len;
end

NewLocation = Location(Location~=0);

end
```

B.4 Shear Wave Velocity Calculation

```
clear all;clc;

%% Velocity Time History
Velocity = xlsread('Vel_Time_History_Saline_Calcite_1.2.xlsx');
Velocity = round(Velocity*1e6)/1e6;
ft2m_factor = 0.3048; % Convert ft to meter

%% First Arrival Method
thickness = 20;
LayerIndex = [1 13 26 41 63 88 113 138 176 226 288 363 476 534];

timeDiffFirst = zeros([1 length(LayerIndex)-1]);
LayerDiffFirst = zeros([1 length(LayerIndex)-1]);
indexDispFirst = zeros([1 length(LayerIndex)-1]);
threshold = 1e-6;
for i = 1:length(LayerIndex)
   indexDispFirst(i) = find(Velocity(:,i+1)>=threshold,1);
end
dispTimeFirst = (indexDispFirst-1)*0.001;
for i = 1:length(LayerIndex)-1
   timeDiffFirst(i) = dispTimeFirst(i) - dispTimeFirst(i+1);
   LayerDiffFirst(i) = LayerIndex(i+1) - LayerIndex(i);
end

distanceFirst = LayerDiffFirst.*thickness;
distanceFirst(end) = (LayerDiffFirst(end)-3)*thickness + 3*200;
velocityPwaveFirst = distanceFirst./timeDiffFirst;
velocitySwaveFirst = velocityPwaveFirst/1.73;
VelSwaveLineFirst = velocitySwaveFirst(ones(1,2),:);
VelSwaveLineFirst = VelSwaveLineFirst(:).';
depthPeak = cumsum(distanceFirst);
depthLine = zeros([1,2*length(depthPeak)]);
depthLine(2:2:end) = depthPeak;
depthLine(3:2:end) = depthPeak(1:end-1);

figure
set(gcf, 'position', [100 100 650 400], 'paperpositionmode', 'auto');
plot(VelSwaveLineFirst,depthLine,'k')
xTLabel = get(gca,'XTick');
set(gca,'XTickLabel',sprintf('%3.0f|',xTLabel))
set(gca, 'ydir', 'reverse', 'fontsize', 10, 'xaxislocation', 'top','FontName','Times New Roman');
xlabel('Shear-Wave Velocity, ft/s','FontName','Times New
Roman','FontSize',12,'FontWeight','bold')
ylabel('Depth, ft','FontName','Times New Roman','FontSize',12,'FontWeight','bold')
title('First Arrival Time Method','FontName','Times New
Roman','FontSize',12,'FontWeight','bold')
WaveSpeed_FirstArrival_Vel_Saline_Calcite_120 = VelSwaveLineFirst
```